Integration and Modeling of a Metasurface Spectropolarimeter for Space Applications

Master Thesis in Aerospace Engineering

Tiberiu Ceccotti

Technische Universiteit Delft

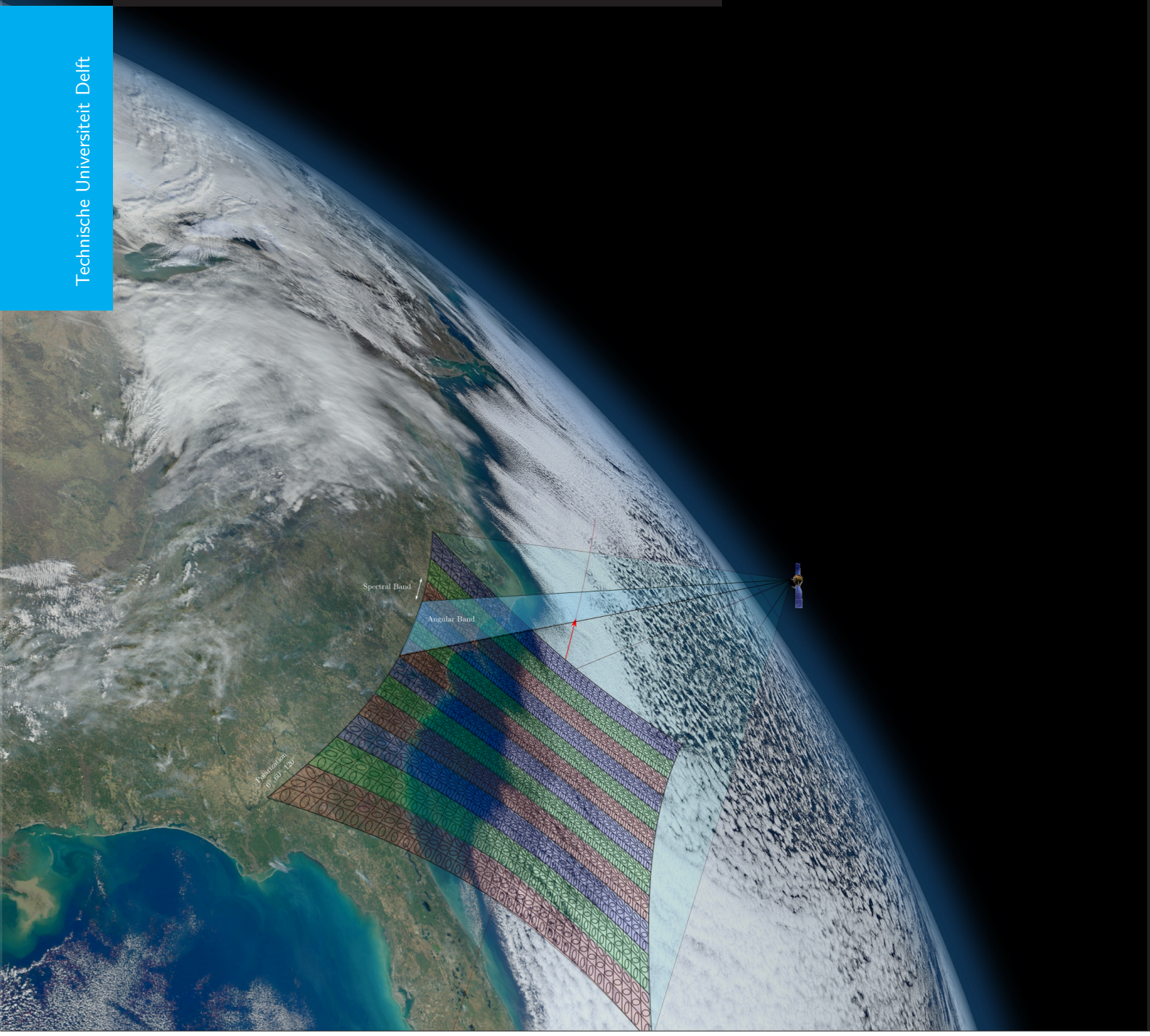

TU Delft Delft University of Technology

Challenge the future

Integration and Modeling of a Metasurface Spectropolarimeter for Space Applications

Master Thesis in Aerospace Engineering

by

Tiberiu Ceccotti

to obtain the degree of Master of Science at the Delft University of Technology

and to be defended publicly on Thursday February 27th, 2020

Space Engineering Track, Faculty of Aerospace Engineering, Delft University of Technology

a MSc Thesis project supported by TNO

Student number: 4725123

Thesis Committee:

Prof. Dr. A. (Angelo) Cervone	TU Delft, Chairperson
Dr. ir. J.M. (Hans) Kuiper	TU Delft, Supervisor
Dr. ir. Wouter van der Wal	TU Delft, Commission Member
Prof. Dr. ir. Giampiero Gerini	TNO, Industry Supervisor

TU Delft Delft University of Technology

Abstract

Electromagnetic metasurfaces in recent years have drawn significant attention in the Optics community due to their novel optical properties and miniaturized integration advantages. Since the optical properties of those materials are complex to model and require finer theory than what implied in geometrical optics, systematic integration study of those solutions is not reported in Literature and motivates this research. In previous work, the design of polarization-sensitive spectral filters based on metasurfaces devices and integrated into Bragg reflectors has been reported. The use of such a spectropolarimeter concept may lead to significant miniaturization improvements in Space applications, where launches of small satellites are becoming accessible to not-governmental companies and trending. Typical spectral and polarimetric functionalities are currently integrated with several additional components required for the propagation of light. The metasurface based spectropolarimeter concept operates in a division of focal plane and can be integrated on off-the-shelf CMOS sensors, when opportune factors are taken into considerations, with the use of a single lithographic step. The main difficulty in their use arises from the limited bandwidth dictated by the Bragg reflector and the polarization response of the metasurface, as well as strict requirements of telecentricity to limit angle-dependence at the focal plane.
In the present work, we offer novel modeling tools to predict the electromagnetic performance of the device in terms of diffraction and spectral response. We explicit how those tools, in comparison with other approaches like Finite Element Methods, can provide an efficient and physical-based assessment for the design of the spectro-polarimetric filters. We apply then such tools to analyze the diffraction of the filters and the integration of the sensor in a Space Mission for aerosol detection in the VIS and SWIR range, by designing a set of filters able to overcome the bandwidth limitations above mentioned, finally providing simple engineering figures in terms of integration requirements to be considered.
The work sets the bases for further improvements, on one side, in the modeling of those structures and on the other side in their integration in complex systems.

Preface

The report presents a 1-year work in terms of performance characterization and integration of a metasurface-based spectral filter, which has been financed and carried out at TNO (Delft) with additional support of TU Delft. Due to clarity in presenting the variety of topics, the report is presented in Parts. With the vision that physical phenomena shall not be simplified much more than necessary for their description in engineering, we use a theoretical and mathematical framework for the performance analysis. To present a self-consistent formulation, when not overly lengthy, we derive results from basic principles. Some preliminary knowledge of the reader in wave, diffractive optics and algebra is however implicitly assumed. We suggest an electronic view of this report. The numerical codes used for implementation in Python may be published on *Github* at the end of the embargo period. They shall, however, be easily implementable with the provided information. Even when thoroughly proof-checked, we are aware that errors are always around the corner. Feel free to contact me in case you determine one.

Acknowledgments When deciding to join TU Delft for my MSc Degree, I was looking for an inspiring environment to live in and further develop my knowledge from a practical point of view. The last two years have certainly met my expectations, having met great people from a variety of international backgrounds and challenged myself in plenty of new experiences.
Those events came also with the price of staying away from my family, which has always been supportive and inclusive of all my decisions. I dedicate the completion of this MSc Thesis to them, with the promise that happy moments are counted in meaningfulness rather than quantity, and many more are to come.
My girlfriend shall surely be also acknowledged as co-author for her patience and constancy. I wish her the best of luck for her MSc Thesis and all the new events to come.
Differently from the experience of other students, I had the luck to share my work with a great TNO Research Team. Giampiero, mentor and supervisor, made me feel at ease and took great care of the details.Pjotr, constantly present for questions and remarks, brought me to a more pragmatic view. Special thanks to Jérôme, which even when overly busy, took always some time to provide advice on system architecture and to James for the insight on the optical system design. I acknowledge also Arvind, with the hope to be present in his Postdoc acknowledgments, Koen for his always curious and concrete remarks, Cameron and Jonas for their interest in our weekly meetings and all new friends I found at TNO.
I have great admiration for the work and approach of Prof. Hans Kuiper, which I thank for his supervision and revision meetings. Hopefully, this research will also contribute to more collaborations and new developments between us.
Plenty of friends eased my stay at Delft and made it feel like home: Samuele, Antonio, Umberto, Liset, Vanessa, Gilles, Mitchell, Joppe, Renato, Francesco and Manuel, which will soon come. Wherever they are gonna be in the future, I hope we will be in touch!

Contents

List of Figures

List of Tables

Terminology and Symbols

In Appendix G, we report a comprehensive list of Constants and Symbols, in alphabetic order, used throughout the report. We invite the reader to refer to those when the meaning of a symbol is not clear from the context. The following the acronyms used:

3MI Multi-viewing, Multi-channel, Multi-polarization Imager

AOT Aerosol Optical Thickness

APD Avalanche Photo-diode Detector

ATF Amplitude Transfer Function

CMOS Complementary Metal Oxide Semiconductor

DBR Distributed Bragg Reflector

FEM Finite Element Method

FOV Field of View

FPA Focal Plane Array

LEO Low-Earth Orbit

NIR Near Infrared (Spectrum)

OMU Opto-Mechanical Unit

OTF Optical Transfer Function

PSF Point Spread Function

SNR Signal to Noise ratio

SPEX Spectropolarimeter for Planetary Exploration

SSA Aerosol Single Scattering Albedo

SWIR Short Wave InfraRed

SZA Solar Zenith Angle

TM-p Electric field p polarization, in the incidence plane

TE-s Electric field s polarization, perpendicular to incidence plane

TRL Technology Readiness Level

VIS Visible (Spectrum)

VISIR Integrated Visible and Infrared detectors

1
Introduction

In this Master Thesis Project, we investigate the modeling and the integration of a polarization-dependent spectral filter, proposed and preliminarily designed in [1] for a Space sensing application. The concept is promising due to its high miniaturization potential, so that we investigate its performance more thoroughly in the framework of a feasibility study for aerosol applications, sharing similar spectral ranges and requirements to the ones achievable with such concept. Nevertheless, the modeling techniques and characterization of the structure is in great part applicable also for very different applications.
This report is organized in Parts, Chapters and Sections. In Part I, after performing a concise design review of the concept in [1], we formulate clear research questions and a research framework from analysis of similar concepts and a systematic requirements analysis, based on the 3MI hyperspectral instrument and science requirements of Sentinel 7. Upon design review, it becomes clear that to perform a feasibility study of various spectral channels, pixels and configurations, a systematic and efficient performance modeling of the filter upon focusing is required. Metasurface-based design in fact usually relies on expensive FEM simulations, which even though accurate become quickly impractical for an extensive set of configurations.
We hence formulate in the Theory disclosure Part II, a threefold analytically model, based on an effective medium formulation, a transfer matrix method and a preliminary diffraction model, which shows great improvement in simulations times. The final scope of the modeling is the determination of an optimal reconstruction matrix from electromagnetic considerations, including diffraction-focusing effects. Even though based on a few assumptions and relatively complex, we demonstrate that the model can well predict the plane-wave performance of manufactured structures when the correct parameters are used (Chapter 8). In Part III, we perform an analysis of the system parameters (mission and orbital analysis, preliminary optical system sizing) for providing reasonable inputs for the feasibility study. We hence apply the previously mentioned theory to the science requirements under consideration by designing a variety of pixels covering, with the use of six DBRs, the required spectral range. We analyze systematically the performance parameters of those designs. We explicit measures to overcome the main limitations cited in [1], by analyzing the spot size and filtering techniques. Finally, we put in application the introduced modeling to experimental results of preliminary manufactured structures and suggest further experimental studies.
In Part IV, we switch point of view to a system perspective. We down-select a feasible detector architecture and perform its noise and power budget in combination with the spectral filter. We clarify on preliminary temperature requirements, dictated by the choice of the detector. We also investigate, from a simplified 1D analysis, uniform thermal expansion effects. Unfortunately, an optimized and realistic optical system for this case study could not be fully designed in the time-frame of this project, hence results of the combined optical performance of optics and filter are not available. However, the modeling techniques discussed in Part II would be still applicable. The integration analysis results in the exposure of some integration requirements, which shall be considered by optical designers when using the filters. Performance maps and parameters of the spectral filter are also reported, which summarize the filter behavior without required preliminary knowledge of the details of the modeling. A few considerations on the mass targets of the Space concept are also drawn in the conclusion of this part, with the understanding that those are rather preliminary. An estimation of cost of the system is deliberately avoided since it can't yet be estimated with any confidence level, being strongly dependent on aspects out of our control.

I

Design and Requirements Review

2

Design Review

In the present Chapter, we perform a concise review of the design proposed in [1], in order to identify areas of improvement and further activities to perform. In particular, we analyze the process-flow which leads to the choice of the modulation technique and the design, highlighting further required analysis.

2.1. Choice of a modulation technique

The main driver for the design of a miniaturized spectropolarimeter device is the necessity of a multifunctional single device able to perform all at once the spectral and polarization measurements of a given scene. Whereas, separately, solutions for spectrometers or polarizers are implemented and widely used in space and on ground, integrated spectropolarimeter measurement with full Stokes retrieval is yet very complex to implement. As reported in [1], [6] typical solutions consist of introducing modulation in the spectrum or the polarization at a certain stage of the optical system. Those modulations may be introduced with the use of filters at the detector focal plane (*division of focal plane*) or at the aperture (*division of aperture*). In the latter case, for example, the beam itself can be split and undercome different filtering, being focused on separate detectors. Modulation can be also performed on the amplitude of the field (*division of amplitude*) with the use of beam-splitters and intermediary analysis of the signal [6]. One may use a color filter on a moving wheel to apply different filtering to the beam at different times, by though jeopardizing time resolution. Other polarimetry methods are based on *channeled imaging polarimetry*, where polarization is spatially modulated in interference fringes due to diffraction of specially engineered gratings.
Many of those concepts require bulky optical systems and multiple devices and, as all optical instruments, result in a tradeoff between temporal, spatial and spectral resolution.
Parameters which influence the choice of modulation technique have been addressed in [1], who highlighted instrument volume, complexity, polarization accuracy and aliasing as main driver criteria for the tradeoff, which leads to the choice and design of a division of focal plane solution. Other important parameters influence the behavior of the spectro-polarimeter: requirements imposed on the optical system, signal to noise, aberration control, diffraction performance, cross-talk between measurements, angle dependence, manufacturing complexity and tolerancing, integration, costs, aging, thermal and radiation stability etc...The uncertainty over the estimations of those performance parameters can be minimized only once a complete optical system is designed and used as a demonstrator for the concept proposed in [1]. Nevertheless, we highlight that a few preliminary considerations regarding the above additional criteria can be drawn by more detailed modeling of the device performance and some knowledge on generic aerosol mission requirements, which is the motivation for the work undertaken in this report and the detailed analysis in the next Chapters.

2.2. Design implementation

Having selected a division of focal plane array as the driving choice for modulation technique, [1] evaluates a metasurface based filter composed of two polarization units and a spectral unit. The spectral unit consists in a narrow spectral band DBR design to provide a bandgap of $\cong 300nm$ with a spectral resolution $\cong 5nm$, depending on the number of mirrors used. The polarizer units consist in an anisotropic cavity modifying the spectral response of the DBR by means of inclusions and a waveplate array to induce phase-shift for the measurement of circular polarization. Intensity is reconstructed from a grid of 4 distinct measurements, one for each Stokes parameter, as represented in Figure 2.1

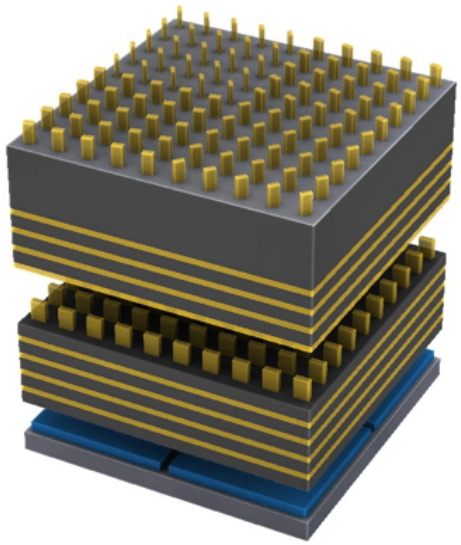

Figure 2.1: Metasurface design proposed in [1] and its integration on the detector FPA. Each pixel is composed of multiple metasurface resonators both in the cavity between the DBR mirrors and in the wave-plate array at the top of the structure.

The reconstruction can be achieved in various ways. Differently polarized light, as we will also extensively demonstrate theoretically, gets transmitted predominantly at different spectral peaks. In either case, the device works by modulating the polarization information in the amplitude of the transmitted light:

- ***Concept 1***: If both x and y polarized peaks are used, one must couple the spectral measurements with the polarization ones. For n spectral measurements, the matrix contains $4n$ entries and is usually degenerate, because of linear dependence of the measurements. As a matter of fact, without filtering at least one of the peaks, the required polarization contrast in the measurements is never achieved, since the whole spectrum is always measured at the detector. To avoid such degeneration, a grating can be used or another element with a high permittivity contrast in the cavity or on the waveplate array, to induce a spectral peak outside of the integration range. The use of this concept is limited by condition number of the reconstruction matrix, but reconstruction has been demonstrated experimentally in [4]. In this concept, more light reaches the single pixel but the information is harder to retrieve, resulting in general in a lower SNR. On the other hand, all spectrum data-points are retrieved simultaneously (so that the filter is more compact) and the statistical uncertainty over their average value after reconstruction is lower with this concept.
- ***Concept 2***: By means of filtering one of the spectral peaks, spectral measurements can be decoupled and reconstruction carried independently for all polarization states, which is the main design proposed in [1]. Such design offers a better condition number, since polarization contrast between the measurements is maximized. However, integration of multiple bands is more cumbersome since all undesired spectral peaks must be suppressed for the different spectral pixels, which requires special considerations. If a bandpass filter is used for the purpose with a single DBR design, the measurement technique is mainly limited in bandwidth and practical realizations of pixel-dependent bandpass filters. However, we propose changes in the design to avoid this intrinsic limitation, in

Section 7.4. In Concept 2, roughly half of the light reaches the single pixel, however, the condition number is greatly improved because of the eliminated inter-dependence between the measurements. As a result, the SNR achievable in the reconstructed Stokes parameters is higher. If filtering is not optimal, however, there is more uncertainty on the statistical mean of the retrieved spectrum.

The focus of the research is on the second measurement technique, since it naturally offers a better reconstruction, maximizing SNR and has already been downselected in previous work [1] for the purpose. We point out that the methods for the analysis of the concept are similar: even in the second concept, some undesired polarized light is always transmitted and influences the condition number also. So all present methods will be equally applicable for both cases by using different reconstruction methods.
The proposed design has the advantage of integration on the detector and integration of both measurements in once. Moreover, it allows achieving very narrow spectral resolution in polarization measurements, which instead on typical aerosol scattering devices is more coarse than the unpolarized intensity measurement. We have observed that in [7], [8] the polarization spectral resolution requirements are less strict than the intensity ones. According to [6] polarimetric information is not as wavelength dependent as spectral intensities. Nevertheless, an improved spectral resolution in the polarized channel is expected to enhance the reconstruction accuracy of aerosol properties.
The use of DBR mirrors, which are widely implemented and manufactured for spectrometer devices, provides flexibility in the manufacturing, with some changes to the process in order to deposit the inclusions and the waveplate array. Of course, the advanced integration does not come for free and the fact that a grid of distinct spatial measurements is used for reconstruction introduces aliasing in the measurements and possible crosstalk between the measurements. The imager arrangement must be thoughtfully designed in parallel with the buffering units in order to match the measurements during an integration time. We review a possible imager arrangement selected for the case aerosol mission considered in this report, in Chapter 6.
We further report that the use of the waveplate array is not necessary in cases in which the circular polarization of the field is negligible and must not be retrieved. Even though measurement of circular polarization has additional benefits, as in applications for exoplanets detection [9], the magnitude of the third Stokes parameter s_3 is order of magnitudes smaller than the linear polarized components [10]. The deletion of the waveplate array component, with an opportune redesign of the cavity inclusions, results in simplified manufacturing and design of the metasurface and also an improved condition number. We review such considerations also in Chapter 6 and implications of such choice on the condition number in Section 5.3.4.

2.3. Optimization of the design

Once the design has been selected, [1] analyzes a few optimization parameters in order to enhance the performance and the reconstruction. In particular, parameters which have been considered are the condition number of the Mueller Matrix associated with a normal incidence plane wave, shape of the cavity to achieve uniformity of angle response, sampling of the grid in relation to the standard deviation of the measurements, choice of sizes of the inclusions in order to minimize mechanical tolerancing effects and spectral drifts at normal incidence.
The condition number is indeed an important parameter in the performance estimation. The retrieved intensity measurements are not directly the Stokes parameters, but related to it by means of the Mueller matrix of the device. Mathematical details on such formalism are revisioned in Chapter 4.4. The Stokes parameters are hence estimated from inversion of such matrix from the input, noisy, measurements, which lead [1] to select an equidistant arrangement of the resonator cell. In the condition number study, moreover, the presence of the additional spectral peak has not been previously considered in the definition of the Mueller Matrix, assuming that a bandpass filter could be engineered for every pixel design. We will review this hypothesis, offering a design choice that may lead to the natural extinction of such a peak. It is finally important to calculate the condition number of reconstruction over a focused beam and upon accurate estimations of the polarization integrals involved in the treatment. We perform this analysis in Chapter 7.
The power budget performed in [1] requires a link with the Jones matrices of the electromagnetic propagation (to account for the partial admittance of light due to polarization filtering) and shall be further generalized in our study to account for the focusing geometry. The sizing criteria used in [1] assumes Rayleigh diffraction with a Nyquist sampling for the superpixel (the composition of the four polariza-

tion pixel cells). This sampling criteria is strongly dependent upon a diffraction analysis and heavily influences the overall transmittance behavior of the integrated solution. Moreover, [1] suggests the use of a telecentric diffraction-limited optical system, which is of too complex realization over wide ranges of wavelength. In results in Chapter 7, we suggest from the formal diffraction solution to use a significantly oversized pixel to limit diffraction cross-coupling. The overall pixel size is however not affected significantly, since [1] sized the pixels at significantly lower NA than what we suggest. As a result, the telecentric optical system is not strictly diffracted limited anymore and, we conjecture, of simpler realization.

2.4. Further required analysis

Further required analysis is suggested in [1], in particular in additional study of multiangular concept, performance upon focusing and diffraction and better characterization of the device. Within the Chapter, we have also highlighted some additional activities and interesting analysis to be performed in order to characterize the structure and its integration. In particular:

- Downselecting high-level requirements of integration from the system (top-down approach) and clarifying on constraints of the metasurface integration in terms of imposed requirements (bottom-up approach). Mainly discussed in Chapter 3.
- Downselecting, from heritage instruments with similar mission requirements, an optical system for a sound feasibility study of the integration of the device. This activity could not be carried in the provided time-frame.
- Performing some preliminary mission analysis, in terms of orbit and observation geometry, at the level required for analysis purposes of the metasurface design and its power budget. Mainly discussed in Chapter 6.
- Expanding the operating bandwidth of the concept and provide a clear design of the required spectral channels in VIS and SWIR, for a given science case set of requirements. Mainly discussed in Chapter 7.
- Determining a new arrangement design for a multiangular measurement science case in the required spectral channel which does not require s_3. Discussed in Section 6.7.
- Characterizing the electromagnetic behavior of the metasurface structure with more accuracy in terms of polarization and angle dependency (also azimuthal). Mainly discussed in Chapter 7 with concepts introduced from the methods in Chapter 4.
- Perform a polarization sensitivity analysis with respect to focusing angle, uniformity of the input signal and aberrations induced by the filter. Also discussed in Chapters 7, 4.
- Performing a formal diffraction study to verify the pixel sizing criteria used in [1] and determine cross-talk between pixels due to diffraction. Discussed in Chapters 7.
- Undertaking a formal power budget study to determine the correlation between angle dependence, spectral resolution, diffraction and NA of the focused beam undergoing a transformation in the filter. Mainly discussed in Chapter 7 and Section 9.1.
- Feed-back the results of the analysis in a list of integration requirements by means of simple engineering parameters. Discussed mainly in Part IV.

3

Requirements Analysis

In the present Chapter, we review general requirements for aerosol scattering retrieval in the VIS-NIR and SWIR. The treatment is mainly based on [7], which deduces high-level requirements for the Sentinel-7 mission. We mainly discuss generic Science Requirements and main physical parameters of importance in aerosol retrieval. The discussion is on purpose relatively broad and high-level at the present stage. From Literature Resources, we extrapolate Optical Requirements in order to meet those Science Requirements and adapt them for the case study under consideration in the Research. The 3MI case, which presents more relaxed specifications with respect to Sentinel-7, is then reviewed and its design and requirements further discussed. The use of spectral bands and the architecture of the module is discussed, as well as the Optical System architecture and thermo-mechanical integration.

3.1. Scope of Science Case

Spectropolarimeter measurements in space are used for a variety of applications:

- **Characterization of Earth atmosphere and scatterers**: the presence of particles in the atmosphere results in scattering of light. The measurement of the spectrum and polarization properties of the scattered light (which may be direct sun-light or have been reflected multiple times on the ground and the atmosphere) offers exceptional insight on the nature of those scatterers (dimensions, composition, shape, temperature, concentration...). Such measurements are used, for example, to monitor pollution in the atmosphere, climate change, weather forecasting and environmental hazards. Many other applications. depending on the mission statement of the customer requesting the measurements, are possible. In particular, narrow spectropolarimeter measurements at various observation angles are pivotal in the characterization of aerosol particles, volcanic ash and similar airborne particles.

- **Characterization of Exoplanets**: several studies have shown ([11], [12]), that exoplanets retrieval can benefit from the knowledge of spectropolarimetric information on the light scattered from their atmosphere. The application of those measurements is still technically challenging, accuracies required being in the order of $10^{-4}\%$ in s_3 [12], and further affected by reflecting surfaces, background stellar flux and gaseous absorption.

- **Defense applications**: light impinging on a surface undergoes a process of reflection which influences the field distribution. Measuring such field and retrieving its spectropolarimeter content allows, within the use of certain models, to predict to a certain extent the shape and composition of such surface. It is well known that, for target detection, the use of IR measurements is of great aid in defense and military applications. Compactness of such solutions is a significant benefit to be considered when developing new concepts for such applications. We condemn any improper use of such technology, which shall be well regulated.

We will hereby focus on the use of spectropolarimeter for Earth Observation Remote Sensing for aerosol retrieval. The choice is by no means restrictive, but somewhat necessary to get a clearer idea on system requirements and performance budgets. The majority of the modeling hereby introduced is hence applicable also for the other cases; when corrections are required, it will be explicitly stated in the report.

3.2. Science Requirements

In aerosol measurements, it is of interest measuring certain specific properties of the aerosol layers which we will review:

- **Aerosol Optical Thickness (AOT)**: is a measure of the optical length of a layer of aerosol within a column of atmosphere. The total optical length is usually known from geometry and atmospheric modeling. To determine the optical thickness of the aerosol only, it is required to subtract from the total optical length the one due to Rayleigh Scattering, vapours, ozone, CO_2, NO_2, methane and other atmospheric molecules. Detailed modeling of optical thickness of the atmospheric layers is out of the focus of the research, but is discussed in [13] within a transfer matrix method similar to the one described in Section 4 and the base for the selection of requirements used in the reference [7]. We point out that accuracy of $< 10\%$ are in the retrieval of AOT are required in [7].

- **Aerosol Single Scattering Albedo (SSA)**: is defined as the ratio between scattering efficiency and total extinction efficiency (attenuance). It mainly depends on the size of the particle, in similarity with the Mie Scattering phenomenon discussed in [14]. It is a useful parameter for determining *radiative forcing*, a measure of the absorbed sunlight in relation to the emitted one used in climate models and green-house estimations [15]. In the Sentinel-7 requirements, accuracy of 3% is used as a threshold for this parameter.

- **Aerosol effective radius**: as the name suggests, is a measure of the effective size of a spherical particle with the same volume. As already described in the simplified Rayleigh scattering model, the size drastically affects the scattering properties of the aerosol, in particular the water uptake [7]. An accuracy of $< 10\%$ $(0.1\mu m)$ is suggested in [13], [7]. The determination of effective size does also applies for missions where atmospheric hazards (e.g. fire and smoke for aero-navigation) are of interest, even though requirements for such cases may differ.

- **Variance**: the measure of an effective radius of parameters for the atmospheric layer does not carry any other information than a statistical mean of that property. Further insight on the distribution of aerosol is usually required by analysis of the variance of those parameters (for fine and coarse modes). Such variance is usually strongly dependant on the Stokes parameters that are required to be measured. The accuracy in variance measurement, according to [7] shall be $< 50\%$.

- **Refractive index**: the measurement of refractive index is required for the identification of the aerosol type and its water uptake [7], in both real and imaginary parts. Accuracy on those measurements is of 2% for the real part and 15% for the imaginary part.

- **Column and height properties**: additionally, one may require further characterizing of the layer height to determine light path

As such, those high-level science requirements still need to be translated into recognizable figures for the Optical System design. As already mentioned, a modeled characterization of those parameters with the Stokes parameters at the entrance pupil would be required for a more detailed analysis of achievable reconstruction performance, but is out of the scope for this research due to limited available time. Fortunately, some studies performed in [16], [17] help in the process of requirements flow-down.

3.3. Payload Requirements

In [18], it is demonstrated that to achieve the Science Requirements before mentioned a multi-angular spectral measurement is required, in the VIS-NIR and SWIR range. The number of required spectral bands and resolution differs depending on the choice of angles.
As we can conceptually understand, the Stokes parameters are strongly influenced by angle variations of the sunlight path even when the same point-source on ground is considered, hence the importance of retrieving Stokes parameters for various angular bands. According to [7], the product between angular bands and spectral bands is a good indication of the information content of the measurement. [7] offers a concise overview of what optical requirements are required in order to provisionally meet the Science requirements above mentioned:

- The lower the band (VIS or even UV), the higher the accuracy in fine mode aerosols and layer height.
- Inclusion of a SWIR, even though not strictly necessary and not used in HARP or some other concepts, improves $C0_2$ retrieval, aerosol size retrieval and sensitivity to coarse modes and could be traded-off with other bands or angular bands [7].
- Only linear degree of polarization is required to be measured (not necessarily s_1 and s_2 separately)
- A spectral range of $> 350nm$ is required, possibly with more than 8 spectral measurements in the band
- Radiance varies more rapidly with wavelength than polarization does [7], so spectral resolution of polarization may be coarser. That's not possible in the design under consideration for the research though (DBR design of all pixels is the same for a given superpixel, [1]).
- A non-equidistant angular band distribution is preferred, with nadir band for calibration purposes and maximum extent up to $\pm 50°$. The minimum suggested number of angular bands is 5, depending on the number of spectral bands and overall achievable spectral resolution
- A ground sampling distance better than $1 \times 1km^2$ shall be achieved for all viewing angles, once radial distortion and smearing effects are taken into consideration. The radial distortion for the required viewing angles and a small altitude may be severe, which motivated our geometrical observation study in Chapter 6.

In conclusion, to meet the science requirements, it is suggested to use more than 5 viewing-angles with a wide FOV ($> 90°$) and a spectral resolution of $5nm$ [7]. The following specifications obviously also depend on the considered orbital parameters, which we'll review in Chapter 6.
The required polarimetric error is more strict on the SNR budget than the radiometric one. In [7], a required polarimetric error of $< 0.3\%$ is required for meeting the Science Requirements with a SNR of > 500 on the reconstructed degree of polarization. Such requirements are likely to be relatively strict for the metasurface design proposed in [1]: in the metasurface concept, spectral bands is the same for polarized and unpolarized channels, and a reconstruction is required, which leads to a significantly higher required SNR on the signal at the pixel depending on the condition number of the reconstruction process. The polarization error requirements further impose rather stringent requirements in terms of anti-reflection coatings and angle-dependence at the spectral filter, as known in the design of 3MI [2]. Meeting such requirements requires an involved optical system analysis and, likely, ad-hoc developed anti-reflection coatings. Hence, a study on the polarization dependence of the metasurface is also down-selected as a driving activity for assessment of the integration.
Even though the requirements here presented are rather stringent and realistic of a real mission, we will propose a relaxation of the spectral requirements due to practical losses in the dielectric design proposed in [1] and also of the SNR requirements. A more accurate estimation of the real science case requirements for the integration of the metasurface must be developed in parallel with the choice of a project framework.

3.4. The 3MI case study: Design Review

In the upcoming Section, we review the design of the 3MI Optical System from available literature. 3MI stands for multi-viewing, multi-channel, multi-polarisation imager. The 3MI is part of the payloads of the ESA/Eutmetsat MetOp Second Generation Programme, supporting environment monitoring [19]. Along with other payloads characterizing clouds, CO_2, land surfaces, humidity, 3MI main driver is the measure of the aerosol properties, surface albedo (via measurement of the bidirectional reflectance distribution function, BRDF), water vapors and cirrus clouds, to support Numerical Weather Prediction (NWP) and calculations of Air Index Quality and Aerosol Load Masses for scientific communities [20].

3.4.1. Science Specifications and Bandwidth

The report [20] also identifies polarization retrieval as an important parameter for characterization of the ice-water clouds and estimations of aerosol sizes once information on the molecular scattering and the ground polarization contributions are properly characterized [19]. The instrument operates over VNIR and SWIR bands, which science scope is discussed in [19] and channels represented in Table 3.1. With respect to the Sentinel-7 requirements, the 3MI concept operates over the SWIR module also and with $0.4\mu m$ channels for ash clouds, finer aerosol particles and albedo determination. The addition of a SWIR channel allows for the determination of water vapor and cirrus clouds, as well as finer modes of the aerosol. The channel on $0.91\mu m$ is duplicated for coregistration purposes, necessary because of the use of two modules. In comparison with the requirements imposed in Sentinel-7, the spectral resolution is significantly degraded in this design. Nevertheless, similar specs have only been previously achieved by Polder, a prior mission for aerosol detection without as many spectral channels and angular bands. The possibility of improving spectral resolution and eliminating co-registration is a further reason for investigating the use of a metasurface as an alternative to the 3MI measurement concept. We further observe that polarized channels (channels for which measurement of s_1 and s_2 are required) have in general a coarser spectral resolution. This is likely due to science requirements and power budget considerations. The pixel pitches used in the detectors of 3MI, in fact, are relatively big ($25\mu m$ for the VNIR module and $30\mu m$ for the SWIR module). The SNR ratio on the reconstructed Stokes parameters is also degraded to 200 at some unknown reference radiances values, with respect to the Sentinel-7 requirements. Those requirements are more realistic also for the present case-study and will be used as a hard threshold for the feasibility conclusions. We further point out that the FWHM requested in 3MI is at times bigger than the channels interval in Table 3.1. Even though transmissivity spectrums of the filters are not documented, we conjecture that such configuration is still required to resolve the overlapping spectral peaks and FWHM has been traded-off in power budget estimations in some of the design phases of the 3MI concept.

3.4.2. Measurement and Observation Geometry

In 3MI, the measurement is based on a mechanical filter wheel, with a 7sec delay between the acquisition of measurements. Due to this concept, the number of angular samples (even if angular oversampling is implemented in the SWIR channel) in 3MI required to be traded-off and their displacement is not uniform in the FOV, as discussed in [20]. The required angular and time-coregistration of the two modules is also a significant challenge. The filter wheel further requires appropriate bearings and certified cleanliness levels [20] of its sealings and lubricants. Those difficulties offer opportunities to improve on in the metasurface based design, where we claim a single module would be present and no filter wheel would be necessary. The mission design of 3MI sets on a LEO orbit at $\cong 800km$, higher than the one of Parasol, with an eccentricity of $e = 0.001165$ [20]. The achieved swath corrected for severe radial distortion of an idealized system is $S_w = 2200km$ [20]. As depicted in [20], it is important to consider radial distortion and non-linear projection effects of the observation geometry when performing calculations, in particular to depict the degradation of spatial resolution off-axis. The main important science requirements that the mission design shall accomplish are specific Sun Zenith Angles (SZA) and Scattering Angles of the observation, which allow specific reconstruction methods. Even though those specific requirements have not been reported in Literature, we have determined small variations of those angles through simple trigonometry for typical LEO altitudes. Choosing a smaller altitude would allow for the use of smaller instruments and simpler launch platforms, more in line with the philosophy of this case study. The choice shall however be always considered in unison with some clear science requirements and based also on observation geometry, ground-track communication, etc...

	Central Wavelength [μm]	*Channel Spectral Width, FWHM [nm]*	*Polarization*	*Science Use*
VNIR	0.410	20	Yes	- Aerosol Absorption - Ash Clouds
	0.413	20	Yes	- Aerosol Absorption - Height Indicators
	0.490	20	Yes	- Aerosol - Albedo - BRDF - Cloud Optical Depth
	0.555	20	Yes	Surface Albedo
	0.670	20	Yes	Aerosol Properties
	0.754	20	No	Cloud and Aerosol Height
	0.763	10	No	Cloud and Aerosol Height, O_2A band
	0.865	40	Yes	-Vegetation -Aerosol -Clouds -Surface Features
	0.910	20	No	- Water Vapour - Atmospheric Correction
SWIR	0.910	20	No	- Water Vapour - Atmospheric Correction
	1.370	40	Yes	- Cirrus Clouds - Water Vapour
	1.650	40	Yes	- Ground Characterization for aerosol inversion
	2.130	40	Yes	- Ground Characterization for aerosol inversion - Clouds - Vegetation - Fire effects

Table 3.1: Spectral Channels used in 3MI

3.4.3. Design of the Optical System

The Optical System of 3MI presents significantly sharp design features and is the result of complex trade-offs due to the wide FOV, stringent polarization sensitivity requirements and chromatic distortion. The Optical System is divided into two units, a Galilean telescope and a focusing group, for a total of 12 lenses, some of them non-spherical.

Incidence angle is maintained to a minimum throughout the system to minimize induced polarization from the optics as much as possible, even though affecting stray-light and ghost-images. Ad-hoc anti-reflection coatings have been also developed for the purpose according to [2]. A wide FOV of 104° is achieved by the Optical System. With such field of view, the radiometric fall-off is considerable and must be corrected. The correction in 3MI is achieved by means of a parabolic lens (L2) which increases the pupil area of axis with a magnification of 10× at the edge but has the drawback of introducing lateral chromatism [2]. Strong radial distortion must be corrected for various wavelengths, and it is proven in [2] that such correction negatively affects the polarization accuracy. The beam angles further increases in the second section of the Galilean Telescope and in the focusing group, likely to correct for Petzval Curvature or other aberrations. The system achieves a worst-case $MTF > 0.7$ at Nyquist Frequency across all spectral bands, with degradation towards the SWIR. Distortion is limited to 2% at the edge of the FOV, which with respect to the geometric radial distortion of the observation geometry is significant. In [2] is pointed out that the radiometric fall-off is different for the polarized channels. Ultimately, the design still presents a (smaller) degree of radiance fall-off. Achieved polarization sensitivities are across the FOV > 0.99, but strongly degrade to $\cong 0.95$ at the edge of the FOV even with the use of special coatings and careful angle design. Polarization sensitivity of the non-polarized channels settles at 3% (5% for the edge of the FOV). Those values, to our knowledge, are only reported for the VNIR module. Lenses materials present anomalous chromatic dispersion choice to minimize chromatism and further possess stringent requirements on the stress birefringence (max $4nm/cm$) for limiting induced polarization effects. Fused Silica (Heraeus Suprasil) has been used in L1 for shielding, which according to [2] shall suffice in the expected operating environment. CaF_2 elements are used in the focusing group. We have also observed significant differences in the lens curvatures between the VNIR and the SWIR module, likely due to different chromatic trade-offs of the two modules. By using a single module in a metasurface design, those tradeoffs will likely be affected negatively and additional compromise shall be

investigated in future work. The 3MI Optical System represented in [2] has been partially retro-back engineered for the case-study. Unfortunately, a simple ray tracing with reasonable material properties has not sufficed to yield a similar performance in image space. Due to uncertainties on the use of materials and anti-reflection coatings, we can't yet provide computable figures for polarization and aberration response of such a wide-FOV telecentric system, whose design is another activity on its own. We believe the added value of integration in a simplified and not optimized design is rather questionable, being its aberrations, spectral and polarization properties not comparable with the 3MI-Harp designs.

3.4.4. Thermal and Mechanical Integration

In 3MI, the main challenge in the thermo-mechanical design is the presence of two modules operating at significantly different temperatures (SWIR is cooled at $-110°C$, VNIR at $-10°C$). Two heat pipes with thermal-straps are used to cool the detectors, which are mounted by means of a DSA (detector support assembly) on an iso-static mounting that controls their thermal deformation on top of a base plate, maintained to a stable temperature and connected to the front-end-electronics [21]. The thermal gradients on the SWIR channels impose a high thermal coupling with the cold sink and high insulation with the base-plate, to limit thermal losses [21].
A mechanical driver for the design of the mounting architecture of the FPA is related to dynamic couplings, which imposes that the first vibration eigenfrequency of the structure must be $> 500Hz$ [21]. Determining an architecture with the correct thermal-coupling and rigid enough, to be also modular and reusable for both channels, has been the challenge presented in [21], which downselects a hexapod configuration of titanium meeting both requirements. Temperature variations between sinks and detectors are in the order of $20°C$ according to [21], provided that correct insulation with the base-plate is engineered. That's an important figure for our case-study.
Some considerations are also important for the mounting of the detector, since the type of mounting (addition of glue, number of screws) strongly influences the temperature gradients and the heat flows and may lead to overheating. Gluing is suggested in [21] to limit thermal resistance. The dissipated power of the detectors is roughly $0.14 - 0.18W$ in that design. The integrated system is represented in Figure 3.1.

a) 3MI Opto-Mechanical Unit

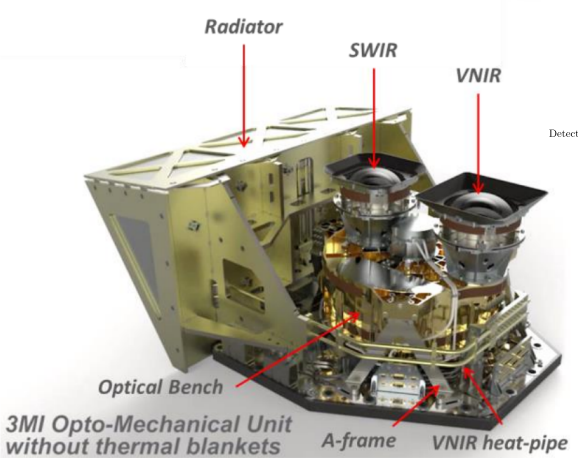

b) 3MI Hexapod FPA mounting (SWIR only)

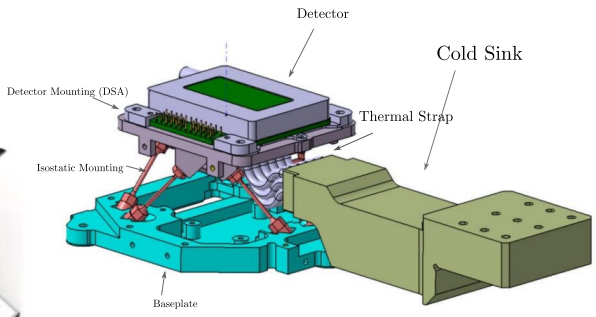

Figure 3.1: a) Optomechanical Unit of 3MI. b) Hexapod FPA Mounting of the SWIR module of 3MI. Electronic harnesses and auxiliary proximity electronics are not represented. Adapted from [2] for clarity.

3.5. SPEXone

For completeness and further comparison with existing systems, we succinctly review also the design of SPEXone, represented in Figure 3.2 from [3]. The 6-unit CubeSat concept operates in spectral modulation technique to measure the Stokes parameters in the range $[0.385, 0.770]\mu m$, with a spectral resolution of $\cong 20 - 40nm$ in the reconstructed Stokes. The input field is directed by 5 distinct slits into 5 pre-optics polarization modules, which induces the polarization modulation in the spectrum. A single pre-optics module consists of a quarter-wave retarder, a multiple order retarder and a beam splitter. It can be proven ([3], [22]) that the introduction of a retardance at that stage of the optical system results in a cosinusoidal modulation in the frequency spectrum $k = 2\pi/\lambda$, enabling for a given modulation period to achieve the reconstruction of the Stokes parameters at a certain spectral resolution. The spectral modulation is instead achieved by means of a spectrometer design consisting of a slit-array, a collimator and a diffraction grating. The design is integrated into an aluminum frame with a single detector channel, to achieve a low-weight but stiff structure ($m \cong 0.9kg$), with no moving parts, and must be opportunely athermalized [22] to achieve good reconstruction.
Due to the fairly different optical architecture of SPEXone and its modulation technique, we have rather decided to use the 3MI concept for a more detailed comparison, which also operates in a division of focal plane array. However, we explicit in Section 9.5 some advantages of adapting the SPEX design with the metasurface filtering concept.

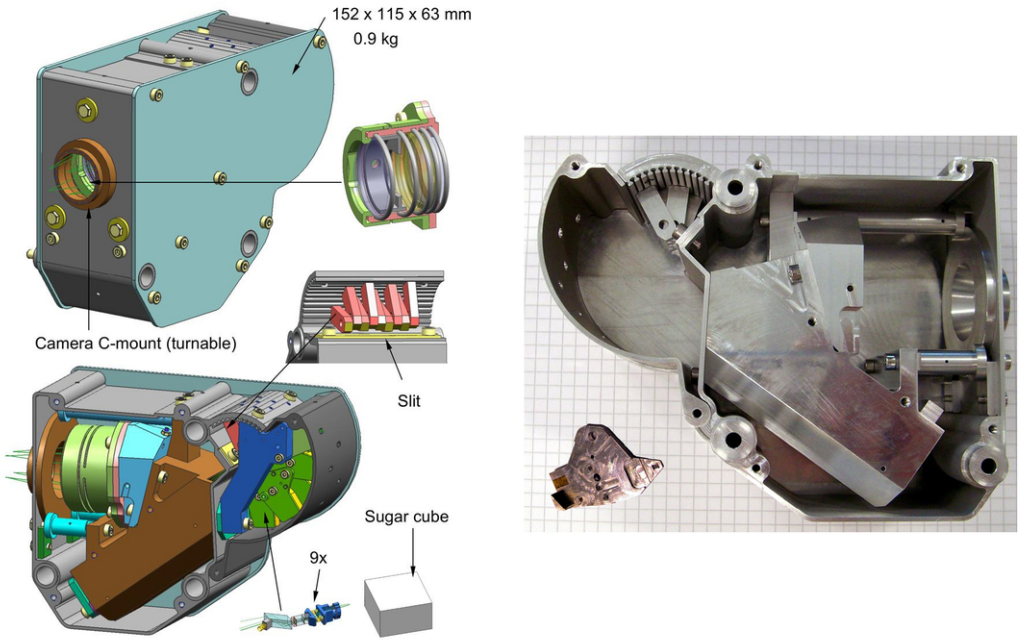

Figure 3.2: Representation of the optical system used in SpexOne and its mechanical design. All copyrights to [3].

3.6. Applications of the Framework for the Metasurface Design

In the application of the research in this project, many relevant science and optical requirements can be derived from our review. The measuring concept shall be multi-angular and wide FOV. We pertain the spectral resolution of Sentinel-7, since they seem achievable with the current design and would greatly improve spectral performance with respect to the 3MI concept. We degrade the requirement of Sentinel-7 in terms of SNR, MTF and polarization accuracy to the more realistic ones of 3MI. A metasurface design system would be further different from the 3MI case study, due to the fact that we propose a single module comprehensive of SWIR and VNIR. Likely, the lower bands of the VNIR module will not be achievable and the Optical System corrected for chromatic aberrations would require some compromises which would need further relaxation of the requirements. The selection of a detector possibly covering both ranges is very challenging and discussed in Section 9.1.2. Regarding the operating environment

and thermo-mechanical integration, till further details will be available, we borrow specifications of the 3MI architecture, in particular regarding temperature variations and regimes. Table 3.2 summarizes the main important requirements derived in this Section, given those premises. Some uncertainties are still present regarding the aberrations and telecentricity requirements to be imposed, which we try to answer in Chapter III.

3.7. Research Questions

Various research questions can be formulated from our preliminary analysis. The initially developed research framework was rather broad and required several iterations. It involved a modeling activity to be carried out in parallel to the integration study, with further optimization of the results and analysis of experimental results. The following the *research objective* of the research:

The objective of the research project is to make recommendations for the design of a metasurface spectropolarimeter integrated into a System and improve the design presented in [1]. The necessary information will be gained by:

- *Down-selection of feasible requirements and a mission case concept for the feasibility study.*
- *Extension of the modeling proposed in [1] to include efficient designs of multiple configurations and evaluation of focused and diffraction performance, by reported analysis over various illumination regimes.*
- *Design changes to overcome bandwidth limitations and focusing uncertainties.*

Various the connected research questions:

1. What is the wider mission concept and requirements? Answered in Chapter 6.
    - What are reasonable estimates of the performance required from the metasurface? Are those requirements achievable?
    - What is the main mission concept and operating environment of the satellite? (e.g. orbit, observation time, signal processing, etc...)
2. How to model efficiently the transmittance and focal response of the filter for various angles? Answered in Part II and with experimental results from Chapter 8.
3. What techniques can be used to overcome bandwidth limitations in the design of [1]? Answered in Section 7.4 and Chapter 7 mainly.
4. What is the achieved performance of the design, in terms of FWHM, transmission spectrums, diffraction, polarization response, power budget? Answered in Chapter 7 and Section 9.1 mainly.
5. What are the main concerns in terms of integration of the filter on a given design (e.g. choice and mounting on a detector, power budget, etc...). Answered mainly in Part IV.

ID	Category	Requirement	Rationale
R.01	Spectral	The instrument shall operate within the $0.4 - 2\mu m$ band (TBC)	The VIS-NIR channels are required for finer aerosol modes determination. The SWIR channel improves CO_2 retrieval and characterization of finer particles as also cirrus [7]
R.02	Spectral	The instrument shall operate within at least the spectral bands depicted in Table 3.1	A minimum number of bands is required for reconstruction of aerosol parameters [7]
R.03	Spectral	The spectral resolution of both intensity and polarized channel shall be better than 5nm (TBC) upon focused illumination with $10° NA$ (TBC)	In the design under consideration, spectral resolution of both polarized and non-polarized bands must be the same. The provided value of NA comes from preliminary inspection of the transmission spectrum reported in [1]
R.04	Spatial	The spatial sampling distance (GSD) shall be finer than $1 \times 1km^2$ for all viewing angles, once corrected for temporal smearing, diffraction effects and radial distortion	Such figure is the proposed spatial resolution requirement in [7], where we have further considered addition of influencing parameters. Requirement shall specify some reference model values for verification, not yet available.
R.05	Polarization	The instrument shall measure the DOLP within an accuracy of $< 1\%$ for the reference spectrum reported used in Sentinel-7 from [7] (TBC)	The DOLP accuracy reported is the one requested in [7]. Once again, a reference spectrum must be used for verification, but depends on orbital considerations which will be performed in the Thesis
R.06	Power	The SNR of the reconstructed Stokes parameters shall be > 200 for all viewing angles and positions at the detector, for the reference spectrum reported in [7] and comprehensive of the reconstruction process upon focused illumination	The SNR ratio reported is representative of the one required in 3MI. It is important to specify upon what condition such requirement shall apply for verification.
R.06	Optical	The (total) FOV of the instrument shall be bigger than $> 90°$ for proper multiangular measurements	According to [7], the maximum angular band for compliance with Science Requirements sets at $\cong \pm 48°$. We have relaxed this requirement slightly due to radial distortion effects
R.07	Optical	The spectrometer instrument shall be multiangular, with more than > 5 angular bands	As demonstrated in [7], the minimum amount of angular bands for reconstruction complying with the Science Requirements is 5 (but further depends on down-selected spectral resolution and bands)
R.08	Integration	An angular band ad nadir shall be used for vicarious calibration	This calibration architecture is suggested in [7]. This is an implementation requirement.
R.09	Optical	The MTF at Nyquist Frequency shall possess a confidence level at two standard deviations greater than $> 80\%$	This requirement has been extrapolated from the achieved performance in 3MI [2]
R.10	Optical	The worst-case MTF at Nyquist Frequency shall be greater than $> 70\%$, within an optical aberration of TBDrms and a telecentricity error of TBD° is considered	This requirement has been extrapolated from the achieved performance in 3MI [2].Worst case refers to the lower MTF of the realistic system once optical aberrations and telecentric deviations are also taken into account
R.11	Optical	The optical system shall be telecentric in image space within 1(TBC) ° across the whole detector	This requirements has been extrapolated from the reported work of [1]. It is required to limit spectral shift in the transmission of the spectral filters
R.12	Integration	The spectral filters shall operate within a maximum variation of $5°C$ for expected thermal variations across the FPA array of $20°C$ with a maximum reference temperature of $T = -50°C$	This requirement is necessary for taking into account the temperature effects and spectral variations due to expansion and curvature, so detector performance. Further studies and quantification to be performed in the Thesis
R.13	Demonstration	The optical payload shall be comprehensive of one-module for VIS and SWIR channels	This is an implementation requirement, due to the nature of the feasibility study and the demonstration purposes. Since focus is on miniaturization of the system, this is selected as a design goal. It implies a proper choice of detector with enough dynamic range as well as trade-offs to consider in the design of the optical system.

Table 3.2: Preliminary high-level requirements for mission case, science case and optical system.

II

Theory

4

Analytical Methods and Background Concepts

Optical design relates many different fields of physics, engineering, material science, statistics. The present section summarizes for future use some of the relevant main concepts from literature, to provide a common framework for use in the project and select the relevant methods. In particular, nomenclature and terminology will be defined for future use and to analyze from a breakdown approach the relevance of the various topics.
Extensive book-based literature has been used for the purpose: [23] in the acclaimed *Handbook of Optics* provides an excellent structured overview, ranging from Geometric to Quantum Optics, image detectors and processing, fabrication and design and many others. [24] and [25] discuss practical guidances and techniques for Optical Systems Engineering, whereas more detailed information regarding general Space Applications can be found in [26]. Theoretical foundations in terms of Electromagnetism and Physical Optics are discussed in [27], [28], [29] and [30]. Various journals and technical notes complement those resources.
In Section 4.1.1 we revision the Maxwell Equations and their time and space Fourier expansions. Such revision is required to derive explicit relations for the propagation of the polarized fields in various materials and to introduce Fourier Optics formulations.
In Chapter 5 the transmission of the metasurface based DBR will be modeled analytically through an effective model. This process requires transfer matrix methods and the characterization of the propagation of fields in homogeneous media, both isotropic and anisotropic. The laws governing reflection and transmissions phenomena (such as Fresnel's and Snell's law) are derived directly from the Maxwell Equations and validated with readily available literature formulations. The necessity to do so lies in the fact that we require explicitly some of the intermediary steps of the derivation for the anisotropic model and the conventions present in literature in terms of transmissions coefficients easily create confusion and inconsistencies. The propagation laws in anisotropic media are discussed in Section 4.2. These methods are all finally merged together in Section 4.2.2 where the analytical solution of a multilayered structure with anisotropic materials is considered.
We further revision in Section 4.5 the main formulations of diffraction theory and Fourier optics for polarized light, which are relatively more novel and complex than formulations of scalar theories but required for the determination of the PSF of the device.
Polarization-dependent intensities are treated in literature in terms of a well-developed framework named Mueller Formalism. Main aspects of the relevance of the Mueller Formalism are discussed in 4.4. Modern radiometric theory, which generalizes classical radiometric theory to include electromagnetic theory, has also been revisioned in Section 4.3, since we have observed a lack of insight in classical radiometric theory applied to polarizing devices with angle-dependent behavior. In particular, coherence properties of light are also revisioned and connection of modern radiometry with the Mueller Formalism. The concepts discussed in that Section are the basis of the finite transmittance calculation, used in the power budgets.
We warn the reader that some of the analytical steps hereby introduced are rather lengthy and involved and when overly complex are better presented in the Appendix. We have decided to pursue a derivation from basic principles of all formulas used, to standardize notation and have a structured overview of the involved hypothesis. Nevertheless, in order not to *'reinvent the wheel'*, validation with known literature results, when available, is always discussed and guides the reader in the verification of the results presented.

4.1. Electromagnetic Fields

In this Section, we recall the differential Maxwell Equations in a continuous model and their relevant main implications for future use in the report. We further introduce the macroscopic effective parameters in their spectral representations.

4.1.1. Maxwell's Equations in frequency domain

For sake of clarity, we refer to $\mathbf{E}$, $\mathbf{H}$ as polychromatic deterministic electric and magnetic fields (respectively, in $[V/m]$ and $[A/m]$) in the time domain, obeying to the general Maxwell equations reported [31], [32]. For a time t, a pulsation frequency $\omega = 2\pi f$, they assume the Time Fourier representation:

$$\begin{cases} \mathbf{E}_\omega = \displaystyle\int_{-\infty}^{\infty} \mathbf{E} e^{i\omega t} dt & [V \cdot s/m] \\ \mathbf{E} = \dfrac{1}{2\pi} \displaystyle\int_{-\infty}^{\infty} \mathbf{E}_\omega e^{-i\omega t} d\omega & [V/m] \end{cases} \tag{4.1}$$

and similarly for the magnetic field. With the use of appropriate material constitutive equations, Maxwell's laws are derived in the frequency domain in many reference textbooks in time harmonic medias ([27], [29]). Within the present report, it will further be assumed that free sources are not present in the domain and material properties may be described by use of an (absolute) effective permittivity tensor $\overleftrightarrow{\epsilon}_{eff,\omega}$, including Ohmic losses due to free currents, and an (absolute) effective permeability tensor $\overleftrightarrow{\mu}_\omega$. With such assumptions a formal derivation from the Maxwell equations with (4.1) leads to the following frequency domain for of the Maxwell Equations (in SI Units):

$$\begin{aligned} \nabla \cdot (\overleftrightarrow{\epsilon}_\omega \mathbf{E}_\omega) &= 0 \\ \nabla \cdot (\overleftrightarrow{\mu}_\omega \mathbf{H}_\omega) &= 0 \\ \nabla \times \mathbf{E}_\omega &= i\omega \overleftrightarrow{\mu}_\omega \mathbf{H}_\omega \\ \nabla \times \mathbf{H}_\omega &= -i\omega \overleftrightarrow{\epsilon}_{eff,\omega} \mathbf{E}_\omega \end{aligned} \tag{4.2}$$

The material parameters may also be referred to vacuum by introducing the relative permittivity $\overleftrightarrow{\epsilon}_r$and permeability tensors $\overleftrightarrow{\mu}_r$ as:

$$\overleftrightarrow{\epsilon} = \epsilon_0 \overleftrightarrow{\epsilon}_r \qquad \overleftrightarrow{\mu} = \mu_0 \overleftrightarrow{\mu}_r \tag{4.3}$$

where ϵ_0 and μ_0 are the permittivities and magnetic permeability in vacuum, respectively (in Table G.1). Within the present assumptions of no surface currents, to ensure that the integral form of the Maxwell's equation is met between a surface of normal $\hat{n}_{ij}$, both electric and magnetic fields transverse components must be conserved:

$$\begin{aligned} \hat{\mathbf{n}}_{ij} \times (\mathbf{E}_j - \mathbf{E}_i) &= 0 \\ \hat{\mathbf{n}}_{ij} \times (\mathbf{H}_j - \mathbf{H}_i) &= 0 \end{aligned} \tag{4.4}$$

which applies both in time and frequency domains.

4.1.2. Power Conservation

We revision here for further use some properties of the power conservation of fields, in particular applied to frequency domain and averaging over significant periods of time. It is known that the carrier of electromagnetic power is given by the (time-dependent) Poynting-Vector $\mathbf{S}$, defined as:

$$\mathbf{S} = \mathbf{E} \times \mathbf{H} \tag{4.5}$$

which is shown to obey a conservation law in [27]. In the time spectrum, averaging of the Poynting Vector over an observation time significant bigger[1] than $2\pi/\omega$ is shown to be given by [27]:

$$\langle \mathbf{S}_\omega \rangle = \frac{1}{2} \Re \{ \mathbf{E}_\omega \times \mathbf{H}_\omega^* \} \tag{4.6}$$

[1] one may argue that ω is arbitrary for a polychromatic field so such conditions does never apply for a real finite pulse. We however refer to the frequencies ω with a known non negligible field spectrum in the region of interest

Within the assumption that the field is further spectrally and temporally uncoherent within such observation time, the total averaged power is given by the Parseval Theorem:

$$\langle \mathbf{S} \rangle = \int_{-\infty}^{\infty} \langle \mathbf{S}_\omega \rangle d\omega \tag{4.7}$$

which will be used extensively in Section 4.3 and in Appendix C.
The treatment for the energy density is, instead, rather more complex if we have to account for the dispersion of the effective properties in the material, due to kinetic and potential energy stored in the material. We refer to [27] for such treatment and discussion of other energetic quantities.

4.1.3. Space-Fourier Decomposition

In the characterization of the field and their solution one may further introduce a Space Fourier transformation, which further provides some more insight on the nature of the fields and their oscillations. Similarly to before, such a decomposition is of values when the geometry of the problem is such that plane waves are eigenfunctions of the optical response of the system. To apply the decomposition we require choosing a reference frame x, y, z and a plane of decomposition. We will choose $z = constant$ for this purpose. If the structures under considerations are not uniform in the transverse plane, the origin $x = y = 0$ shall be specified and used consistently for all transforms. The z axis may represent, for instance, the optical axis of a complex optical system in convenience, or the axis perpendicular to the layers of a multilayered structure. Such decomposition introduces two degree of freedom, k_x, k_y, whereas k_z is restrained by the Maxwell equations. The decomposition reads, within our sign conventions[2]:

$$\begin{cases} \mathbf{E}_{\omega,k} = \displaystyle\int_{-\infty}^{\infty}\int_{-\infty}^{\infty} \mathbf{E}_\omega e^{-i(k_x x + k_y y)} dx dy & [V \cdot m \cdot s] \\ \mathbf{E}_\omega = \dfrac{1}{4\pi^2} \displaystyle\int_{-\infty}^{\infty}\int_{-\infty}^{\infty} \mathbf{E}_{\omega,k} e^{i(k_x x + k_y y)} dk_x dk_y & [V \cdot s/m] \end{cases} \tag{4.8}$$

and similarly for all other quantities. The phasors $\mathbf{E}_{\omega,k}, \mathbf{H}_{\omega,k}$ are hence only functions depending on z. We will use this notation and decomposition consistently throughout the report. The Fourier representation could of course be again introduced in the Maxwell equations, which would explicit the z variations of the field; in this case, however, the effective properties variations in space are usually not negligible. In general, cross-terms of the various Fourier components would be present, so that the propagation of a plane wave at (k_x, k_y) would result in a full spectrum of plane-waves for a generic distribution of effective properties, at least in the near field. This result is well known in scattering problems, where scatterers are said to *excite* certain (k_x, k_y) modes depending on the periodicity in the dimensions of the scatterers themselves. If instead the effective properties are homogeneous in a given medium, fully contained between two planes $z = constant$, the systems admit a plane-wave eigenfunction (by inspection of the Helmholtz equation) and such intercoupling of the spectrums is not present. That's the case of multilayered structures with uniform materials.

4.2. Propagation of Fields in medias

We will hence consider classical methods for the solution of those structures, validating usual approaches with the equations hereby introduced. For the sake of conciseness, we first introduce the general anisotropic solution, then localizing it to the isotropic one as a special case by recalling its polarization decomposition for further use in the report. Starting again from the Maxwell equations and introducing the Space Fourier decomposition, one can arrange the third and fourth Maxwell equations as two separate linear systems (see Appendix B for demonstration and validation of this formula). In the case of

[2] The signs and position of the scaling factor $4\pi^2$ (required for orthogonality) are far from consistent throughout literature.

diagonal permittivity tensor (the general case is treated in Appendix B) such system reads:

$$\frac{d}{dz}\begin{pmatrix} E_{x,i} \\ E_{y,i} \\ \eta_0 H_{x,i} \\ \eta_0 H_{y,i} \end{pmatrix} = ik_0 \begin{bmatrix} 0 & 0 & \frac{s_x s_y}{\epsilon_{r,zz}} & \frac{\left(\epsilon_{r,zz}\mu_{r,yy} - s_x^2\right)}{\epsilon_{r,zz}} \\ 0 & 0 & \frac{\left(-\epsilon_{r,zz}\mu_{r,xx} + s_y^2\right)}{\epsilon_{r,zz}} & -\frac{s_x s_y}{\epsilon_{r,zz}} \\ -\frac{s_x s_y}{\mu_{r,zz}} & \frac{\left(-\epsilon_{r,yy}\mu_{r,zz} + s_x^2\right)}{\mu_{r,zz}} & 0 & 0 \\ \frac{\left(\epsilon_{r,xx}\mu_{r,zz} - s_y^2\right)}{\mu_{r,zz}} & \frac{s_x s_y}{\mu_{r,zz}} & 0 & 0 \end{bmatrix} \begin{pmatrix} E_{x,i} \\ E_{y,i} \\ \eta_0 H_{x,i} \\ \eta_0 H_{y,i} \end{pmatrix} \tag{4.9}$$

$$\begin{pmatrix} E_{z,i} \\ \eta_0 H_{z,i} \end{pmatrix} = \begin{bmatrix} -\frac{\epsilon_{r,xz}}{\epsilon_{r,zz}} & -\frac{\epsilon_{r,yz}}{\epsilon_{r,zz}} & \frac{s_y}{\epsilon_{r,zz}} & -\frac{s_x}{\epsilon_{r,zz}} \\ -\frac{s_y}{\mu_{r,zz}} & \frac{s_x}{\mu_{r,zz}} & -\frac{\mu_{r,xz}}{\mu_{r,zz}} & -\frac{\mu_{r,yz}}{\mu_{r,zz}} \end{bmatrix} \begin{pmatrix} E_{x,i} \\ E_{y,i} \\ \eta_0 H_{x,i} \\ \eta_0 H_{y,i} \end{pmatrix} \tag{4.10}$$

or more concisely, respectively:

$$\frac{d}{dz}\tilde{\boldsymbol{\mathcal{F}}}_i = ik_0 \tilde{\mathbb{P}}_i \tilde{\boldsymbol{\mathcal{F}}}_i \qquad \tilde{\boldsymbol{\mathcal{F}}}_{z,i} = \tilde{\mathbb{M}}_{z\to xy} \tilde{\boldsymbol{\mathcal{F}}}_i \tag{4.11}$$

where k_0 is the wave-number in vacuum for a vacuum velocity of light c_0 ($k_0 = \omega/c_0$) and s_x, s_x are cosine directors (also in vacuum):

$$s_x = \sin\theta_0 \cos\phi_0 \qquad s_y = \sin\theta_0 \cos\phi_0 \tag{4.12}$$

Arranged in such form the propagation of the fields is a linear differential problem of known solution with ease numerical implementation. Its solution can be determined by two methods:

- An eigenvalue decomposition, like the one followed in [33]: the eigenvalues of $ik_0\tilde{\mathbb{P}}_i$ represent the four wave-vectors $k_z^{\pm}$ supported in the medium by the anisotropic structure, one for each polarization state, whereas the eigenvectors are the modified directions of polarization of the transverse fields $\tilde{\boldsymbol{\mathcal{F}}}_i$. An eigenvalue decomposition of this propagation matrix is known analytically only for isotropic mediums or in the general case for $\phi = 0, \pi/2$. Numerical implementation of such resolution methods for anisotropic structures with arbitrary illumination requires careful managing of the orders of eigenvalues, their sign and multiplicity to avoid cumbersome numerical instabilities.
- b) The exponential of the matrix $\mathbb{M}_i = ik_0 z_i \tilde{\mathbb{P}}_i$ provides the solution [34]:

$$\tilde{\boldsymbol{\mathcal{F}}}_{i(z_i)} = e^{i(k_0 z_i \tilde{\mathbb{P}}_i)} \tilde{\boldsymbol{\mathcal{F}}}_{i(0)} \tag{4.13}$$

  directly and can be computed numerically by expansion or by means of a Laplace Inverse Transform of the auxiliary matrix $s\mathbb{I} - \mathbb{M}_i$. The exponential of the matrix is defined by generalizing its scalar series definition:

$$e^{\mathbb{M}_i} = \mathbb{I} + \sum_{j=1}^{\infty} \frac{\mathbb{M}_i^j}{j!} \tag{4.14}$$

  and usually computed numerically to arbitrary precision by using a Pade Approximation algorithm. Such a method is of more simple implementation for the anisotropic structure and of much greater numerical efficiency when operating over wide grids.

Differently from what implied by some authors, an eigenvalue decomposition is not strictly necessary for all layers. Using the given state-vectors simplifies also the use of the matching matrix reported in [27], since boundary conditions on the transverse fields are naturally implied by matrix multiplications. The eigenvalue decomposition is however required for the starting and last mediums of a multilayered structure, where the fields must be projected in back-reflected and forward propagating components to correctly retrieve the transmission and reflection coefficients. The inclusion of losses also requires a more careful managing of the sign of the eigenvalue decomposition for an arbitrary illumination condition. In all cases under our treatment, the last mediums will be represented by air or other isotropic mediums. To resolve the eigenvalue decomposition hence we quickly revision the eigenvalue decomposition of the above matrix for isotropic layers with a novel projection matrix approach, directly implying the Fresnel's Laws at the interface.

4.2.1. Isotropic Mediums

From matrix algebra, the eigenvalues for the isotropic propagation in a medium i, are found to have double multiplicity:

$$k_{z,i}^{\pm} = \pm\sqrt{k_i^2 - k_x^2 - k_y^2} \tag{4.15}$$

with:

$$k_i = \omega\sqrt{\mu_i\epsilon_i} = \frac{\omega}{c_i} = n_i\frac{\omega}{c_0} = \frac{2\pi}{\lambda_i} = n_i\frac{2\pi}{\lambda_0} = n_i k_0 \tag{4.16}$$

We have introduced various notation for the refractive index n_i, the wavelength in the medium and in space and the local velocity of light, for which we refer to the Symbols Table G.2. Formally:

$$n_i = \sqrt{\epsilon_{r,i}\mu_{r,i}} \qquad c_0 = 1/\sqrt{\epsilon_0\mu_0} \tag{4.17}$$

However, the definition $n_i = \sqrt{\epsilon_{r,i}}$ is shown to comply with experimental results in boundary conditions also in the case of magnetizable materials [35], an effect explainable with microscopic boundary conditions of the field. So we will use the a-posteriori empirical relation $\mu_r = 1$. In case of effective medium formulations, the full permeability tensor shall be retained instead.
The sign in (4.15) refers to the traveling direction of the wave. We further notice that a clear distinction can be made in terms of the magnitude of k_x, k_y. A field for which:

$$k_x^2 + k_y^2 \leq k_i^2 \qquad (propagating) \tag{4.18}$$

is said to be propagating, since $k_{z,i}$ is real. A field for which

$$k_x^2 + k_y^2 > k_i^2 \qquad (evanescent) \tag{4.19}$$

is said to be *evanescent* since, with the complex factor of the Fourier Transform accounted for, the solutions are exponential damped[3]. Further defining the wave-vector $\mathbf{k}_i^{\pm} = (k_x, k_y, k_{z,i}^{\pm})$ and an index of polarization m, the polarization directions $\boldsymbol{\mathcal{E}}_{\omega,k,i,m}^{\pm}, \boldsymbol{\mathcal{H}}_{\omega,k,i,m}^{\pm}$ must be restrained (as derived from the first two Maxwell Equations) to planes perpendicular to the wave-vectors:

$$\boldsymbol{\mathcal{E}}_{\omega,k,i,m}^{\pm} \cdot \mathbf{k_i}^{\pm} = 0 \qquad \boldsymbol{\mathcal{H}}_{\omega,k,i,m}^{\pm} \cdot \mathbf{k}_i^{\pm} = 0 \qquad \forall m = 1, 2 \tag{4.20}$$

meaning that the front and back-traveling are transverse. The latter is a rather interesting result, which further suggests to use $\mathbf{k}_i^{\pm}$ and two arbitrary directions of polarization on the plane as a reference system for both waves.
We may also perform a parameterization of the wave-vectors in order to describe the waves. A parameterization we will use throughout the report is the spherical one:

$$\mathbf{k}_i^{\pm} = k_i \begin{pmatrix} \sin\theta_i\cos\phi \\ \sin\theta_i\sin\phi \\ \pm\cos\theta_i \end{pmatrix} = k_i\hat{\mathbf{s}}_i^{\pm} \tag{4.21}$$

which satisfies the form of Equation (4.15). This parameterization creates a natural spanned plane in which the polarizations can be located. We will use such *natural* reference frame when describing the multilayered solution within the DBR structure and the focusing of the field on the detector. Due to reasons relating to the boundary conditions simmetry we'll select the following reference system:

$$\hat{\mathbf{s}}_i^{\pm} = \begin{pmatrix} \sin\theta_i\cos\phi \\ \sin\theta_i\sin\phi \\ \pm\cos\theta_i \end{pmatrix} \qquad \hat{\boldsymbol{\varepsilon}}_{\parallel} = \begin{pmatrix} -\sin\phi \\ \cos\phi \\ 0 \end{pmatrix} \qquad \hat{\boldsymbol{\varepsilon}}_{\perp,i}^{\pm} = \pm\hat{\boldsymbol{\varepsilon}}_{\parallel} \times \hat{\mathbf{s}}_i^{\pm} = \begin{pmatrix} \cos\theta_i\cos\phi \\ \cos\theta_i\sin\phi \\ \mp\sin\theta_i \end{pmatrix} \tag{4.22}$$

which are also represented in Figure 4.1 for clarity. The signs in Equation (4.22) are carefully chosen to enforce the nature of the solution[4]. We define an electric field along $\hat{\boldsymbol{\varepsilon}}_{\parallel}$ as a TE (s-polarized) field and one along $\hat{\boldsymbol{\varepsilon}}_{\perp,i}^{\pm}$ as a TM (p-polarized) field[5].

[3] once the proper branch of square root operation is taken into account
[4] there is no physical difference in reflection of the two polarizations at normal incidence, whereas the reference systems would change handedness due to the reflection if not defined with a change in the sign of one of the versors as we do
[5] nomenclature may vary. Here the suffix $\parallel$ refers to the versor parallel to the transverse plane (perpendicular to the incidence plane) as represented in Figure 4.1

We further notice that one of the fields can be arbitrarily determined from the other. For example, using the Third Maxwell Equation we determine, for the versors:

$$\boldsymbol{\mathcal{H}}^{\pm}_{\omega,k,i,m} = \hat{\mathbf{s}}^{\pm}_{i} \times \boldsymbol{\mathcal{E}}^{\pm}_{\omega,k,i,m} \tag{4.23}$$

and for the magnitudes:

$$H^{\pm}_{\omega,k,i,m} = \frac{1}{\eta_i} E^{\pm}_{\omega,k,i,m} \qquad \eta_i = \frac{\omega\mu_i}{k_i} = \sqrt{\frac{\mu_i}{\epsilon_i}} = \frac{\eta_0\sqrt{\mu_{r,i}}}{n_i} \tag{4.24}$$

where we have introduced the wave magnetic impedance η_i of the medium and the wave impedance of vacuum η_0.

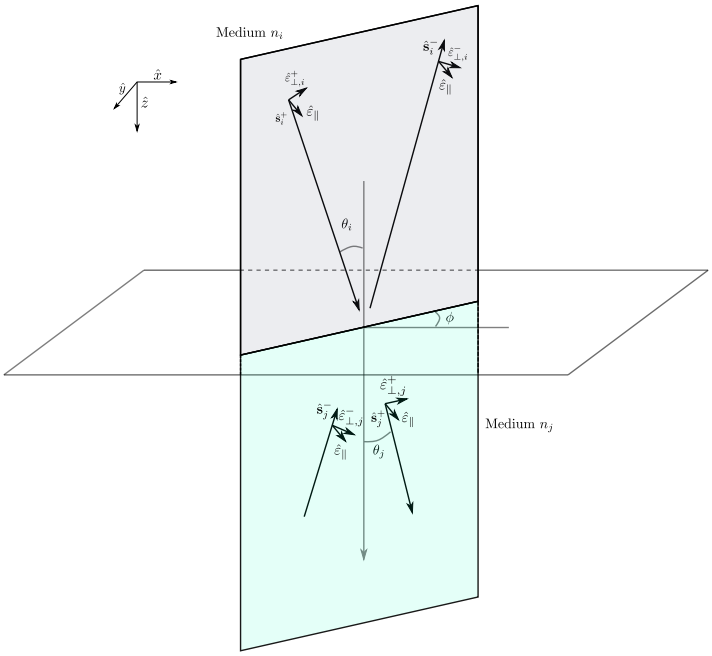

Figure 4.1: Incident field decomposition between two isotropic mediums and supported $k^{\pm}$ with defined versors and angles. Note that the reflected reference system is left-handed to enforce physical similarity of $p-s$ polarization at normal incidence

We switch attention to the description of the boundary conditions in (4.4) for this case. We transform the state-vector by eigenvector decomposition in the natural base as (easing notation):

$$\begin{pmatrix} E_{x,i} \\ E_{y,i} \\ \eta_0 H_{x,i} \\ \eta_0 H_{y,i} \end{pmatrix} = \begin{bmatrix} \hat{\boldsymbol{\epsilon}}^{+,xy}_{\perp,i} & \hat{\boldsymbol{\epsilon}}^{-,[xy]}_{\perp,i} & \hat{\boldsymbol{\epsilon}}^{[xy]}_{\parallel} & \hat{\boldsymbol{\epsilon}}^{[xy]}_{\parallel} \\ n_i \left(\mathbf{s}^{+}_{i} \times \hat{\boldsymbol{\epsilon}}^{+}_{\perp,i}\right)^{[xy]} & n_i \left(\hat{\mathbf{s}}^{-}_{i} \times \hat{\boldsymbol{\epsilon}}^{-}_{\perp,i}\right)^{[xy]} & n_i \left(\hat{\mathbf{s}}^{+}_{i} \times \hat{\boldsymbol{\epsilon}}_{\parallel}\right)^{[xy]} & n_i \left(\hat{\mathbf{s}}^{-}_{i} \times \hat{\boldsymbol{\epsilon}}_{\parallel}\right)^{[xy]} \end{bmatrix} \begin{pmatrix} E^{+}_{p,i} \\ E^{-}_{p,i} \\ E^{+}_{s,i} \\ E^{-}_{s,i} \end{pmatrix} \tag{4.25}$$

Or more concisely:

$$\boldsymbol{\mathcal{F}}_i = \mathbb{R}_i \boldsymbol{\mathcal{F}}^{\pm}_i \tag{4.26}$$

In the present formulation $E^{+,-}_{p/s,i/j}$ represents magnitudes of the electric field in the direction of polarization (with the phase factor $e^{ik^{\pm}_{z,i}z}$ accounted for) and the notation $[xy]$ refers to the x, y projection of the three-dimensional versors. The boundary conditions on the fields $\mathbf{E}, \mathbf{H}$ in Equation (4.4) imply the continuity of the tranverse components so that simply leads, for two mediums i, j, to:

$$\boldsymbol{\mathcal{F}}_i = \boldsymbol{\mathcal{F}}_j \tag{4.27}$$

All boundary conditions further enforce, due to the necessary continuity of the wavefront for all x, y in the plane, the condition:

$$k_{x,i} = k_{x,j} \qquad k_{y,i} = k_{y,j} \tag{4.28}$$

which in the given parametrization directly provides the Snell's Law. The provided and rather concise equations introduced can be used to fully described by means of the transfer matrix approach propagation in various multilayered systems, since the projection matrix $\mathbb{R}_i$ describes the requested eigenvalue decomposition in the last mediums. To validate our approach, we demonstrated the Fresnel's Laws from our perspective and verified consistency with the matching matrix reported in [27], which uses ratios of the fields in the transverse plane rather than on the full polarization direction.

4.2.2. Fields in Multilayered Systems

With the introduced background, we are able to formulate a solution to a generic homogeneous multilayer problem. We will assume the input and output medium between the multilayered structure to be the same and isotropic, with an index of refraction n_0. This is representative of air in the model we will introduce. The input k_x, k_y wavevectors components are arbitrary and represent plane-waves at various angular orientations as introduced in the parametrization Equation 4.21.
Irrespectively of whether the medium is isotropic or anisotropic, the transfer matrices of the medium relating the state vectors $\boldsymbol{\mathcal{F}}_i$ at the boundaries delimiting the medium are given by:

$$\mathbb{T}_i^{[xy]} = \left(e^{ik_0 z_i \tilde{\mathbb{P}}_i}\right) \tag{4.29}$$

since the state-vectors already enforce the required boundary conditions in Equation (4.27), the total transverse transfer matrix of a multilayer is given by:

$$\mathbb{T}_{mul}^{[xy]} = \mathbb{T}_n^{[xy]} ... \mathbb{T}_2^{[xy]} \mathbb{T}_1^{[xy]} = \prod_{i=1}^{n,left} \mathbb{T}_i^{[xy]} \tag{4.30}$$

When transformed to the polarization base in the ps frame for transmitted and reflected waves, the final transfer matrix of the state-vectors $\boldsymbol{\mathcal{F}}_i^{\pm}$ is given by:

$$\mathbb{T}_{mul}^{[ps]} = \mathbb{R}_0^{-1} \mathbb{T}_{mul}^{[xy]} \mathbb{R}_0 \tag{4.31}$$

Alternatively, one can directly multiply together the matrices $\mathbb{T}_{mul}^{[ps]}$ due to the fact that $\mathbb{R}_0 \mathbb{R}_0^{-1} = \mathbb{I}$. When using the relations there-depicted the matrix shall be ordered from the bottom layer to the upper one (to avoid a numerical troublesome inversion). This process provides the transmissions and reflection Jones matrices of the multilayered structure, once the corresponding scattering matrix is calculated by means of the procedure highlighted in Appendix A. To validate our formulation, we performed various FEM simulations of anisotropic multilayered structures with known materials properties and verified to numerical precision the soundness of the transmission and reflections coefficients.

4.3. Concepts of Modern Radiometry and Coherence Theory

Conventionally, power estimations are treated in terms of radiometric physical quantities (radiance, spectral intensity and powers), which are of practical ease of determination. Power budget in terms of classical radiometry lacks insight in terms of diffraction, the polarization of light and coherence properties, since it is mainly applicable for scalar incoherent and unpolarized fields. In order to perform an accurate power budget of the metasurface design, hence, we must generalize classic radiometry concepts to include such electromagnetic phenomena, leading to a *modern radiometry* approach. Modern radiometry theory has been developed in decades and is well summarized in [36], [37]. [38], in particular, offers an overview in terms of a diffracting lens and radiometric quantities, as well as [23] (see Coherence Chapter) describes the propagation laws. We will hereby recall only the main physical quantities playing a role, application to diffraction theories and also some simplified results. We also determined a radiometric link relation, which connects the electromagnetic theory with the radiance by means of dimensional scaling. The approach we used and widely validated in Literature is to associate a deterministic field $\tilde{\mathbf{E}}_\omega$ to the input random signal, such that once integrated in the spectrum over an arbitrary small window the same (spectral) power is found.
The physical characterization starts with the definition of a cross-correlation tensor, which is a statistical ensemble average of the vectorial field intensities between two certain points and distinct time measurements as:

$$\Gamma_{(\mathbf{r}_1, \mathbf{r}_2, t_1, t_2)} = \langle \mathbf{E}_{(\mathbf{r}_1, t_1)} \mathbf{E}^T_{(\mathbf{r}_2, t_2)} \rangle \qquad [V^2/m^2] \tag{4.32}$$

where we have used conventional vectorial notation. Similar quantities may be defined for magnetic fields and mixed correlation between electric and magnetic field (related to the Poynting Vector). In literature, an hypothesis on the stationary of the fields in the wide sense is usually used, assuming that the fields are only dependent on the difference $\tau = t_2 - t_1$. We will assume instead the fields to be quasi stationary, in the sense that it may vary slowly with the variable $t = (t_1 + t_2)/2$ (representative in our case of the motion of a satellite or some real temporal change).
Similarly to what performed in terms of the electromagnetic fields a Time Fourier transform $\tau \to \omega$ is introduced for the cross-correlation tensor, which leads to a cross-spectral density function of the fields, $\mathbb{W}_{(\mathbf{r}_1,\mathbf{r}_2,\omega,t)}$.

$$\mathbb{W}_{(\mathbf{r}_1,\mathbf{r}_2,\omega,t)} = \int_{-\infty}^{\infty} \Gamma_{(\mathbf{r}_1,\mathbf{r}_2,\tau,t)} e^{i\omega\tau} d\tau = \langle \tilde{\mathbf{E}}_{(\mathbf{r}_1,\omega,t)} \tilde{\mathbf{E}}^{\dagger}_{(\mathbf{r}_2,\omega,t)} \rangle \qquad [V^2 s/m^2] \tag{4.33}$$

We have used the result that the cross-spectral density function can be decomposed in monochromatic realizations of an observable quantity, pointed out in [23], [37], [38], [39]. That's an important conclusion arising from the wave equations of the quasi-stationary fields and is applicable only when the fluctuation of the intensities (beating periods) are on significant longer time-frames than the frequency of light.

Dimensional Note *We point out at the fact that the observable field phasor $\tilde{\mathbf{E}}_{(\mathbf{r}_i,\omega,t)}$ is not an electric field measured in $[Vs/m]$ (as time Fourier transform of a field in $[V/m]$), as expected for a polychromatic wave, but is actually measured in $[V\sqrt{s}/m]$ as we can conclude by performing dimensional analysis on any of the formulas reported in the literature considered. That's not an inconsistency, and is due to the fact that only one transform in the intensities is performed. The observable $\tilde{\mathbf{E}}_{(\mathbf{r}_i,\omega,t)}$ is a deterministic field associated with the random energy and is merely a variable of convenience, undergoing to the Maxwell Equations as an electric field would do. More precisely, by allowing the cross-correlation tensor to slightly fluctuate in time with some finite set of beating periods $T_{beat,i}$ and pulsations $\omega_{beat,i} = 2\pi/T_{beat,i}$, we observe that the link between the observable quantity and the real electric fields is of the form:*

$$\langle \tilde{\mathbf{E}}_{(\mathbf{r}_1,\omega,t)} \tilde{\mathbf{E}}^{\dagger}_{(\mathbf{r}_2,\omega,t)} \rangle = \sum_i \frac{1}{T_{beat,i}} e^{i\omega_{beat,i}t} \langle \mathbf{E}_{(\mathbf{r}_1,\omega)} \mathbf{E}^{\dagger}_{(\mathbf{r}_2,\omega)} \rangle \tag{4.34}$$

We are in reality not that much interested in what the coherent mode decomposition of the fields is (all equations are linear in field amplitudes and the powers low), as much on the fact that we can associated to the spectrum an an effective field $\tilde{\mathbf{E}}_{(\mathbf{r}_1,\omega,t)}$ which well describes the second order statistics (see [39] in particular for supporting this understanding). If the beating periods would be known the previous equations would allow to gain insight on what are the real electric fields associated with the random process. The beating period can be estimated for a coherence spectral width of $\Delta\lambda_{co}$ as:

$$T_{beat} \cong \frac{\lambda^2}{c\Delta\lambda_{co}} \tag{4.35}$$

It follows that if the fields are assumed to be completely spectrally uncoherent (never realized in practice neither for a a Lambertian source) a coherent electric field phasor in $[Vs/m]$ is intrinsically ill-defined for such source. Moreover, assuming quasi-stationarity of the field automatically leads to a field which is very poorly spectrally correlated ($\Delta\lambda_{co} \cong 0$), indication of the fact that also the coherence time (time where a coherence is observed) tends to zero. The interested reader may further reconsider this derivation in terms of a more generic non-stationary fields treatment which is not reported for succinctness.

The cross-spectral intensity of the radiated field in a region is defined by setting $\mathbf{r}_2 = \mathbf{r}_1 = \mathbf{r}$, but its propagation generally depends on both variables (demonstrated experimentally in various occasions). When a transverse direction of the fields can be determined and a transverse plane $[\xi, \eta]$ can be defined (for example in the far field), there is a simple relationship between the intensity matrix and the Stokes Parameters, which is revisioned in the next Section.
The cross-correlation tensor propagates in free space, accordingly to [38]:

$$\mathbb{W}_{(\mathbf{r}_1,\mathbf{r}_2,\omega)|\mathbf{r}_i \in \mathcal{A}_p} = \frac{1}{\lambda_0^2} \int\int_{\mathcal{A}_s} \mathbb{W}_{(\mathbf{r}_{1ob},\mathbf{r}_{2ob},\omega)|\mathbf{r}_{iob} \in \mathcal{A}_s} \left(\frac{e^{ik_0(\mathbf{d}_2 - \mathbf{d}_1)}}{d_1 d_2} \right) \cos\theta_1 \cos\theta_2 d^2\mathbf{r}_{1ob} d^2\mathbf{r}_{2ob} \tag{4.36}$$

where the radiometric cosines are defined by:

$$\cos\theta_i = \frac{\mathbf{d}_i \cdot \hat{n}_{i\mathcal{A}_s}}{d_i} \qquad \mathbf{d}_i = \mathbf{r}_i - \mathbf{r}_{iob} \qquad \forall \mathbf{r}_{iob} \in \mathcal{A}_s, \forall \mathbf{r}_i \in \mathcal{A}_p \tag{4.37}$$

and integration is carried over the source area $\mathcal{A}_s$ with local normal $\hat{n}_{i,\mathcal{A}_s}$. Symbols in Equation (4.36) are summarized in Figure 4.2.

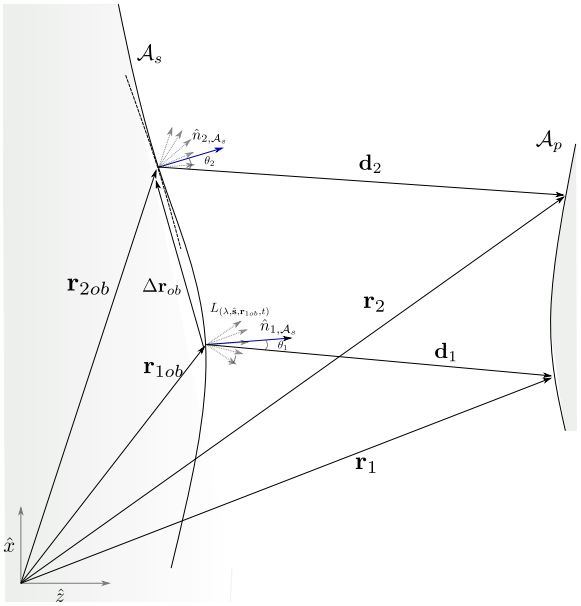

Figure 4.2: Propagation of cross-correlation tensor from a source area $\mathcal{A}_s$ and symbols used in Equation (4.36). Also the spectral radiance is represented for a given point-source and a few directions

The variable $\Delta\mathbf{r}_{ob} = \mathbf{r}_{2ob} - \mathbf{r}_{1ob}$ appearing in Figure 4.2 distinguish between the coherence of the field. A totally spectrally and spatially incoherent field will have a nill cross-correlation tensor for $\Delta\mathbf{r}_{ob} \neq 0$ [38], which we will assume in the following Chapters of the report to model in first approximation a Lambertian source. Note that even an uncoherent field in general gains spatial coherence by propagation (see *Van Cittert-Zernike* theorem), as the coherence is also a property of the observation geometry. On a pupil, the contribution due to a *spectral directional intensity* (see Table 4.1) is fully coherent (at the neglection of atmospheric and propagation deviations) and the pupil area acts as a coherence area. Upon focusing, imaging is possible only because of this finite but not negligible coherence area at the pupils.
Similarly to the propagation of electromagnetic coherent fields, in the far-field, a simple relationship applies between the far-field cross-correlation tensor and the angular spectrum Fourier transform at the source plane.
Even if more complicated than electric field propagation, the treatment in terms of the cross-correlation tensor is necessary for two reasons: to gain understanding on what are the measurables under considerations (in this case, $\tilde{\mathbf{E}}_{(\mathbf{r_i},\omega,t)}$) and to correctly account both for polarization effects and incoherence of the field in the extended source but full/partial coherence of any single point-source contribution. It is not straightforward to apply classic propagation theories when a polarization-dependent transmittance is present since results like the classical well-known PSF convolution have been derived under the assumption that no additional transparencies (apart from the pupil function) are present.
The present treatment is consistent with known spectral quantities of interest in classic radiometry, represented and summarized for the notation in Table 4.1.

Definition	Symbol	Description	Units
Spectral Radiance	$L_{\lambda(\mathbf{r},\mathbf{r}_{ob},t)}$	A measure of the energy radiated per unit time and unit area in a given direction along an infinitesimal solid angle from a point-source contribution. Defined for extended sources.	$W/(m^2 \cdot \mu m \cdot srad)$
Spectral Directional Power	$\Theta_{\lambda(\mathbf{r}_{ob},t)}$	Measure of the radiance radiated from a point-source across a certain area.	$W/(\mu m \cdot srad)$
Spectral Intensity	$I_{\lambda(\mathbf{r},t)}$	A measure of the point-wise spectral power per unit area due to all point-sources contribution. Equivalently, spectral radiance across the entire solid angle subtended by the extended source on a generic point on the area of interest.	$W/(m^2 \cdot \mu m)$
Spectral Power	Φ_λ	Measure of the power of an extended source across a certain defined area, per unit wavelength.	$W/(\mu m)$

Table 4.1: Classic Radiometry variables of interest. Nomenclature may differ in various literature resources.

Relationships that link the quantities to the correlation tensor are rather complex and cumbersome for coherent light and will not be reported for succinctness, but can be revisioned in [38]. A simpler treatment is possible in our case due to the Lambertian nature of the source and the fact that a far-field propagation can be used. Simplified radiometric link relationships for our case have been derived in Appendix C given the introduced framework.

4.4. Concepts of Mueller Formalism

Mueller formalism is a well-developed tool for the description of partially polarized light. We review some of the basic principles of this formulation.
Upon propagation, transverse electromagnetic waves can be characterized by their polarization, usually referred to electric fields. Polarization is an intrinsic physical properties of light providing information of reflection, sources of the fields and its propagation. The envelope of electric field directions varying in time across a section generally creates an ellipse, for which in general the field is said to be *elliptically polarized*. A useful representation of this most generic polarization state is possible by means of two spherical angles, the angle of polarization γ and the polar angle of circular polarization χ. The ellipse tangent directions (representative of the directions of the electric field in the transverse plane for various phases) spanning the transverse plane perpendicular to the local wave-vector in directions ξ, η, can be characterized as a complex vector in those two angles as:

$$\mathbf{e}^{[\xi,\eta]} = e^{i\psi}\left(\cos\chi\begin{pmatrix}\cos\gamma\\ \sin\gamma\end{pmatrix} + i\sin\chi\begin{pmatrix}-\sin\gamma\\ \cos\gamma\end{pmatrix}\right) \tag{4.38}$$

where ψ is an arbitrary phase on the section under considerations. The given field is non-dimensional and can without loss of generality be representative of a plane-wave, a focal two-dimensional field both in the spectral or spatial domain, depending on the case under study. In Mueller Formalism, a transformation of the vectorial field components is performed in terms of linear combination of the components intensities. Various definitions are possible which are all consistent. In particular a simple concise formulation links the cross-correlation tensor above discussed with the Stokes parameters, defined for the non-dimensional field as:

$$s_j = \mathrm{Tr}\{\sigma_j \langle \mathbf{e}\mathbf{e}^\dagger\rangle\}^{[\xi,\eta]} \qquad \mathbf{s} = \begin{pmatrix}1\\ p\cos(2\gamma)\cos(2\chi)\\ p\sin(2\gamma)\cos(2\chi)\\ p\sin(2\chi)\end{pmatrix} \tag{4.39}$$

where the (re-ordered) Pauli matrices defined by:

$$\sigma_0 = \begin{bmatrix}1 & 0\\ 0 & 1\end{bmatrix} \qquad \sigma_1 = \begin{bmatrix}1 & 0\\ 0 & -1\end{bmatrix} \qquad \sigma_2 = \begin{bmatrix}0 & 1\\ 1 & 0\end{bmatrix} \qquad \sigma_3 = \begin{bmatrix}0 & -i\\ i & 0\end{bmatrix} \tag{4.40}$$

and p the so defined *degree of polarization*. Light can also possess an unpolarized component carrying not-nill power, since the direction of polarization is intrinsically referred to a statistical field. The interested reader can verify the consistency of the above definitions with other well-known definitions of the Stokes parameters for the field parametrization hereby chosen. In particular, the phase ψ is lost when

transforming from a Jones vector to the Stokes representation, which is important to remember when considering aberrations and other focusing effects.
The Stokes parameters so defined can be represented on a Poincaré sphere, since by definition $ps_0 = \sqrt{s_1^2 + s_2^2 + s_3^2}$. In literature, s_1, s_2, s_3 are also known as Q, U, V and represent, respectively, linear polarization at $\pm 90°$, at $\pm 45°$ and circular polarized light. They are of important use in optical applications since directly related to optical measurables of statistical fields.
The Poincaré sphere and the polarization ellipse are represented in Figure 4.3. Upon a linear vectorial deterministic transformation of the fields (as the one under study within the report), the electric field directions of the fully polarized field components may variate according to a Jones transformation of the form:

$$\mathbf{e}' = \mathbb{J}\mathbf{e} \tag{4.41}$$

Since non-polarized light can for those transformation be determined from an averaging ensemble of the polarized transformation, the transformation can equally be depicted also in terms of the Stokes vector, by means of a Mueller Matrix:

$$\mathbf{s}' = \mathbb{M}\mathbf{s} \tag{4.42}$$

where the Mueller Matrix is defined by the algebric operation ([40]):

$$\mathbb{M} = \left[\mathbb{A}\left(\mathbb{J} \otimes \mathbb{J}^*\right)\left(\mathbb{A}^{-1}\right)\right] \tag{4.43}$$

where $\otimes$ is the Kronecker Product, $*$ indicates the complex conjugation, and the auxiliary matrix $\mathbb{A}$ (found by permutation of the Pauli matrices) is defined by:

$$\mathbb{A} = \begin{bmatrix} 1 & 0 & 0 & 1 \\ 1 & 0 & 0 & -1 \\ 0 & 1 & 1 & 0 \\ 0 & -i & i & 0 \end{bmatrix} \tag{4.44}$$

When operating the above transformation the fields shall be represented with respect to the transverse plane or a general 2-dimensional plane. Cartesian representation of the plane-wave fields of a focused beam are instead three-dimensional and can't in general be represented with only four Stokes parameters without generalizing those concepts. Fortunately we are generally interested in the components of a focused plane-wave field decomposition along the detector plane, which is two-dimensional. When Mueller formalism is used in spectral representations like the Fourier Transforms above introduced, known spectral theorems of scalar fields also apply for each components of the Mueller Matrix.

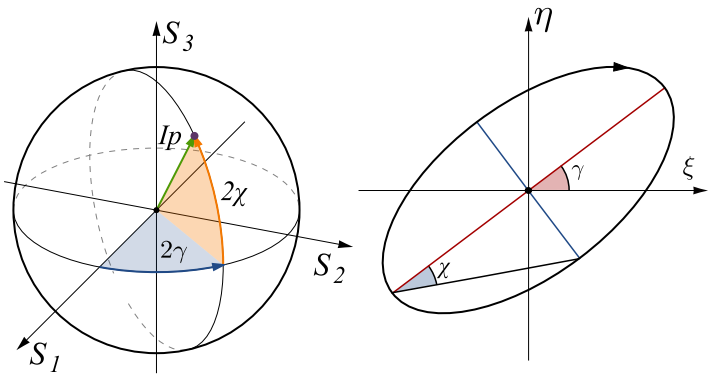

Figure 4.3: On the left, Poincaré sphere and visualization of the Stokes parameters. On the right, polarization angles in the ξ, η transverse frame and relationship with the local direction of the electric field. Adapted from the Web.

4.5. Concepts of Diffraction Theory

It is well known that the propagation of a generic wave in a given geometry medium with variable properties results in diffraction, a physical phenomenon for which the path of a photon is redirected by the surrounding of the medium. In this section, we review the applicable results of Diffraction Theory for the description of the PSF of the metasurface device and its Power Budget. We will conveniently assume that the reader is familiar with all concepts related to scalar diffraction theory. Due to the inapplicability

of scalar wave theories, we will focus attention on the statistical treatment of the cross-correlation tensor, which includes both polarization and coherence effects. A conventional and historical explanation of diffraction effects for scalar fields is given by the Huygens-Fresnel principle: *across a boundary every point of the wavefront can be considered as a source of spherical wavelets which do mutually interfere with each other.*

The principle can be proved and generalized to vectorial fields or correlation tensors by considering the Green's Function solution of the Maxwell Equation for a magnetic and electric generic excitation, as performed in [41]. A Green dyadic tensor can be defined which resolves for a given geometry the Maxwell Equations and represents the field excitation at a certain position due to an arbitrarily oriented infinitesimal current (which may be physical or artificial). The green dyadic may be corrected as in [42] to account for special geometries in the near-field. The fields across a point can be then determined as a composition of surface and volume integrals, reported in [41] and which represents a generalized Kirchoff Diffraction Integral applicable for both near and far-field and polarized fields. Ideally, one shall apply such characterization for the metasurface itself once the currents and field distributions in a region are known. This approach is clearly impractical (due to lack of characterization of the fields and numerical complexity) so we will hereby use some conventional assumptions to simplify the treatment.

According to [38], any non-linear transformation of an optical system can be described in terms of a Volterra Series relating the input cross-correlation tensor and the output cross-spectral intensity by means of a linear integration. In practical applications, the series is truncated to a bilinear transformation with a good approximation for real optical systems as (see [38], adapted for tensorial notation):

$$\mathbb{W}_{(\mathbf{r}_1,\mathbf{r}_2,\omega)} = \int_{-\infty}^{\infty}\int_{-\infty}^{\infty}\int_{-\infty}^{\infty}\int_{-\infty}^{\infty} \mathbb{H}_{(\mathbf{r}_1,\mathbf{r}_{1ob})}\mathbb{W}_{(\mathbf{r}_{1ob},\mathbf{r}_{2ob},\omega)}\mathbb{H}^*_{(\mathbf{r}_2,\mathbf{r}_{2ob})} d^2\mathbf{r}_{1ob} d^2\mathbf{r}_{2ob} \tag{4.45}$$

which can also be recasted to an expression involving the Mueller Matrix of $\mathbb{H}$ and the Stokes parameters in the two regions. We'll simplify such formula in the next Chapter to take into account that the fields are spectrally uncorrelated in the source (Lambertian) and determine a closed expression for the transfer functions $\mathbb{H}$. The latter can be determined from the free-propagation of the cross-correlation tensor in space (leading to a generalized Fraunhofer propagation regime of the deterministic fields) and a proper modeling of the filter transparencies.

Diffraction of the pupil is automatically included in the treatment once a finite extension transmittance is taken into consideration in such propagation with a certain pupil function, as conventionally done in scalar diffraction optics. Induced polarization of the optics is also easily included. Consider the case in which $\mathbb{W}_{(\mathbf{r}_1,\mathbf{r}_2,\omega)}$ is referred to the focal plane. The focal plane spectral intensity is proportional to the trace of the centered autocorrelation tensor (e.g. the one for which $\mathbf{r}_2 = \mathbf{r}_1 = \mathbf{r}$). In Appendix C we demonstrate the dimensionally sound result that, for a vacuum impedance η_0, the spectral intensity is given by:

$$I_\lambda = \left(\frac{\pi c_0}{\lambda_0^2 \eta_0}\right) \mathrm{Tr}\{\mathbb{W}_{(\mathbf{r}_f,\mathbf{r}_f,\omega)}\} \qquad [W/(\mu m \cdot m^2)] \tag{4.46}$$

which is proportional to the first Stokes parameter at the focal plane ($\mathrm{Tr}\{\mathbb{W}_{(\mathbf{r}_f,\mathbf{r}_f,\omega)}\}$). Formula (4.46) is strictly valid as a representation of an intensity associated with the Poynting Vector for small NAs, or, equivalently, for the energy density once assumed that the magnetic energy density is on average the same as the electric one. We can compare and validate this result with the one proposed in [43] (Gaussian Units) for the electric energy density of a monochromatic contribution or with generalized spectral quantities derived in [38]. We more generally pertained the polychromatic nature of the field and used spectral quantities in unit wavelengths instead, as natural in classic radiometry.

With such in mind, we can recognize the classical PSF of the system for a point-source contribution as the Mueller Matrix associated with $\mathbb{H}_{(\mathbf{r}_i,\mathbf{r}_{iob})}$ in the Space Domain. In case in which a Fraunhofer diffraction can be used, then expressions for $\mathbb{H}_{(\mathbf{r}_i,\mathbf{r}_{iob})}$ are known as in [38] and represent the inverse Fourier Transform of an amplitude transfer function (ATF). The latter is finally the Jones transformation of the plane-wave fields in our treatment, depending on the transmittances along the way and the pupil function of the pupils (in Fraunhofer diffraction regime).

5

Modelling the Optical Response

In the following Chapter, we consider the problem of characterizing the optical response of the optical system and metasurface device in the Fourier Spectrum, for a coherent plane-wave excitation. The chapter is meant to be a reference for theoretical formulas used in the results Part III, as also several performance parameters are introduced for further reference.
The characterization has partially been already performed in [1]. However, a polarization sensitivity study (with respect to s and p decomposition) has not been fully considered, the effects of azimuthal angle dependence on the transmission spectrum have not been investigated and the diffraction response of the device not been discussed. More importantly, an analytical model is required for quick estimations of hundreds of pixels performances, which is impractical via FEM simulations.
We initially draw some consideration on the input field at the entrance pupil and its coherence properties in Section 5.1. The source field will be assumed to be Lambertian with a low degree of spectral and spatial coherence, statistically quasi-stationary in wide-sense. We further relate electromagnetic quantities of interest to radiometric ones by means of modern radiometry in Section 4.3, simplifying the treatment by means of the introduced assumption on the input field. A radiometric link between radiances and the electromagnetic quantities in Appendix C is paramount to quantify the spectral power and the polarization to be measured.
A preliminary concept of importance is the geometrical vectorial plane-wave $p-s$ decomposition of the polarized field, introduced in Section 5.2. Such decomposition is used in FEM models for excitation of the structure and characterization of its response and is of physical importance when depicting the transformation of a lens or of the metasurface device.
The metasurface modeling, discussed comprehensively in 5.3 requires solution of a cumbersome finite diffraction coupled problem discussed in 5.3.1. Even though introducing possible numerical means for its resolution, we simplify the treatment by operating a wide pixel limit to describe the coupling with the diffraction of the pupil and the aberrations, quantifying our assumptions. Within such a framework, the transmittance of the device is well described by the combination of an effective medium model, integrated in a multilayered structure, to provide the amplitude transfer function of the device. Such an approach leads to resonance curves of the cavity in the multilayer, comprehensive transmittances plots for the design of the metasurface cavity. With an opportune expansion of the Fraunhofer pupil diffraction integral, the solution of the diffraction pupil contribution can be found in a closed compact form, which allows also definitions of various performance parameters.
In particular, focal transmissions at wide pixels are defined in 5.3.4 but also finite transmissions taking into account the finite of the pixel and the encircled energy in the diffraction pattern. Band transmittances are definable for all of those quantities by opportunely integrating in the band. The latter is likely to be the closest reconstruction matrices to one of the real structure when we consider the real signal reconstruction process by image creation.

5.1. The Input Field

We hereby consider the entrance pupil of the Optical System depicted in Figure[1] 6.7 and characterize the input field at the entrance pupil.

Ultimately, the field can be, in second-order statistics, be thought of as realizations of the correlation tensor appearing in Equation 4.32, which then characterize completely, in the space spectrum, the degree of polarization, angle of polarization, distribution and coherence degrees of the incoming light. Unfortunately, such degree of information is rarely available for modeling of the input field and one must use radiometric quantities to estimate the magnitude of the fields and assume a certain degree of polarization and angle of polarization of the fields.

In Chapter 4.3, along with other parameters of interest in this Section, it is discussed how the propagation and field characterization of a generic partially-polarized and partially-coherent field can be done by means of propagation of the cross-correlation tensor. We hereby present some simplified results of this theory to correctly take into account the polarized nature of the field and the imaging of the extended source.

We start by considering the source as a typical Lambertian (secondary) source. In remote sensing Earth radiation/reflection has a negligible spatial coherence and due to the scattering of the atmosphere and the Lambertian nature of the source a negligible spectral coherence. We will further consider the generated field to be quasi-stationary to use literature results that have been presented in agreement with such assumptions. The cross-correlation tensor at the source can hence be written as:

$$\mathbb{W}_{(\mathbf{r}_{ob},\mathbf{r}_{ob}+\Delta\mathbf{r}_{ob},\omega,t)} = \mathbb{W}_{(\mathbf{r}_{ob},\omega,t)}\tilde{\sigma}_{(k\Delta\mathbf{r}_{ob})} = \tilde{\sigma}_{(k\Delta\mathbf{r}_{ob})}\langle\tilde{\mathbf{E}}_{(\mathbf{r}_{ob},\omega,t)}\tilde{\mathbf{E}}^{\dagger}_{(\mathbf{r}_{ob},\omega,t)}\rangle \qquad [V^2s/m^2] \tag{5.1}$$

where $\tilde{\mathbf{E}}_{(\mathbf{r}_{ob},\omega,t)}$ is a deterministic observable as defined in Chapter 4.3 and $\tilde{\sigma}_{(k\Delta\mathbf{r}_{ob})}$ a weak spatial coherence function, approximated by a two-dimensional Delta Dirac. In the Appendix C, we derive a closed expression, based on results from [44], of the cross-correlation tensor in the far-field, in terms of a radiometric radiance, directly related the Poynting Vector. In particular, we determined that the radiance emitted in the far field from a poorly-correlated Lambertian point-source in a direction $\hat{\mathbf{s}}_i$ connecting a point source and the entrance pupil is given by:

$$L^{\infty}_{\lambda(\hat{\mathbf{s}}_i,\mathbf{r}_{ob},t)} = \frac{\pi c_0}{\lambda_0^2\eta_0}\cos\theta_n \,\mathrm{Tr}\{\mathbb{W}^{[\xi,\eta]}_{(\mathbf{r}_{ob},\omega,t)}\} \qquad \left[W/(m^2\mu msr)\right] \tag{5.2}$$

where $\mathbb{W}^{[\xi,\eta]}_{(\mathbf{r}_{ob},\omega,t)}$ is the two-dimensional cross-correlation tensor at the source, in the transverse plane $[\xi,\eta]$ of normal $\hat{\mathbf{s}}_\mathbf{i}$, η_0 is the vacuum impedance and $\theta_n = \theta_{in} + \theta_{ob}$ (see image 6.1 and Chapter 6). The cross-correlation tensor at the entrance pupil can then be found as:

$$\mathbb{W}^{\infty}_{(\mathbf{r}_{e1},\mathbf{r}_{e2},\omega,t)} = \int_{\mathcal{A}_{sc}} \left(\frac{\lambda^2\eta_0}{\pi c_0}\right)\cos^2\theta_g\cos\theta_n L^{\infty}_{\lambda(\hat{\mathbf{s}}_i,\tilde{\mathbf{q}},t)}\langle\mathbf{e}\mathbf{e}^{\dagger}\rangle e^{-ik\cos\theta_g\tilde{\mathbf{q}}\cdot(\mathbf{r}_{e2}-\mathbf{r}_{e1})}d^2\tilde{\mathbf{q}} \qquad [V^2s/m^2] \tag{5.3}$$

where the relevant quantities are defined in the Appendix C and Chapter 6. We note that the field can be thought of as a superposition of coherent plane-waves, each one with a weighting factor proportional to the radiance emitted by a point source. Moreover, the fields have gained spatial coherence across the pupil (that's obvious since a plane-wave is seen by a spatial extent aperture). The phase factor $e^{-ik\cos\theta_g\tilde{\mathbf{q}}\cdot(\mathbf{r}_{e2}-\mathbf{r}_{e1})}$ is the phase that requires correction in the optical system, corrected for observation viewing geometry.

In formula (5.3) $\mathbf{e}$ stands for a normalized electric field. The field is normalized such that the first Stokes parameter associated with the field is unitary:

$$s_0 = \mathrm{Tr}\{\langle\mathbf{e}\mathbf{e}^{\dagger}\rangle^{[\xi,\eta]}\} = 1 \tag{5.4}$$

since the intensity is considered with appropriate scaling factors in the radiance term. We point at the fact that atmospheric transmission and scattering modifies the geometry of observation, polarization and coherent structure of the fields (see Appendix C). Any stray-light from the Sun or other direction is also dis-considered. On the other hand, since the main aim of aerosol scattering retrieval is the determination of the scatterers' properties by analysis of the Stokes parameters, we consider the (normalized) Stokes parameters fully arbitrary due to scattering effects and in the angular representation defined in Equation

[1] some overlap with the analysis Chapter 6 is unavoidable in this part of the treatment

(4.39). The normalized Stokes parameters are point and direction dependent and fully determined in terms of the Pauli matrices defined in equation (4.40).
The radiance $L^{\infty}_{\lambda(\hat{\mathbf{s}}_i,\tilde{\mathbf{q}},t)}$ shall also be corrected for all atmospheric interactions. We will consider that the variable of interest for the science requirements is the retrieval of this radiance and the Stokes parameters associated with the input light at the field plane of the Optical System. With an appropriate atmospheric model, the knowledge of the *BRDF* (*Earth-Bidirectional Reflectance Distribution Function*) and the solar irradiance, one may compute more accurate atmospheric parameters for the given science and mission case in consideration.
Once the focusing problem is resolved and the electric field transformation properly described, the equation (5.3) describes the integration in the object plane directly in terms of radiance emitted by the source, similar to the corresponding scalar radiance definition. We finally show consistency with the power conservation in classic radiometry. According to classic radiometry, the total power in the beam is given by an integration over the spectrum and the optical etendue G of the system:

$$\Phi = \int_{\partial G}\int_0^{\infty} L^{\infty}_{\lambda(\hat{\mathbf{s}}_i,\mathbf{r})} d^2G d\lambda \qquad [W] \tag{5.5}$$

where d^2G is a second-order differential defined by:

$$d^2G = \hat{\mathbf{s}}_i \cdot \hat{n}_{ep} dA_{ep} d\Omega_{gr\to e} \qquad [m^2] \tag{5.6}$$

$\hat{n}_{ep}$ being the normal of the pupil surface of differential area dA_{ep} and $d\Omega_{gr\to e}$ an infinitesimal solid angle subtended by an area of ground to a point on the pupil. According to coherence theory, we may regard the total power as the integration of the incident (mean-averaged) Poynting vector across the pupil, hence:

$$\Phi = \frac{1}{2\eta_0}\int_{A_{ep}}\int_0^{\infty} \mathrm{Tr}\{\mathbb{W}^{\infty}_{(r\hat{\mathbf{s}}_i, r\hat{\mathbf{s}}_i,\omega)}\}\hat{\mathbf{s}}_i \cdot \hat{n}_{ep} d\omega dA_{ep} \qquad [W] \tag{5.7}$$

by considering the change of variable $\omega \to \lambda$, the two equations are the same in the far field[2].

5.2. Field Decompositions

In this section, we derive expressions for the refracted electric field of the Optical Systems both in a p-s reference, in a cartesian reference frame and in the local transverse frame $\xi\eta$. This allows us to describe the focal fields right on top of the metasurface structure, but is a formalism which can be applied in much wider applications. Such transformations are required when performing integrations and analyzing the polarization properties of the focal fields undergoing the transformation in the Optical System. Focusing diffracting integrals must, in fact, be carried out all in a consistent cartesian frame and the azimuthal and polar dependence of the fields are not fully arbitrary due to geometry constraints.
Consider a generic ray, in the cartesian frame of direction $\hat{\mathbf{s}}_i^+$ (see Equation (4.21)). An arbitrary base can be used to the description of its transverse fields. In particular, two bases are of practical ease (see Chapter 4 for the notation used):

- The base determined from the minimum rotation which leads from $\hat{\mathbf{z}}$ to $\hat{\mathbf{s}}_i^+$. When applied to the whole cartesian frame such base is the closest orthonormal and tranverse base which can be determined. We will refer to it as ξ, η frame. It can be determined through a rotation of θ_i around the axis $\hat{\boldsymbol{\varepsilon}}_{\parallel,i} = (-\sin\phi_i, \cos\phi_i, 0)$. Is the cartesian base for $\theta_i = 0$.
- A base for which one of the versors lays in the incidence plane (p) and the other one is the normal of the incidence plane (s), once a surface normal has been specified. That's the p, s frame. It can be determined by initial rotation of ϕ_i around the axis $\hat{\mathbf{z}}$ and subsequent rotation of θ_i around the axis $\hat{\boldsymbol{\varepsilon}}_{\parallel,i} = (-\sin\phi_i, \cos\phi_i, 0)$. Such definition is valid for a generic ray when a normal surface $\hat{z}$ is considered or when not-skewed rays with a normal in the incidence plane are considered. For fully arbitrary rays and surfaces, one must retrieve the incidence plane normal first and then perform such decomposition, case we won't require explicitly yet. This frame is useful to describe polarization effects, which are diagonal in such frame for not-skewed rays and due to their simpler form and wide use in electromagnetic treatments.

[2]The Poynting vector generally depends on the magnetic field, which however is fully determined by the electric field in the far-field, since the coherent mode decomposition of the fields behave as a local plane-wave. That allows us to consider the intensities in terms of electric energy intensity only. Such conditions shall be reviewed in near-field applications.

Recalling the matricial property of rotation of a frame to an angle β around an axis $\mathbf{w}$ (the cross-product matricial operator $\chi_{\{\mathbf{w}\}}$ is defined in Appendix B):

$$\mathbb{R}_{(\mathbf{w},\beta)} = \cos\beta\mathbb{I} + \sin\beta\chi_{\{\mathbf{w}\}} + (1-\cos\beta)\mathbf{w}\mathbf{w}^T \tag{5.8}$$

we determine for the two bases:

$$\Sigma_i^{[\xi,\eta]} = [\hat{\boldsymbol{\xi}}_i, \hat{\boldsymbol{\eta}}_i] = \begin{bmatrix} (-\cos(\theta_i)+1)\sin^2(\phi_i)+\cos(\theta_i) & -(-\cos(\theta_i)+1)\sin(\phi_i)\cos(\phi_i) \\ -(-\cos(\theta_i)+1)\sin(\phi_i)\cos(\phi_i) & (-\cos(\theta_i)+1)\cos^2(\phi_i)+\cos(\theta_i) \\ -\sin(\theta_i)\cos(\phi_i) & -\sin(\phi_i)\sin(\theta_i) \end{bmatrix} \tag{5.9}$$

and, for the p and s polarization directions at a surface $z = constant$:

$$\Sigma_i^{[p,s]} = [\hat{\boldsymbol{\varepsilon}}_\perp, \hat{\boldsymbol{\varepsilon}}_\parallel] = \begin{bmatrix} \cos(\phi_i)\cos(\theta_i) & -\sin(\phi_i) \\ \sin(\phi_i)\cos(\theta_i) & \cos(\phi_i) \\ -\sin(\theta_i) & 0 \end{bmatrix} \tag{5.10}$$

It is useful to visualize graphically the $p-s$ frame for a given input polarization direction at the entrance pupil. The focusing geometry is depicted in Figure 5.1, along with the versors of the $p-s$ introduced up to now. The components on the $p-s$ frame are represented for illustration on a Gaussian sphere in Figure 5.3, for an ξ polarized excitation and ideal optical transmission. The p distribution does also present a z component whose signs depend on the azimuthal angle. For further use in the report, we further define :

$$\Sigma_i^{[\phi]} = [\hat{\boldsymbol{\varepsilon}}_{\perp,0}, \hat{\boldsymbol{\varepsilon}}_{\parallel,0}] = \begin{bmatrix} \cos(\phi_i) & -\sin(\phi_i) \\ \sin(\phi_i) & \cos(\phi_i) \end{bmatrix} \tag{5.11}$$

which represents an arbitrary rotation along the local third bases of a reference frame. At the entrance of the Optical System, we decompose the field in the ξ,η frame. This is equally applicable also for not-paraxial beam and the ξ,η frame tends to the x,y frame in the paraxial limit. The polarized field component of the normalized electric field, associated with the Stokes parameters defined in Equation 4.39, is written in that frame as per Equation (4.38). The given electic field direction applies for a ray of the sub-bundle, defined in Chapter 6. In principle, the polarization direction may present a distribution across the entrance pupil for a sub-bundle (for example, be azimuthally or radially polarized in part and further apodized), which influences the focusing. We will hence refer to $\overline{\mathbf{e}}^{[\xi,\eta]}$, a pupil averaged electric field over the sub-bundle. An apodization matrix can always be used to link the two as:

$$\mathbf{e}^{[\xi,\eta]} = \overleftrightarrow{\alpha}\overline{\mathbf{e}}^{[\xi,\eta]} \tag{5.12}$$

The vectorial transformations described, opportunely combined can describe the coherent polarized focusing of an arbitrary pupil-diffracted system with other non-diffracting transmittances along the way. We explicit for further use hence the focal fields focused right on top of the metasurface structure under study (at distance f from principal surface)

Paraxial Sub-Bundle For this sub-bundle, the local $\xi-\eta$ frame at the entrance pupil is exactly the $x-y$ frame. Since depolarization is minimal for this sub-bundle, there is no need to further transform to the $p-s$ frame at the exit pupil. The sub-bundle gets directly mapped in the $\xi_f-\eta_f$ frame spanned by the focused angles. The final expression of the vectorial field focused by the system for this sub-bundle in the cartesian frame $\Sigma_0 = \{x,y,z\}$, at a distance f is given by:

$$\mathbf{e}_{k,f|\Sigma_0}^{(top,+)} = \left(\frac{ife^{ikf}}{2\pi k_z}\right)\Sigma_f^{[\xi,\eta]}\overleftrightarrow{\alpha}_{eff}\overline{\mathbf{e}}_{in}^{[x,y]} \qquad [m^2] \tag{5.13}$$

where $\Sigma_f^{[\xi,\eta]}$ is the matrix defined in Equation (5.9) evaluated in the focused angles ϕ,θ as represented in Figure 6.7, and we have considered the Fraunhofer far-field propagator depicted in [28] for a focal length f. Note that the units of the normalized field are now m^2.
The apodization $\overleftrightarrow{\alpha}_{eff}$ can be corrected to include any further apodization of the optical system (for example, a $\sqrt{\cos\theta}\mathbb{I}$ apodization is proposed in [28], which we will use from now on). Apodization however strongly depends on the realization of the optical system. A spurious term $\propto(1-\cos\theta)$ is present which has opposite polarization to the one of the input. This spurious term is represented in Figure 5.2 and

its existence is a consequence of projection effects inherent with the refraction, sketched in the same figure. The deviation is minimal for small NA and known as *maltese* in practical applications [24], but is important to consider for applications in which the polarization sensitivity requirements are critical. A field on z is also naturally present due to refraction.

Arbitrary Sub-Bundle Consider now the general case of not paraxial focusing. When a real optical system is considered, we first transform the $\overline{\mathbf{e}}^{[\xi,\eta]}$ in the input $p-s$ field by applying the tranverse of the rotation matrix depicted in Equation 5.11. A transformation $[\xi,\eta]\rightarrow[p,s]$ can in fact be seen as a rotation of $-\phi$ along the ray axis. The response of the optical system for a ray, from the $p-s$ of the entrance pupil to the one at the exit pupil, can always be written as a Jones matrix of the form:

$$\mathbb{J}^{(o)}=\begin{bmatrix}\tau_{pp}^{(o)} & \tau_{ps}^{(o)}\\ \tau_{sp}^{(o)} & \tau_{ss}^{(o)}\end{bmatrix} \tag{5.14}$$

where $\tau_{ps}^{(o)}=\tau_{sp}^{(o)}=0$ when the rays are not-skewed. The coefficient in such a matrix shall be retrieved by ray-tracing propagation in the Optical System and are in general complex-valued. The final vectorial expression of the focused field in the cartesian reference is hence of the form:

$$\mathbf{e}_{k,f|\Sigma_0}^{(top,+)}=\left(\frac{ife^{ikf}}{2\pi k_z}\right)\Sigma_f^{[p,s]}\mathbb{J}^{(o)}\left(\Sigma^{[\phi]}\right)^T\overleftrightarrow{\alpha}_{eff}\overline{\mathbf{e}}_{in}^{[\xi,\eta]} \tag{5.15}$$

The measurements of the fields is now biased by induced polarization in the optics. The magnetic field can also be fully retrieved from the input electric field at the entrance pupil. Without loss of generality we refer to the non-dimensional magnetic field (for dimensional relations involving the vacuum impedance, refer to Appendix C). We must simply rotate of $\pi/2$ along the wave-vector axis. Such rotation is equivalent to the multiplication with $\Sigma^R=\Sigma^{[\phi=\pi/2]}$ within the $p-s$ frame after the optical system depolarization, so that:

$$\mathbf{h}_{k,f|\Sigma_0}^{(top,+)}=\left(\frac{ife^{ikf}}{2\pi k_z}\right)\Sigma_f^{[p,s]}\Sigma^R\mathbb{J}^{(o)}\left(\Sigma^{[\phi]}\right)^T\overleftrightarrow{\alpha}_{eff}\overline{\mathbf{e}}_{in}^{[\xi,\eta]} \tag{5.16}$$

In the Appendix E we work out some validated examples of transformation for a non-ideal lens and a system which presents a non-diffracting polarizer, such examples may clarify the reader on the use of those formulas to model the optical transformation of the tranverse fields.

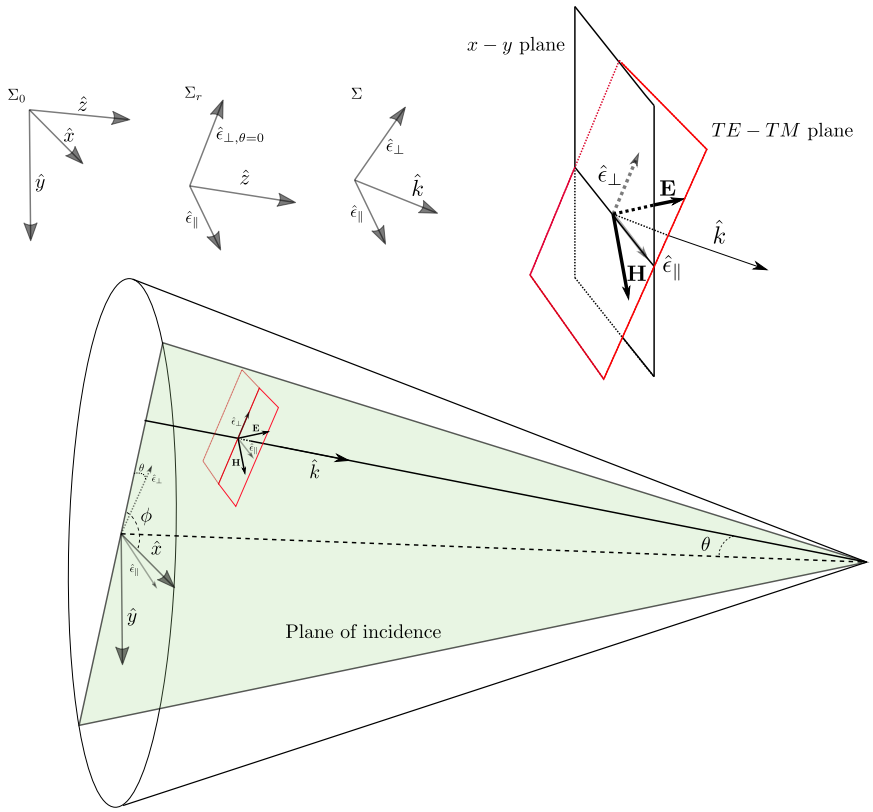

Figure 5.1: Illustration of reference frame and symbols used through the derivation. The plane of incidence is inclined of ϕ with respect to the $\hat{x}$ axis. The plane TE-TM contains the fields and the versor $\hat{\epsilon}_\parallel$ is the intersect between the $x-y$ plane and the $TE-TM$ plane. The versor $\hat{k}$ forms an angle of θ with the optical axis. The plane TE-TM can also be thought to be tangent to a local spherical wave centered in the focus, vertex of the cone.

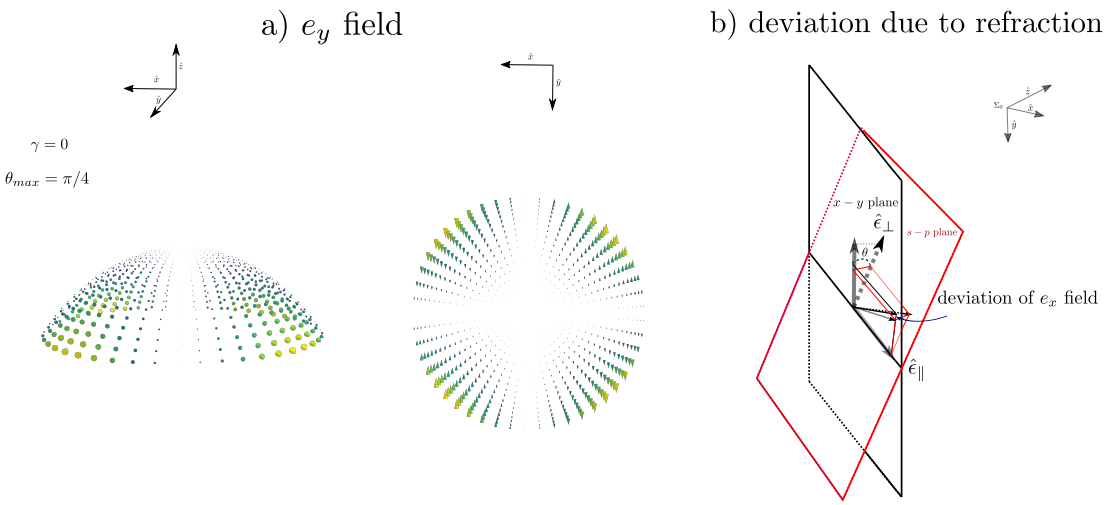

Figure 5.2: a) Spurious e_y field present upon focusing of an x polarized field due to refraction geometrical projection. b) Geometrical projection due to refraction leads to a deviation of the field when x is inclined with respect to the $p-s$ frame. Such deviation creates the spurious term e_y upon recombination of the fields.

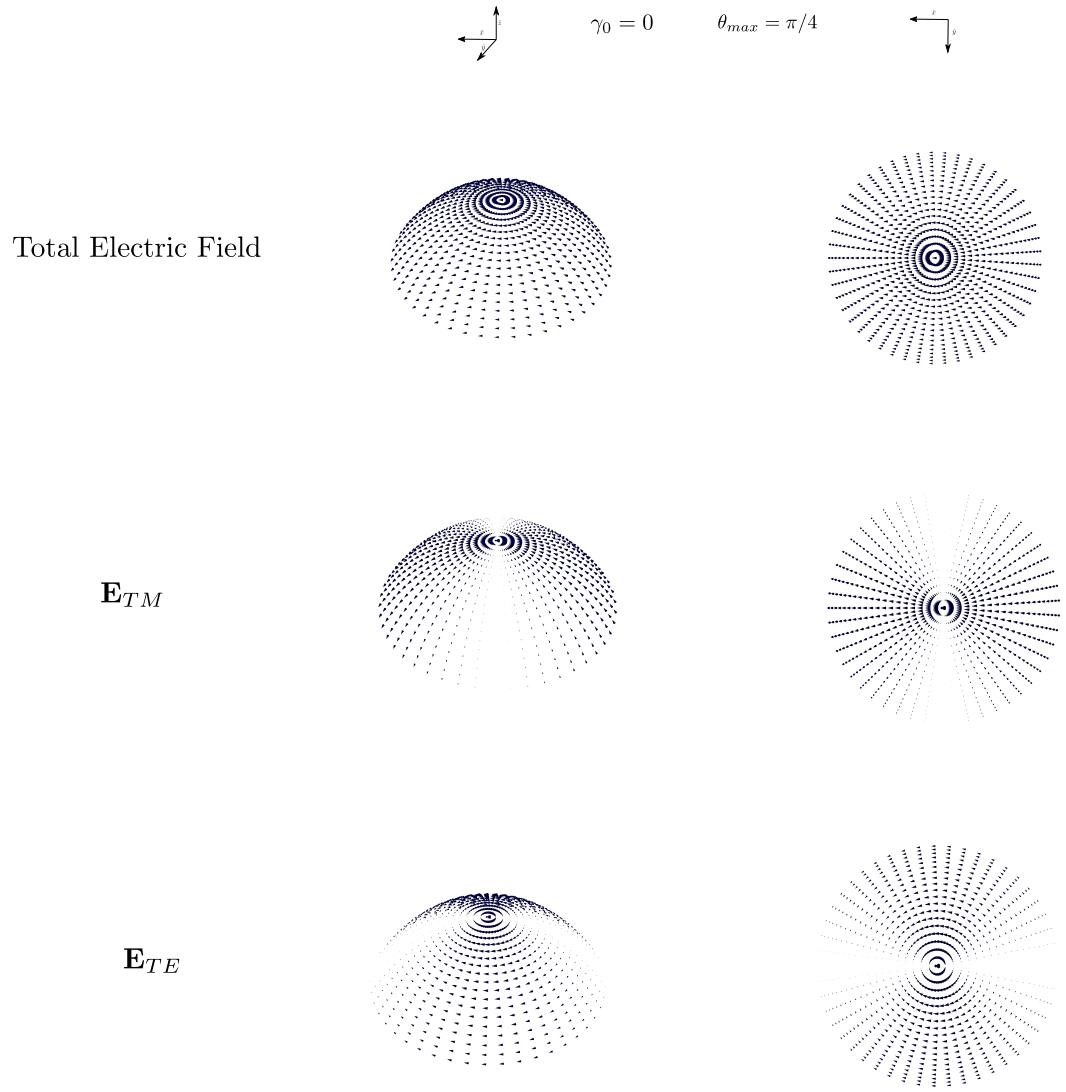

Figure 5.3: Decomposition of the electric field on the reference sphere, in p-TM and s-TE components. The field at the input is here ξ polarized ($\gamma_0 = 0$). The s and p versors forms geodesics on the sphere and the magnitude of the components follows a cosine distribution. The magnetic field would possess a similar distribution, rotated of $\pi/2$ and swapped p-s fields. y polarized light would possess also the same distribution rotated of $\pi/2$.

5.3. Metasurface Optical Response

Even though the response of the metasurface device has been already investigated [1], more detailed characterization is required to describe the angular transmission in more detail, as well as diffraction effects and finer polarization effects due to focusing. A quick selection of inclusion sizes with respect to wavelength itself, it is much more efficiently performed in terms of modeled maps rather than cumbersome FEM simulations. The development of an analytical model to efficiently estimate this performance, supported by FEM analysis for validation, is paramount in our opinion for this purpose. High-level requirements parameters (like spectral resolution, induced polarization, spectral band transmission) do in overall depend on this finer description. In particular, is the transmittance of the filter (in various conditions) to be influencing the whole retrieval process: all other variables are of interest as they influence the power integrated in the pixels and the reconstruction. We hence use a comprehensive view in which diffraction and polarization effects, as well as non-idealities, are comprehensively considered in the definition of the transmittance and other performance parameters defined in Sub-Section 5.3.4. For power budgets, however, transmittance under simpler illumination conditions shall be used (e.g. uniform, non-apodized field) to provide simple engineering figures for the design.

In this Section, we lay down the main concept and formulas used in this characterization. We first analyze, more qualitatively, the real finite structure, as composed of different resonator cells each one representing a finite periodic array. The transmittance of this structure has not been analyzed previously from an electromagnetic point of view, as in fact FEM simulations rely on periodic boundary conditions applicable for infinitely periodic arrays. The relaxation of this hypothesis is not yet possible within our modeling capabilities; nevertheless, we tentatively extrapolate the finite transmittance of the finite filter and outline a methodology for its diffraction modeling. The performance of the real structure assumes a rather important simplification in the case in which we may consider the pixel composed of one periodic array wider than the optical spot of the system, a condition we will refer to as *wide resonator*.

We hence then describe the effective medium formulation, which allows modeling one resonator cell of the cavity with inclusion as an effective medium of certain material properties. The multilayer performance general performance is then described in terms of cavity resonance curves, discussed in Section 5.3.6. Simple performance parameters (directional spectral transmittance under focused illumination, band transmittance) are in particular defined. The diffraction solution of the wide pixel coupled with pupil diffraction is then reported exactly in terms of a Zernike Expansion. Within some assumptions, those results may also be used for the *not-wide pixel* performance by using the enclosed energy in those modes.

5.3.1. Preliminary analysis of the EM performance of the finite structure

A sketch of the real multilayered structure across the border of two resonator cells is depicted in Figure 5.4. This structure can be considered as a composition of a multilayer (top DBR) of which the spectral transmittance has known modeling, a cavity of hexagonal lattice with various orientations of the scatterers, of unknown transmittance, and a bottom DBR. The plane-wave response of the mirrors layers is known and assumed to be non-diffractive (a transparency in the Fourier domain). In the below formulas, all quantities shall be considered to be implicit functions of the focusing point (x_{fi}, y_{fi}) and hence the point on the ground in object space. The cavity with inclusions, invoking linearity of the fields $\boldsymbol{\mathcal{F}}_i^{\pm} = (E_{p,i}^{+}, E_{p,i}^{-}, E_{s,i}^{+}, E_{s,i}^{-})$ in each transverse plane, will possess a spectral response of the type:

$$\boldsymbol{\mathcal{F}}^{\pm(cav,out)}_{(k'_x,k'_y,\omega)} = \int_{-\infty}^{\infty}\int_{-\infty}^{\infty} \mathbb{G}^{(m)}_{(k_x,k_y,k'_x,k'_y,\omega)} \boldsymbol{\mathcal{F}}^{\pm(cav,in)}_{(k_x,k_y,\omega)} dk_x dk_y \tag{5.17}$$

with $\mathbb{G}^{(m)}$ representing a (matrix) transfer function between the spectrums, whose determination is cumbersome both theoretically and experimentally. The electromagnetic performance can hardly be tested experimentally as in doing so any probe positioned for sensing will influence the fields. Theoretically, the response may be determined from finite FEM simulations by performing FFTs of the spatial field distributions and calculating the transfer matrix associated with the so determined scattering matrix, main difficulty being simulation time and proper definition of boundary conditions.

It follows that an exact propagation of the fields from the top layers of the filters to the focal fields can be described by:

$$\boldsymbol{\mathcal{F}}^{\pm(f)}_{(k'_x,k'_y)} = \int_{-\infty}^{\infty}\int_{-\infty}^{\infty} \mathbb{T}^{bottom}_{(k'_x,k'_y)} \mathbb{G}^{(m)}_{(k_x,k_y,k'_x,k'_y,\omega)} \mathbb{T}^{top}_{(k_x,k_y)} \boldsymbol{\mathcal{F}}^{\pm(top)}_{(k_x,k_y)} dk_x dk_y \tag{5.18}$$

The problem with the above equation are various: $\mathbb{G}^{(m)}_{(k_x,k_y,k'_x,k'_y,\omega)}$ is unknown and the field $\boldsymbol{\mathcal{F}}^{\pm(top)}_{(k_x,k_y)}$ does depend itself on the reflected solution of the coupling problem (is the complete field). A scattering matrix cannot be determined from the above expression without prior knowledge of the fields decomposition of the reflected field or opportune discretization of its spectrum. In particular, again invoking linearity in the scattering matrix, the relationships will be of the type:

$$\begin{cases} \boldsymbol{\mathcal{F}}^{\pm(top)}_{(k_x,k_y)} = \mathbb{P}^{+}\mathbf{e}^{(top,+)}_{k,f|\Sigma_{[p,s]}(k_x,k_y)} + \mathbb{P}^{-}\displaystyle\int_{-\infty}^{\infty}\int_{-\infty}^{\infty}\mathbb{J}^{-}_{(k_x,k'_x,k_y,k'_y)}\mathbf{e}^{(top,+)}_{k,f|\Sigma_{[p,s]}(k'_x,k'_y)}dk'_x dk'_y \\ \boldsymbol{\mathcal{F}}^{\pm(f)}_{(k'_x,k'_y)} = \mathbb{P}^{+}\displaystyle\int_{-\infty}^{\infty}\int_{-\infty}^{\infty}\mathbb{J}^{+}_{(k_x,k'_x,k_y,k'_y)}\mathbf{e}^{(top,+)}_{k,f|\Sigma_{[p,s]}(k'_x,k'_y)}dk_x dk_y \\ \mathbf{e}^{(top,+)}_{k,f|\Sigma_{[p,s]}(k''_x,k''_y)} = \left(\Sigma^{[p,s]}_{i(k''_x,k''_y)}\right)^{T}\mathbf{e}^{(top,+)}_{k,f|\Sigma_0(k''_x,k''_y)} \qquad \mathbb{P}^{+} = \begin{bmatrix}1&0\\0&0\\0&1\\0&0\end{bmatrix} \qquad \mathbb{P}^{-} = \begin{bmatrix}0&0\\1&0\\0&0\\0&1\end{bmatrix} \end{cases} \tag{5.19}$$

The system of equations (5.18), (5.19) could be solved to determine $\mathbb{J}^{-}_{(k_x,k'_x,k_y,k'_y)}$ and $\mathbb{J}^{+}_{(k_x,k'_x,k_y,k'_y)}$ as functions of $\mathbb{G}^{(m)}_{(k_x,k_y,k'_x,k'_y,\omega)}$ and the transfer matrices of the mirrors, where the expression of $\mathbf{e}^{(top,+)}_{k,f|\Sigma_0(k_x,k_y)}$ is given in (5.15). A possible resolution method involves discretization of the integrals in $m\times n$ gridpoints and definition of reflection and transmissions coefficients for each polarization and grid points. The transfer matrix approach has been generalized to multiple dimensions in Appendix A to allow such transformation. Alternatively, iterative approaches using only the scattering matrices are also possible. One would then determine, in complete generality, the response matrix $\mathbb{H}$ appearing in Equation (4.45) by inverse Fourier transforming the discretized $\mathbb{J}^{+}_{(k_x,k'_x,k_y,k'_y)}$.

Even though possible, this approach results in inversion of very dense matrices and requires involved numerical analysis of the sampling techniques. The main difficulty arises from the fact that the scattering matrix can only be determined after properly sampling the spectrum of the field and resolving the convolution integrals, due to the fact that diffraction couples with the DBRs stacks. Strictly speaking, the diffraction regime is neither in the Fraunhofer neither in the classical Fresnel regime. Moreover, it is not possible to validate within the research time-frame since finite performance has not been analyzed neither experimentally neither via FEM simulations.

We however observed that coupling of the finite structure is limited to a few inclusions across the border (see Figure 5.5)[3] and that the response of an infinite periodic array exciting one scattering mode in the propagating spectrum is a plane-wave eigenfunction after a certain propagation length. Is it hence reasonable to assume that the transmittance across the spatial region of one pixel can be given by the one of the infinite structure when not in close proximity to the borders. The contribution of a single pixel resonator cell may hence be seen as due to a pixelation function as represented in Figure 5.5, denoted by $P^{(m)}_{(x_m,y_m)}$. When arbitrarily small, they can represent a discretization grid function. Note that the pixelation function must be continuous in order for the wavefront to be continuous across the borders. As knowledge of the response $\mathbb{G}^{(m)}$ is not available, the tapering of this function is unknown (but likely limited to a region of 3-4 inclusions in the transverse direction, unless transverse waveguide modes or scattering are strongly excited). The pixelation function extension depends on the imager arrangement chosen (here, variable in terms of inclusions geometry only on the along-track direction). Upon such assumptions, consider a step-wise representation of the field:

$$\boldsymbol{\mathcal{F}}^{\pm(cav,in)}_{(x_m,y_m,\omega)} = \sum_{j=1} P^{(m)}_{j(x_m,y_m)}\boldsymbol{\mathcal{F}}^{\pm(cav,in)}_{(x_m,y_m,\omega)} \tag{5.20}$$

which in terms of Space Fourier Transform reads:

$$\boldsymbol{\mathcal{F}}^{\pm(cav,in)}_{(k'_x,k'_y,\omega)} = \sum_{j=1}\int_{-\infty}^{\infty}\int_{-\infty}^{\infty}\tilde{P}^{(m)}_{j(k'_x-k_x,k'_y-k_y)}\boldsymbol{\mathcal{F}}^{\pm(cav,in)}_{(k_x,k_y,\omega)}dk_x dk_y \tag{5.21}$$

[3] that's a theoretical results of the coupled interaction in scattering theories, decaying with distance as $1/r^n$ for a certain n

where $\tilde{P}^{(m)}_{j(k_x,k_y)}$ is the Fourier Transform of the pixelation function. It follows that a discretization of $\mathbb{G}^{(m)}$ is given then by:

$$\mathbb{G}^{(m)} = \sum_{j=1} \tilde{P}^{(m)}_{j(k'_x-k_x,k'_y-k_y)} \mathbb{T}^{\infty}_{j(k'_x,k'_y,\omega)} \tag{5.22}$$

where $\mathbb{T}^{\infty}_{j(k'_x,k'_y,\omega)}$ is the 4×4 transfer matrix of the cavity inclusion of an infinitely periodic array with the same arrangement as the cell j (along-track direction), which is derived in next Sub-Sections. If in particular the dimension l_r of the resonator cell is significantly bigger than the extension of the optical spot at a given NA (known to be $\propto 1/(k \sin\theta_{max})$ from the Airy solution), such that:

$$k l_r \sin\theta_{max} >> 1 \tag{5.23}$$

the focal spot not in the proximity of the borders and the diffraction coupling with the mirrors weak, the filter can be treated as a transparency in the frequency domain. In fact, the Fourier Transform of the pixelation function will be in that case well approximated by a Delta Diraq and only one of the terms in the summatory. We would reach the same conclusion by means of simpler energy considerations. In such case:

$$\boldsymbol{\mathcal{F}}^{\pm(f)}_{(k'_x,k'_y)} \cong \mathbb{T}^{bottom}_{(k_x,k_y)} \mathbb{T}^{\infty}_{j(k_x,k_y,\omega)} \mathbb{T}^{top}_{(k_x,k_y)} \boldsymbol{\mathcal{F}}^{\pm(top)}_{(k_x,k_y)} \qquad \forall (x_{fi}, y_{fi}) \in P^{(m)}_{j(x_m,y_m)} \cong 1 \tag{5.24}$$

which has now a simple associated Scattering Matrix. We hence switch attention to the determination of the cavity response $\mathbb{T}^{\infty}_{j(k_x,k_y,\omega)}$ by means of an effective medium formulation.

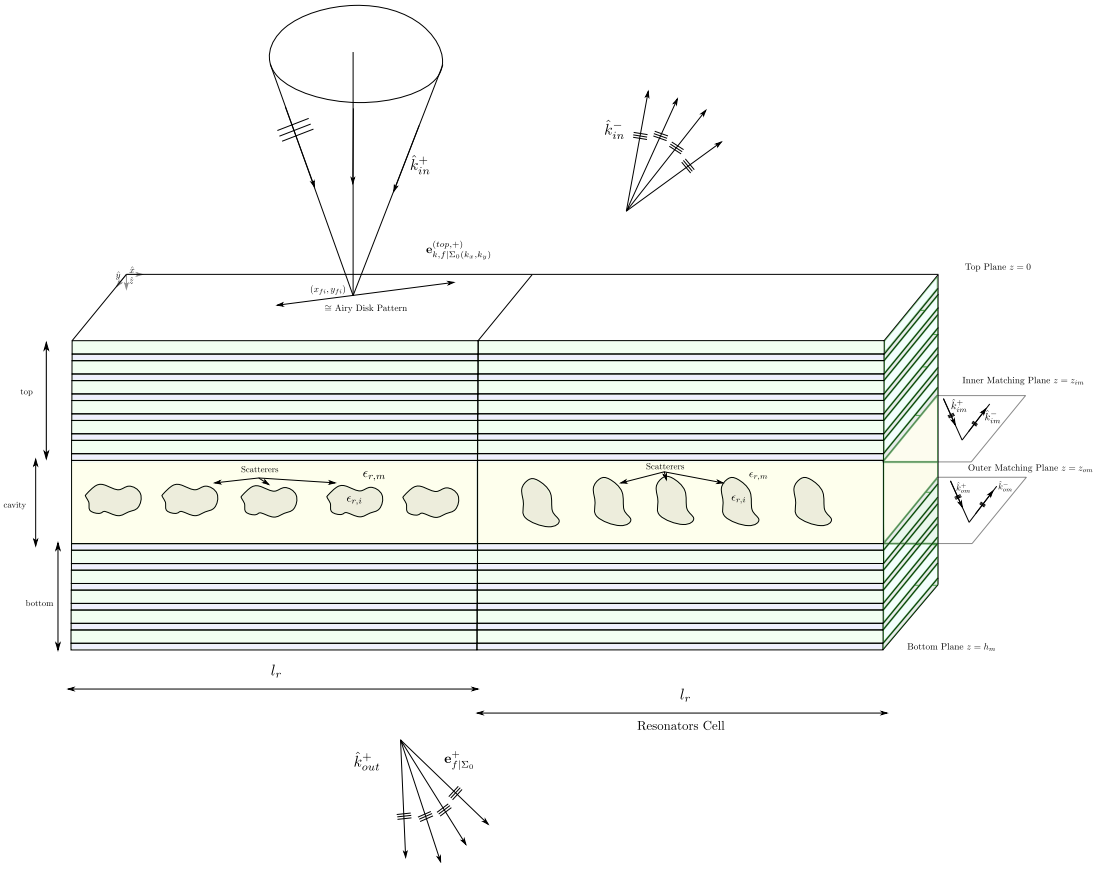

Figure 5.4: Sketch of multilayered structure with inclusions across two resonator cells (pixels). Scatterers are periodic but at different orientations or with different dimensions. The input field is a focused field. The structure is divided into top, cavity and bottom stacks, each one having their complete 4×4 transfer matrix describing their couplings in terms of plane-wave response. It is considered the inner matching plane to be the diffracting layer.

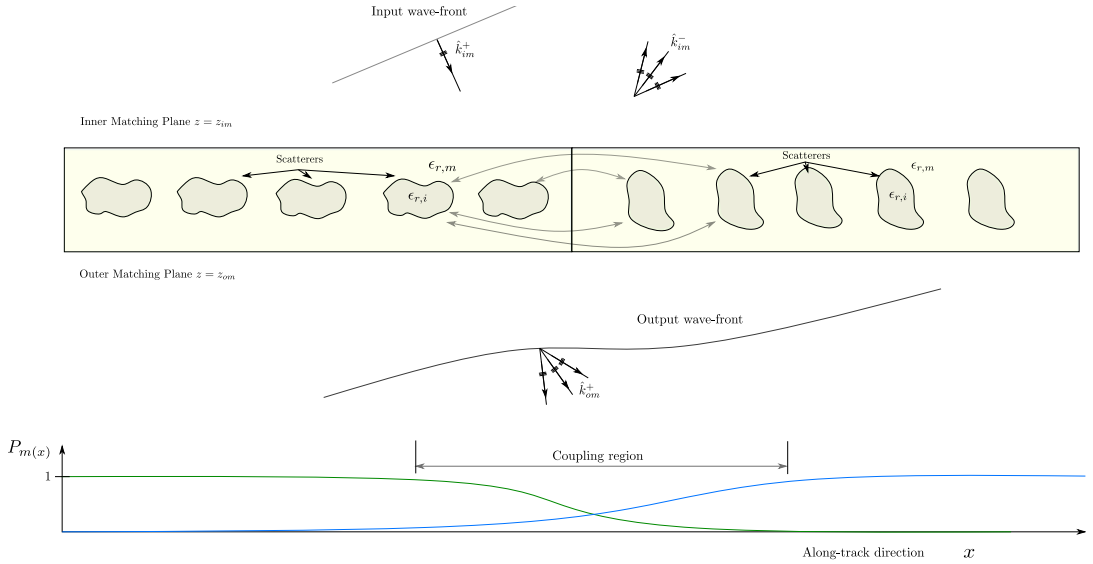

Figure 5.5: Representation of the cavity layer with inclusions across borders and its transformation for an input plane-wave, with one propagating mode. Only the top excitation is represented. Only a few of the scatterers are field coupled between cells. Wavefront must be continuous across the border so that a plane-wave spectrum is excited for a single plane-wave excitation. Below, a qualitative sketch of a pixellation function is represented.

5.3.2. Effective Medium Formulation

The multilayer is composed of isotropic slabs of different dielectric materials and a cavity with inclusions. Since wide resonators are under considerations, the response of the cavity with inclusions will create a set of discrete and distinct plane wave excitations k_x, k_y depending on the lattice Floquet modes excited by the scatterers. Since for imaging we must avoid the presence of multiple propagating modes, the wide effective cavity can be also treated by means of a transparency function in the frequency domain, after a certain extinction length of the cavity, z_{ext}. In other words, it responds to a plane-wave excitation by means of a plane-wave output. We claim that all such structures can be modeled by means of an anisotropic slab effective model, with a (relative) effective permittivity of the form:

$$\overleftrightarrow{\epsilon}_r = \begin{bmatrix} \epsilon_{x,r} & 0 & 0 \\ 0 & \epsilon_{y,r} & 0 \\ 0 & 0 & \epsilon_{z,r} \end{bmatrix} \tag{5.25}$$

We further claim that such permittivity tensor shall be diagonal, since the geometry of the structure presents clearly such simmetry and that when used in transfer matrix formulations it shall also describes the coupling of the metasurface with other layers accurately, as far as the additional disconsidered modes are negligible. The diagonality condition may, in reality, vanish upon illumination at an angle (since both illumination and geometry have to be simmetric in order to apply simmetry considerations) but we will neglect this factor for now. The effective permittivity parameters are obviously correlated to the fields induced by the geometry of the particle (its aspect ratio, height, diameter). In particular, known relationships are present in literature for the quasi-static problem (e.g. $\omega \to 0$) for such effective mediums. Such simplified relationships, derived from the Eshelby Tensors approach used also in Mechanics, are implicit relations of the approximated form [45] (dropping the subscript r for ease):

$$\begin{aligned} 1 - c &= \frac{\epsilon_i - \epsilon_x}{\epsilon_i - \epsilon_m} \left(\frac{\epsilon_m}{\epsilon_x} \right)^{AR/(AR+1)} \\ 1 - c &= \frac{\epsilon_i - \epsilon_y}{\epsilon_i - \epsilon_m} \left(\frac{\epsilon_m}{\epsilon_y} \right)^{1/(AR+1)} \qquad (quasi - stationary\ model) \\ \epsilon_z &= c\epsilon_i + (1-c)\epsilon_m \end{aligned} \tag{5.26}$$

where ϵ_i is the permittivity of the inclusion (particle), ϵ_m is the permittivity of the matrix (bare cavity), c the volume fraction of inclusions present in the cavity, AR the aspect ratio D_y/D_x, with D the diameter of

the ellipse along the local x, y directions and $\epsilon_{x,y}$ the resulting (relative) permittivities in those direction. The behavior for various refractive indices and aspect ratio is represented in Figure 5.6. According to

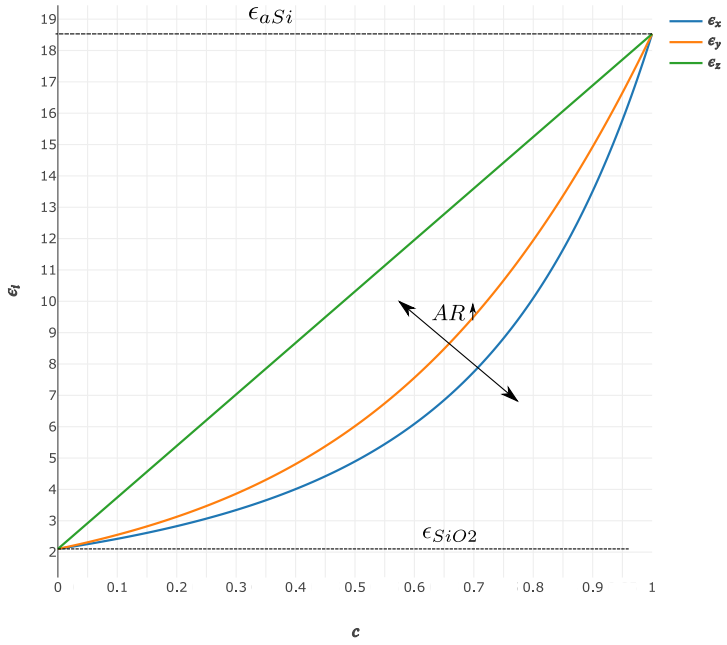

Figure 5.6: Plot of the permittivities appearing in the implicit equation (5.26) as a function of the volume percentage c for a given aspect ratio of $AR = 1.5$. The matrix has been assumed to be made of SiO_2 and the elliptical inclusion of aSi

such a stationary model, an optimal value of c exists, for a given aspect ratio, to maximize the contrast in permittivities. That has been demonstrated to be the case also the real simulated structures. In the present geometry, consist of an hexagonal shaped cavity of lattice size a (between two parallel edges) and length l_{cav} with an elliptical inclusion of height h_i, the volumetric percentual of inclusion in a resonator cell is given by:

$$c = \left(\frac{\pi}{2\sqrt{3}}\right)\left(\frac{h_i D_x D_y}{a^2 l_{cav}}\right) \tag{5.27}$$

The effective formulas (5.26) results from some severe simplifications on the uniformity of the fields and does not include the dependence of frequency ω, neither takes into account the possible non-uniform distribution of the fields in the particle or its precise location. Is hence applicable only for the case in which $\max(D_x, D_y) < \lambda_0$ and $c < 1$, which are somewhat interconnected assumptions in our case.
Dispersive relations, taking into account the formal solution in presence of elliptical geometry, are also reported in terms of Mathieu functions for a single scatterer in [46], which is of too complex use for our treatment.
Irrespectively of what is the considered geometrical link relating the inclusion sizes, the wavelength and the effective permittivities, the advantage of using such a model is threefold: first, better understanding of the macroscopic influence of the fields and geometry can be provided by analyzing the related effective parameters; second, as we wish to verify via FEM simulations, those parameters will be relatively uniform in both spectrum and angles whenever resonances of the scattering are not induced; third, when coupled with a multilayer solver, such model can greatly enhance the simulation time of those structures and provide new inputs for the design. It, however, comes also with its own limitations: as used throughout the report, it can only describe one mode propagation for the cavity layer, so that the real cavity must be a plane-wave eigenfunction.
In principle, the effective parameters could be derived from a Floquet-Bloch mode formulation and decomposition of the fields. Such approach is for example used in [47], [48], [49]. Such models usually

rely on homogenization techniques, which, for a given θ_{max}, minimizes the errors in the fields distributions across the volume or the boundaries by use of a single-mode described with its own effective matrix. Some given constraints are actually physical for the determination of $\overleftrightarrow{\epsilon}_r$ due to the lattice periodicity only, irrespectively of the scatterer geometry, but the optimal values of $\overleftrightarrow{\epsilon}_r$ depend on the expansion's coefficients of the Bloch waves decomposition.
Another way to retrieve the value of permittivity is by performing FEM simulations with a small number of datapoints and matching exactly the transmission spectrum and its phase. An analytical model for the retrieval has been implemented but the analysis of the results still undergoing.

5.3.3. Plane-Wave Transmissions

Since we have assumed the inclusion cavity may be modeled by the use of an anisotropic layer, we can now investigate the plane-wave transmissions of the multilayer, by modeling the real structure with a bare anisotropic cavity. The plane-wave transmission is evaluated through the transfer matrix approach introduced in Chapter 4, which in comparison with FEM models offer a significantly faster calculation. The transfer matrix of the total multilayered structure is computed by means of Equation (4.30). Typical problems of instability in transfer matrix calculations can be avoided by using the transverse field transmission coefficients as in [27] (which ensures that the determinant of the transfer matrix is unitary) and by pertaining symbolic expressions by means of symbolic toolboxes. The Scattering Matrix associated with such transformation is computed in the $p-s$ frame by means of the procedure depicted in Appendix A, which leads to a final Jones matrix of the whole multilayered structure:

$$\mathbb{J}^{(m)}_{|\Sigma} = \begin{bmatrix} \tau^{(m)}_{pp} & \tau^{(m)}_{ps} \\ \tau^{(m)}_{sp} & \tau^{(m)}_{ss} \end{bmatrix} \tag{5.28}$$

The coupling terms $\tau^{(m)}_{ps}, \tau^{(m)}_{sp}$ may be in general present if the particle inclusion is elliptical (has an aspect ratio different than one), since axial-symmetry of the structure is broken. We have demonstrated the presence of those terms also with FEM simulations discussed in Appendix E. Moreover the given coefficients are always function of the angle of illumination θ of the plane-wave excitation and also functions of the azimuthal angle ϕ if the particles are elliptical.
One must remember that such coefficients (which may be alternatively also determined via FEM simulations) are represented in a $p-s$ frame. The base can be changed in the transverse ξ, η in both domain and co-domain by:

$$\mathbb{J}^{(m)}_{|\Sigma^{[\xi,\eta]}} = \Sigma^{[\phi]} \mathbb{J}^{(m)}_{|\Sigma} \left(\Sigma^{[\phi]}\right)^T \tag{5.29}$$

Or the full transformation from the entrance pupil can be considered as[4]:

$$\mathbf{e}_{\mathbf{k},f|\Sigma_0} = \left(\frac{ife^{ikf}}{2\pi k_z}\right) \Sigma^{[p,s]}_f \mathbb{J}^{(m)}_{|\Sigma} \mathbb{J}^{(o)} \left(\Sigma^{[\phi]}\right)^T \overleftrightarrow{\alpha}_{eff} \overline{\mathbf{e}}^{[\xi,\eta]}_{in} = \left(\frac{ife^{ikf}}{2\pi k_z}\right) \mathbb{J}_e \overline{\mathbf{e}}^{[\xi,\eta]}_{in} \qquad [m^2] \tag{5.30}$$

which transforms from the input ξ, η frame to the $x-y-z$ frame at the focal plane.

5.3.4. Performance Parameters

Before diving into the numerical analysis (discussed in Part III), it is worth describing main design criteria of DBR and the phenomena of cavity resonance from our perspective and defining two simple *performance criterias*: the (wide pixel) transmission under focused illumination and the (wide pixel) spectral band transmission.

Focused Transmissions for wide pixels

Once the transmission matrix is fully characterized for all angles and spectrum, enough information is available to define a transmission on focused illumination. In this section we define the wide pixel transmittance neglecting aberrations of the device and finiteness effects. Those will be tentatively included in the definition of a finite transmittance in Section 5.3.7.

[4] reflection coupling between system and metasurface is neglected (so that the Jones matrices directly multiply). Moreover, such expression is valid only in the wide-pixel limit. If the focused beam spot-size is comparable or bigger than the size of the resonator pixels, one shall used the formal diffracted field formulation as in Chapter (5.3.1) and a much more complex integral relationship applies instead

In the Section 5.1, we have normalized the fields such that $s_0 = 1$ at the entrance pupil and considered the weight of each ray to be given by a generalized radiance proportional to the trace of the cross-correlation tensor. The input spectral directional power at the entrance pupil (e.g. the coherent contribution of a point source over the whole pupil, measures in $[W/(\mu msr)]$ as defined in Table 4.1) is the integration of the radiance over the pupil (which acts as a coherence area). Neglecting possible apodization factors due to pupil orientation:

$$\Theta^{e}_{(\lambda,\mathbf{r}_{ob})} = \int_{A_{ep}} L_{\lambda(\mathbf{r}_{ob})} dA_{ep} = \left(\frac{\pi c_0}{\lambda^2 \eta_0}\right) \int_{A_{ep}} \mathrm{Tr}\{\mathbb{W}^{[\xi,\eta]}_{(\mathbf{r}_{ob},\omega,t)}\} dA_{ep} \qquad [W/(\mu msr)] \tag{5.31}$$

The focal fields at the detector from a point-source contribution will also be characterized, in the focal plane at negletion of aberrations, by a cross-correlation tensor:

$$\mathbb{W}^{[x,y]}_{(\mathbf{r},\omega,t,\hat{\mathbf{s}})} = \left(\frac{\lambda^2 \eta_0}{\pi c_0}\right) L_{\lambda(\mathbf{r}_{ob})} \langle \mathbf{e}_{f|\Sigma_0} \mathbf{e}^{\dagger}_{f|\Sigma_0} \rangle \qquad [V^2 s/m^2] \tag{5.32}$$

where the radiance $L_{\lambda(\mathbf{r}_{ob})}$ is the same one appearing in (5.31) (averaged over the sub-bundle if not-uniform) and $\mathbf{e}_{f|\Sigma_0}$ are the normalized focal fields in space domain. Recalling the Fraunhofer diffraction also depicted in [28], the fields $\mathbf{e}_{f|\Sigma_0}$ are the inverse Fourier Transform of the plane-wave representation appearing in Equation (5.30) so that:

$$\mathbf{e}_{f|\Sigma_0} = \frac{1}{4\pi^2} \int_{-\infty}^{\infty} \int_{-\infty}^{\infty} \mathbf{e}_{\mathbf{k},f|\Sigma_0} e^{ik_x x + ik_y y} dk_x dk_y \tag{5.33}$$

The spectral directional power at the focal plane of one pixel is then given, in complete analogy with the entrance pupil, as an integration over the whole detector plane:

$$\Theta^{\infty(f)}_{(\lambda,\hat{\mathbf{s}})} = \lim_{kl_p \sin\theta_{max} \to \infty} \lim_{kl_r \sin\theta_{max} \to \infty} L_{(\lambda,\mathbf{r}_{ob})} \int_{A_p} \mathrm{Tr}\{\langle \mathbf{e}_{f|\Sigma_0} \mathbf{e}^{\dagger}_{f|\Sigma_0} \rangle\} d^2 A_p \qquad [W/(\mu msr)] \tag{5.34}$$

where we have also considered the limit operation of wide pixels. In the limit, the integral can be resolved by means of the Parseval Theorem in an integration in the space spectrum as:

$$\lim_{kl_p \sin\theta_{max} \to \infty} \int_{A_p} \mathrm{Tr}\{\langle \mathbf{e}_{f|\Sigma_0} \mathbf{e}^{\dagger}_{f|\Sigma_0} \rangle\} d^2 A_p = 4\pi^2 \int_{\Omega} \mathrm{Tr}\{\langle \mathbf{e}_{\mathbf{k},f|\Sigma_0} \mathbf{e}^{\dagger}_{\mathbf{k},f|\Sigma_0} \rangle\} dk_x dk_y \qquad [m^2] \tag{5.35}$$

The trace in the right integral is simply the Fourier representation of the Stokes parameter $s_0^{(f)}$ at the focal field (by definition), which is then related to the input Stokes parameters defined in Equation (4.39) by (Fourier Domain):

$$s_0^{(f)} = \left(\frac{f^2}{4\pi^2 k_z^2}\right) \mathbf{M}_0^{\infty} \mathbf{s}^{(in)} \qquad [m^4] \tag{5.36}$$

where $\mathbf{M}_0^{\infty}$ is the first row of the plane-wave Mueller Matrix associated with $\mathbb{J}_e$ appearing in Equation (5.30). Further, integration in the space spectrum is simply an integration in the cone angle once the parametrization in Equation 4.21 is used. Since (due to differential analysis also performed in [28], Chapter 3):

$$dk_x dk_y = k_0^2 \cos\theta \sin\theta d\theta d\phi \tag{5.37}$$

Connecting all together, the following dimensionally sound equation is found:

$$\Theta^{\infty(f)}_{(\lambda,\mathbf{r}_{ob})} = L_{\lambda(\mathbf{r}_{ob})} f^2 \int_{\Omega} \mathbf{M}_0^{\infty} \mathbf{s}^{(in)} \sin\theta d\theta d\phi \qquad [W/(\mu msr)] \tag{5.38}$$

where we consider $\mathbf{s}^{(in)}$ to include any variation in the cone angle of the radiance distribution and further radiometric apodization has been considered [28]. It makes sense to define the transmission of the wide pixel as a ratio between focal spectral directional power and input spectral directional power at the pupil, for a uniform radiance and field distribution at the sub-bundle. Note that the real intensity will instead always be affected by the transmission of the optics and non-uniformity of the radiance over the pupil.

With such considerations, hence, we define the idealized wide-pixel transmission of the metasurface under focal illumination as:

$$\overleftrightarrow{\tau}^{\infty}_{(\lambda,\mathbf{r_{ob}})} = \frac{\Theta^{\infty(f)}_{(\lambda,\mathbf{r_{ob}})}}{\Theta^{e}_{(\lambda,\mathbf{r}_{ob})}} = \alpha_{(\theta_{max})} \frac{\int_{\Omega} \mathbf{M}^{\infty}_{0} \sin\theta d\theta d\phi}{\pi \sin^2 \theta_{max}} \tag{5.39}$$

Since for an unknown geometrical view factor $\alpha_{(\theta_{max})}$, the area of the pupil is related to the focal length by:

$$A_{ep} = \frac{\pi f^2 \sin^2 \theta_{max}}{\alpha_{(\theta_{max})}} \qquad [m^2] \tag{5.40}$$

and further that $\mathbf{s}^{in}$ is by definition normalized on s_0. Unless differently stated, we will suppose the view factor to be $\alpha_{(\theta_{max})} \cong \cos^2 \theta_{max}$, representative of a planar principal plane.[5]
Even if the demonstration is rather lengthy, the end result is simple: in the case of a wide-pixel arrangement, the spectral transmission over focused illumination is averaged over the focal cone angle and is a row vector, given by integration of the first Mueller row over all angles. We have performed such derivation to show why an averaging over a cone angle, rather than being an assumption, is actually a physical implication of the Fraunhofer model used and the Parseval Theorem. The spectral directional transmittance $\overleftrightarrow{\tau}^{\infty}_{(\lambda,\mathbf{r}_{ob})}$ hence represents a theoretical maximum transmittance over focused illumination, not including aberrations or finiteness effects. Alternatively, the integral (5.38) may be regarded as an integration over the pupil area, which is the coherence area of the field.
The end result is a transmission which is polarization dependent, as expected. The provided transmission is a directional one, in the sense that it takes into account the contribution of a point-source only. Note that in the real arrangement, such transmission is dependent on the focal point chosen on the detector (e.g. the PSF is a strongly point-dependent function), which is important to know when dealing with image creation. We will further try to depict how in Chapter 5.3.9.
The resolution of the integral in (5.39) is ill defined for $\theta_{max} \to 0$. By using the De L'Hospital rule we conclude that the integral is always defined, in fact it tends to be exactly the plane wave transmittance for small angles:

$$\overleftrightarrow{\tau}^{\infty}_{(\lambda,\mathbf{r}_{ob})|_{\theta_{max}=0}} = \mathbf{M}^{\infty}_{0} \tag{5.41}$$

To avoid singularity, we use the change of variables:

$$\xi' = \sin\theta' = \frac{\sin\theta}{\sin\theta_{max}} \tag{5.42}$$

which upon substitution and rearrangement leads to:

$$\overleftrightarrow{\tau}^{\infty}_{(\lambda,\mathbf{r}_{ob})} = \frac{\alpha_{(\theta_{max})}}{\pi} \int_0^1 \int_0^{2\pi} \tilde{\mathbf{M}}^{\infty}_{0(\xi',\phi)} \xi' d\xi' d\phi \tag{5.43}$$

Where:

$$\tilde{\mathbf{M}}^{\infty}_{0(\xi',\phi)} = \left(\frac{\mathbf{M}^{\infty}_{0(\theta,\phi)}}{\cos\theta} \right)_{|\theta=\arcsin(\xi' \sin\theta_{max})} \tag{5.44}$$

The integration has been resolved by means of the splines interpolator described in Appendix D, which iterates efficiently over grids in angles and wavelengths and the numerical results are discussed in Chapter III, where more suited.

Band Transmission

The above wide pixel focused transmittance presents a distribution in the wavelength. For radiometric purposes, it is useful to determine what's the transmission across a small spectral band in which the signal of interest may be regarded as uniform, assumption hereby required only in order to provide a simple engineering figure for the performance of the device. The real signal will not and is not desired to be uniform (otherwise such resolutions would not be required in the first place) so that its real band transmittance may in reality differ. The performance parameter here depicted however is however a good indication of the power in the band for a power budget estimation.
To define a band transmission, we must integrate $\overleftrightarrow{\tau}^{\infty}_{(\lambda,\mathbf{r}_{ob})}$ across a small spectral region $[\lambda_{min}, \lambda_{max}]$,

[5] the view factor cannot be unitary, as it would not fulfill conservation of energy

which we take here to be the quiet zone of the DBR bandgap (to a certain thresold defined from case to case).
It follows that the directional power at the (full) focal plane $\Theta^{\infty(f)}_{(\mathbf{r}_{ob})}$, not to be confused with the spectral one $\Theta^{\infty(f)}_{(\lambda,\mathbf{r}_{ob})}$, is given by:

$$\Theta^{\infty(f)}_{(\mathbf{r}_{ob})} = L_{\lambda(\mathbf{r}_{ob})} f^2 \pi \sin^2\theta_{max} \left\{ \int_{\lambda_{min}}^{\lambda_{max}} \overleftrightarrow{\tau}^{\infty}_{(\lambda,\mathbf{r}_{ob})} d\lambda \right\} \mathbf{s}_{in} \qquad [W/(sr)] \tag{5.45}$$

Or, in similarity with radiometry and ease of definition:

$$\Theta^{\infty(f)}_{(\mathbf{r}_{ob})} = L_{\lambda(\mathbf{r}_{ob})} f^2 \pi \sin^2\theta_{max} \Delta\lambda \overleftrightarrow{\tau}^{\infty}_{(\mathbf{r}_{ob})} \mathbf{s}_{in} \qquad [W/(sr)] \tag{5.46}$$

where we have defined the spectral band transmittance as:

$$\overleftrightarrow{\tau}^{\infty}_{(\mathbf{r}_{ob})} = \frac{\int_{\lambda_{min}}^{\lambda_{max}} \overleftrightarrow{\tau}^{\infty}_{(\lambda,\mathbf{r}_{ob})} d\lambda}{\Delta\lambda} \tag{5.47}$$

for an arbitrary $\Delta\lambda$ (which can be taken for instance to be close to the FWHM at normal incidence and is used for normalization purposes). The latter does not influence the directional power since by definition it simplifies in (5.46).
The band transmittance is hence regarded here as a radiometric transmittance fully derived from electromagnetic propagation theory and applicable for an arbitrary polarization state of the incoming light. The quantity $f^2\pi\sin^2\theta_{max}$ is in fact, roughly the area of entrance pupil. The transmittance is in general a function depending on the NA of the system and polarization, a row vector of the form:

$$\overleftrightarrow{\tau}^{\infty}_{(\mathbf{r}_{ob})} = \left[M^{\infty}_{0,0}, M^{\infty}_{0,1}, M^{\infty}_{0,2}, M^{\infty}_{0,3} \right] \tag{5.48}$$

Condition Number

In Section 6.7, we have discussed an arrangement allowing to determine three Stokes parameters. For such arrangement, the inclusions of the arrangement are assumed to be rotated of $\delta = \pm 60°$ with respect to the baseline one, to equally sample the π region of interest. This sampling is clearly the optimal one if we assume the angle of polarization of the incoming light to be statistically homogeneous, whereas it may differ as already depicted previously in [1] in case also circular polarization is included. We have verified the optimal condition of this arrangement for various PDL modules (discussed below) in Figure 5.7a).
The determination of the transmittance property of a rotated inclusion is simple, from the knowledge of $\overleftrightarrow{\tau}^{\infty}_{(\mathbf{r}_{ob})}$. It is simple to demonstrate in fact that rotation of the inclusion relates to a rotation around the z axis of δ degrees, which can be achieved by a rotation matrix in the cartesian frame, to be formally placed after the optical transformation and before the metasurface transformation. Since the optical system is regarded as ideal in the metasurface performance parameters above defined, that rotation is equivalent to considering an angle $\gamma - \delta$ rather than γ in the input field (e.g. rotate the $\xi - \eta$ frame of δ with respect to the input wave-vector at the pupil).
Upon such considerations, the rotated band transmittance is given by:

$$\overleftrightarrow{\tau}^{\delta,\infty}_{(\mathbf{r}_{ob})} = \overleftrightarrow{\tau}^{\infty}_{(\mathbf{r}_{ob})} \begin{bmatrix} 1 & 0 & 0 & 0 \\ 0 & \cos(2\delta) & -\sin(2\delta) & 0 \\ 0 & \sin(2\delta) & \cos(2\delta) & 0 \\ 0 & 0 & 0 & 1 \end{bmatrix} \tag{5.49}$$

The reconstruction matrix (at wide pixel focusing) is defined hence by, considering $\delta = 60°$:

$$\mathbb{M} = \begin{bmatrix} M_{0,0} & M_{0,1} & M_{0,2} & M_{0,3} \\ M_{0,0} & -\frac{M_{0,1}}{2} + \frac{\sqrt{3}M_{0,2}}{2} & -\frac{\sqrt{3}M_{0,1}}{2} - \frac{M_{0,2}}{2} & M_{0,3} \\ M_{0,0} & -\frac{M_{0,1}}{2} - \frac{\sqrt{3}M_{0,2}}{2} & \frac{\sqrt{3}M_{0,1}}{2} - \frac{M_{0,2}}{2} & M_{0,3} \end{bmatrix} \tag{5.50}$$

where we dropped the apex ∞ (such definition is applicable also for finite transmittances, defined further in the report). In Section 5.3.9 we show how this matrix can be used to provide reconstruction from the

corrected number of charged particles measured at the detector. The reconstruction process is affected by a certain condition number, κ which would hence be a function of the geometrical shape of the inclusions, the design of the DBR and the NA of the system as well as the point on the detector considered. The condition number of the matrix $(\mathbb{M}^{\infty,[3,3]})^{-1}$ (left square matrix minor), defined as ratio between its maximum and minimum singular values, has been calculated with symbolic tools to be:

$$\kappa = \frac{\max\left(\sqrt{3}, \sqrt{6}\rho/2\right)}{\min\left(\sqrt{3}, \sqrt{6}\rho/2\right)} = \frac{\sqrt{2}}{\rho} \qquad \rho = \frac{\sqrt{M_{0,1}\overline{M}_{0,1} + M_{0,2}\overline{M}_{0,2}}}{M_{0,0}} \tag{5.51}$$

Since it can be shown that $\rho \leq 1$, its theoretical minimum is achieved at $\kappa \cong \sqrt{2} \cong 1.414$. The quantity ρ is also known as *(partial) PDL module vector*, a scalar variable depending on the integrated band transmission here defined. Figure 5.7b) shows the condition number in relation to the PDL module vector. For small PDLs the reconstruction is not possible and this result would conceptually hold for all other arrangements (also with four pixels). The PDLs of various designed inclusions will be revisioned in Chapter 7, where we explicit that a small PDL is associated with an element which is poorly polarizing or an element with two polarized spectral peaks within the integration band, such that $M_{0,1}, M_{0,2} << M_{0,0}$

a) Condition number for various arrangements angles

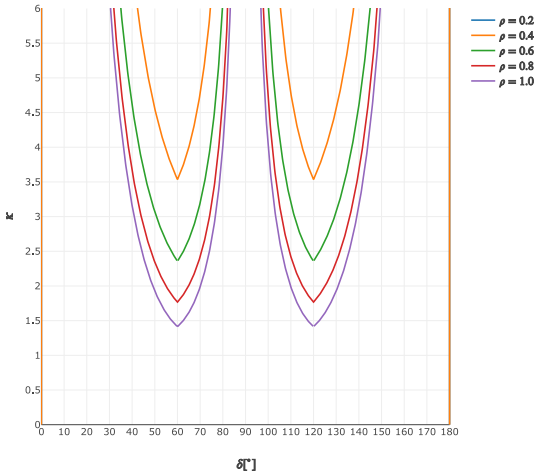

b) Condition number vs. PDL module at optimal angle

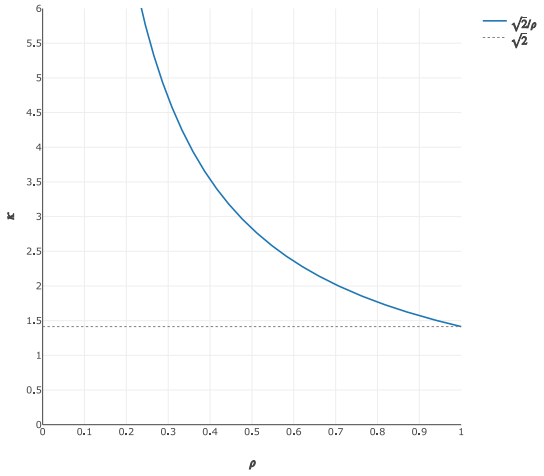

Figure 5.7: Condition number in relation to the partial PDL module vector depicted in formula (5.51), defined for a band transmission

The condition number is a good indication of the SNR amplification and is an important performance parameter. In [4] it is in fact demonstrated that for a noise following normal distribution and equidistributed measured signals, the SNR in reconstructed Stokes parameters is given by:

$$SNR^{St} = \frac{SNR^{(0)}}{\kappa} \tag{5.52}$$

where $SNR^{(0)}$ is the averaged SNR of the measured charges at the detector (for an arbitrary angle of polarization variance, given by the unpolarized field SNR). It is also interesting to discuss the dependence on s_3 of the previous measurement; for the arrangement under consideration measurement of circular polarization has been disregarded as elicited in Chapter 6 due to small values of s_3 and simplifications in the integration of the device. The presence of circular polarized light does not influence the measurement if the device is engineered such that $M_{0,3} \cong 0$ or, trivially, $s_{in,3} \cong 0$. In the first case, however, the total degree of polarization cannot be reconstructed but only linear degree of polarization, further underestimated by a factor $\cos(2\chi)$. Only the latter is requested practically according to science requirements and both the condition above explicated are met by the device under study and its input field.
There are possibilities to further minimize the condition number of the reconstruction process by repeating measurements or using redundant pixels, at the drawback of time or space resolution in the

measurement. A detailed study on data redundancy has been proposed in [50], which showed no significant improvement in the condition number. Improvement may, however, be possible by repeated measurements. We further point that in [1] it is reported a minimum value of the condition number of $k = \sqrt{3}$ as also in other literature resources. Their analysis is based on various assumptions, not verified in our case:

- a) The reconstruction is based on all four measurements, including circular polarization-sensitive arrangement. The reconstruction matrix is hence denser and the reconstruction less efficient.
- b) The reconstruction is based on a matrix with $M_{00} = 1/2$, so that the polarizer is idealized as fully polarization sensitive. In other words, in those studies, the PDL is always taken as $\rho = 1$ and the transmittance of the device idealized.

With respect to the design proposed in [1], hence, choosing not to include circular polarization in the reconstructions enables a better SNR. Moreover, the integration is also simplified, since the reaching strictly $k = \sqrt{3}$ in the design proposed in [1] was impossible within angles tolerancing of all the inclusions, whereas an angle of $\delta = 60°$ is a simple measure for the manufacturing process. As we notice in image 5.7a), deviating from this condition leads to more than a linear increase in the condition number in both error directions (a non-uniform error, however, has not been investigated for succinctness).

Spectral Resolution

When defining spectral resolution, one has to be clear on what is the desired retrieval information. A sound definition of the spectral resolution must intrinsically depend on the expected statistical properties of the field wish to be measured in the spectrum, the reconstruction technique. The spectral resolution can, in fact, be smaller than the FWHM if multiple peaks are used for the sampling and an optimized reconstruction algorithm is used. We will preliminarily consider the spectral resolution to be bounded by the minimum separation between sampled peaks which are still resolved, similar to what done in the definition of spatial resolution in PSF in Fourier Optics.

Spectral Quality

To depict the confidence level at which the radiance is reconstructed, one may consider what is the amount of spectral power falling in a certain region. Supposing that the retrieval of the fields properties close to a wavelength λ_c are of interest, one may define in generality of the transmittance distribution of the DBR filter, a function depicting the enclosed energy close to λ_c with respect to the total transmitted one. Limiting the treatment to fields which have a statistically homogeneous distributions in the angle of polarization, only the $M_{0,0}$ would be of interest:

$$\mathcal{S}_{(\Delta\lambda)} = \frac{\int_{\lambda_c-\Delta\lambda/2}^{\lambda_c+\Delta\lambda/2} M_{0,0} d\lambda}{\int_{\lambda_{min}}^{\lambda_{max}} M_{0,0} d\lambda} \tag{5.53}$$

where $[\lambda_{min}, \lambda_{max}]$ are wavelength intervals of a wider bandpass filter in the DBR. When the active transmissivity spectrum is localized to a finite region in the wavelengths, the confidence function $\mathcal{S}$ evaluated at the $FWHM$ will be close to unity. If the transmission spectrum does, instead, present features also in other regions of the spectrum, the confidence level associated with the $FWHM$ will be lower. We have previously mentioned that the SNR is affected by the reconstruction process more severely when the PDL module is not close to unity (two polarized spectral peaks are present in the integration band). If the filter is supposed to work as a polarizer but $\rho << 1$, also the spectral quality would naturally be affected, since we cannot discern uniquely the distribution in the spectrum which originated the integrated energy. In other words, the reconstruction and the PDL module, do, in general, affect both the noise and the statistical mean of the input signal. Since a more detailed statistical treatment would be too detailed for the purpose of this report, we can preliminary depict the latter effect by means of the introduced value of $\mathcal{S}_{(FWHM)}$ evaluated at FWHM, which acts similarly to a simplified probability density function. We will refer to the latter with the name of *spectral quality* of the filter. Alternatively, one may also operate in terms of FFTs of the transmissivity spectrum in frequencies of wavelengths, depending on the science requirements of interest. If strong variations of the field's spectrum are expected, one may consider switching to other reconstruction methods that do affect less strongly the statistical variance of the reconstructed field, like the one depicted in [4]. Usually, there is a trade-off

between how much the variance and the mean of the input field are affected by the reconstruction process, both in the spectrum, in time and in space; the method in [4] in fact does possess a condition number of $\kappa \cong 8$. The reconstruction method discussed in Section 5.3.9, later on in the report, does implicitly assume that the variations of the input field in the spectrum are minimal in between the two polarization peaks and corrects for the presence of leakings in the other polarizations with such assumption in mind.

5.3.5. DBR General Sizing Criterias

A typical DBR structure is composed of two mirrors stacks, each one composed by two alternating materials of refractive indices n_i and n_j, assumed to be lossy-dielectric and non-magnetic ($\mu_r = 1$) in accordance with the Model in Chapter 4, with a high refractive index contrast. The two stacks are separated by a cavity which couples by reflection in certain narrow spectral regimes, usually of the same material as one of the mirrors but not necessarily. The structure is represented in Figure 5.8. To maximize this coupling the mirrors, as a separate stack, have to possess a high reflection with a *bandgap region*, a quiet zone with a low value of the transmission.
It is well proven than in DBR structures the highest-quality reflective coupling with the cavity is found for quarter-wavelength mirrors:

$$z_i = \lambda_{mir}/(4n_i) \tag{5.54}$$

and reflection and coupling are enhanced by the use of more mirrors (till manufacturing limits). For a fixed length of the mirrors, we refer to λ_{mir} as *design wavelength of the mirrors*. This shall ideally be the same for both mirrors and maintained uniform within tight tolerancing across the layers, to avoid mirrors detuning in the DBR, which has been observed to induce strong undesired spectral shifts and limit the DBR bandgap. In practice upon manufacturing the achievable lengths of the mirrors may be constrained and the material properties are known within a certain accuracy only.
The location of the spectral peak is mainly dependent upon such design on the size and effective properties of the cavity, in terms of its optical effective length only in a first approximation. Its FWHM is strongly dependent on the number of mirrors and dispersion properties of the materials: within a higher number of mirrors the transmission decades more rapidly with a small change of the optical length of the cavity. FWHM it is further influenced by the polarization state of the incoming light, increasing off-angle for the p polarization and decreasing for the s polarization.
The bandgap region extension, in general, depends on material properties and on the type of resonance excited in the cavity (first, second...). A general properties of the spectrum is in fact that to higher optical lengths of both mirrors and cavity, a bigger change in the spectrum is present for the same small perturbation (angle, tolerancing, temperature, change of wavelength or material properties, etc...), hence a bigger bandgap region is associated with the first resonance $m = 1$ of the cavity, which is desirable, but may offer a limited geometrical extent for the introduction of bigger inclusions.
The phase of the transmission is observed to be roughly $\cong \pm\pi/2$ at peak wavelength, with the sign depending on whether the resonance integer m is even or odd and equality holding only when the cavity and mirrors are matched at the same wavelength. A detailed study of aberrations induced from the metasurface due to those spectral dependent phase changes of the transmission spectrum is more suited in Section 5.3.7, within the diffraction formulation.
Those considerations are summarized in Table 5.1.

Note on the order and conventions *There is a certain confusion on the definition of what the cavity is for the below structure (how to define its length in particular). The definition must be consistent with what is considered a stack of mirrors. We consider here the (effective) cavity to be the physical domain delimited by boundaries of change of permittivity (excluding internal scatterers). For example, if an empty cavity is made of SiO_2 and the mirrors of SiO_2 and TiO_2, the cavity is the domain between the TiO_2 mirrors (leading the size of the cavity to be an even multiple of quarter wavelengths). Some other authors exclude, in this example, one of the SiO_2 mirrors from the cavity definition by including it in the DBR stack (leading to an odd multiple of quarter wavelengths). This is merely a convention in the case of an empty cavity of the same materials of the mirrors, but is an important difference in the case in which we wish to change the material of the cavity or include a scatterer. Physically, the required condition for a resonance between mirrors stack is that a phase-shift of multiple of π shall be achieved by propagation in between any reflection, which results in even multiples of π for the optical length of*

the cavity and hence the first definition. A physics-based general definition is hence the first only if one wants to use an effective medium formulation. In Figure 5.8 that results in an additional 'half-pair' in the bottom stack. The structure is moreover not symmetrical upon rotation on the out-of-plane axis of π degrees. As a result, the transmission spectrum of the structure from the bottom will be different than the one from the top and correct order must be used in the definition of the multilayer. The proposed

Description	**Symbol**	**Change Upon**
Bandwidth of the DBR* *as % of peak transmission	B_λ	Number of mirrors m resonance of cavity Materials
Peak Transmission	τ_{max}	Reflection Coupling; Losses Position in the bandwidth ; Apodization at incident angle
Peak Wavelength	λ_{max}	Optical length of cavity (mainly)
FWHM of transmission spectra	$FWHM$	Number of mirrors ; Losses Position in the bandwidth ; Dispersion of materials Reflection coupling ; Polarization (p, s)
Phase of transmission	φ_τ	Spectral position with respect to peak transmission Polar angle and polarization

Table 5.1: Parameters of interest in DBR structures and their variations

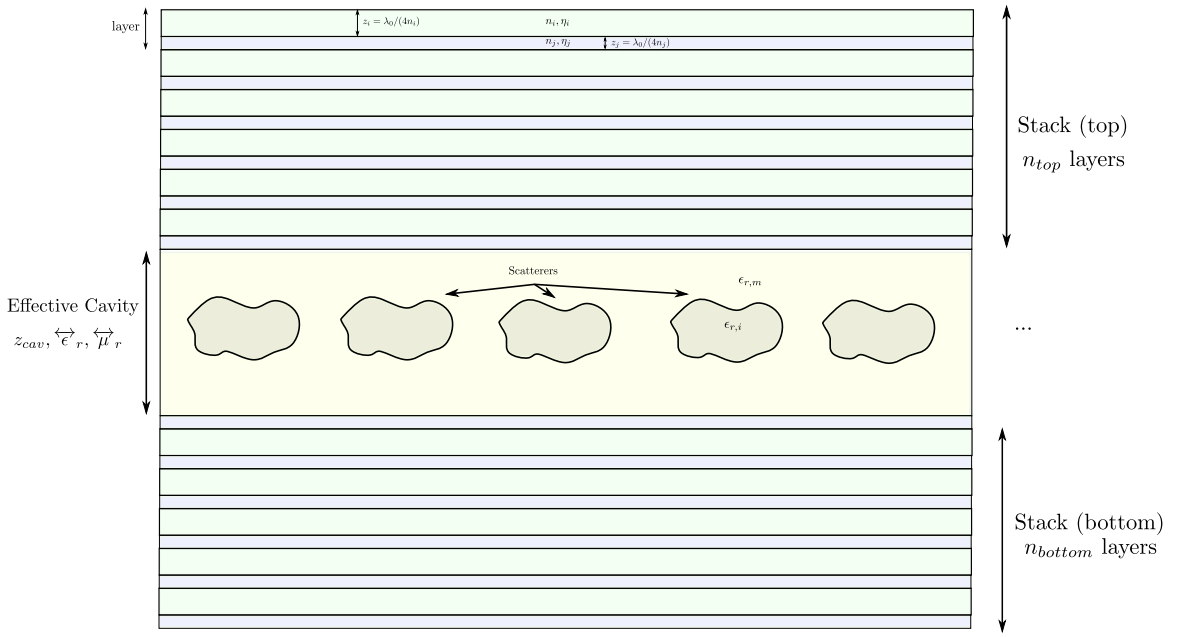

Figure 5.8: Representation of a DBR structure with a cavity that presents some generic inclusions. The mirrors are quarter wavelength (in the given medium) and the cavity follows the conventions in the notes of this Section.

design has the advantage of allowing to change the optical length of the cavity by shaping opportunely the inclusions. It would be useful, for quick design purposes, to determine a simplified relationship to link the desired spectral peak location (λ_{peak}), for a given choice of mirrors and length of the cavity, with the required sizes of the inclusions. In order to do so within our framework, one must first determine the effective permittivity of the cavity and, within a geometrical link as the one discussed in Section 5.3.2, from there determine the geometry of the inclusion. The cavity resonances curves, discussed in the next Section, aid in this process.

5.3.6. Cavity Resonance Curves

It is further interesting to analyze the behavior of the structure at normal angle for varying cavity effective parameters. It can be proven in fact that when an elliptical inclusion is inserted, a normal-angle field directed on one axis of the ellipse behaves as in the isotropic case with the permittivity of that axis (see analysis in Appendix B in support). The transmission spectrum module for various permittivities sizes is represented in Figure 5.9a) and its angle in 5.9b). The latter provides important information regarding the aberrations.

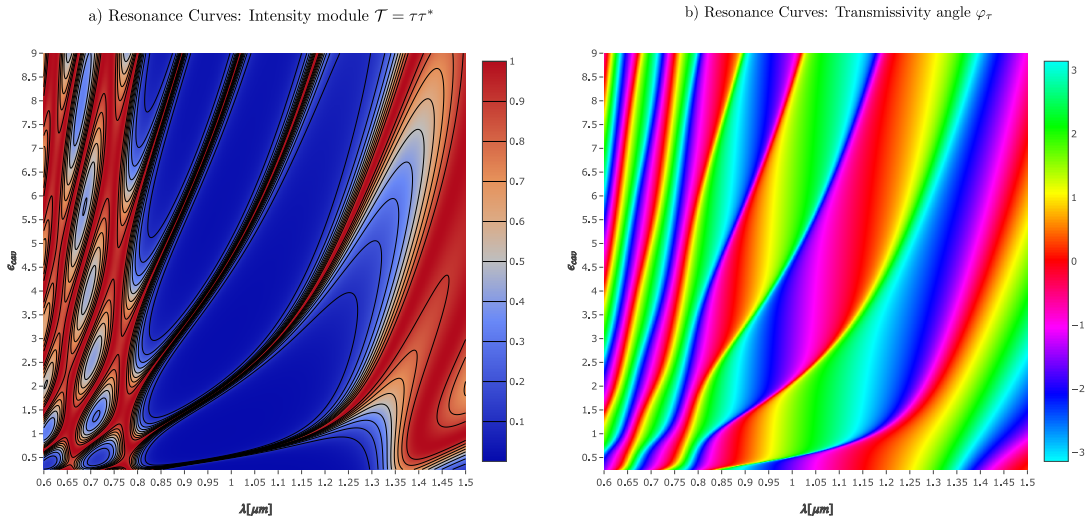

Figure 5.9: a) Plot of the transmissivity spectrum in intensity for various cavity permittivities b) Plot of the amplitude transmissivity angle in the complex domain in the spectrum for various permittivities, in color wheel scale.

The mirrors have been designed at $\lambda_d = 1\mu m$ in this numerical example and the cavity size is at one optical wavelength, with 4 pairs in each DBR for clarity in the plot of SiO_2, TiO_2. Resonance curves for other design wavelengths are qualitatively similar. The Figure clearly represents more possible resonance regimes of the cavity, which are approximately at phases difference of $\pm\pi/2$. For wavelengths close to the design wavelengths of the mirrors, those are approximately given by the condition:

$$\lambda_{peak} \cong 2mz_{cav}\cos\theta_i n_{cav} \qquad \forall m \in \mathbb{N} \tag{5.55}$$

where $\mathbb{N}$ is the set of positive integers and $\cos\theta_i$ is the incidence polar angle in the cavity and $n_{cav} = \sqrt{\epsilon_{cav}}$. In practice design, the previous relationship can be inverted to determine the effective refractive index of the cavity for a desired spectral peak. The effective impedance of the cavity does not strongly influence the location of the spectral peaks, but rather the FWHM and the transmission module. So does also increasing the number of layers. The addition of an imaginary part in the refractive index, representative of a loss in the cavity or the mirrors, does also mainly influence the FWHM and the module of the transmissivity. The above resonance curves can hence be used also in the generality of impedance or losses presence if only spectral information is required. They are strictly valid only at normal incidence: illumination over an angle influences the slope of those resonances. It is clear then that by making the cavity anisotropic, two different spectral peaks can be excited, which explains the design in [1] from our framework point of view. It moreover provides additional information regarding the possible presence of two peaks when higher refractive indices in the cavity are used. As a result, having a high contrast of the refractive indices due to aspect ratio of the particles (by using a grating for instance) does not always lead to more separation in the spectral peaks: if the cavity size is not chosen accordingly (ad example, too long), such design choice may also lead to additional spectral peaks due to higher resonances modes of the cavity in the bandgap of the DBR mirrors. The phase behavior of the transmission is also interesting, since it is roughly $\pi/2$ to $-\pi/2$ at the peaks depending on the m integer chosen. We could envision, an aspect ratio such that x polarized light would be transmitted with a $\pi/2$ phase-shift and y polarized light with a $-\pi/2$ shift. Such design would flip the handedness of the circular-polarized light and is interesting for other studies, but is of no additional use for the present

case-study. The fact that at the peak transmittance the phase-shift induced by the multilayer is of $\pm\pi/2$ is a clear indication of a resonant structure. The plot in Figure 5.10 provides further insight on the fact that, by using a permittivity which possesses a certain spectral dispersion, one may engineer the shape of the peaks (their FWHM, their amplitude), an aspect which we will investigate thoroughly in Part III. Angle dependence can also be visualized straightforwardly (in first approximation) by changing the local slope of the resonances curves according to Equation (5.55). A material having a dispersion law $n_{(\lambda_0)}$ such that its intercept would remain roughly constant at the variation of this slope, would be solid in terms manufacturing tolerances, angle dependence and also thermal expansion, resulting in smaller spectral changes of its transmissivity.

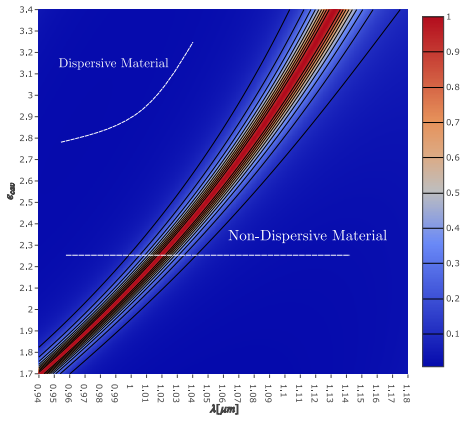

Figure 5.10: Plot of the resonance regimes in a smaller spectral window and illustration of the permittivities intercepts for a dispersive material and a non-dispersive one. The intercepts define the presence of a spectral peak in the transmission spectrum. In the above example, no spectral peak would be intercepted (in this spectral window) by the dispersive material.

The angle behavior is, in reality, more complex and starts diverging from the one reported in Equation (5.55). Nevertheless we found the $(\epsilon_{cav}, \lambda)$ spectrum in Figure 5.9 to be a useful design tool for the characterization of structure, also when inclusions are present. The clear question is obviously determining a characterization of the permittivity $\epsilon_{(\lambda)}$ in relation to the optical properties of the cavity and of its inclusions, as well as the geometry of the inclusions. If such law can be engineered with the degree of freedom of shape of the inclusions, a new design solution which is not limited by the angle dependence and neither by bandwidth separation of the two spectral peaks could be envisioned.

5.3.7. Diffraction for wide resonator arrangement

Diffraction of the DBR arrangement with scatterer inclusions is a complex physical problem to resolve. The inherent strongly space-dependent properties of the filter (varying from pixel to pixel) and the necessity of using vectorial treatment complicates the matter.
Diffraction in the metasurface filter device is introduced because of various reasons (in order of increasing importance and partly interconnected):

- a) Finite extent of the entire filter
- b) Disuniformities at inclusions level between one scatter and another
- c) Imperfections in the manufactured mirrors, inclusions shapes and other geometrical sizes
- d) Possible presence of cavity of different height across the detector
- e) Presence of pixel of strongly different properties at a finite height from the detector (a few wavelengths): this is a near-field effect, but does not obey to the Fresnel diffraction integral since it relates to coupled propagation in dielectric structures
- f) Coupling with the pupil diffraction: the filter acts also as a transparency for the diffracted field of the optical system. Its narrow-angle dependence and introduced phase-shifts modify the effective

spot size and the aberrations of the fields. In case of effect e) can be neglected, this can be treated by means of a Fraunhofer far-field transparency effect.

In the preliminary analysis in Section 5.3.1 we have outlined a possible solution to the effect e), by means of a pixelation function for an arbitrarily sized pixel, which extrapolates finite transmission behavior from the infinite one. Up to now we also neglected aberrations since the Mueller transformation has been performed in the plane-wave representation. If condition (5.23) applies (wide resonator), then the transmittance of the device is in good approximation simple transparency and the driving diffraction effect is given by f). With such consideration in mind, the electric field transformation from the entrance pupil to the focal plane can be written as:

$$\mathbf{e}^{(f)}_{k,f|\Sigma_0} = \left(\frac{ife^{-ikf}}{2\pi k_z}\right)\Sigma_f^{[p,s]}\mathbb{J}^{(m)}\mathbb{J}^{(o)}\left(\Sigma^{[\phi]}\right)^T \overleftrightarrow{\alpha}_{eff}\overline{\mathbf{e}}^{[\xi,\eta]}_{in} = \left(\frac{ife^{ikf}}{2\pi k_z}\right)\mathbb{J}_e\overline{\mathbf{e}}^{[\xi,\eta]}_{in} \tag{5.56}$$

and the magnetic one:

$$\mathbf{h}^{(f)}_{k,f|\Sigma_0} = \left(\frac{ife^{-ikf}}{2\pi k_z}\right)\Sigma_f^{[p,s]}\Sigma^R\mathbb{J}^{(m)}\mathbb{J}^{(o)}\left(\Sigma^{[\phi]}\right)^T \overleftrightarrow{\alpha}_{eff}\overline{\mathbf{e}}^{[\xi,\eta]}_{in} = \left(\frac{ife^{ikf}}{2\pi k_z}\right)\mathbb{J}_h\overline{\mathbf{e}}^{[\xi,\eta]}_{in} \tag{5.57}$$

Note the difference with respect to equations (5.15) where the fields were represented at the top of the metasurface structure. The transformation $\mathbb{J}_e$ and $\mathbb{J}_h$ are the final Jones transformation matrices of the whole system, relating the input fields at the entrance pupil from the $\xi-\eta$ frame to the focal fields at the detector in the cartesian frame. The focal distance f is always referred to the top of the metasurface structure (where the plane-wave decomposition is performed). Such way no correction for the geometrical reference Gaussian sphere with respect to a plane-surface needs to be performed[6]. As a result the defocusing distance z hereby used is the distance of the focusing point with respect to the top layer of the spectral filter. Now that the plane-wave representation of the focal fields is known, one may use the Fraunhofer diffraction integral to resolve the integrated focal fields as a distribution in space. Due to the inherent hypothesis hereby introduced, such distribution will be strictly valid only for $\rho < l_r$. Moreover, as long as the device can be seen as a transparency in the frequency domain (non-diffractive filter), it does not matter whether it is placed in the near field or the far-field. The Fraunhofer diffraction integral to resolve is reported in [28] and reads, for $\mathbf{g} = \mathbf{e}, \mathbf{h}$:

$$\mathbf{g}_{f|\Sigma_0} = \left(\frac{ikfe^{-ikf}}{2\pi}\right)\left\{\int_0^{\theta_{max}}\int_0^{2\pi}\mathbb{J}_{g(\theta,\phi,\lambda)}e^{ik\rho\sin\theta\cos(\phi-\alpha)}e^{ikz\cos\theta}\sin\theta d\theta d\phi\right\}\overline{\mathbf{e}}^{[\xi,\eta]}_{in} \tag{5.58}$$

where for ease of notation we have omitted the pedix 0 referring to vacuum for k, θ. In (5.58), z is the defocusing distance from the top layer of the metasurface layer, α the azimuthal angle at the detector plane with respect to an origin center at the focal spot (x_{fi}, y_{fi}) of the given sub-bundle, ρ the radial distance from this point. With respect to a fixed cartesian frame on the detector:

$$\rho = \sqrt{(x_f - x_{fi})^2 + (y_f - y_{fi})^2} \tag{5.59}$$

Due to required accuracy in the angle and spectral representation and further manipulations, an analytical solution to this integral is preferred, rather than an FFT numerical implementation. The solution can be written in terms of a (complex-valued) Zernike Expansion. Due to integration of the series expansions (see Appendix F) it is first required to correct the Jones matrix for a $\cos\theta$ area differential and for the possible off-focusing of the focal plane (treated therefore as an aberration):

$$\mathbb{J}'_{g(\theta,\phi,kz,\lambda)} = \mathbb{J}_{g(\theta,\phi,\lambda)}\frac{e^{ikz\cos\theta}}{\cos\theta} \tag{5.60}$$

Due to bounding intervals of the analytical integral solution, it is necessary to introduce the trigonometric transformation already discussed in Equation (5.42), where θ_{max} refers to the maximum half-cone angle of focusing. Due to the change of variable the Jones terms are stretched on the new interval $\theta' \in [0, \pi/2]$

[6] we have demonstrated in previous internal reports that such correction is equivalent to a defocusing effect

for all values of θ_{max}. An expansion of the effective Jones matrix is then performed in terms of complex Zernike Coefficients as:

$$\mathbb{J}'_{g(\theta,\phi,kz,\lambda)} = \sum_{q=-\infty}^{\infty} \sum_{s=|q|,step=2}^{\infty} \mathbb{J}^{[q,s]}_{g(\theta_{max},kz,\lambda)} e^{iq\phi} R^{|q|}_{s(\xi')} \tag{5.61}$$

which can be retrieved in two steps by:

$$\mathbb{J}^{[q]}_{g(\theta,kz,\lambda)} = \frac{1}{2\pi}\int_0^{2\pi} \mathbb{J}'_{g(\theta,\phi,kz,\lambda)} e^{iq\phi} d\phi \qquad \mathbb{J}^{[q,s]}_{g(\theta_{max},kz,\lambda)} = 2(s+1)\int_0^1 \mathbb{J}^{[q]}_{g(\xi,z,\lambda)} R^{|q|}_{s(\xi')} \xi' d\xi' \tag{5.62}$$

and where $R^{|q|}_{s(\xi')}$ represents the radial polynomial of a Zernike conventional polynomial as described in the Appendix D.
Equation (5.62) along with many others in this Section, is demonstrated in appendix F. In the above relationships, hence, we resolve the focal fields by means of a Zernike mode decomposition in terms of azimuthal modes q and radial modes s, which has the advantange of being orthogonal on the cone angle which will prove rather useful in the next considerations. The expansion is operated on the Jones matrix of the plane-wave, which pertains the aberration effects. The transformation, even though conceptually straightforward, is rather lengthy to numerically implement, especially when evaluated in populated numerical grids and typical numerical implementation suffer from numerical instability at high orders. Moreover, the transformation implicitly depends on the NA of the system since the non-linear transformation in Equation 5.42 is necessary to remap a finite cone-angle to a semisphere. A spline-based efficient and stable Zernike transform algorithm of arbitrary order at numerical precision has been implemented and is discussed in Appendix D.
By means of the introduced Zernike Mode decomposition, the focal fields can be written, according to the demonstration performed in Appendix F as:

$$\mathbf{g}_{f|\Sigma_0} = kf\sin^2\theta_{max} e^{-ikf} \left\{ \sum_{q=-\infty}^{\infty} \sum_{s=|q|,step=2}^{\infty} \mathbb{J}^{[q,s]}_{g(\theta_{max},kz,\lambda)} f_{[q,s]} \right\} \bar{\mathbf{e}}^{[\xi,\eta]}_{in} \qquad f_{[q,s]} = i^{s+1}\left(\frac{J_{s+1(\tilde{\rho})}}{\tilde{\rho}}\right) e^{iq\alpha} \tag{5.63}$$

where $\tilde{\rho} = k\rho\sin\theta_{max}$ and $J_{s+1(\tilde{\rho})}$ is a Bessel Function of the first kind of order $(s+1)$ evaluated in $\tilde{\rho}$. The bases functions $f_{[q,s]}$ are represented for various modes in contour-plots in Figure 5.12. It is clear from the plots that an higher radial order s is associated with a wider spot.

(Electric Density) PSF and associated directional transmittance

The PSF associated with this field (see Appendix F for definition of relevant quantities) is given by:

$$\langle \mathbf{e}_{f|\Sigma_0} \mathbf{e}^{\dagger}_{f|\Sigma_0} \rangle = k^2 f^2 \sin^4\theta_{max} \left\{ \sum_{s,s'} \mathbb{M}^{[q,q',s,s']}_{(\theta_{max},kz,\lambda)} f_{[q,s]} f^{\dagger}_{[q',s']} \right\} \mathbf{s}_{in} \tag{5.64}$$

A directional focused transmission can again be defined for, this time, a finite integration in the detector in a certain region $\mathcal{A}_p : \{\tilde{\rho} \leq \tilde{\rho}_{max}\}$. Such performance parameters provides information on the encircled energy of one point spread function. Performing the same derivation of Section 5.3.4, again assuming a quasi-planar principal plane, we determined in Appendix F the solution:

$$\overleftrightarrow{\mathcal{T}}^{(f)}_{(\mathbf{r}_{ob},\lambda)} = \alpha_{(\theta_{max})} \sum_{q,q',s,s'} \frac{2}{(s+s'+2)} \mathbb{M}^{[q,s,q',s']}_{(\theta_{max},kz,\lambda)} \mathcal{F}_{[q,s,q',s'](\tilde{\rho}_{max})} \tag{5.65}$$

where the functions $\mathcal{F}_{[q,s,q',s'](\tilde{\rho}_{max})}$ (analytically resolved in the Appendix) are represented in Figure 5.11. Those are nill for $q \neq q'$ due to orthogonality of $e^{i(q-q')\alpha} \in \mathcal{A}_p$ and their analytical expression the same for all q. In particular, the contribution for $s = s' = 0$ is equivalent to the conventional Airy Disk encircled energy. The contribution in 5.11a) for $s = s' > 0$ represent higher order modes associated with a wider spots, and all tend asymptotically to 1 for the limit of $\tilde{\rho}_{max} \to \infty$. Not-centered contribution $s \neq s'$ represented in 5.11b) are also, in general, present and not necessarily positive. Due to orthogonality of the Bessel Functions they tend to 0 for the limit of wide pixel. The positiveness

of $\overleftrightarrow{\mathcal{T}}_{(\mathbf{r}_{ob},\lambda)}$ is always verified once the summatory is completed. In particular, a connection with the previous wide transmittance defined in (5.39) is found, due to those limit operations, as:

$$\overleftrightarrow{\mathcal{T}}^{\infty}_{(\mathbf{r}_{ob},\lambda)} = \alpha_{(\theta_{max})} \sum_{q=-\infty}^{\infty} \sum_{s=|q|,step=2}^{\infty} \left(\frac{1}{s+1}\right) \mathbb{M}^{[q,s]}_{(\theta_{max},kz,\lambda)} \tag{5.66}$$

which is useful for validating numerical errors in the mode expansions. Strictly speaking, the encircled energy of the pixel in a square region would fall in between $\rho_{max} = 1/2[l_p, \sqrt{2}l_p]$. Its exact value can only be estimated numerically solving the integral (F.10) reported in the Appendix. Moreover, the real energy integrated in the pixel is in reality dependent on a convolution integral yet to be performed, which would result in a smaller value of enclosed energy, but is more complex to treat.

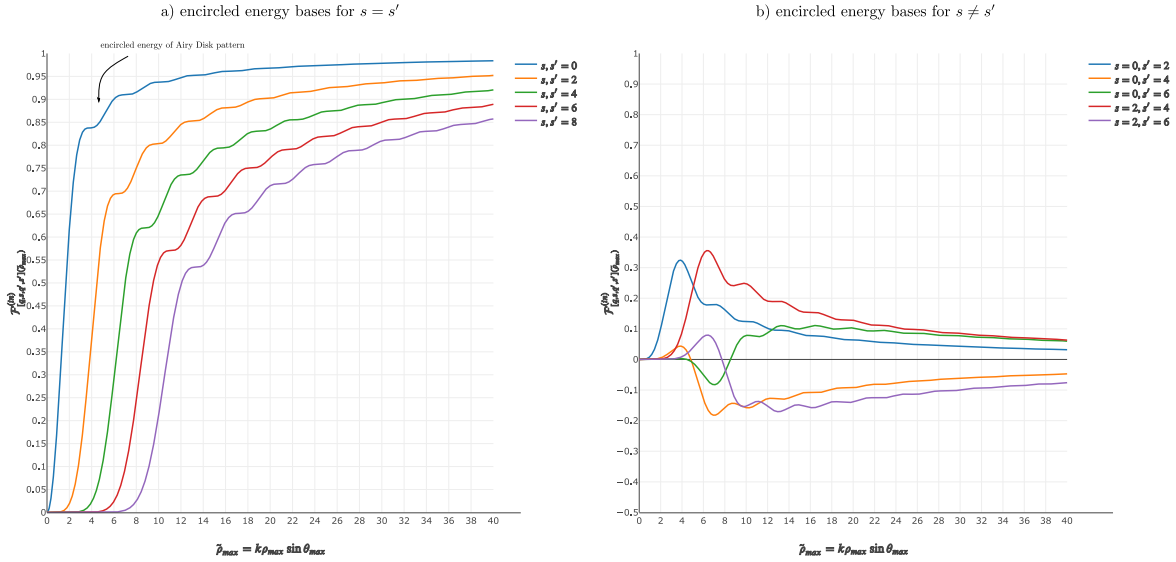

Figure 5.11: Encircled energy basis function $\mathcal{F}^{(in)}_{[q,s,q',s']}(\tilde{\rho}_{max})$ a) for the case in which $s = s'$, all plots asymptotic to 1 b) for the case in which $s \neq s'$, all plots asymptotic to 0. The encircled energy of the Airy Disk pattern corresponds to the $s = s' = 0$ mode and is the steeper one. Values for the off-center correlation can be negative, but the sum contribution of all modes is always real and positive.

Incident Poynting Vector

The expression of the focused Poynting Vector can be found in complete similarity with the PSF. The electric field expansion is described by $\mathbb{J}^{[q,s]}_{e(\theta_{max},kz,\lambda)}$ and the magnetic one by $\mathbb{J}^{[q',s']}_{h(\theta_{max},kz,\lambda)}$. For simplicity, we refer to the normalized non-dimensional Poynting Vector defined by:

$$\mathbf{p} = \langle \mathbf{e}_{f|\Sigma_0} \times \mathbf{h}^*_{f|\Sigma_0} \rangle = \begin{pmatrix} \mathbf{e}_{f|\Sigma_0,y}\mathbf{h}^*_{f|\Sigma_0,z} - \mathbf{e}_{f|\Sigma_0,z}\mathbf{h}^*_{f|\Sigma_0,y} \\ \mathbf{e}_{f|\Sigma_0,z}\mathbf{h}^*_{f|\Sigma_0,x} - \mathbf{e}_{f|\Sigma_0,x}\mathbf{h}^*_{f|\Sigma_0,z} \\ \mathbf{e}_{f|\Sigma_0,x}\mathbf{h}^*_{f|\Sigma_0,y} - \mathbf{e}_{f|\Sigma_0,y}\mathbf{h}^*_{f|\Sigma_0,x} \end{pmatrix} \tag{5.67}$$

for dimensional scaling factor to link the present quantity to radiance and directional intensity please refer to Appendix C. By opportunily transforming the magnetic vectors according to the above cross-product (an example is provided in the Appendix) we can use the same expression (5.64) to determine:

$$\mathbf{p} = k^2 f^2 \sin^4\theta_{max} \left\{ \sum_{q,q',s,s'} \mathbb{M}^{[q,q',s,s']}_{p(\theta_{max},kz,\lambda)} f_{[q,s]} f^{\dagger}_{[q',s']} \right\} \mathbf{s}_{in} \tag{5.68}$$

When considering the incident Poynting Vector p_z a fully similar expression to (5.65) can be defined to the transmittance. In general, the two quantities slightly differ and the Poynting Vector may be partly complex valued. The (small) imaginary components of the focused Poynting Vector are representative

of energy which is stored in the multi-layered structure (or, in other words, of slight dephasing between magnetic and electric fields). More in detail, the dephasing is due to depolarization effects between p and s polarizations, which affects differently electric and magnetic fields. This stored energy is not dissipated but fully transmitted once a real time-finite pulse field is considered. For small NAs the distinction between the two transmittances is negligible.

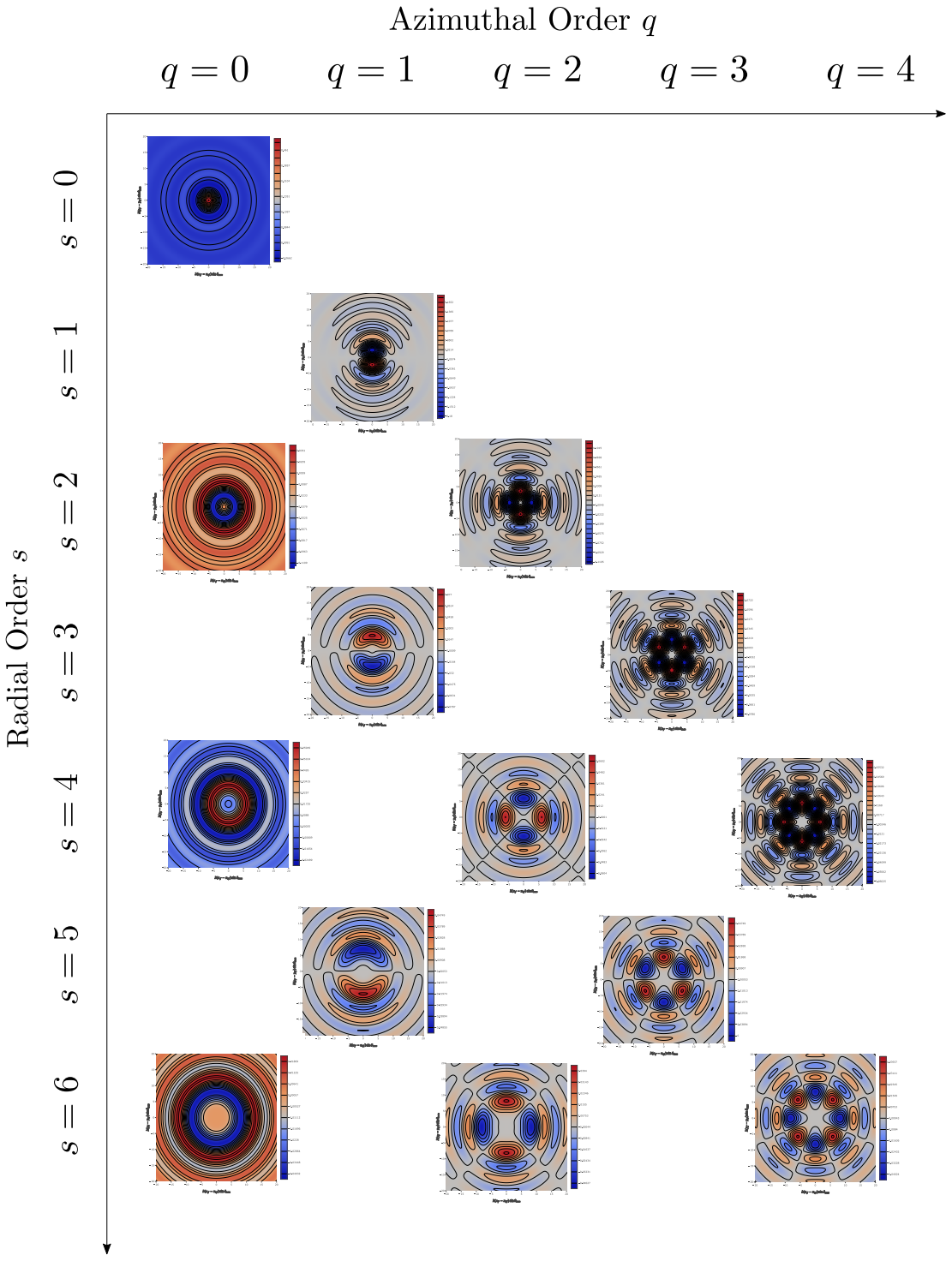

Figure 5.12: Plot of the (imaginary part) of the Zernike modes ($\Im\{f_{[q,s]}\}$) up to $q_{max} = 4, s_{max} = 6$ in the detector plane, in non-dimensional variables $x = k(x_f - x_{if})\sin\theta_{max}, y = k(y_f - y_{if})\sin\theta_{max}$. Zoom in for improved visibility.

The OTF

The OTF of the arrangement is defined by the Fourier Transform of the PSF in Equation (5.64), opportunely normalized. In Fourier Optics, the OTF provides valuable information on the reconstruction of the input signal in terms of spatial frequencies and brightness. Having decoupled the spatial distribution of the PSF by means of the function $f_{[q,s]}f^*_{[q',s']}$ only, in Appendix F this expression for the OTF is derived:

$$\overline{OTF}_{(\xi_k,\phi_k)} = \alpha_{(\theta_{max})} \frac{\left\{\sum_{q,q',s,s'} \mathbb{M}^{[q,q',s,s']}_{(\theta_{max},kz,\lambda)} f^{[q,q',s,s']}_{(\phi_k)} \mathcal{I}^{[q,q',s,s']}_{(\xi_k)}\right\} \mathbf{s}_{in}}{\overleftrightarrow{\mathcal{T}}^{\infty}_{(\mathbf{r}_{ob},\lambda)} \mathbf{s}_{in}} \tag{5.69}$$

where:

$$f^{[q,q',s,s']}_{(\phi_k)} = \frac{2i^{q-q'+s-s'}e^{i(q-q')\phi_k}}{(s+s'+2)} \qquad \xi_k = \frac{\sqrt{k_x^2+k_y^2}}{k\sin\theta_{max}} \tag{5.70}$$

The analytical expression of the functions $\mathcal{I}^{[q,q',s,s']}_{(\xi_k)}$ is depicted in the Appendix F and those are plotted in Figure 5.13. They are always real and representative of the OTF associated with each mode. Note that the OTF possess also azimuthal dependance, oscillating in $(q-q')\phi_k$ (not represented). In 5.13a) the centered cross-correlation terms $\mathcal{I}^{[q,q',s,s']}_{(\xi_k)}$ for $q=q'$, $s=s'$ are plotted. As the spot widens for higher orders of s, also the spectral reconstruction is affected. In 5.13b) some mixed terms are represented, which are always nill at the origin. All plots converge to $\mathcal{I}^{[q,q',s,s']}_{(\xi_k)} = 0$ at $\xi_k = 2$. As discussed in the Appendix, the given formulation is consistent with the Airy Disk solution found for the mode $q=q'=s=s'=0$.

Note on normalization *The OTF is normalized as conventionally such that* $[\xi_k = 0, |OTF| = 1]$. *Such normalization procedure is conventionally used in Fourier Optics. However, we observe that the value of the un-normalized OTF in the origin is equivalent to the wide pixel transmittance (corrected for an eventual apodization) and hence not unitary. Normalizing the OTF provides information regarding the aberrations and spatial frequency that can be reconstructed, but the un-normalized expression depicted in the Appendix F shall rather be used when the transmission module information is important. Moreover, the OTF is itself a function of polarization input (the un-normalized one, linear in the Stokes parameters), wavelength and NA.*

a) OTF bases functions for centered modes

b) OTF bases function for not-centered modes

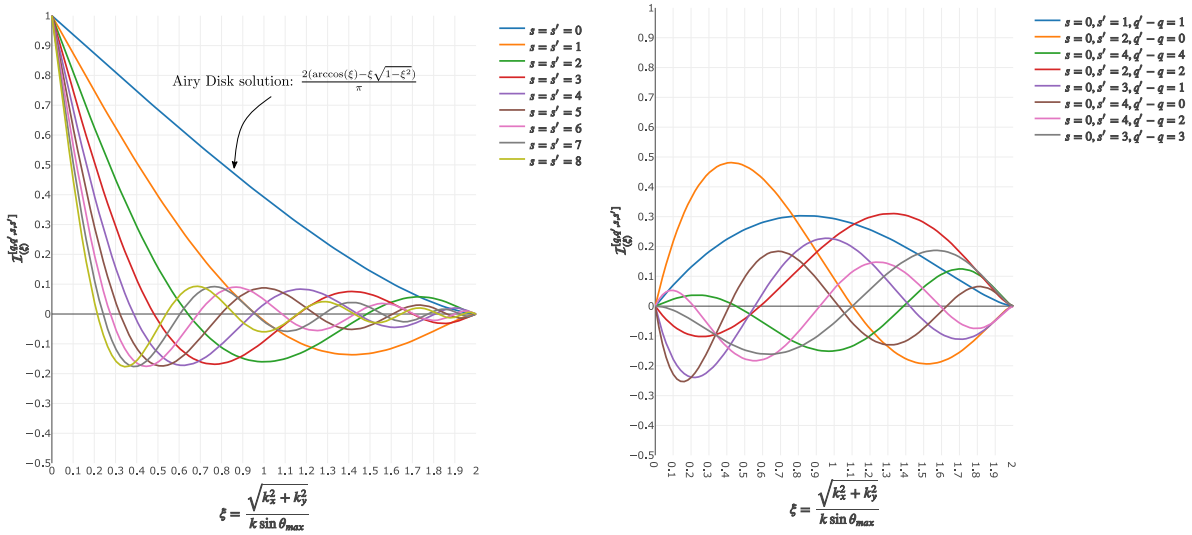

Figure 5.13: a) OTF radial bases $\mathcal{I}^{[q,q',s,s']}_{(\xi_k)}$ for the centered indeces $q=q'$ and $s=s'$. b) OTF bases $\mathcal{I}^{[q,q',s,s']}_{(\xi_k)}$ for some not-centered modes

5.3.8. Modelling of detectors: generalized charge to radiance conversion

The signal is measured by conversion of the photons of the electromagnetic radiation in forms of digitalized bits. In CMOS and CCD sensors, the charge is stored in quantum-wells at pixels level and subsequently converted by the electronic circuits in an analogic voltage and then in a digital signal. For the purpose of this Section, we characterize the sensor by its *quantum efficiency* η_e and *spectral responsivity* R_λ. The quantum efficiency, a spectral quantity, is a measure of the incident electrons created by the incident photons at a pixel level:

$$\eta_e = \frac{n_e}{n_\gamma} \tag{5.71}$$

It is a measure of the absorption at the detector level. Unless the electromagnetic radiation is such to excite cascades of electrons, usually one electrons is excited for each absorbed photons. In reality, non-ideal effects and reflection are present furthe present. The amount of absorbed electrons, per unit area, wavelength, solid-angle and time, contained in electromagnetic polychromatic radiation can be calculated from the definition of spectral radiance and energy of the photon e_γ[7]:

$$\frac{d^{(4)}n_e}{dA_p d\Omega_p d\lambda dt} = \frac{d^{(4)}(\eta_e n_\gamma)}{dA_p d\Omega_p d\lambda dt} = \frac{\eta_e L_\lambda}{e_\gamma} \qquad \left[\frac{electrons}{m^2 \times \mu m \times sr \times s}\right] \tag{5.72}$$

The energy of the photon (in vacuum) is further given by the well-known Planck's Formula (vacuum pedix used):

$$e_\gamma = h\nu = \frac{hc_0}{\lambda_0} \tag{5.73}$$

which is inversely proportional to the wavelength, with h the Planck Constant. Alternatively, one can use the the spectral responsivity R_λ, measured in $[A/W]$. By definition, the current associated with the storage of energy process is given, for an electric charge q_e by:

$$i_s = \dot{q} = q_e \frac{d(n_e)}{dt} = \eta_e q_e \frac{d(n_\gamma)}{dt} \tag{5.74}$$

Differentiating in the etendue and the spectrum:

$$\frac{d^{(3)}i_s}{dA_p d\Omega_p d\lambda} = \frac{\eta_e q_e L_\lambda}{e_\gamma} = R_\lambda L_\lambda \qquad \left[\frac{Ampere}{m^2 \times \mu m \times sr}\right] \tag{5.75}$$

The choice of which parameter to use depends on the available sensor information and its architecture. Useful for noise and signal estimations is the estimation of n_e.

5.3.9. Image Creation by Signal Reconstruction

With the introduced framework, we are ready to discuss the image creation upon polarized focusing of the device. Imaging is possible in sake of the fact that across a limited region of space on the detector radiance from a neighbourhood in the object space are imaged, with some imperfections. Consider the output of a detector in terms of a signal. The purpose of the whole modelling is determining the relationship between the real signal and the one measured in order to depict the best reconstruction matrix.

The signal at the detector read-out, is representative of a certain number of absorbed electrons for a pixel k on the detector. This number can be corrected in post-processing to account for the electronics read-out process and other effects. We refer to the correct number of electrons, representative of the absorbed ones, as $n_{e,k}^{(abs)}$. For a polarizer arrangement $\mathcal{K}_i$, the signals vector can be arranged in a vector, $\mathbf{n}_{e,\mathcal{K}_i}^{abs}$. Considered the above analysis, we wish to reconstruct the average value of $\overline{L}_{(\Delta\lambda_i,\mathcal{K}_i)}$ in a spectral band i and its averaged non-dimensional Stokes parameters $\mathbf{s}_{(\Delta\lambda_i,\mathcal{K})}$, in a relationship of the type:

$$\begin{cases} \overline{L}_{(\Delta\lambda_i,\mathcal{K}_i)} = \left(\mathcal{C}\mathbb{M}_{\mathcal{K}_i}\mathbf{n}_{e,\mathcal{K}_i}^{abs}\right)_{[0,0]} \\ \mathbf{s}_{(\Delta\lambda_i,\mathcal{K}_i)} = \dfrac{\mathcal{C}\mathbb{M}_{\mathcal{K}_i}\mathbf{n}_{e,\mathcal{K}_i}^{abs}}{\overline{L}_{(\Delta\lambda_i,\mathcal{K}_i)}} \end{cases} \tag{5.76}$$

[7] analytical differentiation is used for ease of notation, but in reality all quantities are defined for a very small spectral window $\Delta\lambda$

with the constant:

$$\mathcal{C} = \left(\frac{e_\gamma}{\overline{\eta_e} A_p \Omega_p \Delta t_j \Delta \lambda_i} \right) \qquad \left[\frac{W}{m^2 \times \mu m \times sr \times electrons} \right] \tag{5.77}$$

where $\overline{\eta_e}$ is a representative quantum efficiency of the arrangement in the band. The constant is chosen in such a way to have a non-dimensional reconstruction matrix. This is merely one of the possible reconstruction methods; more complex methods may be envisioned by using integral equations, more signal measurements, time-integration delay, Fourier sampling methods etc...
Question arises hence, for this proposed reconstruction method, to determine the best $\mathbb{M}_{\mathcal{K}_i}$ that minimizes the variance error between the real radiance and Stokes vector quantities in the band, time interval of measurement Δt_j and space region of interest with respect to the averaged reconstructed ones:

$$\min_{\{\Delta\lambda_i, \mathcal{A}_{sc}, \Delta t_j\}} \{ \langle \mathbf{s}_{(\Delta\lambda_i, \mathcal{K})} - \mathbf{s}_{in(\hat{\mathbf{s}}_i, \tilde{q}_x, \tilde{q}_y, t)} \rangle, \langle \overline{L}_{(\Delta\lambda_i, \mathcal{K})} - L_{\lambda(\hat{\mathbf{s}}_i, \tilde{q}_x, \tilde{q}_y, t)} \rangle \} \tag{5.78}$$

The resolution of this problem is difficult if one has to include noise and statistical considerations.
To determine a solution close to the global statistical minimum, we analyze the real signal creation process within the model developed up to now. Up to now, we have described the transformation:

$$\langle \mathbf{e}\mathbf{e}^\dagger \rangle_{[\tilde{q}_x, \tilde{q}_y]} \rightarrow \langle \mathbf{e}_{f|\Sigma_0} \mathbf{e}^\dagger_{f|\Sigma_0} \rangle_{[x_f, x_{fi}, y_f, y_{fi}]} \tag{5.79}$$

where $\tilde{q}_x, \tilde{q}_y$ are non-dimensional object-space coordinates and $\tilde{x}_{fi}, \tilde{y}_{fi}$ non dimensional focal spot locations on the detector (and further $\tilde{x}_f = k x_f \sin\theta_{max}, \tilde{y}_f = k y_f \sin\theta_{max}$), correlated to each other by the mapping law of the Optical System discussed in Chapter 6, time-mapping and a local magnification factor. For example, for the nadir pixel, those relations would read (see Chapter 6 in support) considering x as the along-track direction and the nadir ground-track velocity $v_{gt,0}$:

$$\begin{cases} \tilde{q}_x^{(nadir)} = \dfrac{x_{fi}}{f} + \dfrac{v_{gt,0}}{h_s}(t - t_0) \\ \tilde{q}_y^{(nadir)} = \dfrac{y_{fi}}{f} \end{cases} \tag{5.80}$$

The spectral intensity at the focal plane is given by:

$$I_{\lambda(x_f, y_f, \lambda, t)} = \int_{\mathcal{A}_d} \cos^2\theta_g \cos\theta_n \overline{L}_{\lambda(\tilde{q}_x, \tilde{q}_y, t)} \langle \mathbf{e}_{f|\Sigma_0} \mathbf{e}^\dagger_{f|\Sigma_0} \rangle d\tilde{q}_x d\tilde{q}_y \qquad \left[\frac{W}{m^2 \cdot \mu m} \right] \tag{5.81}$$

The above is a generalization of known convolution integral of the PSF. The main difficulty arises from the fact that the PSF is hereby a point-dependent function of the focal variables (x_{fi}, y_{fi}), so that the above is not merely a convolution integral. With the above introduced modes solution, however, each PSF mode is only a function of the variables $(x_f - x_{fi}, y_f - y_{fi})$, whereas are the expansion coefficients $\mathbb{M}^{[q,q',s,s']}_{(\theta_{max}, kz, \lambda)}$ do possess an (unknown) dependence with the focal point position. In Appendix F we demonstrate the useful result that, in generality of the filter response and the radiance distributions:

$$n^{(abs)}_{e,k} = \int_{\Delta\lambda_i} \int_{\mathcal{A}_d} \sum_{q,q',s,s'} \left(\frac{\eta_e \Omega_p \Delta t_j}{e_\gamma} \right) \frac{2}{s + s' + 2} \mathbb{M}^{[q,q',s,s']}_{(\theta_{max}, kz, \lambda)} \mathbf{S}_{av} \mathcal{G}_{(kl_p \sin\theta_{max}, x_{fi}, y_{fi})} dx_{fi} dy_{fi} d\lambda \tag{5.82}$$

where:

$$\mathbf{S}_{av} = \mathbf{S}_{av(\mathbf{r}_{ob}, t_0)} = \frac{1}{\Delta t_j} \int_{t_0}^{t_0 + \Delta t_j} \cos^2\theta_g \cos\theta_n \overline{L}_{\lambda(\tilde{q}_x, \tilde{q}_y, t)} \overline{\mathbf{s}}_{in} dt \tag{5.83}$$

$\mathcal{G}_{(kl_p \sin\theta_{max}, \tilde{x}_{fi}, \tilde{y}_{fi})}$ is a special geometrical correlation function of the pixel with each OTF mode, and the superscript $\overline{L}, \overline{\mathbf{s}}$ stands for averaging over the coherent sub-bundle as in Equation (5.12). Such equations are the formal solutions of the imaging problem with an arbitrary illumination distribution and can also be used to solve the optimization problem above introduced. Unfortunately, the dependence of $\mathbb{M}^{[q,q',s,s']}_{(\theta_{max}, kz, \lambda)}$ in (x_{fi}, y_{fi}) is unknown at the moment. To momentarily solve the optimization problem, we hence prefer using the enclosed energy basis function $\mathcal{F}_{[q,s,q',s'](\tilde{\rho}_{max})}$ rather than the complicated functions $\mathcal{G}_{(kl_p \sin\theta_{max}, x_{fi}, y_{fi})}$. We will hence consider, in similarity to the format of those equations, that $\mathbb{M}_{\mathcal{K}_i}$ is the inverse of the reconstruction matrix (as in Equation (5.50)) associated with the finite (directional) band transmittance for the central focusing point:

$$\overleftrightarrow{\tau}^{(f)}_{(\mathbf{r}_{ob})} = \frac{1}{\Delta\lambda_i} \int_{\Delta\lambda_i} \overleftrightarrow{\tau}^{(f)}_{(\mathbf{r}_{ob}, \lambda)} d\lambda \tag{5.84}$$

Effect of Time Smearing on reconstruction for a given arrangement The time smearing has no effect when considering a (statistically, temporally and spatially) homogeneous Stokes vector, comprehensive of radiance, in the object domain, but has important implications for signals with a spatial distribution. When using an arrangement to reconstruct the polarized image from the values of $\mathbf{n}_{e,\mathcal{K}_i}^{abs}$, it shall be preferred to buffer the charge values read-out by the sensor and define the signal vector depending on the time of permanence of the space region of interest. Even when doing so, the signal may still present time-dependence (due to intrinsic time-dependence of the fields and, more importantly, the stability of the measuring platforms). When considering the reconstruction matrix, this time-dependence modifies also the spatial response of the sensor and the whole reconstruction process (so its condition number). The reader may verify this statement by considering spectral properties of the products $\mathbb{M}_0\mathbf{S}_{av(\mathbf{r}_{ob},t_0)}, \mathbb{M}_0^{[\delta=\pi/3]}\mathbf{S}_{av(\mathbf{r}_{ob},t_0+\Delta t_j)}, \mathbb{M}_0^{[\delta=2\pi/3]}\mathbf{S}_{av(\mathbf{r}_{ob},t_0+2\Delta t_j)}$. Randomness is hence introduced in the definition of the reconstruction matrix itself by imperfections, which may be alternatively thought to directly influence the OTF of the reconstruction. This may lead to stricter requirements for mechanical stability, attitude of the spacecraft and SNR, specifically when considering the read-out and buffering time required by the electronics for a given sensor, which is generally not negligible and bigger than the integration time. This problem does not apply for static imaging (e.g. use of a stable camera on groud) or fast imaging.

5.3.10. Further recommended analysis

Within this involved Chapter, we analyzed various modeling techniques by first describing the field transformation and then the metasurface modeling more in detail. Various performance parameters have been defined (plane wave spectral transmittance, point-source transmittance, extended-source transmittance) and the Zernike Modes expansions solution of the diffraction of the wide pixel been presented, comprehensive of OTF and encircled energy treatment. There is still some uncertainty on the modeling of the structure, mainly related to its finite response as a function of x_{fi}, y_{fi}, discussed in Section 5.3.1. Grasping a better understanding of this dependence allows to better understand the imaging process, but is a complex problem both theoretically and experimentally. PSF experimental determination may aid and validate the process, to be performed experimentally with a well-designed setup once the structures are manufactured on the desired pixellated arrangement. The determination of such dependence would also allow to have an estimation of the cross-coupling due to diffraction and spectral response of the filter itself and to include those in a newly defined (not-directional) finite transmittance, derived from Equation (5.82) and resolving our optimization problem.
Possibly, the (diffractive) spectral filter may modify the coherent structure of the field themselves depending on its initial aberrations, which has also not been investigated yet and may be an important factor. The effective medium formulation shall also be revisioned to provide a more accurate geometrical prediction of the inclusions sizes and dependence of the effective parameters with wavelength and angles. Finally, the effects of imperfections like mirrors wobbling and finesse have been demonstrated to affect diffraction behavior of those structures and have been previously modeled in Literature. Statistical studies on the reconstruction process for a known statistical field shall also be performed for more sensitive estimations of achieved performance, coming hand in hand with the choice of the downselected reconstruction and post-processing method.
We have however developed tools to describe various important phenomena: the spectral adrift between polarizations is well described by the anisotropy in the effective medium model, as we will show in Chapter 7. The resonance curves of the DBR allows an efficient sizing and performance review of the multilayer design and achievable bandwidths. The defined band transmittance allows to include effects of polarization leakings in the reconstruction matrix, so in its condition number, revision in Section 5.3.4. The effect of focusing can be formally included in terms of aberrations induced by the filter and angle-adrift of the peaks, with the finite transmission defined in Equation (5.65). The latter does provide a first estimation of the diffraction cross-couplings between pixels due to aberrations of a wide resonator structure. The OTF - PSF structure can also be now be modeled through use of the Zernike expansion for an arbitrary illumination and wavelength.

III

Results

6

Optical Parameters

In the present Chapter, we consider the problem of defining the optical specifications of the system relevant to the design of the metasurface and the evaluation of its performance. This procedure is necessary to quantify the validation of the requirements as well as identify any criticality in the requirements. Since we are interested in a feasibility study of the concept for a variegate ranges of applications, we keep the science requirements somewhat fluid in this assessment phase. Nevertheless, we down-select some general mission requirements regarding the orbit and specifications for similar aerosol-detection observation missions. The optical system is treated as a black-box model (in terms of optical parameters such as focal length, field of view, angular resolution...terminology being introduced in Section 6.1), due to impossibility of designing a complex optical system in the given framework. A few modeling guidelines are drawn, the hypothesis of collimation is discussed and the non-linear viewing geometry equations derived in Section 6.2. The optical transformation is then discussed in Section 6.3, determining the paraxial coefficients of its transfer matrix by imposing the telecentricity requirement and using conservation of etendue considerations. The radial distortion is quantified in order to meet the GSD requirements through the introduction of the local metric of the transformation, discussed in 6.4. The various geometrical parameters are analyzed as functions of the height of the orbit, keeping a focus on LEO orbits. The latter choice is justified in view of this analysis and requirements of remote-sensing for aerosol applications in 6.5, where the orbital parameters of a preliminary orbit are described and a Sun-Synchronous orbit is downselected for this preliminary case-study. The velocity of observation and permanence time of a generic object point in a pixel are also discussed in Section 6.6 in terms of the introduced metric. Finally in the conclusive Section 6.8 the preliminary sizing of the Optical System variables is performed in terms of the equations introduced.
This simple quantitative assessment outlines the need for more modeling detail of the DBR device for the power budget calculation, which will be dealt with in the next Chapter.

6.1. Common Terminology

Before continuing in the treatment, a common set of terminology shall be drawn. Note that this may be different from what used in other Literature but will be retained consistently in the present document. We define as *ground sampling element area*, A_{gse} the smaller physical discernible area in the object plane associated with the *pixel element area* A_p in the detector plane array, which possess an edge of dimension l_p. To every pixel element, a set of multiple resonators of the same shape is associated, dimensions and design (for a given wavelength and polarization state). We define as *ground sub-resolution element area* A_{gsre} the smaller physical discernible area in the object plane reconstructed for only one given value of wavelength and polarization. Various imager arrangements are possible, in which pixels may merge together in a superpixel to image bigger area than the ground resolution element. The *spatial resolution area*, A_{gre} is hereby defined, overall positions of the object plane, as the smaller physical area discernible with full information over wavelength and polarization state. Depending on the imager arrangement, hence, the latter can be bigger or equal to the ground resolution element. The ground sampling element instead, can be bigger or smaller depending on sampling requirements. We define as *ground velocity*, v_{gt} the velocity in m/s at which the ground resolution element is scanned. We define as *scanning window*, $\mathcal{V}_{sc}$ the volume region (quasi-solid angle) which in every instant connects the scanned area to the entrance pupil of the optical system. The ground velocity is hence the relative velocity of the scanning area with respect to the ground resolution element as viewed from the satellite and the former is jointed with the orbital rotational velocity of the satellite. We define as A_{sc} the scanning area, related to the

swath of the optical system S_w, which we consider to be an arc on the Earth sphere at distance r_{ob} from its center of mass. Some of those quantities and other geometrical parameters are summarized in Figure 6.1 We define as *aperture stop* the physical aperture, perpendicular to the optical axis, which limits the extension of the bundles of light in the optical system. We consider an optical geometrical model is applicable everywhere in the optical system with exception of the pupils (or equivalently the aperture) where diffraction may take place, and consider a *light ray* to be locally perpendicular to the wavefront of a transverse electromagnetic wave of a coherent field associated with the real statistically partially coherent field. We define as *chief rays* the rays intersecting the optical axis on the aperture stop. We define as *entrance pupil* and *exit pupil*, as conventionally, the two virtual apertures, if any, delimited by the other intersections of the chief rays with the optical axis, the distinction being clear by imagining the entrance pupil as image of the aperture stop from the part of optical system preceding the physical aperture. The aperture stop size boundary further delimits the *marginal rays* of the optical device for a given observation scene. We define as *bundles of rays* the set of rays associated with a ground sampling element on ground and *sub-bundles of rays* the (coherent) set of rays associated with a point on the ground. Every sub-bundle of rays has a unique chief-ray, used as a datum line for the angular deviation $\Delta\theta_{in}$ of the other rays in the sub-bundle. Some quantities are further defined with respect to the response of the optical system to a collimated sub-bundle of rays, incoming from the front or the rear of the system. The *rear principal surface* is defined as the unique surface over which a collimated sub-bundle of rays (entering from the rear) would appear to bend with its real exiting focal angles θ. The *rear principal plane* is the plane locally tangent to the surface along with the optical axis intersection point, denoted as *rear principal point*. The distance measured along the optical axis between the rear principal point and the paraxial rays of the sub-bundle is the *rear effective focal length*. The distance between the local tangent image plane and the rear principal plane is z_1. A similar definition applies for the front principal surface, plane, point and focal length, with characteristic distance z_2. The latter is in practice the distance between the satellite and the object point. The distances between principal planes and pupils are, in paraxial approximation, related by the *pupillary magnification*, ratio of magnification of exit pupil diameter over entrance pupil diameter. As will be clear in the following, we may assume the input light to be collimated, e.g. the angle of the sub-bundles of rays to be a constant for each ray. In such case, a few other quantities are of aid. We define as *GSE angular resolution*, θ_r the angle between the chief ray focused at the center of the pixel and the chief-ray focused at its extreme. In other words, the angle between the central sub-bundle and the marginal sub-bundle of a given bundle. We define as *collimation GSE angle*, θ_{in} the collimation angle of every sub-bundle with the optical axis at the entrance pupil, and as *focal angle* θ the angle every ray of the sub-bundle forms with the respect to the optical axis after the exit pupil.

The introduced terminology and notation is summarized in the sketches in Figure 6.2, which describes the paraxial, aberration-free, working principle of a complex axial-symmetric optical system and Figure 6.3, which illustrates the focusing of the same optical system at finite conjugates for on object point source. We further consider the temporal resolution of the reconstructed signal overall polarization and wavelengths, defining it as simply *temporal resolution*. Depending on the application, however, it may be only requested to have a certain resolution over the measurement of the same polarization (which are being combined together in the reconstruction process) and consistency of temporal measurement for different bands would not be a priority. To distinguish the two cases we define also a *spectral temporal resolution*, t_λ, discernible time variation between the measurement of the Stokes parameter for a given wavelength. We finally remember the reader that a comprehensive list of Symbols is present in Table G.2 for reference.

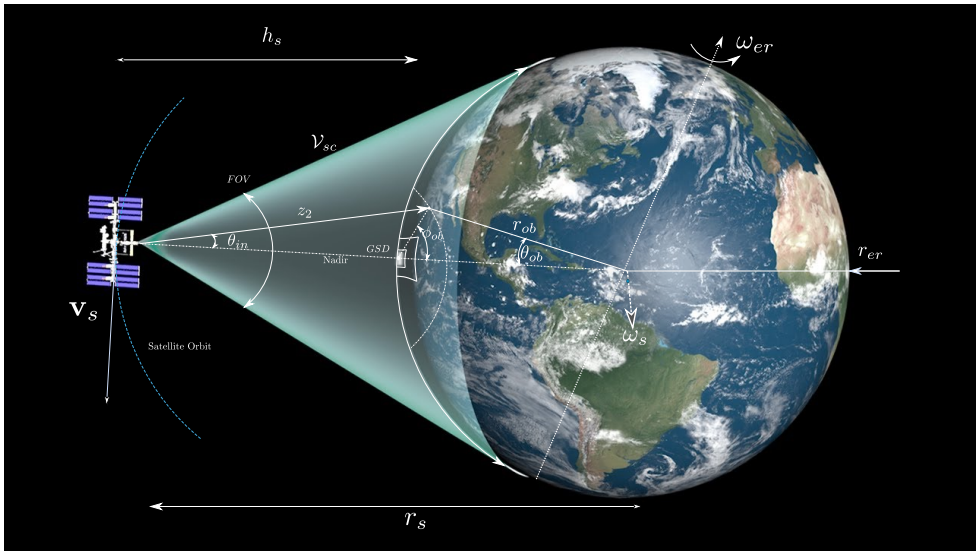

Figure 6.1: Illustration of the scanning geometry and the definitions introduced. It is supposed that the pointing of the satellite is at Nadir. The satellite velocity is locally tangent to its orbit which possesses a rotational velocity ω_s with respect to a non-inertial reference frame centered on Earth center of mass jointed with the Earth-Sun reference. The scanning volume $\mathcal{V}_{sc}$ possesses distortion due to the high FOV and intersect the observation area A_{sc}. The collimation angle and conjugate distance are represented. An arbitrary point of observation delimits two polar angles and an azimuthal angle. The altitude of the satellite is h_s. The rotational velocity of Earth is ω_{er}. We'll assume $\mathbf{r}_{ob}$ to be jointed with Earth (even though it is not strictly necessary)

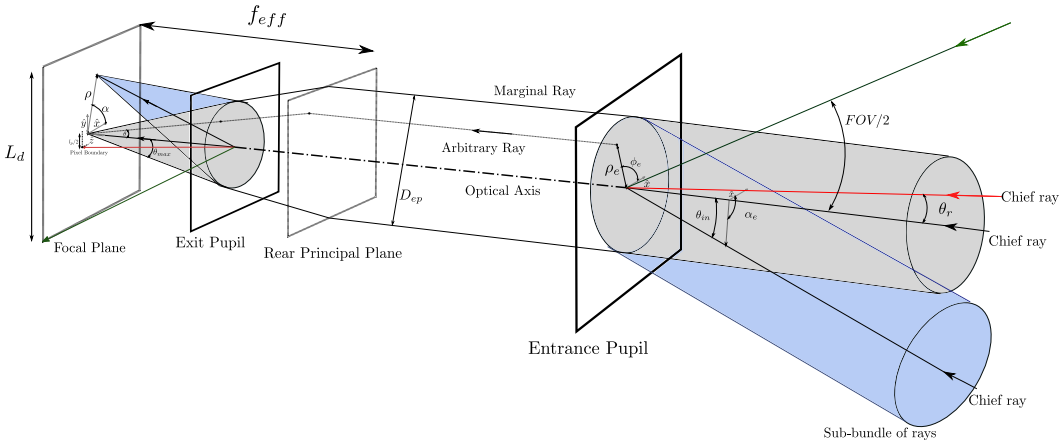

Figure 6.2: Collimated paraxial imaging of an optical system. The complex optical system is fully determined by its entrance pupil and exit pupil and the location of the principal plane (only rear is represented). The effective focal length is the distance measured along the optical axis between the focal plane and the rear principal plane. The optical system, excluding aberrations and higher-order effects, operates as paraxially as an ideal lens of the size of the entrance pupil aperture, D_{ep}, positioned on the rear principal plane. A sub-bundle of rays is the group of all collimated rays coming from a point on the infinite conjugate object domain. The most extreme chief-ray focusing on the pixel determines the angular resolution θ_r of the optical system. Similarly, the most extreme chief-ray focusing on the edge of the detector delimits the FOV of the optical system (the detector is assumed to be the field-stop of the system). An arbitrary ray entering at coordinates (ρ_e, ϕ_e) gets mapped in (θ, ϕ) on the focal plane. Within the paraxial approximation, all rays part of the same sub-bundle delimited by a chief-ray of inclinations (θ_{in}, α_e) get focused on the focal point mapped by (ρ, α) on the detector plane. Marginal rays delimit the maximum focusing angle θ_{max}, also related to the f-number of the system.

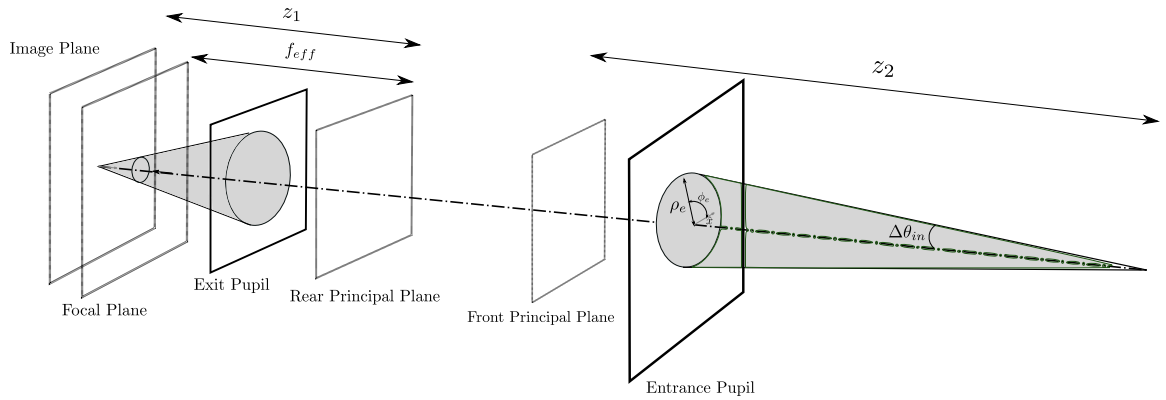

Figure 6.3: Illustration of the (paraxial) operation principal of the same system at finite conjugates and definition of main parameters. The image plane is not positioned at the focal plane due to the paraxial lens-equation. The finite conjugate distances of object and image are referenced to the principal planes. The cone angles subtended by the pupils on the object and image point are represented. The rays of a given sub-bundle are now not necessarily parallel but possess a deviation of $\Delta\theta_{in}$ with respect to their chief-ray

6.2. Observation Geometry

We consider the finite geometry represented in Figure 6.1 and wish to determine the geometrical relationships between the angles θ_{in}, θ_{ob}, the distance z_2 and the degree of angular deviation $\Delta\theta_{in}$ that the field present from ideal collimation for all ρ_e. We hereby consider the imaging of layers on the Earth surface position at r_{ob} from its center of mass. This may be an actual surface or an atmospherical layer. For simplicity, we'll assume $r_{ob} = r_{er}$ equal to the radius of Earth in the calculations and this observed point to be jointed with Earth. The z_2 distance can be calculated from simple geometry as:

$$z_{2(\rho_e,\phi_e)} = \sqrt{h_s^2 - 2h_s r_{er}\cos(\theta_{ob}) + 2h_s r_{er} - 2r_{er}^2\cos(\theta_{ob}) + 2r_{er}^2 - 2r_{er}\rho_e\sin(\theta_{er})\cos(\phi_e - \phi_{ob}) + \rho_e^2} \tag{6.1}$$

Similarly by performing a cross-product we can determine the angle of every ray:

$$\theta_{in(\rho_e,\phi_e)} = \text{asin}\left(\frac{\sqrt{r_{er}^2\sin^2(\theta_{ob}) - 2r_{er}\rho_e\sin(\theta_{ob})\cos(\phi_e - \phi_{ob}) + \rho_e^2}}{z_{2(\rho_e,\phi_e)}}\right) \quad [rad] \tag{6.2}$$

We wish now to quickly determine quantitatively the extent at which the field can be considered collimated.
The chief-ray of every bundle is determined by $\theta_{in(\rho_e,\phi_e)|\rho_e=0} = \theta_{in}$ by definition. Since $\rho_e/h_s << 1$ we can pertain only the linear term in ρ_e without loss of accuracy, so that we determine the *angular deviation*:

$$\Delta\theta_{in} = \theta_{in(\rho_e,\phi_e)} - \theta_{in} = \left(\frac{\partial\Delta\theta_{in}}{\partial\rho_e}_{|\rho_e=0}\right)\rho_e\cos(\phi_e - \phi_{ob}) + o_{(\rho_e^2/h_s^2)} \tag{6.3}$$

The angular deviation derivative in (6.3) is plotted for various observation points and altitudes in Figure 6.5a). Being in the order or arcseconds/meter it is negligible with respect to the angular resolution θ_r for typical achievable GSD on ground. We quickly analyze also the paraxial focusing equation:

$$\frac{1}{z_1} + \frac{1}{z_2} = \frac{1}{f_{eff}} \tag{6.4}$$

Even if the variation of z_2 in the viewing geometry of Figure 6.1 is severe (see Figure 6.4a)), we do not expect a significant focusing error due to the three-dimensionality of the object. The defocusing error is in fact negligible for all observation regimes of interest, as represented in Figure 6.5b). We conclude that a collimation hypothesis is perfectly acceptable for regimes of $h_s > 400km$. Note that even if the collimation hypothesis is surely pertinent, the phase-shift difference at the entrance pupil derived in Appendix C is not negligible (scaling with $2\pi/\lambda$) and requires correction in the Optical System.
The collimation hypothesis allows to neglect ρ_e in the formulas (6.1) and (6.2) and to use the geometry depicted in Figure 6.2 rather than 6.3. In particular, the FOV is directly correlated only with the angle

θ_e subtended by the point of observation on Earth and hence the swath S_w. Defining the swath as the maximum arc subtended by the scanning area:

$$S_w = 2\theta_{ob,max} r_{er} \tag{6.5}$$

One readily determines:

$$FOV = 2\arcsin\left(\frac{r_{er}\sin\left(\frac{S_w}{2r_{er}}\right)}{\sqrt{h_s^2 - 2h_s r_{er}\cos\left(\frac{S_w}{2r_{er}}\right) + 2h_s r_{er} - 2r_{er}^2\cos\left(\frac{S_w}{2r_{er}}\right) + 2r_{er}^2}}\right) \tag{6.6}$$

which can numerically be inverted to determine the swath for a given FOV. The solid angle of the scanning volume $\mathcal{V}_{sc}$ limits the maximum FOV for a certain height. The limiting FOV can be calculated by determining the stationary points of equation (6.6), which leads to an envelope (FOV_{max}, h_s). The relationship between swath and field of view (and equivalently, collimation angle θ_{in} and observation polar angle θ_{ob}) is illustrated in Figure 6.4b) for various altitudes. The graph shows that strongly non-linear behavior is present for $FOV > 90°$ within the altitude range of a LEO satellite.

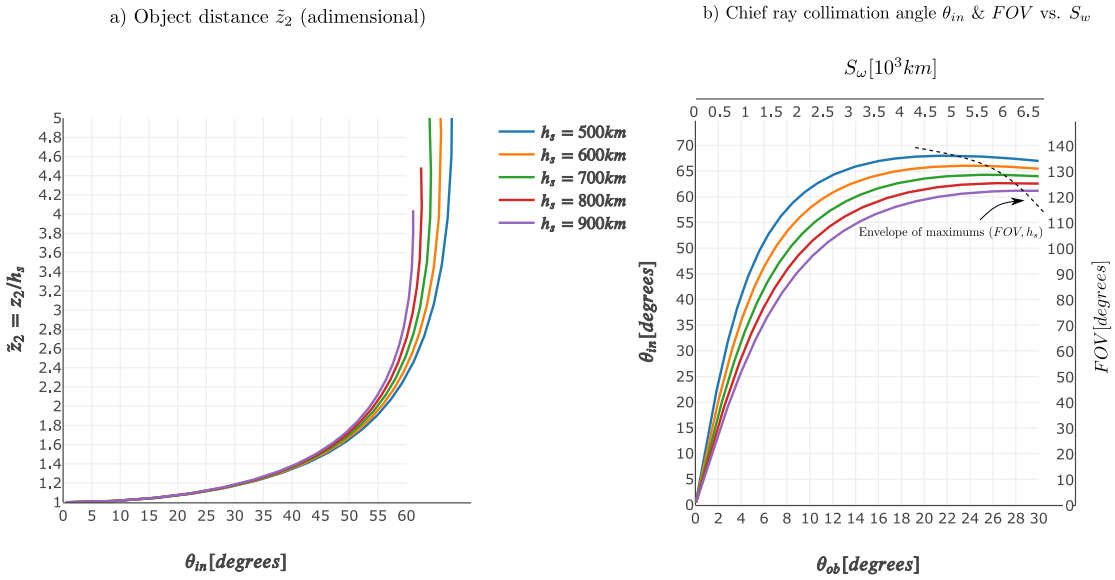

Figure 6.4: a) Non dimensional object distance (at the center of the entrance pupil) for various angles θ_{ob} and altitudes (LEOs). For high FOV the distance presents significant variations due to the low altitude.
b) Collimation angle θ_{in} of the central chief-ray for various altitudes. Upon tangency of the vector $\mathbf{z}_2$ on the Earth's sphere, the collimation angle reaches its maximum represented in the envelope. The graph can also be used to determine the FOV as a function of the swath, by simply considering equation (6.5) and $FOV = 2\theta_{in,max}$

We switch attention now to the mapping of the optical system in relation to this geometrical transformation in order to calculate an accurate expression of the ground sampling distance and its area A_{gse}. It is important to evaluate the GSD off-axis, since due to geometrical distortion at high FOV the nadir GSD would be severely underestimated. Therefore a non-linear treament is necessary. We moreover use a continuum of coordinates in image plane and object space rather than a discrete set of finite areas given by the mapping of each pixels, for simplicity. Expliciting a mapping relationships allows to determine the trajectory of the object points in relation to the image plane.
By means of equations (6.1), (6.2) the mapping is of the form:

$$(\rho, \alpha, \theta, \phi) \to (\theta_{in}, \alpha_e, \rho_e, \phi_e) \to (\theta_{ob}, \phi_{ob}) \tag{6.7}$$

We hence need to characterize the optical transformation first.

a) Collimation deviation $\Delta\theta_{in}$ on entrance pupil

b) Geometrical defocusing $\tilde{z}_1 - 1$ (adimensional)

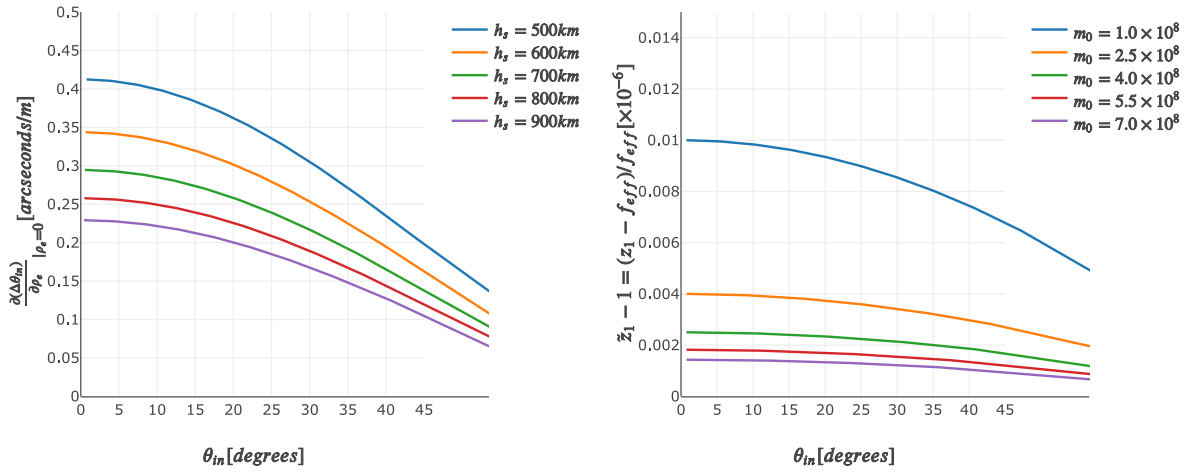

Figure 6.5: a) For each point on object plane at θ_{ob}, $\Delta\theta_{in}$ represents the difference between the angles of the upcoming rays with respect to the angle of collimation of the respective chief-ray of the sub-bundle and its derivative is plotted. b) The geometrical offset of three-dimensional focusing as prescribed by paraxial the lens-equation for various magnification factors and an altitude of $500km$. The magnification factors are ranging from $1\mu m/100m$ to $1\mu m/1km$. The offset is negligible for typical effective focal lengths.

6.3. Characterization of the optical system transformation

Assuming the optical system to be axial-symmetric, we can conclude as clear from figure 6.2 that $\alpha = \alpha_e, \pi - \alpha_e = \phi_{ob}, \pi - \phi_{ob}$ depending on the inversion nature of the optical system (as far as the attitude system mantains a nadir pointing). The optical system can then be related, similarly to what done in [51] where higher orders for a few surfaces are discussed, with transfer matrices of the form:

$$\begin{pmatrix} \rho \\ \sin\theta \end{pmatrix} = \begin{bmatrix} t_{00} & t_{01} \\ t_{10} & t_{11} \end{bmatrix} \begin{pmatrix} \rho_e \\ \sin\theta_{in} \end{pmatrix} + \begin{bmatrix} t_{00}^{(2)} & t_{01}^{(2)} & t_{02}^{(3)} \\ t_{10}^{(2)} & t_{11}^{(2)} & t_{12}^{(3)} \end{bmatrix} \begin{pmatrix} \rho_e^2 \\ \sin\theta_{in}\rho_e \\ \sin^2\theta_{in} \end{pmatrix} + \dots \tag{6.8}$$

The coefficients depending on the realization of the optical system and may be retrieved with ray tracing softwares or detailed analytical geometrical models. It is usual to pertain a few of the transfer matrix coefficients (and often use a paraxial approximation $\sin\theta_i \cong \theta_i$) when analyzing the performance in the paraxial regime . We will use only the first of such approximations, neglecting the higher power terms till more details are available. The reason not to use strictly a paraxial approximation is due to the fact that the detector size will be estimated from the field of view by means of those introduced coefficients, which requires to mantain the $\sin(\theta_{in})$ factor. We recognize the effective focal left inverse (by definition) in the paraxial regime as t_{10}. Assuming that the geometrical locus of the rear principal surface is a sphere (which is not far from the truth for many corrected optical systems) than we generalize for the non-paraxial regime this relationship:

$$t_{10} = 1/f_{eff} \tag{6.9}$$

Using the collimation hypothesis introduced in the previous chapter and considering that the system is an imaging one, we conclude that $t_{00} \cong 0$ to achieve focusing of the object points in the focal plane array, valid if further the off-focusing due to aberrations of the optical system is not too severe.
As is discussed in great detail in [52], [53], the operation of the DBR and in general spectral filters is greatly dependent on the angle θ of the chief-ray. The spectral response of the resonance multilayered structure is greatly angle-dependant and [53] also explicits asimmetries in PSF focusing due to non-perfect telecentricity. Systems using such devices are then usually designed to be approximately telecentric in image space, hence with an exit pupil at infinity. The geometrical implications of an image plane telecentric system requires that $t_{11} \cong 0$. The new transformation of such a system is depicted in Figure 6.7.

The factor t_{01} is still to be characterized. We may use conservation of etendue formulations for such matter. The solid angle depicted in Figure 6.6 are defined as follow: $\Omega_{gr\to e}$ is the solid angle subtended by Earth images object surface on an entrance pupil point, whereas $\Omega_{f\to e|f_{eff}}$ is the solid angle subtended by the detector on the entrance pupil positioned at the rear principal plane location. Similar and opposite definition applies for the solid angles $\Omega_{e\to gr}$ and $\Omega_{e\to f|f_{eff}}$. It is more conventional to refer at the solid angle subtended by/to the detector on the exit pupil. However, in the present case for a telecentric system, that's ill-defined and given by the solid angle of the entrance pupil posited at the rear principal plane point as we can demonstrate by operating a limit procedure:

$$\Omega_{ex\to f} = \lim_{z_{ex}\to\infty} \frac{A_{ex}}{z_{ex}^2} = \lim_{z_{ex}\to\infty} \frac{\pi r_{ex}^2}{z_{ex}^2} = \Omega_{e\to f|f_{eff}} \tag{6.10}$$

That's merely a consequence of the fact that in first approximation, the complex optical system operates as a lens with effective focal length f_{eff} positioned at the rear principal plane location and aperture equal to the entrance pupil size[1].
Applying the same reasoning to, this time, the etendue subtended by the focal plane array to the exit pupil (the solid angle tends to zero) we determine:

$$G_{f\to ex} = \lim_{z_{ex}\to\infty} A_{ex}\frac{A_d}{z_{ex}^2} = A_d\Omega_{e\to f|f_{eff}} = A_{ep}\Omega_{f\to e|f_{eff}} \tag{6.11}$$

From conservation laws of etendue in an optical system ([54] for the inequality) we further know that:

$$G_{f\to ex} \leq G_{gr\to e} \to \rho_{max} = \pm f_{eff}\sin\theta_{in,max} \tag{6.12}$$

Where ρ_{max} is the detector size assumed to be the field-stop of the ideal system without losses. The given results suggests that, using a localization lemma[2]:

$$t_{01} \cong -f_{eff} \tag{6.13}$$

where we have kept the minus sign in sake of Figure 6.7. We can verify that the determinant of the transfer matrix is unitary, as conservation of energy dictates. The proposed coefficients are exact at the extent that the higher order terms do not interfere with the transformation. The optical system transformation is therefore in conclusion given by:

$$\begin{pmatrix}\rho\\ \sin\theta\end{pmatrix} = \begin{bmatrix}0 & -f_{eff}\\ 1/f_{eff} & 0\end{bmatrix}\begin{pmatrix}\rho_e\\ \sin\theta_{in}\end{pmatrix} + o_{(\rho_e^2,\sin^2\theta_{in},\rho_e\sin\theta_{in})} \tag{6.14}$$

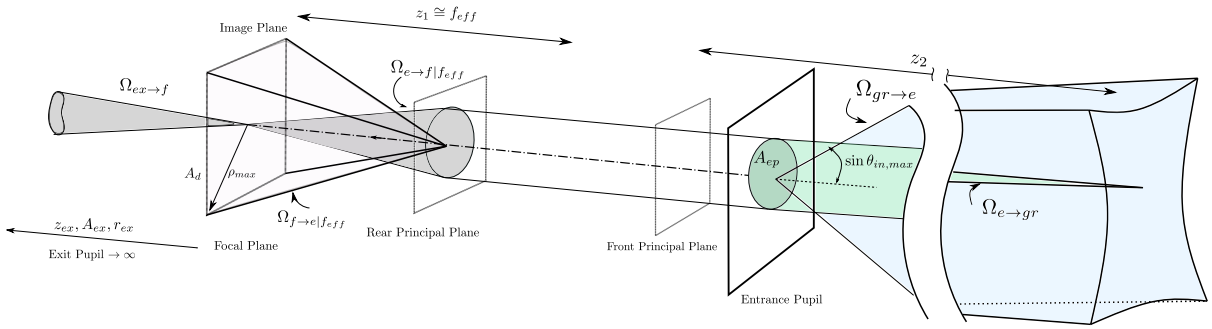

Figure 6.6: The figure represents the solid angle of the viewing geometry. On the right side, the object domain (in the far-field) defines the extension of the FOV through means of the solid angle $\Omega_{gr\to e}$. Instead of referring the solid angles to the exit pupil in the image domain, being the latter ill-defined, we refer them to an aperture of the size of the entrance pupil positioned on the rear principal plane. As demonstrated through the limit operations (6.11) and (6.12) the two points of view are consistent for a telecentric optical system in image space with a collimated input field

[1] more in general, as far as an aperture is considered in the image domain and of the appropriate sizing with respect to the NA, it could be referred to any section without loss of generality (invariance of Etendue).
[2] the conservation laws scrictly applies to the integral representation, so local variations may exists if the transfer matrix depicted in (6.8) presents non negligible higher order terms

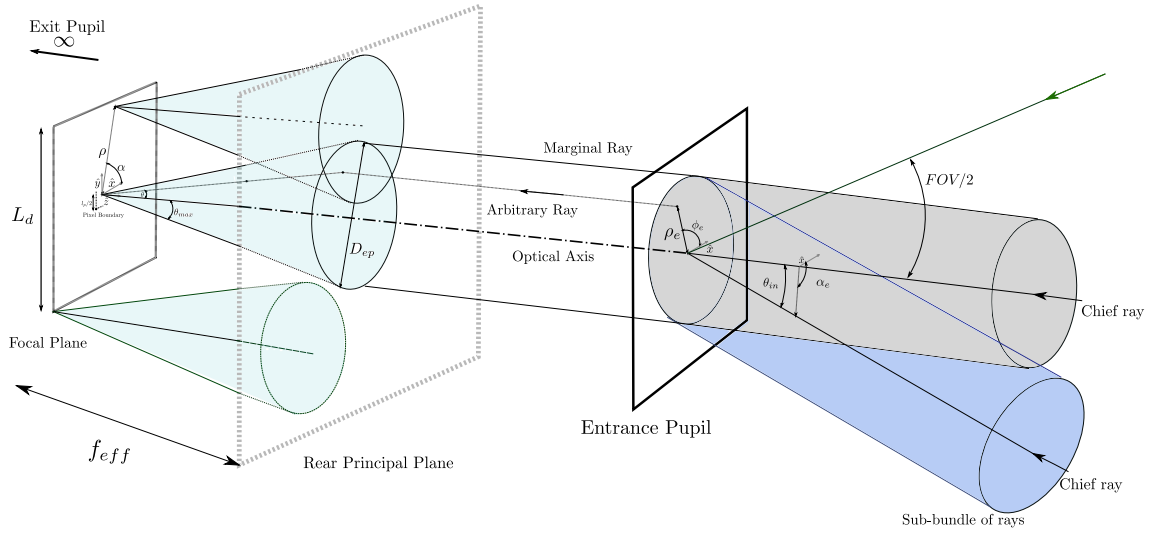

Figure 6.7: The figures represents the (geometrical) operating principle of a complex optical system which is telecentric in image space. It also models the optical system that will be considered from now on for the performance estimation of the metasurface. Since chief-rays are (ideally) parallel for all sub-bundle of rays, the exit pupil is positioned at infinity by definition. It, however, subtends a finite etendue due to conservation of energy. Hence also its diameter will tend to infinity. The focusing of this system can in first approximation be related to a single lens positioned on the rear principal plane and appropriately displaced. If the input field is further collimated, like in the present case, the dimensions of this effective aperture is equal to the size of the entrance pupil. In a real system higher geometrical displacement are surely present and the operation principle will slightly differ from the ideal one presented

6.4. The metric and GSD determination

With the previous results we can now explicit the metric of the transformation and the GSD. We therefore switch attention to the equivalent mapping from the detector array to an azimuthal Earth's projection:

$$\frac{1}{f_{eff}}(x,y) = \tilde{\mathbf{r}}_f = \frac{1}{f_{eff}}(\rho\cos\alpha, \rho\sin\alpha) \rightarrow \frac{1}{h_s}(q_u, q_v) = \tilde{\mathbf{q}} = \frac{r_e}{h_s}(\theta_{ob}\cos\phi_{ob}, \theta_{ob}\sin\phi_{ob}) \tag{6.15}$$

where we have introduced a local map q_u, q_v as depicted in 6.8 and conveniently normalized the various dimensions to account for the paraxial magnification factor. The transformation possess its own metric given by the Jacobian of the transformation, e.g. the matrix $\mathbb{J}_f$ for which:

$$d\tilde{\mathbf{q}} = \mathbb{J}_f d\tilde{\mathbf{r}}_f \qquad \mathbb{J}_f = \begin{bmatrix} \frac{\partial \tilde{q}_u}{\partial \tilde{x}} & \frac{\partial \tilde{q}_u}{\partial \tilde{y}} \\ \frac{\partial \tilde{q}_v}{\partial \tilde{x}} & \frac{\partial \tilde{q}_v}{\partial \tilde{y}} \end{bmatrix} \tag{6.16}$$

The derivatives shall be explicited by means of derivation of relationships (6.2) and (6.14) (opportunily normalized).
As a result the magnification factor relating the ground sampling area with the area of the pixel is given in the local continuum approximation by the determinant of such matrix:

$$A_{gse} = \int_{A_p \rightarrow A_q} dudv \cong m^2 A_p \qquad m = \pm m_0 \sqrt{\mathrm{Det}\,\mathbb{J}_f} \qquad m_0 = \frac{h_s}{f_{eff}} \tag{6.17}$$

where the $\pm$ sign relates to the inversion nature of the optical system. We then define the *distorted ground sampling distance* GSD_ρ as the dimensional ground sampling distance of a square pixel which would lead the same area as the parallelogram for a given pixel position. In relation to the nadir ground sampling distance GSD_0, by definition one has:

$$\frac{GSD_\rho}{GSD_0} = \sqrt{\mathrm{Det}\,\mathbb{J}_f} \tag{6.18}$$

is important however to maintain the complete description of $\mathbb{J}_f$, since for a generic off axis point the induced distortion depends on the direction α considered and the matrix represents fully the linearized

distortion in the given point as shown in 6.8. For validation, we can verify that in the nadir case:

$$\lim_{\theta_{ob}\to 0} \mathrm{Det}\, \mathbb{J}_f = 1 \tag{6.19}$$

so that the magnification factor is exactly the one predicted paraxially. The picture 6.9a) illustrates the detector grid (with only a few of the pixel for clarity) projected on the local mapping q_u, q_v. Picture 6.9*b*) illustrated the variation of the distorted ground sampling distance (at the edge) in relation to the FOV of the system, illustrating how for small altitude such effect is relevant and it jeopardizes the spatial resolution achievable on the ground. In Section 6.8 we will use this graph to determine the GSD meeting the spatial resolution requirement of the system. This treatment takes only into account the geometrical radial distortion. Higher distortion may be present (e.g. lateral distortion due to misplacement of the focal plane array) in a real system.

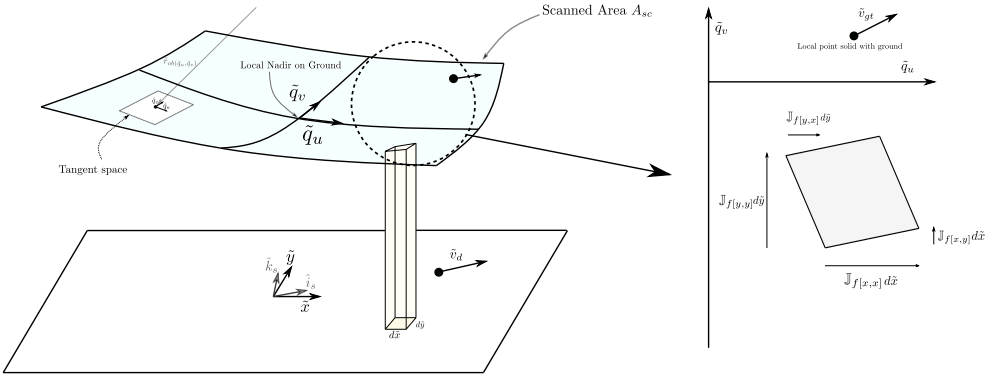

Figure 6.8: Illustration of the mapping of coordinates, geometrical interpretation of $\mathbb{J}_f$ and point's velocity in the tangent space. The local detector versors are in the same plane delimited the the satellite versors $\hat{i}_s, \hat{k}_s$ depicted in Figure 6.10 (introduced later in the report). The vector $\tilde{\mathbf{r}}_{ob}$ (same appearing in Figure 6.1 upon normalization) parametrizes the object space domain and its tangent space.

a) Projection of detector grid on Earth Surface*

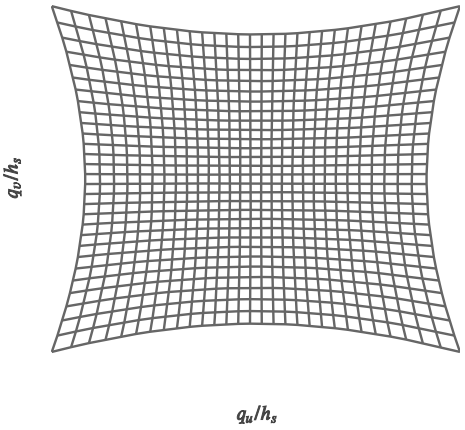

* for a $FOV = 80°$, $h_s = 500km$

b) Ground sampling variation off-axis

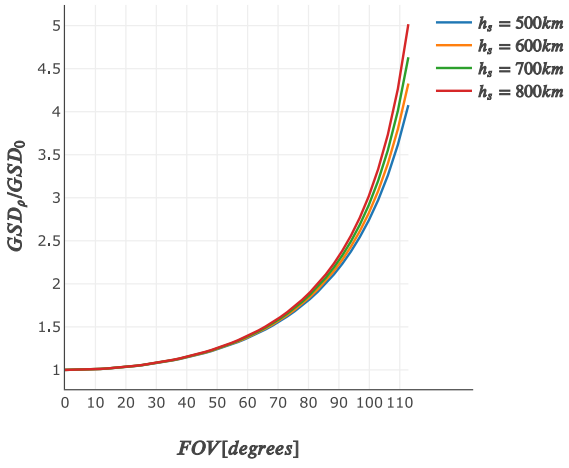

Figure 6.9: a) The figure illustrates the detector grid remapped in the q_u, q_v plane, with a smaller number of pixel for illustration purposes for a $FOV = 80°$ and altitude of $h_s = 500km$. The radial distortion is naturally induced by the observation geometry.
b) The figure illustrates the variation of effective ground sampling distance (defined as in (6.17)) for various altitudes and FOV. The mapping distortion is only a weak function of the altitude and is simil-parabolic in the FOV. $FOV > 90°$, as already pointed, present high radial distortion and shall be avoided within all ranges of altitudes.

6.5. Orbital parameters

In order to have a clearer picture of the required parameters for sizing the optical system, in particular the integration time, we require knowledge of the orbit of the satellite. Since the science case requirements are rather fluid and the study is a feasibility assessment, we will select a range of altitudes for allowing flexibility. As discussed in [20], [8], [7] spectropolarimeter applications for aerosol detection required high FOV within variegate spectral bands, with viewing angles up to 70° for some bands. As depicted in figure 6.4b) distortions are limited for such FOV only for LEO altitudes. The metasurface concept further exploits the integration and miniaturization of the device. It is hence suited for micro&nano-satellites mission concepts with small aperture diameters and even lower altitude, in the range $[400, 600]km$. The altitude has important implications in terms of orbiting drag and mission life, so we will downselect a preliminary altitude of $h_s \cong 500km$ for this study.
We will further consider, for simplicity, a circular orbit with a mean motion of:

$$\omega_s = \sqrt{\frac{g_0}{h_s + r_{er}}} \tag{6.20}$$

Reference [8], [20] further explicits the importance of the angle of observation in relation to the sun-illumination on ground and the angle with the normal surface $OZA = \theta_{ob} + \theta_{in}$. In [55], [56] the use of Sun-Synchronous orbits is suggested for similar science requirements. Figure 6.10 depicts the precession of such orbit and the orbital parameters we will use of its characterization. The perturbations of Earth's oblateness are actively used to mantain the orbit precession $\dot{\Omega}$ equal to the revolution mean motion ω_p of Earth, such to maintain the same sunlight visibility throughout the revolutions. Such conditions imposes[3] (see Table G.1 for parameters definition and reference [57] for the formula (6.21)):

$$\dot{\Omega} = \omega_p = -\frac{3}{2}\left(\frac{r_{er}}{r_{er} + h_s}\right)^2 J_2 \cos I \omega_s \tag{6.21}$$

which wields a relations between the inclination of the orbit depicted in figure 6.10 and its altitude. We further define the rotational velocity of a point rotating in the frame solidal with the satellite and on the Earth surface as:

$$v_{gt0} = \omega_s r_{er} \tag{6.22}$$

which will be used in the next Section. Figure 6.12b) depicts the (minimal) variations of inclination and relative ground velocity v_{gt0} for various LEO altitudes.
Using the change of reference frame depicted in 6.10b) we can also explicit the time-dependance ground-track projection on Earth of the local orbiting satellite, which is represented in Figure 6.11. In particular, we may further relate the mapping (q_u, q_v) previously discussed into this Earth projection, so visualizing the (exact) projection FOV on earth, which is also depicted in the same figure.

6.6. Ground velocity and residence time on detector

We finally switch the attention to the determination of the residence time of an object point in a given region of the detector array. We, in particular, derive an expression for the local relative velocity of all points in object space, accounting for Earth's rotation. It is simple to show that (6.16) applies also for the velocities of the mapping coordinates, by means of simple derivation, hence the velocity observed on the detector is:

$$\mathbf{v}_d = \frac{1}{m_0}\mathbb{J}_f^{-1}\mathbf{v}_{gt} \qquad \mathbf{v}_{gt} = h_s \frac{\partial \tilde{\mathbf{q}}}{\partial_{\Sigma_s} t} \tag{6.23}$$

It is important to explicit the reference frame at which the integration shall be referred: the $\mathbf{v}_{gt}$ is the velocity of a point on the ground represented in the local tangent space associated with q_u, q_v as sketched in Figure 6.8 and jointed with the rotation of the satellite. From simple kinematics and geometrical projection one determines that:

$$\dot{\mathbf{r}}_{ob} = \frac{\partial \mathbf{r}_{ob}}{\partial_{\Sigma_s} t} = \left(\omega_{er|\Sigma_s} - \omega_{s|\Sigma_s}\right) \times \mathbf{r}_{ob} - \frac{\partial r_s}{\partial_{\Sigma_e} t}_{|\Sigma_s} \hat{\mathbf{r}}_s \qquad \mathbf{v}_{gt} = (\dot{q}_u, \dot{q}_v) = (\dot{\mathbf{r}}_{ob} \cdot \hat{\mathbf{q}}_u, \dot{\mathbf{r}}_{ob} \cdot \hat{\mathbf{q}}_v) \tag{6.24}$$

[3] the perturbation influences also to some extent the other orbital parameters, effect which we disconsider since orbital considerations are not the focus of this discussion

a) Illustration of a SSO orbit

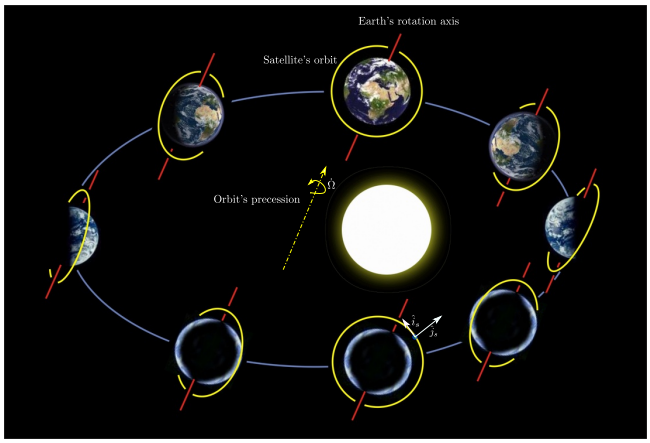

b) Orbital parameters

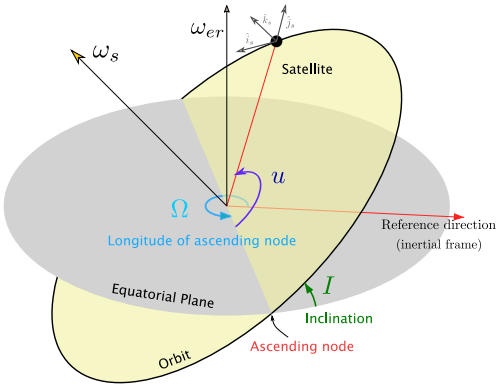

Figure 6.10: a) [Arranged from the web] Illustration of an SSO orbit and its precession along with Earth's revolution, for different time realizations.
b) [Arranged from the web] Illustration of the orbital parameters used for the description of the circular orbit under consideration. The reference frame jointed with the satellite is also depicted with the along and cross-track directions. The angular motion of the satellite and Earth is also depicted (both objects rotate in the represented frame). The other orbital parameters (true anomaly, eccentricity...) are not of interest for this preliminary analysis

where the radial velocity of the satellite is derivated in a non-rotating frame solidal with Earth and the local versors of the tangent space $\hat{\mathbf{q}}_u, \hat{\mathbf{q}}_v$ are given by derivation of the mapping equation[4]:

$$\hat{\mathbf{q}}_u = \frac{\partial \mathbf{r}_{ob}}{\partial q_u} \qquad \hat{\mathbf{q}}_v = \frac{\partial \mathbf{r}_{ob}}{\partial q_v} \tag{6.25}$$

Introducing the orbital inclination, I (with respect to the rotational axis of the Earth) and the argument of latitute u of the satellite we explicits those vectorial quantities (see Figure 6.10b) in support) as:

$$\mathbf{r}_{ob} = r_{er} \begin{pmatrix} \sin\theta_{ob}\cos\phi_{ob} \\ \sin\theta_{ob}\sin\phi_{ob} \\ \cos\theta_{ob} \end{pmatrix} \qquad \omega_{s|\Sigma_s} = \omega_s \begin{pmatrix} 0 \\ 1 \\ 0 \end{pmatrix} \qquad \omega_{er|\Sigma_s} = \omega_{er} \begin{pmatrix} \cos u \sin I \\ \cos I \\ \sin u \sin I \end{pmatrix} \tag{6.26}$$

The nadir ground track velocity simplifies to:

$$\mathbf{v}_{gt,nadir} = v_{gt,0} \begin{pmatrix} \tilde{\omega}\cos I - 1 \\ -\tilde{\omega}\sin I \cos u \end{pmatrix} \qquad \tilde{\omega} = \frac{\omega_{er}}{\omega_s} \qquad v_{gt,0} = \omega_s r_{er} \tag{6.27}$$

To validate once again the result, we verify the existance of a geostationary orbit for $I = 0, \tilde{\omega} = 1$. The equation derived shows the presence of an adrift velocity ($\hat{j}_s$ component) due to the rotational velocity of Earth and a dependance on time (through u) $\propto \tilde{\omega}$. Simulated results in 6.12a) shows a limited tilt in the streamlines due to this adrift component and small fluctuations due to geometry and rotation. Since at small altitudes the rotational velocity of Earth is rather negligible with respect to ω_s, Earth's rotation is negligible. Moreover, in practice, the adrift component $\mathbf{v}_{corr} = r_{er}\tilde{\omega}_{er}\sin I \cos u \hat{j}$ is often corrected at nadir by means of the attitude control system. Such correction is possible, for instance, by slight rotation on the nadir axis. The radial velocity component does not interfere with the residence time, however, implies a small relativistic frequency Doppler effect $\propto v_{rad}/c$ (with c the velocity of light) which is some applications shall be taken into account but will be hereby neglected.
The trajectory of a point in time can be resolved numerically, with the simplification of assuming a circular orbit such that:

$$u = \omega_s(t - t_{eq}) \qquad \frac{\partial r_s}{\partial_{\Sigma_e} t}_{|\Sigma_s} = 0 \tag{6.28}$$

[4]that's a concept of differential geometry as discussed in [58]. Moreover the versors are the same both in normalized and un-normalized domain

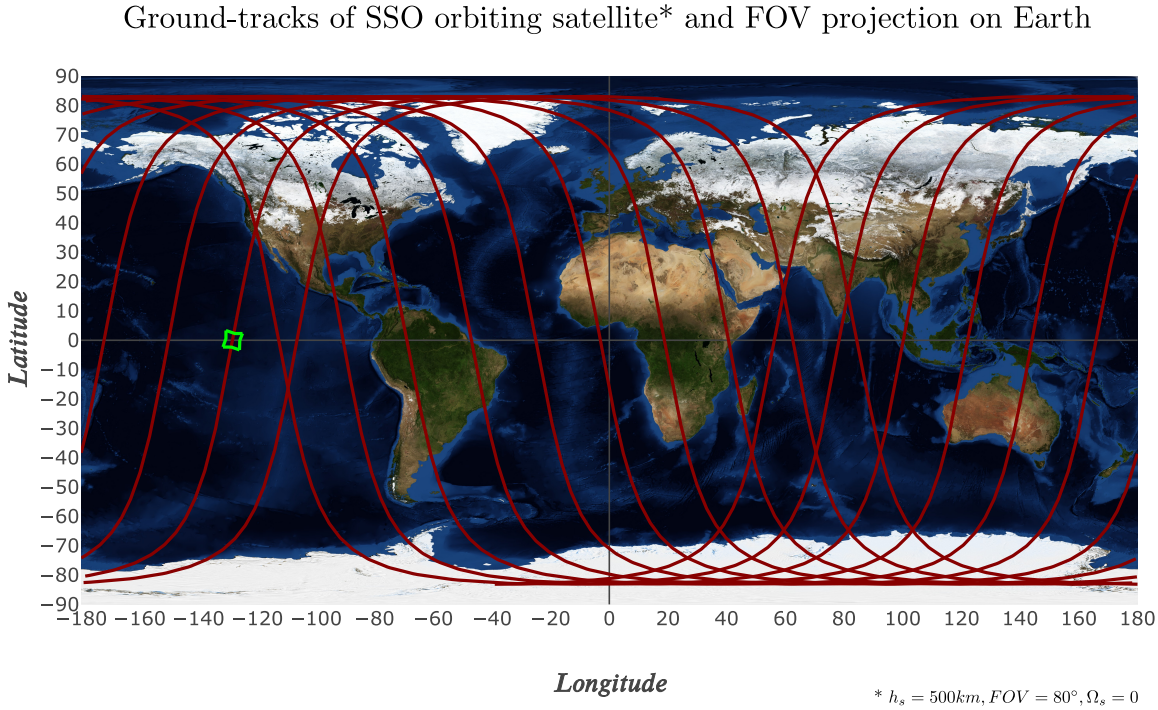

Figure 6.11: Illustration of the ground-tracks during an SSO orbit of a satellite at $h_s = 500km, \Omega_{(t_0)} = 0$. The second-order effect of orbital precession has been neglected in the limited simulated step of height orbital periods. The FOV projection is represented. The present solution does not achieve full consecutive coverage at center latitudes. Full coverage, however, may be possible using a constellation of $3 - 4$ satellites, if required.

Provided that the geometrical mapping relating $(\mathbf{r}_{ob(u)}) \rightarrow (q_u, q_v) \rightarrow (x, y)$ is known, one can determine the streamlines and residence time of any point on the ground or on the detector by means of this solution. Figure 6.13 shows, as computed with such procedure, the time of permanence and streamlines for points entering the detector and 6.12 the same quantities in object domain space. Since the streamlines on the ground are direct as $\hat{i}_s$ in good approximation, the velocity and streamlines in the detector present the same inverse distortion and magnification induced by the geometrical grid. In particular, the detector velocity v_d assumes an simil-elliptical distribution and decays with the inverse of the magnification factor depicted in 6.9b). The way the object points are masked on the pixel with respect to time has important applications for the reconstruction and the determination of the energy integrated on the pixel for a given time. It does further affect the spatial resolution which is possible to reconstruct from a measurement with a finite time of integration t_{int}. In practice, the integration time is dictated by the detector electronics and the same for all pixels. To assess qualitatively what are the effects on the spatial resolution, consider the illustration in Figure 6.14. The permanence time of a point within the integration time-frame for a given pixel is a spatial function varying in the direction of v_d. At nadir, the permanence time distribution is a trapezoid, which represents the sampling window of the signal on ground for a system that does not present diffraction. For off-nadir points since v_d further presents a small deviation the spatial distribution is two-variables dependent. Represented on ground, this permanence time distribution has, at best the dimensions of $2 \times GSD$ is the integration time is chosen to be exactly the permanence time of a point at the nadir pixel. We conclude that the Nyquist sampling requirement is a direct implication of this time variation of the object point on the pixel and the spatial sub-resolution is roughly:

$$GSRE \cong (1 + \chi_s) GSD_\rho \qquad \chi_s = \frac{v_d t_{int}}{l_p} \tag{6.29}$$

In reality, the achievable spatial resolution depends on the post-processing used, and time-delay integration may be used for limiting the effect of time smearing.

Such a picture can be validated by considering the case of a stationary imaging system. In such a case, for all integration times, $\chi_s = 0$, so the spatial resolution is dictated itself by only the pixel size. The local point velocity hence dictates a maximum bound of the integration time. In practice, a minimum bound is also set by the integration time required for a certain SNR requirement which is in those applications the driving constraint. So we set for a given detector choice the integration time to be the permanence time of a ground point at the nadir pixel:

$$t_{int} = \frac{l_p}{v_{d,nadir}} \tag{6.30}$$

In reality, all optical systems present diffraction (and further blurring may even be introduced by the detector electronic themselves). As shown in Section 4, the local velocity on the detector modifies the OTF of the system, so acts directly in the Fourier domain of the signal.

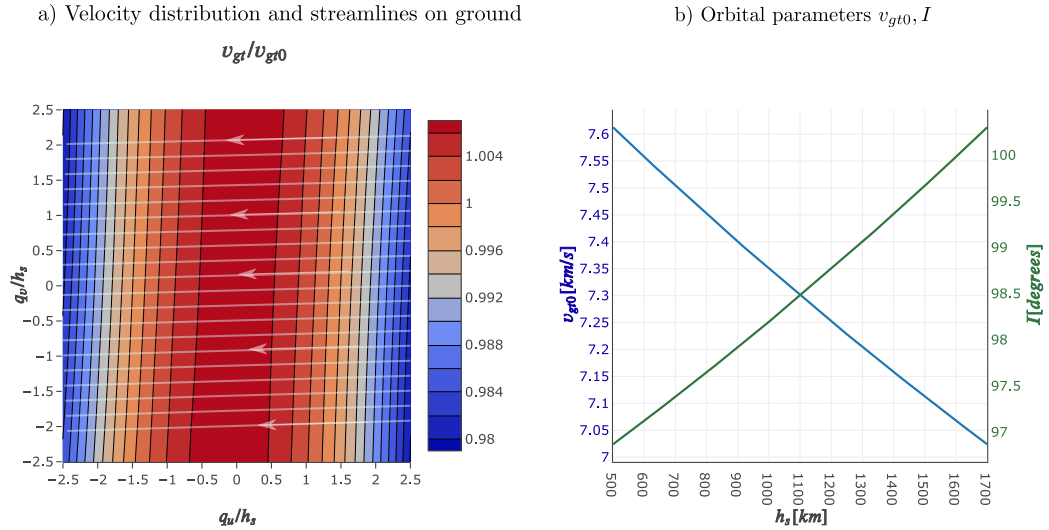

Figure 6.12: a) Velocity streamlines on ground at the equator and relative velocity distribution in space. For other orbital points, the distribution would slightly differ, oscillating in the x directions. It will be from now on assumed that the attitude control system corrects for the small deviation inherent with the Earth's rotation.
b) The variation of the inertial relative ground velocity v_{gt0} and the inclination of an SSO orbiting satellite for various altitudes.

6.7. Imager Arrangement

The metasurface design presented in [1] integrates retrieval of polarization and spectral information on the imager. A question arises hence on what is the optimal arrangement for reconstruction for various applications. In this Section, we preliminary propose an arrangement for the aerosol retrieval mission we are investigating. The dimensional and design details of the imager and filtering are instead discussed in the sizing Chapter 7.
As discuss in [1] the retrieval process for n Stokes parameters of a given point in space necessitates $n \leq n_m \leq 4$ spatially separate measurements, equality applying if a priori information about the Stokes to be retrieved is known. Every pixel design is characterized by its own polarization angle sensitivity, wavelength spectrum and angle-space of observation geometry in relation to the optical system mapping. We disregard in this Section concepts with separate focusing for each pixels (like the one involving lens arrays). Hence, the pixel measuring polarization must be adjacent to each other. It is now important to distinguish the temporal behavior of the source in relation to the imager. We first distinguish between two types of applications:

- *Ground applications*: the imaging is usually static, resulting in the freedom of choosing the integration time. All four Stokes parameters must, in general, be retrieved. The proposed arrangement in [1] would allow reconstruction with a spatial resolution equal to the mapping of a superpixel.

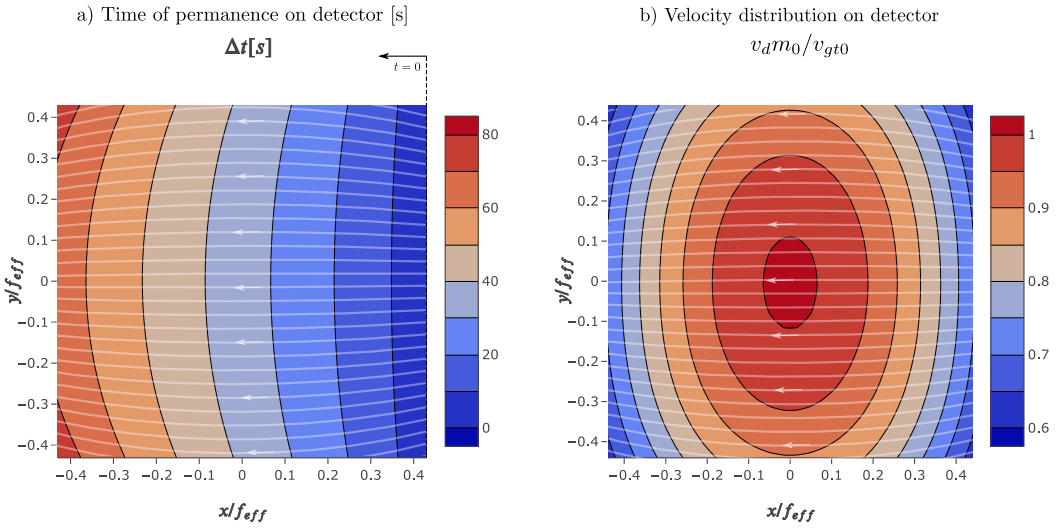

Figure 6.13: a) Time of permanence of a front of points entering the detector at $t = 0$ and their streamlines, calculated from transforming the ground-streamlines. Radial distortion and disuniformity is present far from the nadir region. We refer to a SSO orbiting satellite at $h_s = 500km$, entering at the maximum elevation $u = \pi/2$. Since we have assumed the deviation at the equator to be corrected by the ACDS system, the provided distribution is mostly consistent for all points in the orbit with just minor deviations.
b) Velocity distribution (non-dimensionalized on its ideal value) of the object points velocity on the detector. Due to the inverse of the magnification factor present due to the viewing geometry, the velocity decays for off-axis points. The integration time requirement shall hence be set at the nadir pixel for the most conservative case. The increase in permanence time for off-axis pixels further suggest a way to counteract the increase in GSD_ρ by means of time integration delay and other post-processing techniques

The diffraction behavior of such imager is critical for the performance and may be analyzed in similarity with our analysis in Chapter 7.

- *Airborne - Space applications*: the imaging is not static and the imager is assumed to be aligned with the along-track-across-track directions of relative motion of the satellite/airplane with an integration time given by (6.30). The source (Earth in the proposed concept) is usually an emitting source relatively uniform in time during one integration. Hence, if it wouldn't be for the temporal smearing effects discussed in 6.6, the necessary measurements could be conducted in different time-steps without jeopardizing the spatial resolution but only the temporal one. A proposed arrangement of such is illustrated in the Cover page of this Thesis.

The proposed arrangement requires data allocation for a time greater than the integration time. Aerosol retrieval missions further require the measurement of various angular bands (more than 5 usually) for improved accuracy [7]. Because of the spatial coexistence of all measurements, obviously, there is a direct correlation between the number of angular and spectral bands and resolution time. For such concept, we angular band extent is limited by the characteristic time Δt_{ob} in which we expect a variation in the input Stokes parameters in order to allow reconstruction, which is smaller than the FOV as clearly observed by Figure 6.13 which shows a non-negligible time of permanence over the whole detector. The Stokes vector at the input of the optical systems results from the statistical characterization of the cross-correlation tensor of the field present at the entrance pupil. The linear degree of polarization of such sources is roughly $\cong 250$ times ([10]) more significant than the circular degree of polarization for planets of Earth/Venus like composition. For concepts where is measurement is not required and its contribution is negligible, the design of [1] can be readily simplified by removing the wave-plate array. It is important to finally also consider the design of the resonator cavities in terms of the proposed arrangement and positioning of the spectral bands. In particular, we determined in Chapter 3 how multiple spectral channels with multiple measurements for a channel are necessary for remote sensing [7], [2], [59], whereas the spectral bandwidth is limited in the design of [1] by three main factors:

- One of the advantages of [1] design is the occurrence of a single cavity height for multiple sensitive wavelengths, resulting in a single lithographic step with great ease of manufacturing. For a given

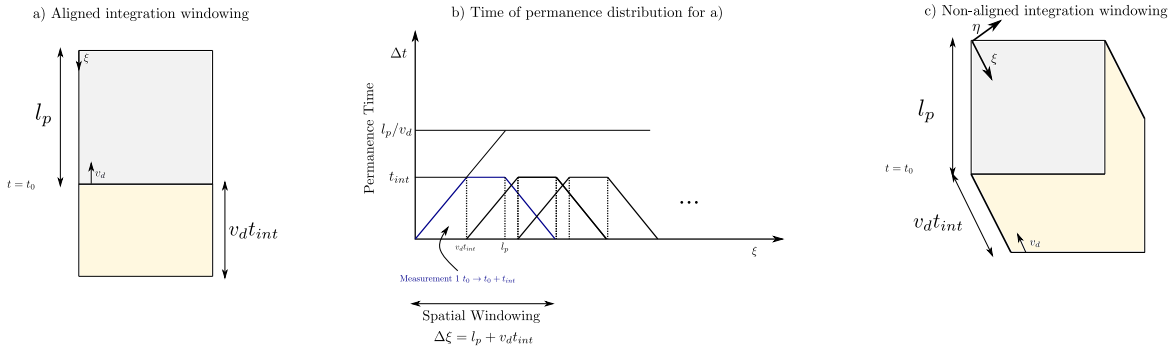

Figure 6.14: a) The figure illustrates qualitatively the correlation between a moving object region mapped on the detector and a pixel, observed for a given integration time, with no deviation of the velocity vector. Points at various coordinates ξ have different permanence times during this measurement.
b) Plot of the spatial distribution of the permanence time for the case discussed in a). During an integration time, the permanence time is a trapezoidal function of ξ and the distribution acts as a spatial windowing in the object space domain. Various windows are overlapped through different measurements (and also different pixels). In the limit $v_d \to 0$ the distributions tends to a square of extension l_p for all measurement as expected. Moreover, the mean averaged time of each point is constant to l_p/v_d once all measurements are considered, as expected.
c) Qualitative illustration of the correlation in the case of not-aligned point-object velocity. The distribution would, in this case, be a function of the two variables ξ, η. Such operation regime can be characteristic of the off-axis points as the streamlines in 6.13 depict.

cavity height, the band-gap bandwidth limits the realizable total bandwidth of the channel. Nevertheless, the cavity height of adjacent pixels can be changed within a bigger spatial scale upon reaching of this limitation, without jeopardizing the above-mentioned manufacturing advantage. Performing multiple lithographic steps is less and less problematic as the spatial extent of those steps is increased, see Chapter 7 for more details.

- The polarization distinction is possible because of the spectral shift of the two polarization directions. Even though the reconstruction process still seems possible with the presence of both spectral peaks [60] the condition number is significantly improved if the second peak is removed. Since multiple measurements are required for the same channel, that must be achieved with careful design of a filter unit depending on the geometrical arrangement chosen. We postpone the consideration of the design of such filtering units to Chapter 7, where we will also discuss various solutions for the reconstruction process with and without filtering and optimize 6 DBRs design for the purpose.

- The materials composing the mirrors and the resonator are not-lossy only for a certain regime of wavelengths, which limits the realizable transmission for a given bandwidth. Also in Chapter 7 we show how, by an opportune choice of the inclusion materials and trading-off the FWHM, it is possible to counteract this effect in the required VIS channels.

6.8. Preliminary sizing of the Optical System

We will hereby settle the preliminary optical specifications in order to meet the requirements depicted in Chapter 3. First, we must select what are design parameters and what parameters shall instead by calculated from the design parameters. Since there is a certain uncertainty over the power budget yet, which will be discussed in Chapter 9.1, we set as free design parameters the size of the pixel and the NA of the system. The number of pixels is also somewhat constrained since it most be an integer and specific values are commonly used in off-the-shelf detectors. That sets also the detector size as a free design parameter. Further constraints come from the nature of the mission, since as discussed in Section 6.5 and Chapter 3 the aerosol detection requires wide FOV, which unfortunately is further bounded for a given altitude by the radial distortion. The field of view and the altitude are hence also settled. With the formulas introduced, in addition to the spatial resolution requirement, those parameters are enough for a preliminary estimation of all other variables. We will hereby consider a detector pixel of $10\mu m$, with an NA of $10°$, with the understanding that those parameters shall be reviewed in sake of the focusing analysis developed in Chapter 7. As discussed in 6.5 we further set an altitude of $h_s = 500km$ for exploiting at

most the advantages of a metasurface miniaturized device, which will result in a smaller optical system. We further consider that for acceptable image quality the distortion of the grid GSD_ρ/GSD_0 shall not exceed $\cong 2$ for the operating altitudes, which sets a FOV of roughly 80° by using the map in Figure 6.9b). The corresponding swath can be calculated by means of equation (6.6) which by means of the map 6.4b) and settles at $S_w \cong 866km$.
We'll further consider that the spatial resolution specified in the requirements, as defined in 6.1, is the spatial extent that can be reconstructed with full information over polarization and spectral content (GRE) over all the field of view. The relationships between a GRE and GSRE (sub-resolution element corresponding to one pixel reading in the imager) depends on the choice of arrangement performed in 6.7, and is hence a tradeoff between spatial and time resolution to consider. We conclude that the $GRE \cong GSRE$ for the imager downselected in 6.7, at the expense of a decreased time resolution and hypothesis of negligible time variance in the signal. Assuming for the most conservative GSRE the one depicted in equation (6.29) for the distorted edge of the detector and considering that the integration time is sized according to (6.30) as the nadir permanence time, we size a the pixel as:

$$l_p = \frac{1}{m_0}\left(\frac{GSRE}{1+\chi_s}\right)\left(\frac{GSD_0}{GSD_\rho}\right) \tag{6.31}$$

Equation (6.31) hence takes into account radial distortion and temporal sampling of the signal. Acknowledged that the realizable spatial resolution would also depend on the post-processing and sampling requirements not yet known, we will use formula (6.31) as a preliminary (conservative) estimation. It provides an estimation of the focal length for typical pixel sizes and spatial resolution requirement (with a few iterations of adjustment to also set the correct FOV to the constrained one). We notice in particular how for small altitudes, at equality of GSRE and l_p, the equation settles a smaller effective focal length which makes it realizable to have smaller instruments. The effective focal length is further constrained by the first-order relationship with the FOV and the detector size (6.14), which results in:

$$L_d = n_p l_p \cong 2 f_{eff} \sin(FOV/2) \tag{6.32}$$

Where n_p stands for the number of pixel in the (square) detector. Equation (6.32) is only a preliminary estimation to be corrected once the optical system is designed since the non-linearity of the transfer matrix used in the derivation is rather questionable for such big angles. A few iterations are hence necessary to select, with an integer realizable number of pixels, a configuration that has the correct FOV and meets the spatial resolution requirement. The effective focal length is further related to the entrance pupil aperture. Considering that the operating medium is air with a refractive index of $n_{air} \cong 1$ the effective focal length can be determined directly from the NA by means of the auxiliary equation (6.14) as:

$$f_{eff} = \frac{D_{ep}}{2\sin(NA)} \tag{6.33}$$

Which provides an estimate of the entrance pupil diameter for a given NA. Moreover, the D_{ep} shall not be confused with the (real) geometrical size of the entrance pupil, which is related by pupillary magnification factors depending on the realization of the optical system itself. The introduced value of NA in relation to the pixel shall also ensure that the diffraction spot is significantly smaller than the pixel itself (a formal diffraction solution will further provide more clarity on this sizing, in Chapter 7). For an operating wavelength of $1.1\mu m$, we can verify that the Rayleigh diffraction criteria at 83% threshold are met [26]:

$$l_p > \frac{2.44\lambda f_{eff}}{D_{ep}} = 7.73\mu m \tag{6.34}$$

with respect to what done in [1], we suggest sizing the pixel (not the whole polarized arrangement) above the theoretical limit calculated in (6.34). It will be seen in 7 that an oversizing is further required when considering the aberrations induced by the spectral filter due to its angle-dependence and such sizing will be retrieved for all spectral channels. Finally, we determine the number of spectral and angular bands. We require 5 angular bands to cover with enough time reconstruction accuracy the along-track spatial extent due to Figure 6.13. Selecting an arrangement with 2048 pixels in both directions with the retrieval of 3 Stokes parameters, that leads to $\cong$ 136 spectral distinct measurements that can be covered, which we will share in 6 spectral channels (3 for the VIS, 3 for the SWIR) in Chapter 5. It is important to consider that during Δt_{ob} the measurement for the same object point is carried out through

different observation angles θ_{in}, so the input Stokes parameters must not only be time-independent in the interval Δt_{ob} but also angular independent. Since the scattering does meet the last condition only within a certain angular range $\Delta\theta_{scatt}$, we can define an *angular reconstruction resolution* along with the spatial one and a condition of applicability of such reconstruction:

$$\Delta\theta_{rec(\Delta t_{ob})} \leq \Delta\theta_{scatt} \tag{6.35}$$

which must be verified once mission requirements are defined and more science case information is retrieved. Table 6.1 summarizes the input design variables.

Symbol	Description	Value	Unit
h_s	Altitude of the SSO orbiting satellite	500	km
NA	Numerical aperture, for $n_{air} \cong 1$ equal to the maximum focused half cone angle θ_{max}	$10(TBC)$	$degrees$
n_p	Number of pixels in a lateral dimension of the detector	2048	-
l_p	Edge size of the pixel	$10(TBC)$	μm
FOV	Field of View (diagonal)	81.9 (corrected for iteration)	$degrees$
GRE	Achieved ground resolution element (bounded to the maximum spatial resolution from requirement R.04) at FOV edge	960 (corrected for iteration)	m

Table 6.1: Design parameters (chosen as inputs for the sizing)

Table 6.2 summarizes the calculated performance variables discussed and further intermediary parameters.

Symbol	Description	Value	Unit
T_s	Orbital period of the satellite, $2\pi/\omega_s$	87'38"	$minutes, seconds$
$v_{gt,nadir}$	Ground velocity at nadir (corrected for Earth's rotation in the along track direction)	7643	m/s
t_{int}	Integration time, sized as the permanence time at nadir	41.8	ms
f_{eff}	Effective focal length of the system, sized from (6.31), (6.32)	1.56	cm
D_{ep}	Size of the entrance pupil aperture, size from (6.33)	5.4	mm
$f_\#$	F-Number of the configuration, f_{eff}/D_{ep} (only NA dependent)	2.88	
m_0	Magnification factor at nadir, h_s/f_{eff}	32×10^6	-
GSD_0	Ground sampling element at nadir	320	m
GRE_0	Achieved ground resoluton element at nadir	640	m
L_d	Size of the detector (edge)	2	cm
$t_{\lambda,res}$	Spectral time-resolution (assumed arrangement in Section 6.7 in addition to an un-polarized pixel), $4t_{int}$	167.2	ms
n_λ	Total number of spectral bands across all channels (assumed arrangement in Section 6.7)	136	-

Table 6.2: Computed parameters (calculated from design parameters)

An estimation of the SNR and the spectral resolution is still missing and will be the focus of the next Chapters. We further explicit that significantly higher GSD would be achievable. However, they are practically limited by the power budget and the diffraction limit at the maximum focusing angle for a given focal length, increase of which leads to bigger instruments. With respect to the parameters down-selected in [1], we selected a significantly higher NA of focusing due to power budget considerations, which will be seen to be acceptable in terms of aberrations in the analysis performed in Chapter 7 and achieves significantly smaller focusing spots. The high integration time will further be divided in frame dwelling times at the detector to avoid time-smearings and stability of the platforms concerns.

7

Metasurface Performance Results

In this Chapter, we applied the previously developed theory for estimation of the metasurface response, in various wavelengths regimes and configurations as requested from science requirements. Two case studies are at the heart of this analysis: the non-polarized pixel study, where only the spectral response is tweaked with use of circular inclusions, and the polarized pixel study, composed of an arrangement of three pixels for the reconstruction of the linear degree of polarization as discussed in Section 6.7. Moreover, the performance is initially analyzed both on the design wavelength of the mirrors and in other regions of the bandgap. Various bandgap designs are considered for the two case studies, relating to the overall required bandwidth of the instrument concept. The various transmissivities introduced (wide pixel transmissivity, spectral band transmissivity, finite transmissivity) are all depicted, as well as enclosed energy plots and OTF of the various solutions. The polarization dependence of the non-polarized pixel case is analyzed and the condition number of the polarized arrangement also calculated. Finally, plots of the PSFs as calculated with the wide-pixel diffraction theory are plotted from the Zernike transforms hereby operated.
The analysis, either if rather involved, allows extrapolating high-level performance parameters from the detailed electromagnetic modeling. The finite band transmission $\overleftrightarrow{\tau}^{\infty}$ calculated with the diffraction modeling, together with his normalization radiometric bandwidth $\Delta\lambda$, provides an estimation of the transmitted energy as a function of the polarization, NA and pixel size. The finite spectral focal transmissivity $\overleftrightarrow{\tau}_{\lambda}$ describes the spectral response under focal illumination including also diffraction effects, from which the FWHM as a function of the NA can be extrapolated. In the final part of the Chapter, we consider various possible filtering techniques to overcome the bandwidth limitation present in the design reported in [1]. We down-select one of the filtering techniques and re-optimize the design of all the filters to provide the correct attenuation and FWHM for the desired ranges, performing some trade-offs in the performance of the various parameters.

7.1. Bandgaps designs

To cover the spectral required bandwidth, we use six DBR designs. Unfortunately, it seems not possible to use less than six DBR pairs to cover the desired bandwidth[1]. We expect the six DBR designs to be integrated together, in the along-track direction for all angular bands discussed in 6.7, as in Figure 7.2. The proposed integration of patches of DBRs is less cumbersome than changing the property sizes across each pixel, since by using $n_{bandgap}$ peaks to sample a single bandgap, we required this integration only every each $3n_{bandgap}$ pixels, so over several hundreds of microns rather than very small sizes. In fact, integration of different spectral pixels is widely used in silicon technology in monitors and other similar off-the-shelf technology. We hence assume it is possible from a manufacturing perspective. We, however, use TiO_2, SiO_2 as mirror materials in all DBR patches, in order to limit the manufacturing complexity of integrating different patches together and all compatibility of materials concerns. The inclusion material $aSi:H$ is strongly lossy in the visible spectrum (see Figure 7.1), which resulted in complete loss of peaks in the cavity. Hence, TiO_2 is used as inclusion material in the visible spectrum. This choice comes with the undesired effect that the achievable permittivity contrast is smaller than desired, but this effect can be partly counteracted by properly choosing the cavity heigh, a higher resonance mode and an opportune filtering technique. We shall also clarify that for the visible range, manufacturing may

[1] solutions may be found with wider bandgaps by using arbitrary mirrors dimensions or using more unconventional solutions. The transmission behavior of those solutions has however been observed to possess many resonances peaks in the resonances curves and can't be currently used

be more cumbersome since involved dimensions are smaller and use of TiO_2, a material which treatment may result in additional contaminations during the deposition.
The wavelength of the mirror's design for six DBRs (e.g. the wavelengths λ_{mir} in above relationships) are all selected to be a quarter wavelength in the medium (more precisely, the closest manufacturable value within $1nm$), so that a conventional DBR design is used with only a minimal detuning. All stack are interfacing with air with means of the SiO_2 mirror and cavity is defined in between the TiO_2 layers (see Section 5.3.5). The number of mirrors is preliminarily selected between $4-6$ (depending on DBR, increasing for the infrared channels) for both bottom and top stack, to be reviewed once the power budget is completed. The number of mirrors choice required a trade-off between spectral resolution and overall transmittance peak, since to a higher number of mirrors a higher loss is associated due to the SiO_2 loss present in 7.1. Using the criteria to have all spectrums above $\mathcal{T} > 60\%$ the number of mirrors has been selected accordingly. Spectrum dependent losses and dispersions of materials have been included in those results for all materials from available datasheets, which uses the refractive indices plotted in Figure 7.1 representative of thin-layers as reported here. Temperature dependence of those refractive indices is unknown, but we conducted a simplified thermal sensitive analysis in Chapter IV. The included loss of SiO_2 is also consistent with experimentally determined losses in the bare cavity as discussed in Chapter 8. Even though DBR3 design was initially selected to use $aSi : H$ as inclusion material, the latter resulted in $\cong 20\%$ peak loss due to its high loss in the high-visible region, so this choice has been disregarded. The cavity resonances curves of those 6 DBR designs are presented in Figures 7.3. It is further stressed that those cavity resonances do depend on the cavity size chosen, the resonance curves in the quiet region shifting and changing slope with the choice of the latter. The cavity size has been chosen such to use the lower resonance mode possible, which maximizes the usable bandwidth for a given permittivity contrast, having the smaller possible slope. As clear from the Table and the figures, the available bandwidth to achieve transmission peaks by a change of permittivity contrast are more limited than the bandgap of the mirrors. If the cavity size is chosen properly, those are always limited by the presence of higher-order modes in the cavity. Their location can be changed within the DBR bandgap by choosing a different cavity size. Other methods include the use of dispersive materials (to modify the intercept with the resonances curves) and the use of particular solutions with detuned DBRs. The FWHM and the peak transmission are dependent on the permittivity and spectrum location of interest, as clear from the resonance curves. The proposed DBRs design is roughly covering the spectral channels required in Table 3.1. Successive iterations of the DBRs design shall be implemented upon clarification of those science requirements. In particular, some degree of freedom is available in the choice of the length of the cavity to move the Usable Bandwidth within the DBR bandgap. If the requested permittivity contrast in the DBR3, for example, is too high for the possible use of inclusions, the cavity can be made higher to decrease the slope of the resonant curves. It is also suggested to keep the height of the cavity above a minimum with respect to the height of the inclusions, to avoid coupling of higher scattering modes in the multilayer (which effects is still unknown). We could use relation (5.55) to size the inclusion for a given known wavelength, easily done from the inspection of the resonances curves and the knowledge of a permittivity model. We consider that the whole region of coverage between the permittivity of inclusion and matrix material can be achieved, even if in reality the volume filling factor will not be unitary to limit interaction between too big resonators. It has been observed both in [4], FEM results and experimental results in Chapter 8 that the stationary model underestimates the effective permittivities and values greater than the inclusions maximum are in reality achievable also for $c < 1$, which makes our assumption sound.
Since providing such values and analysis for the thousands of pixels in the arrangement seems excessive and those are either way preliminary, we do not report explicitly the chosen dimensions. We, however, mention that with the given spectral resolution we may fit a dozen measurements for each spectral channel. The choice depends also on the available number of pixels in commercial detectors. The overall total length of the filters is changing significantly from DBR to DBR. Border effects close to the borders of the two patches shall be analyzed and minimized in successive iterations design.
In the next Sections, we further performed a study case on two examples pixels and polarized arrangements in DBR4. The performance of other pixels, even though shall be exactly described separately in more detailed designs, is qualitatively similar. A further small note on spectral filtering is required for clarity: in [1] it has been mentioned that the usable channel bandwidth is limited by the contrast in anisotropy permittivity of the pixel. That is the case if a conventional non-resonating particle is considered and, by inspection of the stationary model (valid in first approximation) we also conclude

that the usable bandwidth would be smaller than the one reported in Table 7.1. For example, for pixels in DBR5, the maximum permittivity contrast has been demonstrated in [4] with FEM analysis to be associated with a separation of $\Delta\lambda = 127nm$ at most, slightly higher for use of a grating. There are however possibilities to undercome this limitation, which we will down-select and analyze in detail in Section 7.4. In either case, a filtering solution is always required outside of the bandgaps regions with a wideband filter, for each one of the DBRs patches, in each angular band, separately. If integration of those bandpass filters is performed on the multilayer, the reflection coupling of such shall be correctly taken into account.

a) Refractive indeces and loss of aSi:H

b) Complex refractive indeces of SiO_2, TiO_2

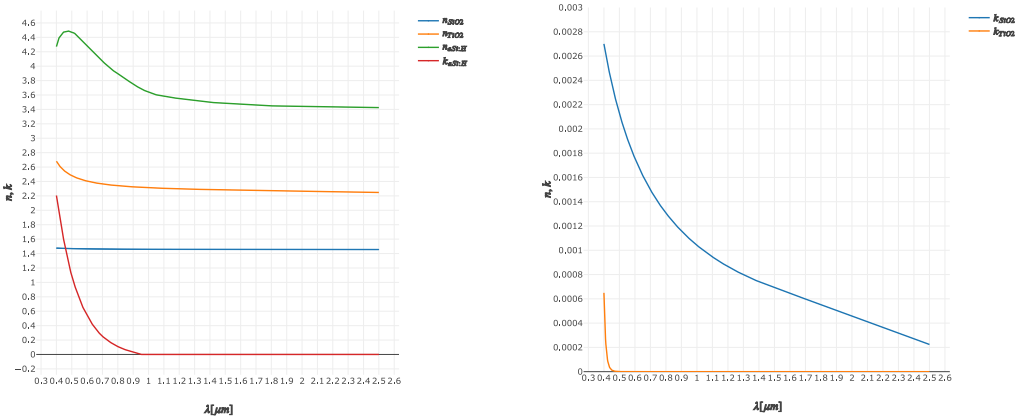

Figure 7.1: a) Plot of the real refractive index of all materials and imaginary refractive index of $aSi:H$ in the spectrum b) Plot of imaginary refractive index of TiO_2 and SiO_2 in the wavelengths of interest.

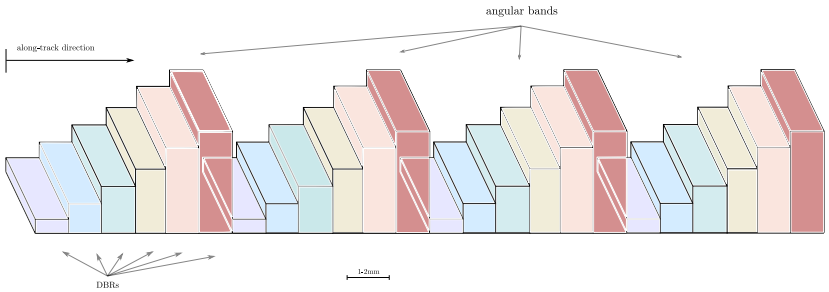

Figure 7.2: Proposed multi-DBR integration concept. For reference, each DBR would contain a few dozens of pixels. Some spacers between angular bands may also be required to avoid light shadowing and vignetting effects.

DBR	Usable Channel $B_\lambda[nm]$	$lSiO_2[nm]$	$lTiO_2[nm]$	$l_{cav}[nm]$	Total Length $[\mu m]$	Bangap of DBRs $\Delta\lambda[nm]$	FWHM [nm]* ($\theta = 0$) *varying in ϵ_{cav}	Inclusion Material	Number of Mirrors	m resonance	Achieved Transmissivity Peak $\mathcal{T}^*_{max}$ (at normal incidence) *varying in ϵ_{cav}	Extinction
1	Visible $[0.44 \text{ to } 0.54]\mu m$	85	50	272	1.352	200 (from 400 to 600)	from 5 to 8	TiO_2	4 (to limit losses)	Second	from 0.62 to 0.79	[0.2, 2] %
2	Visible $[0.64 \text{ to } 0.78]\mu m$	111	68	444	1.876	280 (from 540 to 820)	from 10 to 16	TiO_2	4 (to limit losses)	Second	from 0.75 to 0.88	[0.5, 3]%
3	Visible $[0.83 \text{ to } 0.98]\mu m$	146	91	274	2.644	360 (from 700 to 1060)	from 7 to 10	TiO_2	5	First	from 0.72 to 0.92	[0.2, 4]%
4	Infrared $[0.98 \text{ to } 1.180]\mu m$	171	108	325	3.673	380 (from 840 to 1220)	from 3 to 7	$aSi:H$	6	First	from 0.60 to 0.90	[0.06, 2]%
5	Infrared $[1.36 \text{ to } 1.60]\mu m$	240	153	445	5.161	600 (from 1150 to 1750)	from 5 to 9	$aSi:H$	6	First	from 0.67 to 0.9	[0.06,2]%
6	Infrared $[1.9 \text{ to } 2.2]\mu m$	326	209	635	7.055	750 (from 1600 to 2350)	from 7 to 12	$aSi:H$	6	First	from 0.76 to 0.96	[0.09,3]%

Table 7.1: Downselected DBRs design for covering spectral channels required from science requirements

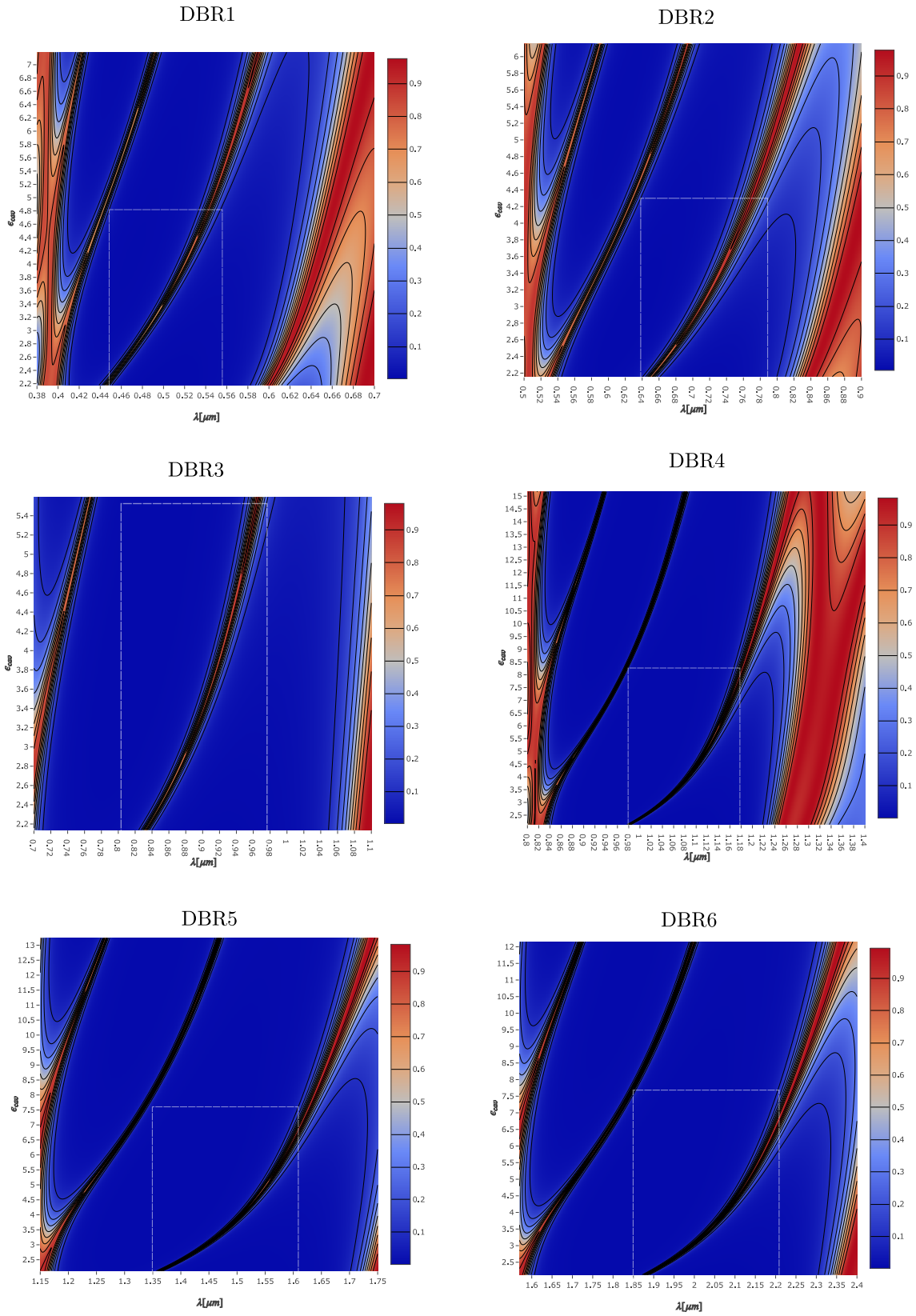

Figure 7.3: Resonances curves of all DBRs designs in Table 7.1. The Usable Channel Bandwidth is also represented in white. The values of permittivities cavities represented are in the range of the matrix-inclusion materials.

7.2. Case Study: Non-Polarized Pixel

We hereby performed a more detailed study of the response of not-polarized pixels. This analysis is motivated by required information of polarization dependence, focused transmission spectrums determination and precise peak localization.

For a non-polarized filter, we would like to avoid any polarization dependence of the filter. We must hence use an inclusion with a unitary aspect ratio. If polarization measurement is not explicitly required (as per some channels in Table 3.1) it is preferred not to use the reconstruction method with three independent pixels in order to avoid conditioning the signal to noise and filtering part of the polarized light in the process. Moreover, we also may envision a solution in which this additional pixel is used for calibration and further noise reduction of the polarized arrangement. With the imager arrangement proposed in Section 6.7, non-polarized pixels can simply be added in the along-track directions as separate spectral channels with no additional burden in the integration on the detector, as far as the cavity and mirrors are kept at the same height-dimensions.

For this case study, we consider a pixel of DBR4 sizes to provide a peak at $\lambda_{peak} \cong 1.1\mu m$, as merely an illustration. The input material properties are the same as represented in Figure 7.1. The required cavity permittivities for such peak, according to the resonances curves, are $\epsilon_x = \epsilon_y \cong 4.58$. If the stationary model is used in a first approximation to size the particles, we may achieve those required permittivities with a volume filling factor of $c \cong 46\%$ (for example, a circular particle of diameter $D_x = D_y = 320nm$ and height $h_i = 200nm$, with fits in the resonant cavity of this DBR). The corresponding off-angular permittivity of this solution would be[2] $\epsilon_z \cong 7.34$. In general, in fact, even with a unitary aspect ratio, the cavity will still be anisotropic in the yz, xz planes due to the geometry of the inclusion.

We hereby analyze all performance parameters defined in Section 5.3.4 for this pixel.

7.2.1. Plane-Wave Transmissions

Due to the unit aspect ratio, the structure is clearly axial-symmetric. No ϕ dependence is hence expected in the $p-s$ frame transmission coefficients. Moreover, no couplings will be present between the transmission, for which $\tau_{ps}^{(m)} = \tau_{sp}^{(m)} = 0$. In general, an azimuthal dependence will be present in the xy frame (known analytically) due to the $p-s$ frame transformation. Due to the fact that p and s polarizations are still subject to different transmissions spectrums upon not-normal incidence, polarization dependence (undesired here) will be present. The transmissions in the $p-s$ frame of this structure is represented in Figure 7.4 for a plane-wave excitation, as calculated with the formal multilayer solution for data in Table 7.1. Such a Figure shows the transmission in the polar angle and the spectrum and clarifies the fact that the two polarization shift apart differently at incidence inclination. The p polarization may precede or succeed the s polarization, depending on the region of interest in the resonances curves. The FWHM of the latter is in general shorter unless losses are high. s polarization is more affected by the presence of a loss, as we also have experimentally shown in Section 8.4. The complex plane plot in Figure 7.4 provides information on the aberrations. It is seen that the two transmissions are slightly out of phase for a given wavelength and angle and the maximum transmission possesses a phase of $\cong -\pi/2$, typical of a resonance regime. A similar plot would hold for the spectral envelope (Section a) in the complex plane, which would be important in case of spectrally coherent light).

The Jones matrix of this arrangement is given by Equation (E.2) in Appendix E. The associated plane-wave Mueller Matrix first-row is then given by:

$$\mathbf{M}_0^T = \frac{1}{2}\begin{pmatrix} \tau_{pp}\tau_{pp}^* \cos\theta^2 + \tau_{ss}\tau_{ss}^* \\ (\tau_{pp}\tau_{pp}^* \cos\theta^2 - \tau_{ss}\tau_{ss}^*)\cos(2\phi) \\ (\tau_{pp}\tau_{pp}^* \cos\theta^2 - \tau_{ss}\tau_{ss}^*)\sin(2\phi) \\ 0 \end{pmatrix} \tag{7.1}$$

When an azimuthal variation in the input Stokes will be present (e.g. due to aberrations, non-telecentricity, real distribution) some polarization dependence will be observed. The real focal integrated spectral intensity across the whole focal plane is in fact given by Equation (5.38). The quantity $(\tau_{pp}\tau_{pp}^* \cos\theta^2 - \tau_{ss}\tau_{ss}^*)$ which appears in that integration is plotted in Figure 7.5 and provides a good indication on the polarization sensitivity of this pixel, which is NA and spectral dependent. It is further stronger when the spectral

[2] the estimation of this value is rather uncertain and heavily influences the angular spectral drifts of the results. In the stationary model, in fact, inclusions with the same volume but different height would possess the same ϵ_z, which is unlikely for the real structure. We suggest more refined retrieval in future work.

variation of the input field is not negligible. No figure can be given for polarization sensitivity of this arrangement until a clear distribution of the field is known by ray-tracing. Since the polarization sensitivity depends strongly on the spectral shift between the two polarization, we conclude that it is maximum for the pixels on the left of the resonances curves (where s polarization precedes the p polarization) and the ones on the right of the resonances curves (where the p polarization precedes the s polarization). The pixels for which the cavity is in matching resonances with the mirrors, do not present significant polarization dependence. Even if the whole focused energy is polarization independent, when including the finiteness of the pixel into consideration the integrated energy may be polarization dependent, to which we refer to the PSF calculation in the next Sections.

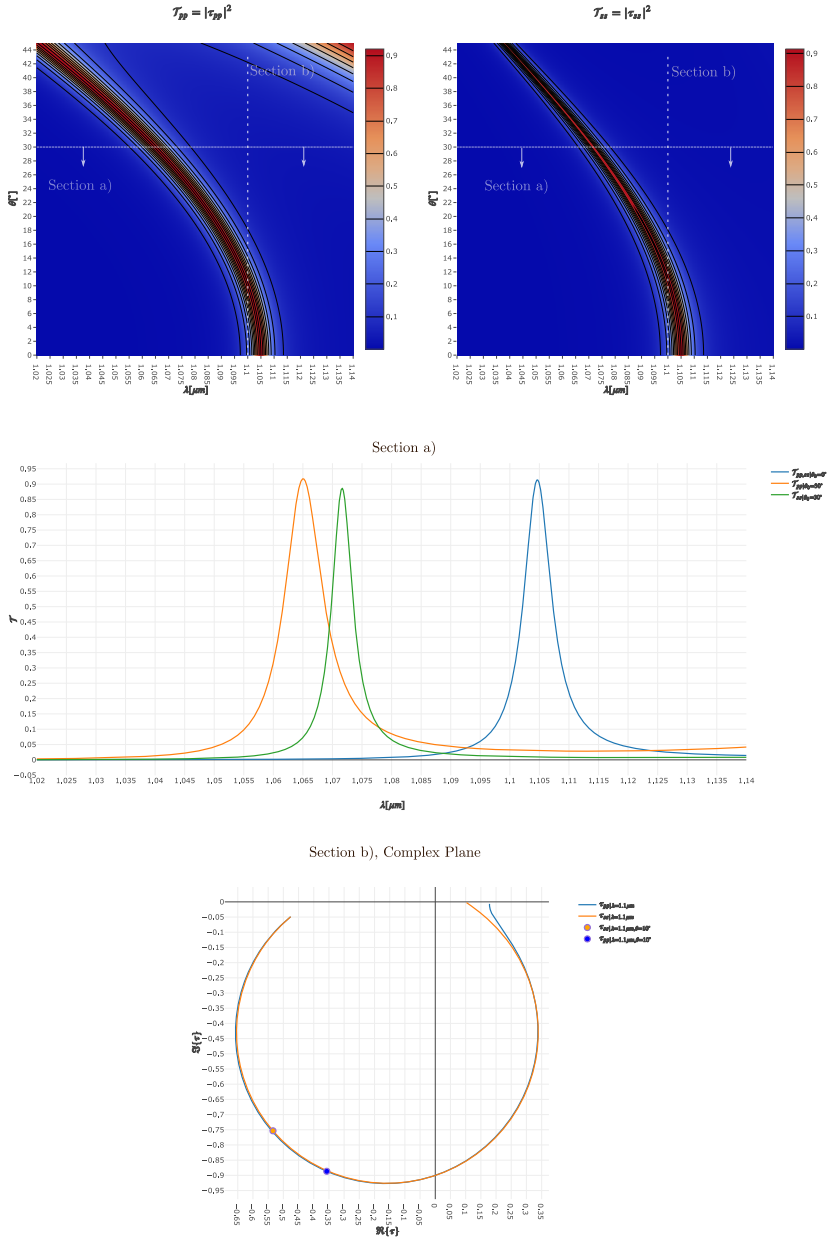

Figure 7.4: Top) Intensity transmission spectrum over an angle, in colour-plot for the p polarization (left) and the s polarization (right). Center) Intensity transmission spectrums in line-plots for normal angle and at $\theta = 30°$ for the two polarizations Bottom) Plot in the complex plane of the amplitude transmission at $\lambda = 1.1\mu m$ for an angle envelope. Point representation of two points at same wavelength and angle of $\theta = 10°$.

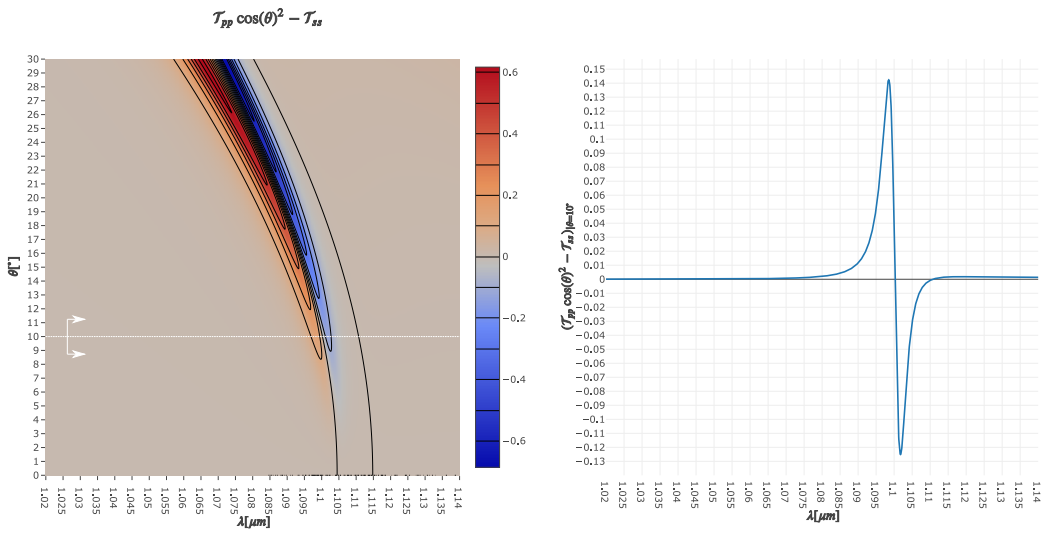

Figure 7.5: Left) Polarization dependence plane-wave transmissivity factor in the polar angle. Right) Spectrum of the same quantity for an angle of $\theta = 10°$

7.2.2. Wide-Pixel Focal Transmission

The wide-pixel transmission of this pixel, defined as in Equation (5.43) upon uniform field illumination, is hence given by only one term, as we conclude after the known azimuthal integration:

$$\overleftrightarrow{\tau}^{\infty}_{(\lambda,\hat{\mathbf{s}})} = [M_{00(\lambda)}, 0, 0] \tag{7.2}$$

where:

$$M_{00(\lambda)} = \alpha_{(\theta_{max})} \int_0^1 \left(\frac{\tau_{pp}\tau^*_{pp}\cos\theta^2 + \tau_{ss}\tau^*_{ss}}{\cos\theta} \right)_{|\theta=\arcsin(\xi\sin\theta_{max})} \xi d\xi \tag{7.3}$$

The $M_{00(\lambda)}$ coefficient of the wide-pixel transmission is represented in Figures 7.6a), and 7.6c) for various angles. It can be regarded as a scalar spectral transmission for this design pixel. Due to polar integration of the angle-dependent spectrum, $M_{00(\lambda)}$ presents a widening of the FWHM with increasing NAs. Due to solid angle normalization (formally proven in Section 5.3.4) the spectral transmission further decreases with increasing NAs. The peak transmission over NAs is plotted in Figure 7.6b) and so is the FWHM over the NAs, referred to the corresponding NAs spectral peak maxima. According to the plots, the FWHM increase strongly above $\theta_{max} > 10°$ and also the spectral peak shifts considerably. It follows that not to penalize spectral resolution an $NA < 10°$ shall be used.
The radiometric energy content of such spectrum is subject hence to an increase due to the FWHM widening and to a decrease due to solid angle normalization and radiometric apodization. The band transmission for $\Delta\lambda = 8nm$, as defined in Section 5.3.4, is represented in Figure 7.7. The plot there presented suggests that the latter effect of normalization is predominant, but only slightly. The overall finite band transmission decades, according to our results, with $\cong \cos\theta^2_{max}$, similarly to our idealized apodized bandpass filter. This result is however strongly dependent on the assumed shape of the principal surface upon which integration is carried out (according to Section 5.3.4) and on the optical apodizations in the system, which are not yet fully known and have respectively been assumed quasi-planar and ideal for calculation purposes. In fact, an apodization is expected also for an ideal bandpass filter according to our model, which is also represented in dotted lines in both 7.7 and in 7.6b). We conclude then that the transmittance under focused illumination is not particularly affected by the angle behavior and is rather ideal, provided the correct normalization value for the radiometric bandwidth $\Delta\lambda$ is used. The angle behavior, however, influences the FWHM and the spectral peak location as depicted in Figure 7.6 much more significantly, as also the general shape of the transmission spectrum.

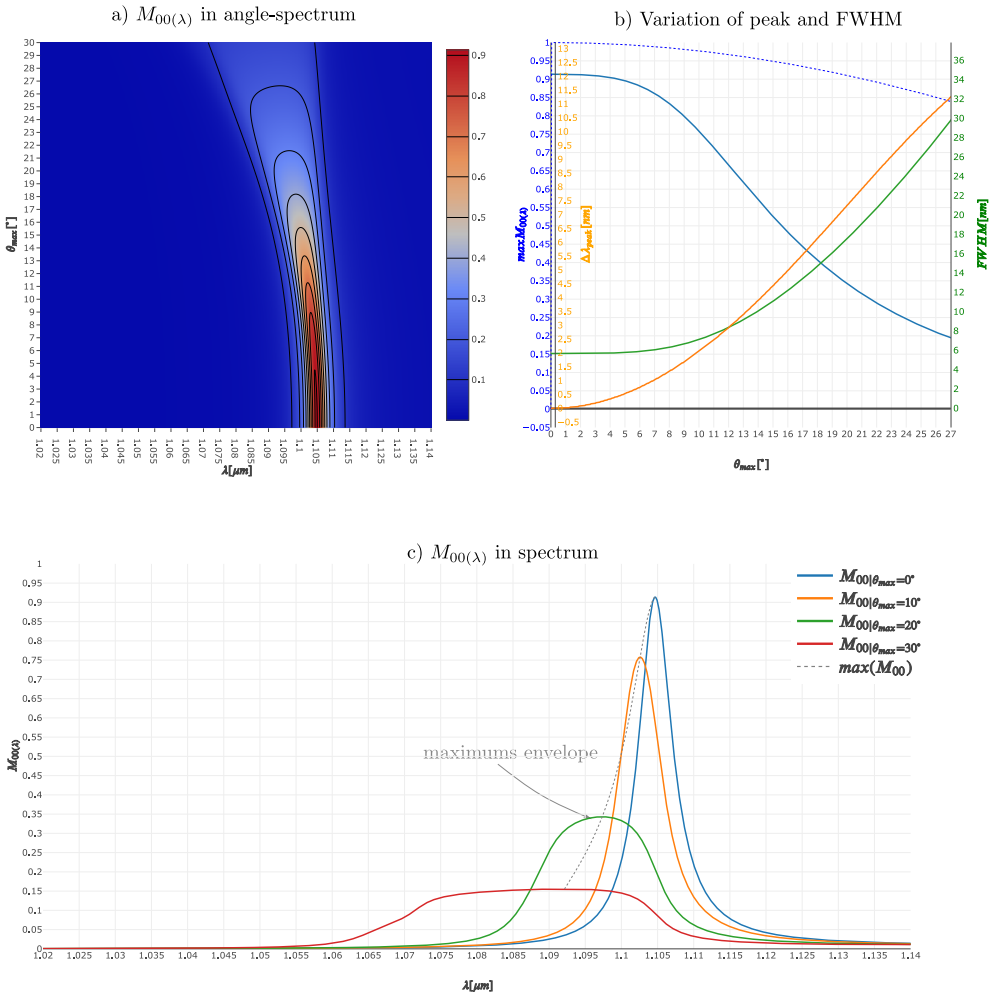

Figure 7.6: a) Contour plot of the spectral focused transmissivity in the spectrum for the various NA of focusing b) Variation of the peaks transmission, peak shift and FWHM in relation to the half-cone angle. Also ideal filter apodization is presented for comparison c) Spectral focused transmissivity for angles of $\theta_{max} = 0°, 10°, 20°, 30°$ and location of maximas.

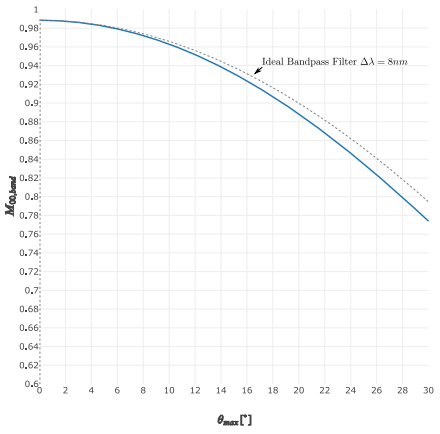

Figure 7.7: Band transmission integrated over the wavelengths. The ideal apodized filter transmission is also represented for comparison

7.2.3. Focal Fields

The focal fields may be found with use of the Zernike Expansion introduced in Section 5.3.7. In case of non-polarized pixel, uniform field and idealized optics, the azimuthal transform appearing in (5.62) in particular is already known (see Equation (E.2)) and given by Zernike transform of three scalar functions:

$$t_0 = \frac{(\tau_{pp}\cos\theta + \tau_{ss})}{2\cos\theta} \qquad t_1 = \frac{(\tau_{pp}\sin\theta)}{2\cos\theta} \qquad t_2 = \frac{(\tau_{pp}\cos\theta - \tau_{ss})}{4\cos\theta} \tag{7.4}$$

for the proof of which we refer to concepts in the Appendix E. The introduced hypothesis may easily be relaxed at the knowledge of the optical transformation.

The transforms $\mathcal{Z}^{[q=i,s]}_{\{t_i\}} = \mathcal{Z}^{[s]}_i$ of the scalar functions appearing in the above can be calculated through Equation (5.62) and the Zernike transform routine depicted in Appendix D. The expansion coefficients module of such expansion are represented in Figure 7.9, where transform has been carried through $n_{splines} = 40$ radial splines, truncated at $s_{max} = 30$, with an estimated maximum truncation error of $\epsilon_{error} < 4 \times 10^{-8}$ across the grid, increasing towards higher NAs. We have also verified that the required smoothness criterias close to the origin, discussed in Appendix D apply for such transform. The square modulus of the mode $[0, 0]$ can be in particular seen to be different than the focal transmissivity above defined, which contains the energy over all modes. The presence of a minimum in the spectrum of such distribution for higher NAs is due to destructive interference between p and s polarization, possessing different phase. The remaining energy is contained in all the higher modes, so that it is not lost but only redistributed to wider regions in the detector plane. The non-dimensional focal fields associated with such decomposition are given, after some rewriting of the known azimuthal terms which we time-save the reader, by the formula:

$$\mathbf{e}_{f|\Sigma_0} = kf\sin^2\theta_{max} e^{-ikf}\left\{\sum_s \begin{bmatrix} \mathcal{Z}^{[s]}_0 + 2\mathcal{Z}^{[s]}_2\cos(2\alpha) & -2\mathcal{Z}^{[s]}_2\sin(2\alpha) \\ -2\mathcal{Z}^{[s]}_2\sin(2\alpha) & \mathcal{Z}^{[s]}_0 - 2\mathcal{Z}^{[s]}_2\cos(2\alpha) \\ -2\mathcal{Z}^{[s]}_1\cos(\alpha) & 2\mathcal{Z}^{[s]}_1\sin(\alpha) \end{bmatrix} i^{s+1}\left(\frac{J_{s+1(\tilde{\rho})}}{\tilde{\rho}}\right)\right\}\bar{\mathbf{e}}^{[\xi,\eta]}_{in} \tag{7.5}$$

The focal fields for uniformly x polarized input field are represented in Figure 7.8, for a wavelength of $1.098\mu m$ associated with the spectral peak at $\theta_{max} = 20°$. Due to the shape of Equation (7.5) the focal fields for other polarization angles illumination are found by simple rotations of those distributions. We observe that the field is elliptical with a wider axis in the direction of polarization, as widely known on focusing of polarized light. With respect to the idealized polarized focusing depicted in [61] the present distributions present sharper features radially, due to presence of higher Zernike modes associated with aberrations. As better seen in the next section, also sharper features in the spectrum and angle are present. A small cross-polarization is always present and observed in those results. That's due to the Maltese effect already depicted in Section 5.2. Such cross-polarization is an increasing function of the NA and is related to the spectrum in image 7.5. A similar expression would hold for the magnetic fields in other transform functions, which can be determined with the same methods but we do not report for succinctness.

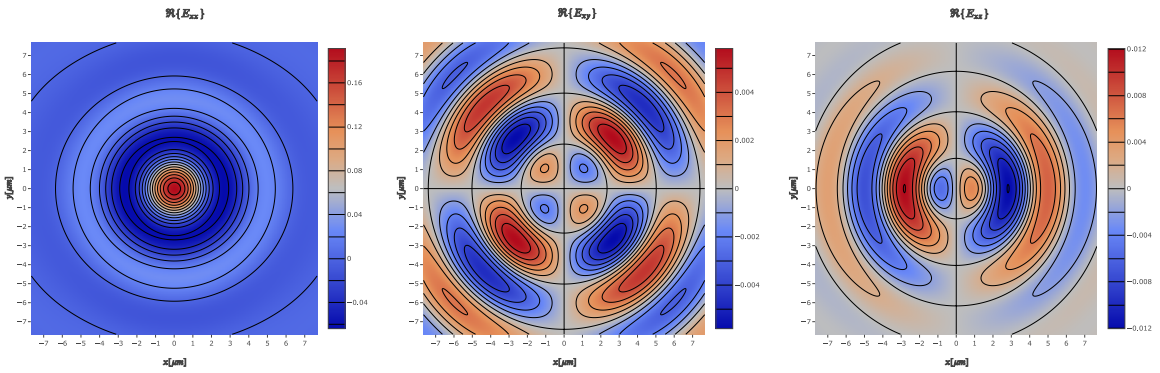

Figure 7.8: Focal fields, from left to right, of x, y, z components respectively, upon uniform illumination of x polarized input light, for a wavelength of $\lambda = 1.098\mu m$ and an $NA = 20°$, chosen to be the peak wavelength at the given NA respectively. The scale bars are associated with the value of the normalized scaled field $\mathbf{e}_{f|\Sigma_0}/(kf\sin^2\theta_{max})$. Dimensional units may be found in accordance to scaling factors in Equation 5.3 in relation to the spectral radiance.

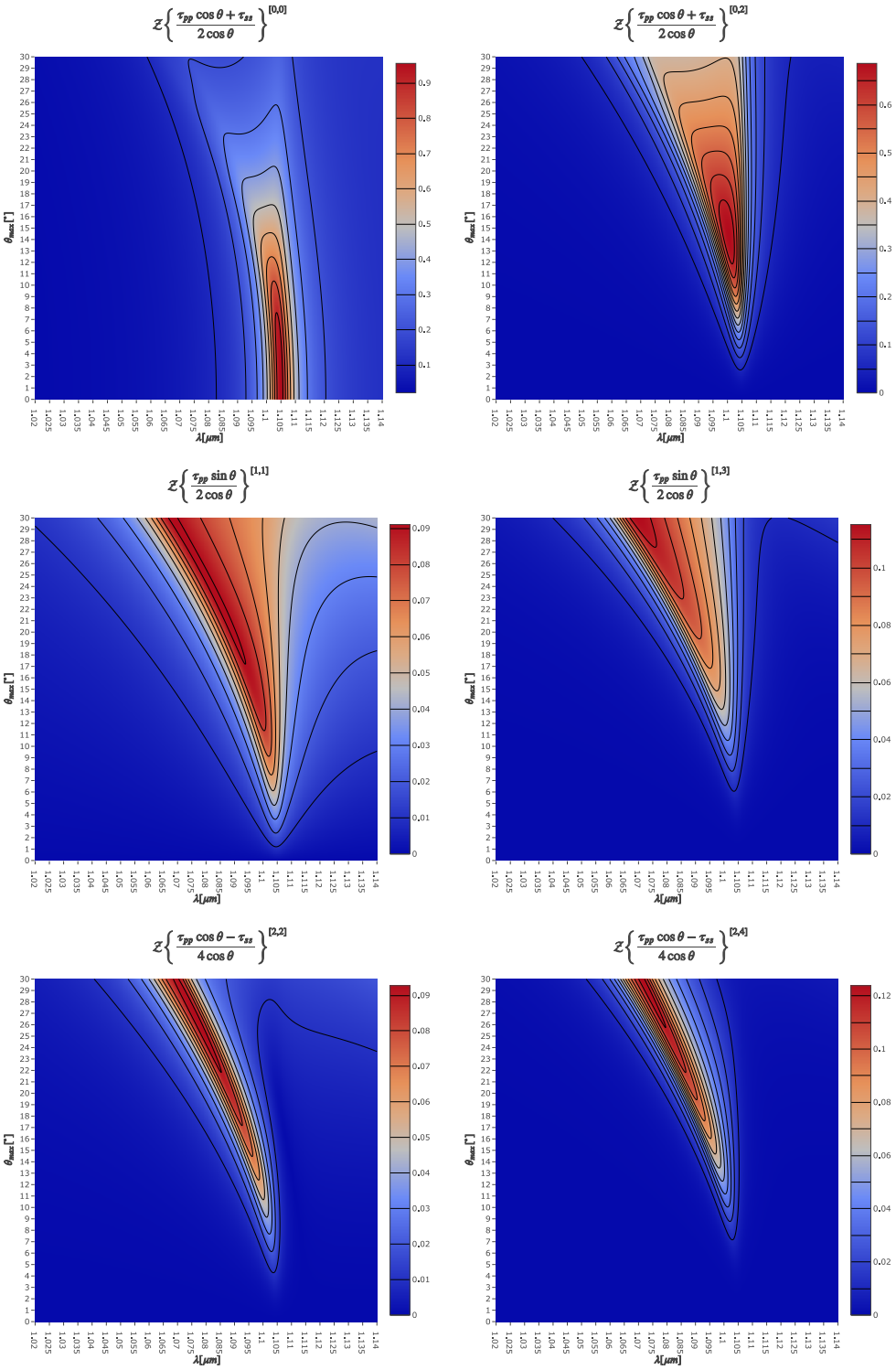

Figure 7.9: Zernike expansions module of the scalar functions appearing in the Jones matrix of the device, for the three function (vertically) and two modes (horizontally). Higher order modes are qualitatively similar, stable, and increasing towards higher NAs

7.2.4. PSFs

With an opportune rewriting, we also determined the expression of the Mueller rows appearing in Equation (5.64). The non-dimensional transverse spectral PSF (defined in Section 5.3.7) is hence given by:

$$\langle \mathbf{e}_{f|\Sigma_0} \mathbf{e}^{\dagger}_{f|\Sigma_0} \rangle = k^2 f^2 \sin^4 \theta_{max} \left\{ \sum_{s_1,s_2} \begin{bmatrix} \mathcal{Z}_0^{[s_1]} \overline{\mathcal{Z}_0^{[s_2]}} + 4\mathcal{Z}_2^{[s_1]} \overline{\mathcal{Z}_2^{[s_2]}} \\ 2\left(\mathcal{Z}_0^{[s_1]} \overline{\mathcal{Z}_2^{[s_2]}} + \mathcal{Z}_2^{[s_1]} \overline{\mathcal{Z}_0^{[s_2]}} \right) \cos(2\alpha) \\ -2\left(\mathcal{Z}_0^{[s_1]} \overline{\mathcal{Z}_2^{[s_2]}} + \mathcal{Z}_2^{[s_1]} \overline{\mathcal{Z}_0^{[s_2]}} \right) \sin(2\alpha) \\ 0 \end{bmatrix}^T \left(\frac{J_{s_1+1(\tilde{\rho})} J_{s_2+1(\tilde{\rho})}}{\tilde{\rho}^2} \right) \right\} \mathbf{s}_{in} \tag{7.6}$$

Note that the contribution for $s_1 = s_2 = 0$ is an Airy distribution and the PSF is always real valued. The PSF under consideration is elliptically shaped when the input field is polarized, as ideal polarized focusing reported in [28]. We'll however see in the study of polarized pixels that this result is applicable only for circular inclusions.

The given PSF is also polarization dependent (which is consistent with our treatment in Section 7.2.1, where coupled diffraction pupil was not yet taken into account), rotating with the angle of polarization. That would result in a small polarization dependence of the finite pixel measurement, dependent on $\left(\mathcal{Z}_0^{[s_1]} \overline{\mathcal{Z}_2^{[s_2]}} + \mathcal{Z}_2^{[s_1]} \overline{\mathcal{Z}_0^{[s_2]}} \right)$.The latter is a negligible quantity for small NAs but it turns out to possess very sharp spectral features and be, in general, also two orders of magnitude greater than what predicted in [28] for an ideal filter, due to the different spectral shifts of p, s polarizations.

The main importance aspect related to the PSF under consideration is its width, which can be seen to be a strongly wavelength dependent function. For illustration of this concept, consider Figure 7.10 where the PSFs of two different wavelengths (at $\cong 20nm$ difference) and at the same NA are plotted, together with the plane-wave transmittance, and Figure 7.11 where the distribution is plotted in the radial direction. For illustration purposes, the PSF associated with not-polarized input light M_0 is logarithmcally scaled. The polarization contribution appearing in Equation (7.6) are also represented in the same figure. The wavelengths are chosen to represent the peak wavelength at $\theta_{max} = 20°$ and the peak wavelength at normal angle, respectively but the simulation NA is kept the same. The plots in Figure 7.11 are further normalized on the local transmissivity values at the given NA and wavelength of consideration, since focused of those plots are on the spatial distribution rather than on the transmissivity value (discussed in Section 7.2.5). For this reason, the non-dimensional variable $k\rho_f \sin\theta_{max}$ (appearing in the classical Airy disk diffraction solution, also represented in dotted lines) is used in the plots of Figure 7.11.

To understand the above results, one shall consider the shape of the plane-wave transmission spectrum in both polarization and in particular their phase. Refer to $\lambda_0 = 1.104\mu m$ as the peak wavelength at normal incidence for sake of this discussion and $\lambda_{min} \cong 1.078\mu m$ as the smaller wavelength over which the amplitude transmittance starts decaying again. For a given wavelength, only a small portion of cone angle is focused by the device; departing from the normal for $\lambda_{min} < \lambda < \lambda_0$, this portion of cone angle is more aberrated than the ones for $\lambda \cong \lambda_0$, if in the active transmission region. The aberrations are in fact dependent on the scalar quantities depicted in Equations (7.4) so on the difference between spectral adrift of the two polarizations. If the transmission module is instead low (as for $\lambda < \lambda_{min}$) over the whole integration range, the cone angle is not highly aberrated and the spot size similar to the ideal one again. The increase of NA naturally leads to increase of spot size also, as seen from 7.11a). Once again, above $\theta_{max} > 10°$ those effects are limiting the diffraction performance of the device. Those artifacts, which we would in great part observe also in conventional DBRs designs without any inclusion, are intrinsically due to the narrow angle-dependence of the device and shall be taken into account in the pixel sizing. To do so, we make use of the finite transmittance, analyzed in Section 7.2.5. We, however, point out that the choice of a different cavity permittivity heavily influences those results, modifying the spectral content of the functions (7.4). Hence, different pixels shall be analyzed separately in terms of diffraction behavior. We will do so in the final optimized design in Section 7.5.

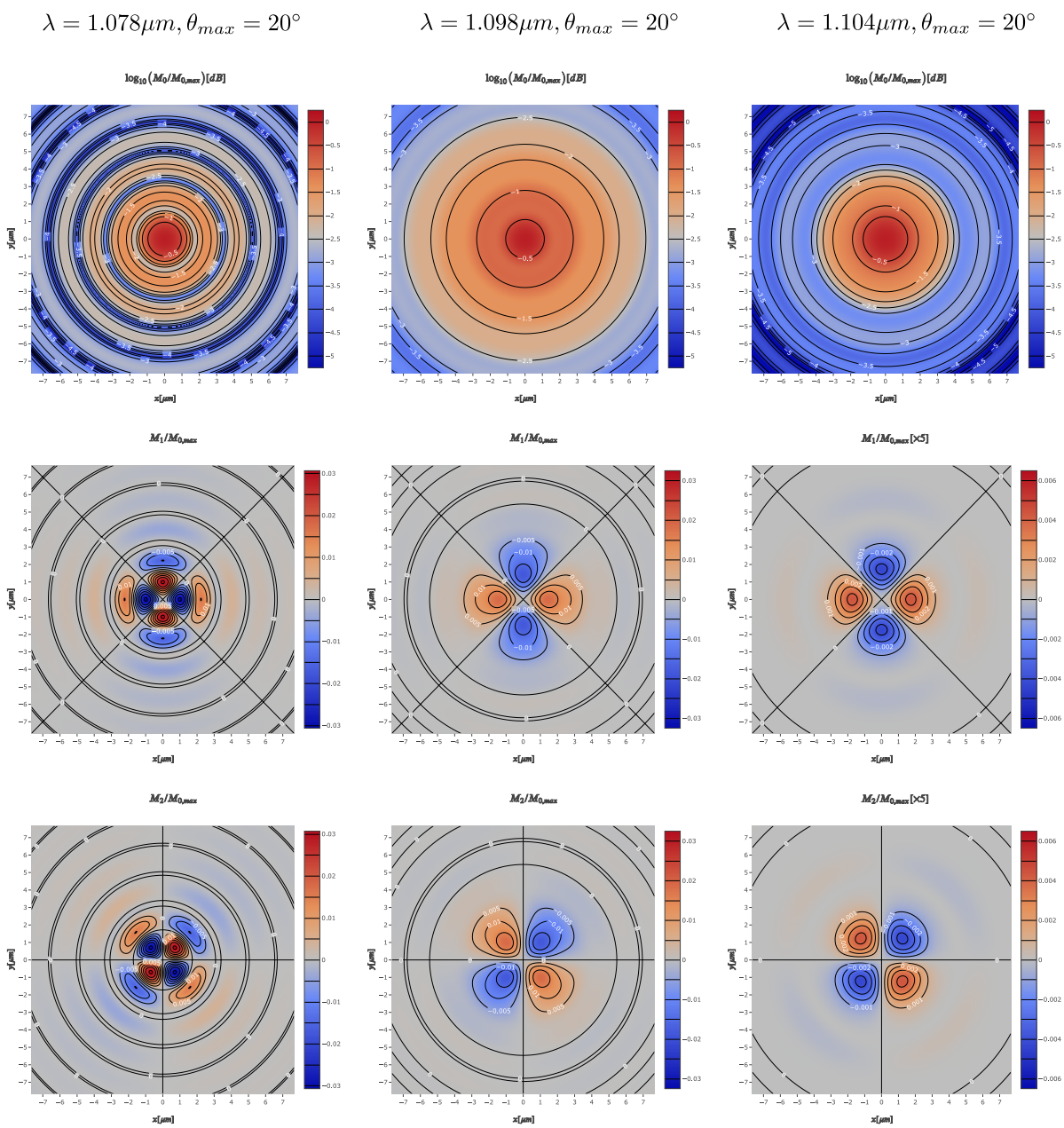

Figure 7.10: On top row, the coefficient M_0 associated with the PSF of unpolarized input light, normalized on its maximum value at the origin, in logaritmic scale. At the center, the contribution M_1 associated with the Stokes parameter s_1, normalized on the same quantity. At the bottom, the contribution M_2 associated with s_2 also normalized accordingly. Left column, represents PSFs at a wavelength of $\lambda = 1.078\mu m$, right outside of the spectral transmission region. Central column, a bigger wavelength of $\lambda = 1.098$, (peak wavelength for $\theta_{max} = 20°$) and on the right column for the plane-wave normal peak wavelength $\lambda_0 = 1.104\mu m$. In all cases, focusing NA is $\theta_{max} = 20°$. Dimensional units in microns and same colorscales used for every row, apart form the M_1, M_2 coefficients at $\lambda = 1.104\mu m$, which have been amplified of $5\times$ for clarity. Zoom in for improved visibility.

a) Intensity distribution for various NAs at $\lambda = 1.097\mu m$

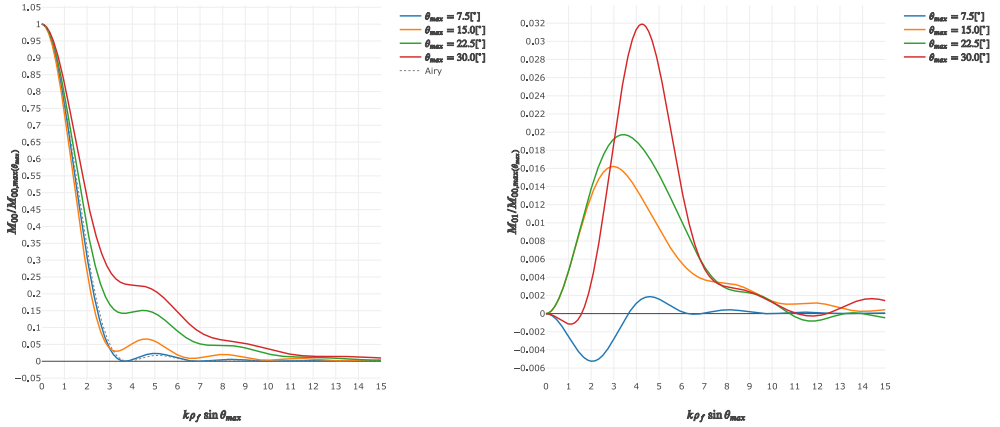

b) Intensity distribution for various wavelengths at $\theta_{max} = 22.5^\circ$

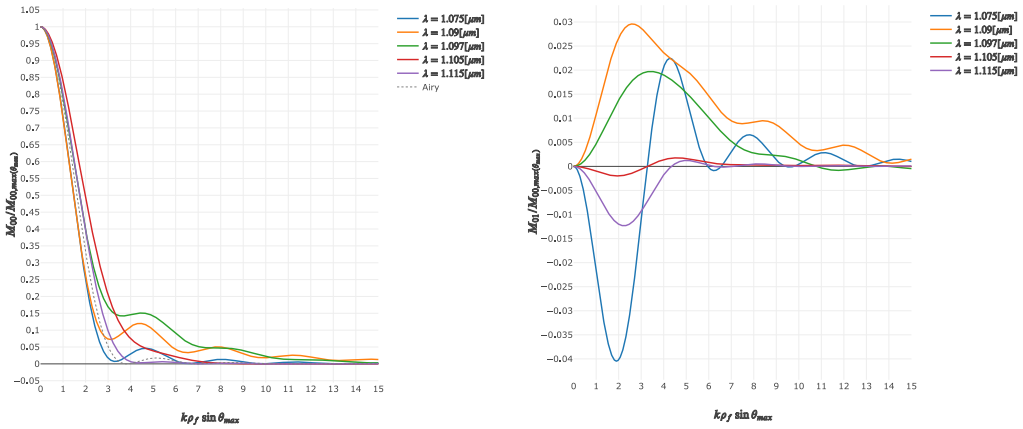

Figure 7.11: a) On top, intensity distributions of the unpolarized term M_0 (left) and M_1 (right) for various focusing half-cone angles for a wavelength of $\lambda = 1.098\mu m$. All the distributions are normalized (differently) on the origin value for illustration purposes and compared with the Airy distribution. b) Same intensity plots at a fixed focusing half-cone angle for various wavelengths. Zoom in for improved visibility

7.2.5. Finite Transmittances

The encircled energy transmittance of the pixel in Equation (5.65) is given by the simpler formula:

$$\overleftrightarrow{\tau}_{(\hat{s},\lambda)} = \alpha_{(\theta_{max})} \sum_{s,s'} \frac{2}{(s+s'+2)} \left(\mathcal{Z}_0^{[s_1]} \overline{\mathcal{Z}_0^{[s_2]}} + 4\mathcal{Z}_2^{[s_1]} \overline{\mathcal{Z}_2^{[s_2]}} \right) \mathcal{F}_{[s,s'](\tilde{\rho}_{max})} \tag{7.7}$$

Where the encircled energy functions $\mathcal{F}_{[s,s'](\tilde{\rho}_{max})}$ are discussed in Section 5.3.7. The finite transmittance is represented in contour plots in Figures 7.12 for various enclosing radiuses ρ_{max}. In Figure 7.13 it is instead compared with the wide-pixel focal transmission discussed in Section 7.2.2. On the right side of Figure 7.2.2 the ratio between the finite and the wide focal transmittance is calculated in the spectrum. As we demonstrated in Equation 5.3.7, the finite transmittance tends to the wide-pixel focal transmission for wide encircled regions. The spectral behavior of the finite transmittance clearly confirms that the spot size is aberrated towards the left side of the active transmission spectrum, more predominantly for higher NAs, as we already observed from analysis of the Figure 7.11. As a result, the finite transmittance possesses a different spectral behavior rather than only being attenuated and the expected peak may shift of up to $10nm$, when referred to the finite energy measured at the pixel. Even though the treatment is strictly applicable for a circular enclosed region, as we addressed in Section 5.3.9, we may use such transmission spectrums for a given pixel pitch $l_p \cong 2\rho_{max}$ for estimation purposes. The remaining energy percentage further represents cross-coupling energy in other pixels[3]. It follows that, at this spectral band, a pixel above $\cong 10\mu m$ shall be used to limit cross-coupling factors and work within 80% of the wide-focal transmittance in all the spectrum range for a $NA \cong 10°$, which is $\cong 50\%$ above what predicted with a Rayleigh diffraction criteria for the given NA (in Section 6.34). Such criteria will be revisioned in Section 7.5 for the other spectral channels and optimized pixels.

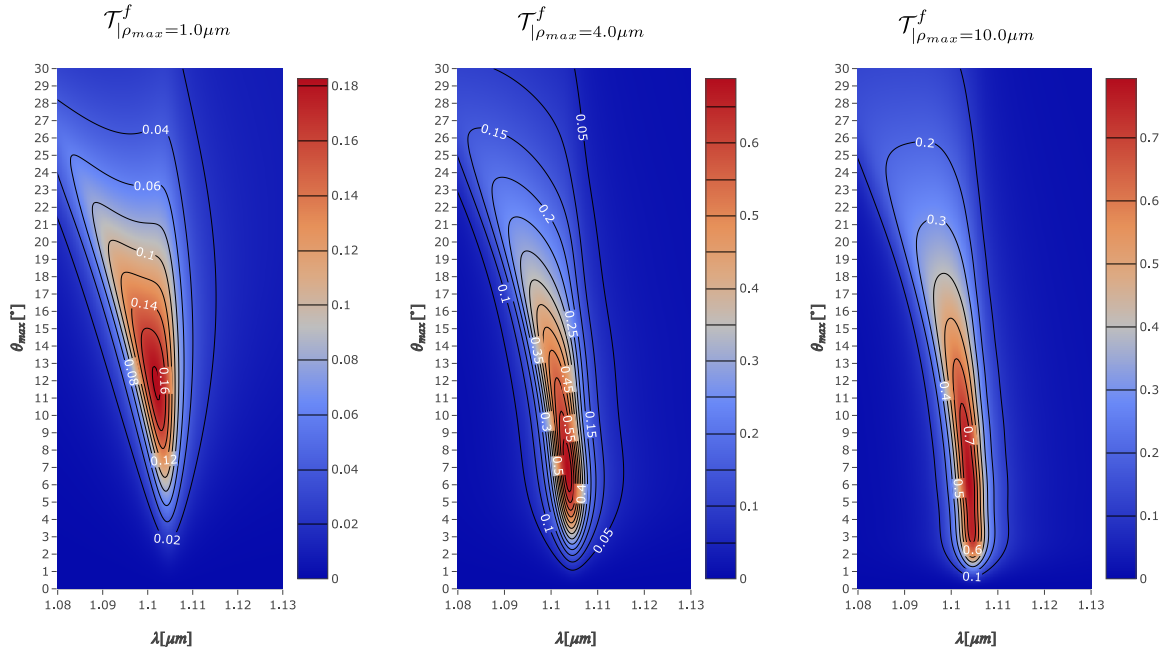

Figure 7.12: Finite transmittances spectrums in various focusing angles for three enclosing radiuses, increasing from left to right.

[3] however, such values are only an estimation. One shall resolve the diffraction problem in Section 5.3.1 and the image creation convolution in Section 5.3.9 for a better estimation of those

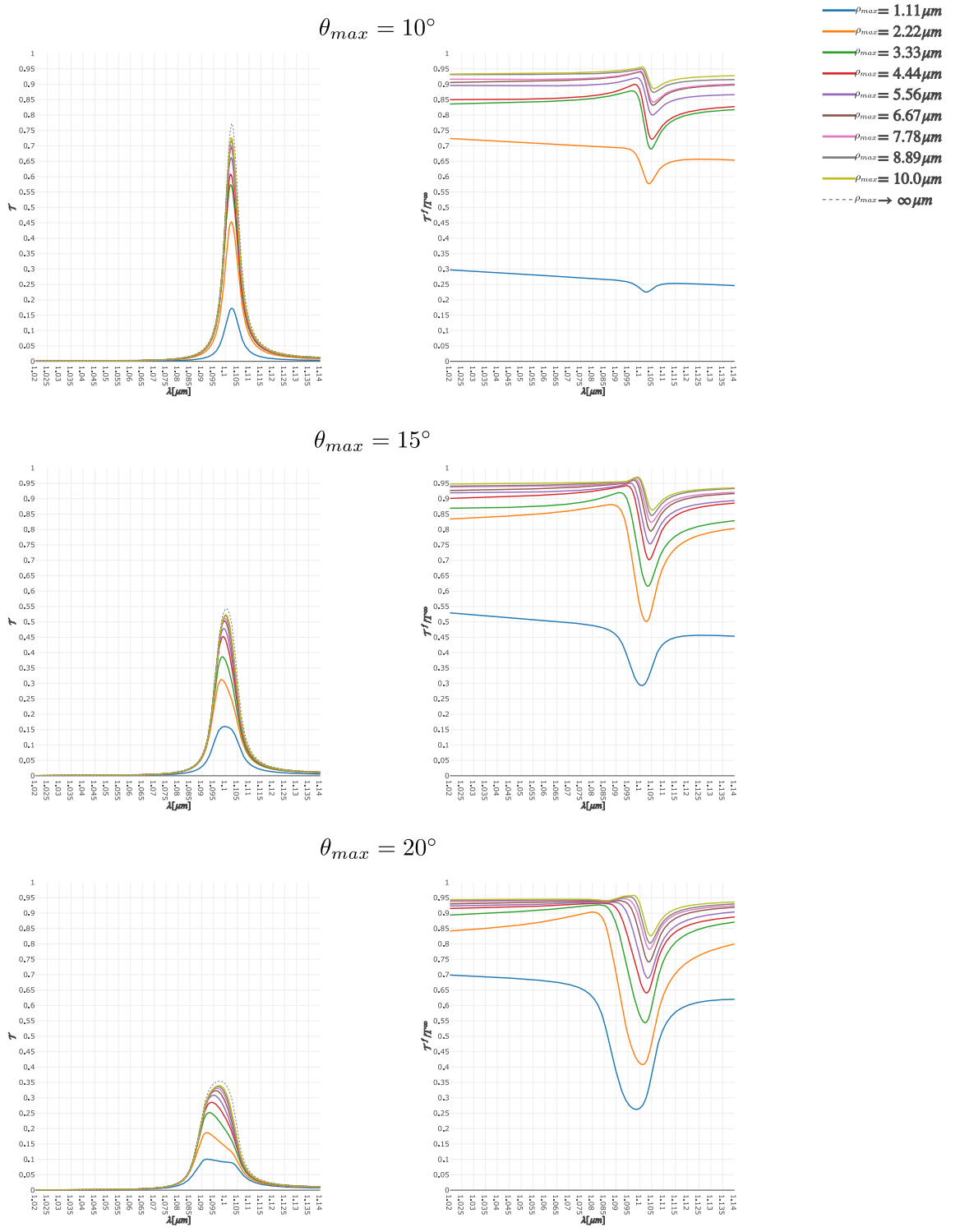

Figure 7.13: On the left column, finite transmittances spectrums for various NAs (in rows) and encircled radiuses (in colours). On the right column, ratios between finite transmissivities and wide focal transmittances in the spectrum within the same quantities variations.

7.2.6. OTFs

With an opportune rewriting to resolve azimuthal dependencies by applying formula (5.69), we determined the following formula for the OTF:

$$\overline{OTF}_{(\xi_k,\phi_k)} = \frac{\alpha_{(\theta_{max})}}{M_{00(\lambda)}} \left\{ \sum_{s,s'} \frac{2\pi}{s+s'+2} \begin{bmatrix} \left(\mathcal{Z}_0^{[s]}\overline{\mathcal{Z}_0^{[s]}} + 4\mathcal{Z}_2^{[s]}\overline{\mathcal{Z}_2^{[s]}}\right)\mathcal{I}_{(0,\xi_k)}^{[s_1,s_2]} \\ \left(\mathcal{Z}_0^{[s]}\overline{\mathcal{Z}_2^{[s]}} + \mathcal{Z}_2^{[s]}\overline{\mathcal{Z}_0^{[s]}}\right)\left(\mathcal{I}_{(-2,\xi_k)}^{[s_1,s_2]}e^{-2i\phi_k} + \mathcal{I}_{(2,\xi_k)}^{[s_1,s_2]}e^{2i\phi_k}\right) \\ i\left(\mathcal{Z}_0^{[s]}\overline{\mathcal{Z}_2^{[s]}} + \mathcal{Z}_2^{[s]}\overline{\mathcal{Z}_0^{[s]}}\right)\left(-\mathcal{I}_{(-2,\xi_k)}^{[s_1,s_2]}e^{-2i\phi_k} + \mathcal{I}_{(2,\xi_k)}^{[s_1,s_2]}e^{2i\phi_k}\right) \\ 0 \end{bmatrix}^T \right\} \mathbf{s}_{in} \tag{7.8}$$

where the mode functions $\mathcal{I}_{(q_1-q_2,\xi_k)}^{[s_1,s_2]} = \mathcal{I}_{(\xi_k)}^{[q_1,q_2,s_1,s_2]}$ have been discussed in Section (5.69).
The (radial contribution for $\phi_k = 0$) MTF for a generic input field, as calculated with numerical methods depicted in Appendix F, is represented in Figure 7.14 for various wavelengths and focusing angles, with respect to the one predicted by scalar unaberrated theory. Similarly to the variations of the PSF, we notice degradation of the MTF above $\theta_{max} > 10°$, more predominant for the peak shifted wavelength of $\lambda = 1.095\mu m$. The MTF is also affected by a polarization contribution as depicted in Equation (7.8), limited to $< 1\%$ for $\theta_{max} < 10°$ which also possesses azimuthal variations.

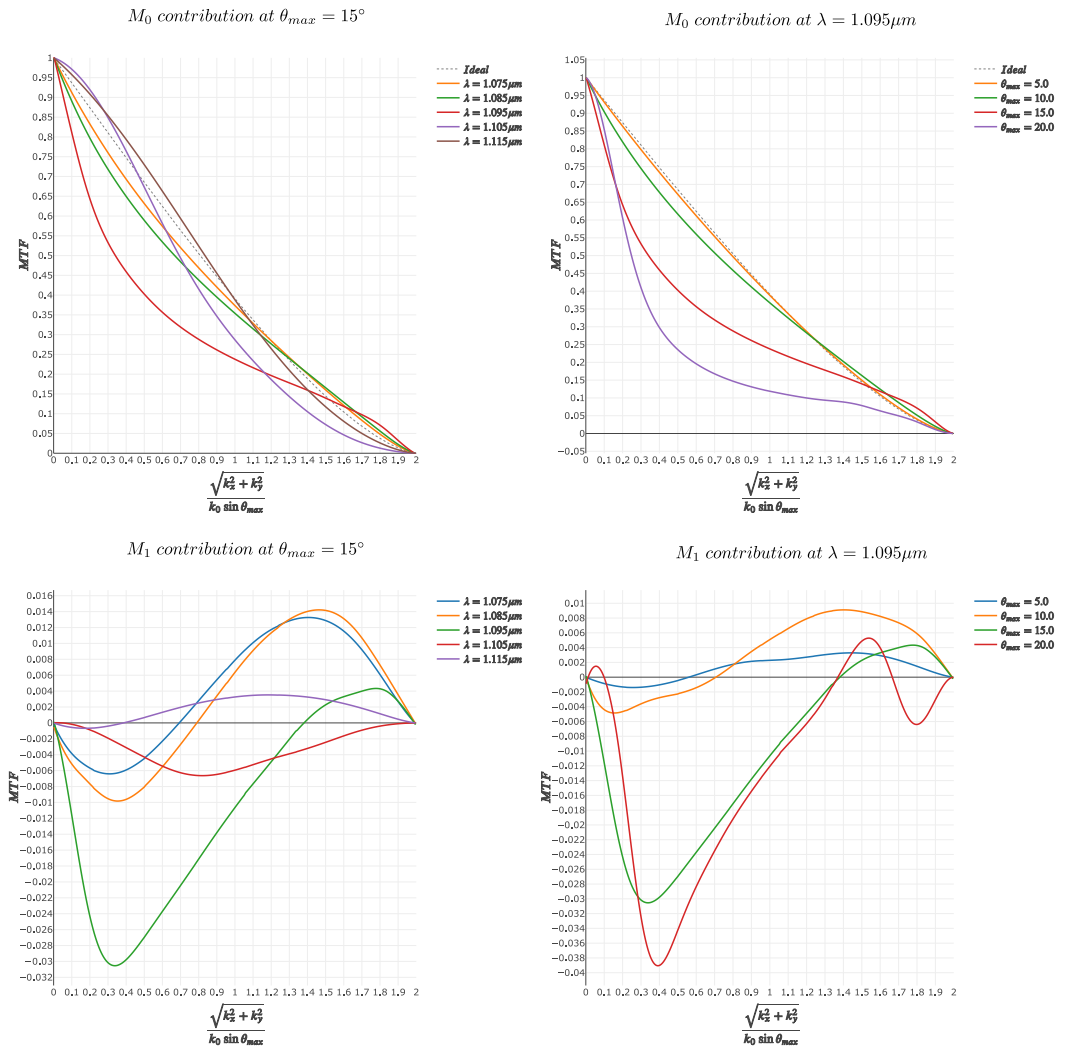

Figure 7.14: Top) MTF contributions for unpolarized input light at various wavelengths, for a $\theta_{max} = 15°$ (left) and the peak wavelength and various NAs (right). Bottom) Real part of OTF contributions due to linearly x polarized light, for $\phi_k = 0$ and various wavelengths for a given NA (left) and various NA for the peak wavelength (right).

7.3. Case Study: Polarized Pixel

For the case study of the polarized pixels, we perform a fully similar analysis by only taking into consideration the anisotropy of the permittivity tensor, representative of an elliptical inclusion. In addition to the previous parameters, we must discuss the condition number of the arrangement and various solutions to filter the undesired polarization peak, as well as the influence of the cross-coupling factors induced by the anisotropy.

For the filtering, in generality, we will analyze the use of a non-dispersive inclusion with a bandpass filter of finite efficiency. For sake of conciseness, we analyze again one pixel of DBR4, with the same sectional area and height of the inclusion but an aspect ratio of $AR = 2.5$. The stationary effective model approximation predicts the following permittivity tensor for such particle:

$$\overleftrightarrow{\epsilon}_r = \begin{bmatrix} 3.92 & 0 & 0 \\ 0 & 5.69 & 0 \\ 0 & 0 & 7.34 \end{bmatrix} \tag{7.9}$$

which has been used in the multilayer solver to determine those results. Losses and natural dispersion of material have been included in the mirrors multilayers but not in the values of $\overleftrightarrow{\epsilon}_r$, for numerical implementation ease. Those permittivities, as also inspection of the cavity resonances of DBR4 implies, induce cavity resonances for $\lambda_x \cong 1.082\mu m$ and $\lambda_y = 1.134\mu m$, with a total separation of $\Delta\lambda_{peaks} \cong 52nm$. The efficiency of the bandpass filter is kept as a variable to analyze its effect. Practical implementation of those filtering techniques are discussed in Section 7.4 in more details.

7.3.1. Plane-Wave Transmissions

We analyze the plane-wave response of the proposed pixel, prior placement of a bandpass filter.

Azimuthal dependence The structure is obviously not axial-symmetric anymore and will possess a Jones matrix $\mathbb{J}^{(m)}_{|\Sigma}$ of the type depicted in Equation (5.28), as a function of both angles θ, ϕ. The azimuthal dependence is introduced because of the anisotropy and is important to analyze since it induces different spot properties and an overall different integrated transmissivity, with small cross-polarization factors. Differently from the simple polarizer validate in the Appendix E, the presence of mirrors couplings results in general in an infinite order of (even) azimuthal frequencies (the structure is however still well represented for polar angles $\theta < 5°$ and perfectly for $\theta = 0$ by a four order expansion as the one depicted in (E.9), with choice of the opportune coefficients to be extracted from the solution of the coupling problem). It could be demonstrated (from the shape of the propagation matrix in Equation (4.9)) that the Jones matrix has a periodicity of π and is mirrored between the quadrants, so that only description between $[0, \pi/2]$ is required. Moreover, the Jones matrix appears to be symmetric, likely to be also a property of (4.9). The double-angle dependence is plotted in Figure 7.15 for $\lambda = \lambda_x$. The qualitative behavior of those plots is similar for other wavelengths, granted that the correct spectral transmissivities modules are used in θ. We may also note some similarities with the validated FEM results in Appendix E. Those transmissions may also be measured experimentally to further validate those results, via simple collimated plane-wave spectral illumination.

Transmissions in $x-y$ frame More important and understandable is surely the transmission in the $x-y$ frame, determinable by use of Equation (5.30). Its transverse minor, is of the form:

$$\mathbb{J}^{[x,y]}_{e|\Sigma_0} = \begin{bmatrix} \tau_{xx} & \tau_{xy} \\ \tau_{yx} & \tau_{yy} \end{bmatrix} \tag{7.10}$$

The presence of cross-coupling factors between the polarization is important for the reconstruction process. It can be seen that those are approximately maximums for $\phi = \pi/4, 3\pi/4...$ hence mainly due to the second-order azimuthal orders[4]. Moreover, they are nill at normal incidence. Their presence is due to physical geometrical constraints in the electric fields deviations for p and s polarizations, as already extensively revisioned in Chapter 4. The real structure may possess different cross-coupling factors depending on the applicability of the effective medium formulation and the variations of such effective parameters in the angles (assumed here uniform). We recall also that those results are well

[4] they would be present also for a circular inclusion pixel, but polarization retrieval is not of interest there

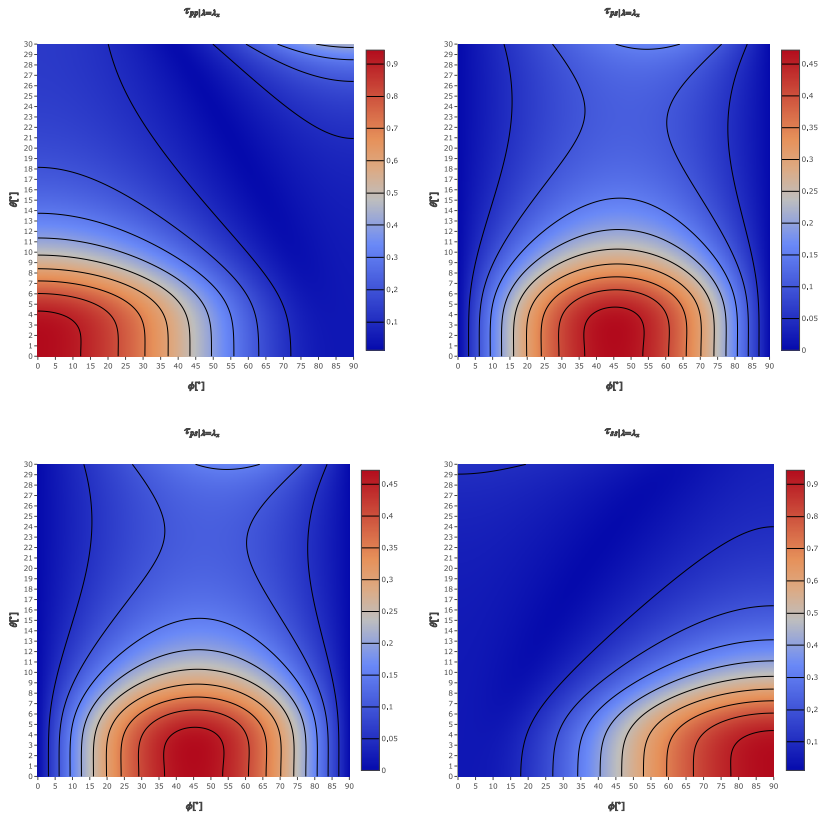

Figure 7.15: Azimuthal dependance of transmission coefficients of case study a) at $\lambda = \lambda_x$ in the polar and azimuthal angle, for p and s polarizations (respectively, top-left and bottom right) and for the cross-couplings factors $ps = sp$.

above the numerical noise, estimated at $\epsilon_{err} = 10^{-13}$ in Appendix A from energetic considerations. The matrix $\mathbb{J}_{e|\Sigma_0}^{[x,y]}$ is plotted in Figure 7.16a) for an azimuthal angle of $\phi = \pi/4$ in the angular spectrum and the corresponding plane-wave intensity transmittances contributions in Figure 7.16b) for an angle of $\theta = 30°$, chosen as such for illustration purposes. The cross-polarizations affect the extinction ratio of the polarizer as the NA of the system is increased. To understand to what extent, it is opportune to calculate the wide-pixel focal transmission.

7.3.2. Wide-Pixel Focal Transmission

The wide pixel transmittance is given by integration of the plane-wave Mueller row. Due to simmetry considerations, we have verified that only $M_{00}, M_{01} \neq 0$:

$$\overleftrightarrow{\tau}^{\infty}_{(\lambda,\hat{\mathbf{s}})} = \frac{1}{2}\begin{bmatrix} \mathcal{T}_{x,\lambda} + \mathcal{T}_{y,\lambda} \\ \mathcal{T}_{x,\lambda} - \mathcal{T}_{y,\lambda} \\ 0 \\ 0 \end{bmatrix} \tag{7.11}$$

with:

$$\begin{aligned} \mathcal{T}_{x,\lambda} &= \frac{\alpha_{(\theta_{max})}}{\pi} \int_0^{2\pi} \int_0^1 \left(\frac{\tau_{xx}\tau_{xx}^* + \tau_{yx}\tau_{yx}^*}{\cos\theta} \right)_{|\theta=\arcsin(\xi \sin\theta_{max})} \xi d\phi d\xi \\ \mathcal{T}_{y,\lambda} &= \frac{\alpha_{(\theta_{max})}}{\pi} \int_0^{2\pi} \int_0^1 \left(\frac{\tau_{yy}\tau_{yy}^* + \tau_{xy}\tau_{xy}^*}{\cos\theta} \right)_{|\theta=\arcsin(\xi \sin\theta_{max})} \xi d\phi d\xi \end{aligned} \tag{7.12}$$

The interested reader may verify with concepts from Section 4.4 that the intensity transmission coefficients $\mathcal{T}_x, \mathcal{T}_y$ are retrieved for fully polarized x and y input light, respectively.

a) Contour-plots of amplitude transmittance

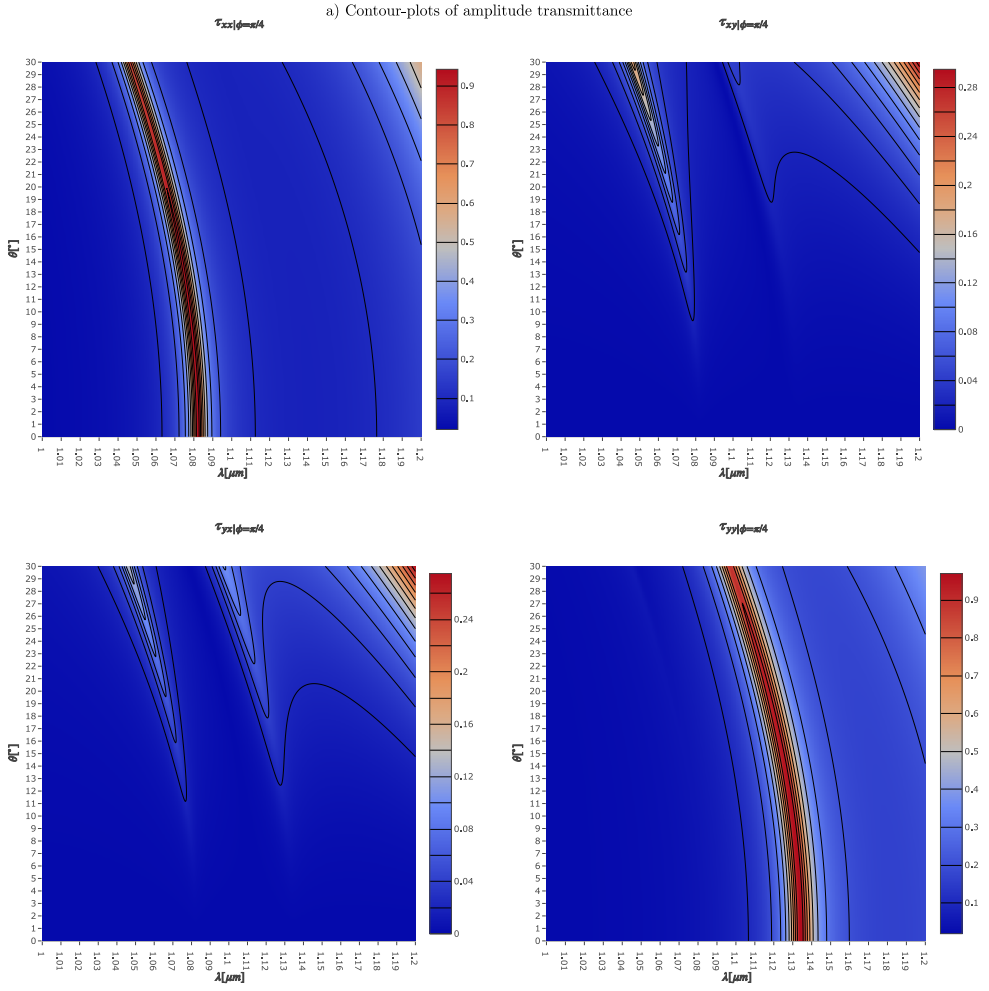

b) Intensity spectrums at $\theta = 30°$

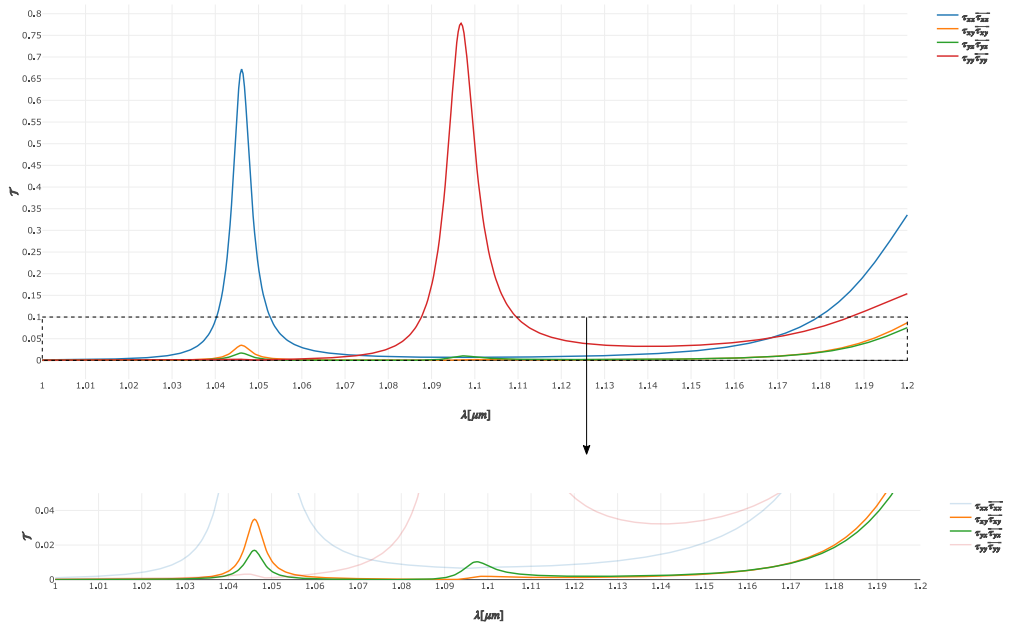

Figure 7.16: a) Amplitude plane-waves transmission module in various wavelength and polar angles for $\phi = \pi/4$ b) Intensity transmittances of various contributions at $\theta = 30°, \phi = \pi/4$, with zoom-in on the cross-coupling components

The two are represented in Figure 7.17 for various angle realizations. The integrals have been calculated with the splines integration routine over numerical grids depicted in Appendix D, with $n_{splines} = 100$ azimuthally and $n_{splines} = 200$ radially, with an estimated truncation error of $\epsilon_{error} = 10^{-9}$. The results are conceptually similar to the ones reported in Figure 7.6. However, it is observed that the y polarized peak is less affected by the angular adrift and generally wider, due to the fact that is approaching the end of the resonance curves in DBR4. Another difference with respect to the non-polarized pixel is the presence of small cross-couplings factors, still affecting the overall transmissivity also after cone-angle integration. According to Figure 7.6, those are recognizable only for $\theta_{max} > 15°$ and are limited to $\mathcal{T}_{cross,\lambda} < 0.005$. They add on the naturally present peak distribution at that spectral location. Before calculating the corresponding band transmittance, consider an idealized bandpass filter of efficiency $1 - \eta_b$, positioned at $\overline{\lambda} = (\lambda_x + \lambda_y)/2$ such that:

$$\mathcal{T}_i' = \begin{cases} 0 & 0 < \lambda \leq \lambda_{min,DBR4} \\ \mathcal{T}_i & \lambda_{min,DBR4} < \lambda \leq \overline{\lambda} \\ \eta_b \mathcal{T}_i & \overline{\lambda} < \lambda \leq \lambda_{max,DBR4} \\ 0 & \lambda_{max,DBR4} < \lambda < \infty \end{cases} \tag{7.13}$$

We integrate the spectral focal transmission to determine the band transmittance in the usable channel bandwidth of DBR4:

$$\overleftrightarrow{\tau}^{\infty}_{(\hat{\mathbf{s}})} = \frac{1}{\Delta\lambda}\left(\int_{\lambda_{min,DBR4}}^{\overline{\lambda}} \overleftrightarrow{\tau}^{\infty}_{(\lambda,\hat{\mathbf{s}})} d\lambda + \int_{\overline{\lambda}}^{\lambda_{max,DBR4}} \eta_b \overleftrightarrow{\tau}^{\infty}_{(\lambda,\hat{\mathbf{s}})} d\lambda\right) = \frac{1}{2}\begin{bmatrix} \mathcal{T}_{x,l} + \mathcal{T}_{y,l} + \eta_b(\mathcal{T}_{x,r} + \mathcal{T}_{y,r}) \\ \mathcal{T}_{x,l} - \mathcal{T}_{y,l} + \eta_b(\mathcal{T}_{x,r} - \mathcal{T}_{y,r}) \\ 0 \\ 0 \end{bmatrix} \tag{7.14}$$

The quantities $\mathcal{T}_{i,j}$ are represented in Figure 7.18left as functions of the NA, to be used for radiometric purposes. The normalization value $\Delta\lambda$ has been selected to be $10nm$ without any loss of generality. It can observed that the overall integrated cross-coupling factors settles at $\mathcal{T}_{cross} \cong 0.02$ and that the radiometric content for not-filtered y polarized light is significantly greater. The cross-couplings factors naturally increase in NAs, even though are roughly uniform below $\theta_{max} < 20°$.
The *PDL* module vector of this band transmission, defined in Equation 5.51 is given by:

$$\rho = \frac{|\mathcal{T}_{x,l} - \mathcal{T}_{y,l} + \eta_b(\mathcal{T}_{x,r} - \mathcal{T}_{y,r})|}{\mathcal{T}_{x,l} + \mathcal{T}_{y,l} + \eta_b(\mathcal{T}_{x,r} + \mathcal{T}_{y,r})} \tag{7.15}$$

The condition number associated with this PDL and the PDL itself are represented in Figure 7.18, along with other quantities, as a function of the bandpass filter efficiency for various NAs. The extinction ratio, defined hereby:

$$\mathcal{X} = \frac{\mathcal{T}_{y,l} + \eta_b \mathcal{T}_{y,r}}{\mathcal{T}_{x,l} + \eta_b \mathcal{T}_{x,r}} \tag{7.16}$$

has also been represented. To understand those results, one shall reconsider the band transmittances and the dependence of the condition number to the PDL depicted in Section 5.3.4. ρ measures, over the complete available band, how much the input transmittances are polarization-dependent with respect to the transmitted light. A value of $\rho \cong 1$ is optimal for the reconstruction process and is in fact achieved for a perfect bandpass filter, for which the arrangement possesses a condition number of $\kappa \cong 1.5$, rather stable in the NA. If the bandpass filter presents a finite efficiency, however, more of the light of the y polarized input will be intercepted, reducing the PDL. When the same amount of light is intercepted for both polarizations the arrangement is polarization-independent and reconstruction is impossible. Since the $\mathcal{T}_y$ radiometric content is higher than $\mathcal{T}_x$, this condition is achieved for an intermediary bandpass filtering. A reconstruction for this arrangement is possible also without the use of a bandpass filter, but the condition number of such reconstruction is heavily biased, possessing a $\kappa \in [6.7 - 8]$ for the various NAs realization. Moreover, when reconstructing with both peaks, one can't discern if the integrated energy is resulting from one peak or another and hence can't properly resolve the variations of the Stokes parameters and the radiance in the spectrum anymore. As we discussed in Section 5.3.4 when the transmissivity spectrum presents features not localized to the FWHM of the desired peak only, reconstruction affects also the spectral resolution, which may differ from the FWHM significantly depending on how it is defined. Due to the presence of cross-couplings factors increasing with the NA

(and the decrease of aligned transmissivities combined with the spectral adrift) the condition number further degrades with increasing NAs. The extinction ratio $\mathcal{X}$, that settles at a minimum of $\mathcal{X}_{min} \cong 2\%$ in the best case, is also generally negatively affected by the increase of NAs. We point out that those results may quantitatively vary when using different off-angle permittivities ϵ_z of the cavity in the model, but will be similar qualitatively. We also point out that all of this analysis shall also be conducted upon varying sizes of the resonators cells l_p with the finite transmittance, calculated later on in the Chapter. If the extinction ratio is deemed to be too high for this reconstruction and polarization dependence of the measurement, one shall consider using more DBR mirrors to achieve higher attenuations regimes.

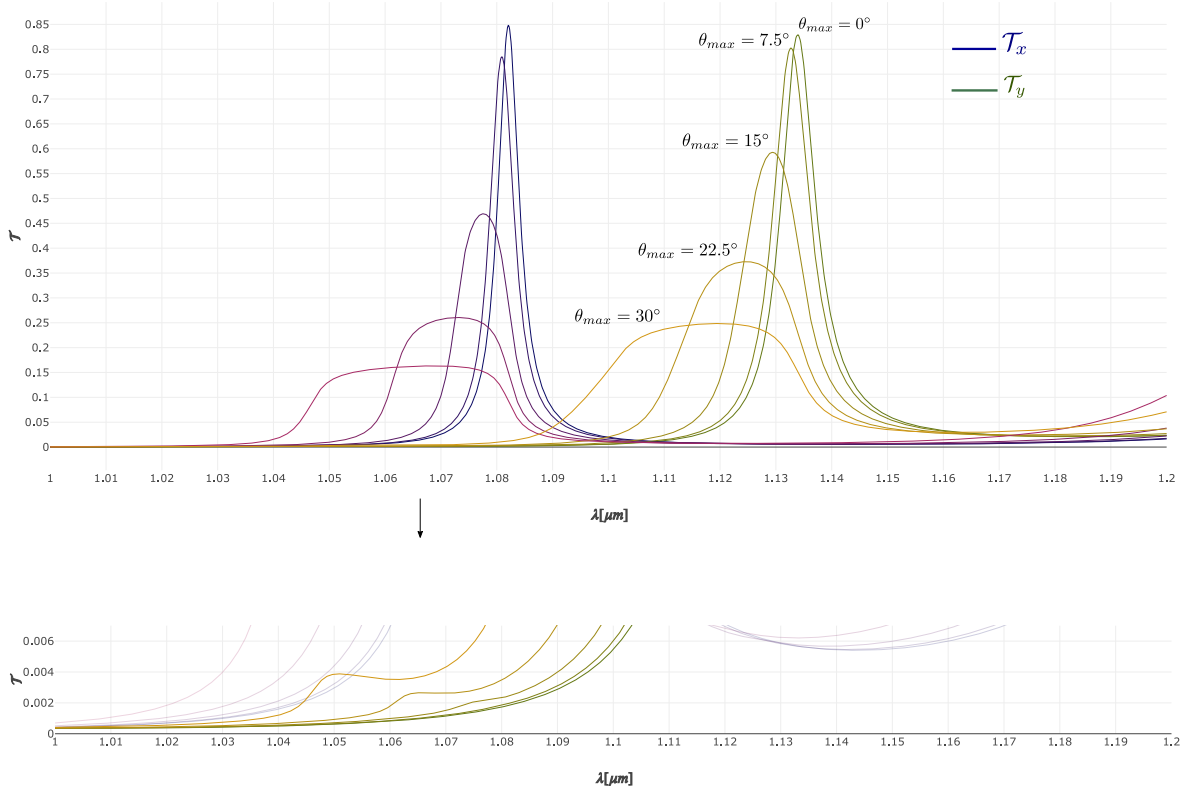

Figure 7.17: Intensity focal transmittances of for fully x polarized input light and fully y polarized input light. Spectral plots for various NAs of the results and zoom-in in the cross-coupling factors region.

7.3.3. Focal Fields

The focal fields associated with the solution of this case study are represented in Figure 7.19. In those plots and all following, the Zernike expansion has been truncated to $q_{max} = 8, s_{max} = 30$ to avoid memory overflow on our 64bit machine. Estimated accuracy of truncation errors from energetic considerations are of the order $\epsilon_{error} \cong 10^{-7}$ below $\theta_{max} = 25°$. For brevity, only a time realization of the real field is represented ($\psi = 0$ in Equation 4.38), in all polarization states for $\theta_{max} \cong 22.5°$ and its peak wavelength $\lambda_{peak} \cong 1.07\mu m$ in the spectrum of Figure 7.17. As clear from Figure 7.19, a focusing spot exists also for y polarized light (inverted in phase) and is one order of magnitude less pronounced than the focusing of the desired polarization, for this focusing angle. Smaller cross-polarization (non symmetric) terms are present. Ringing in the x polarizing focusing can be observed due to additional order modes. The ellipticity of the spot is a function of the position due to higher-order azimuthal modes in the focusing. The curves of the real field for a phase-field $\psi = \pi/2$ are qualitatively similar but possess slightly different distributions in space. Those undesired cross-polarizations can be limited below 1% by reducing the focusing half-cone angle to $\theta_{max} = 10°$. The spectral variations of those focused fields are qualitatively similar to the one of the polarized pixels otherwise.

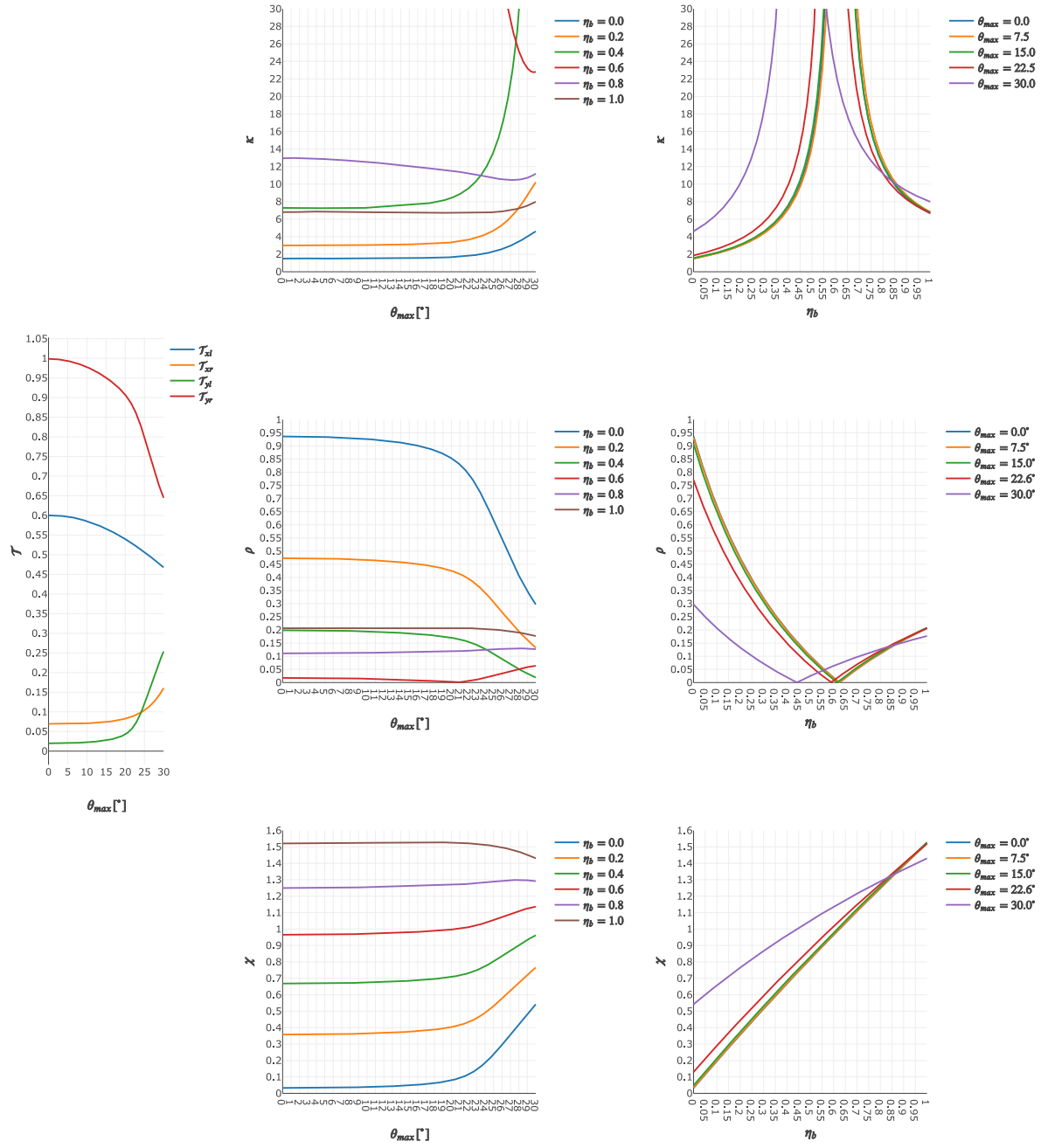

Figure 7.18: Left) Band transmittances variations for the two integrations ranges and the two polarizations. Center column) From top to bottom, variations of condition number, PDL module and extintion ratio as a function of the NA, for various transmittances of the bandpass filter. Right column) From top to bottom, variations of condition number, PDL module and extintion ratio as a function of the transmittance of the bandpass filter, for various NAs.

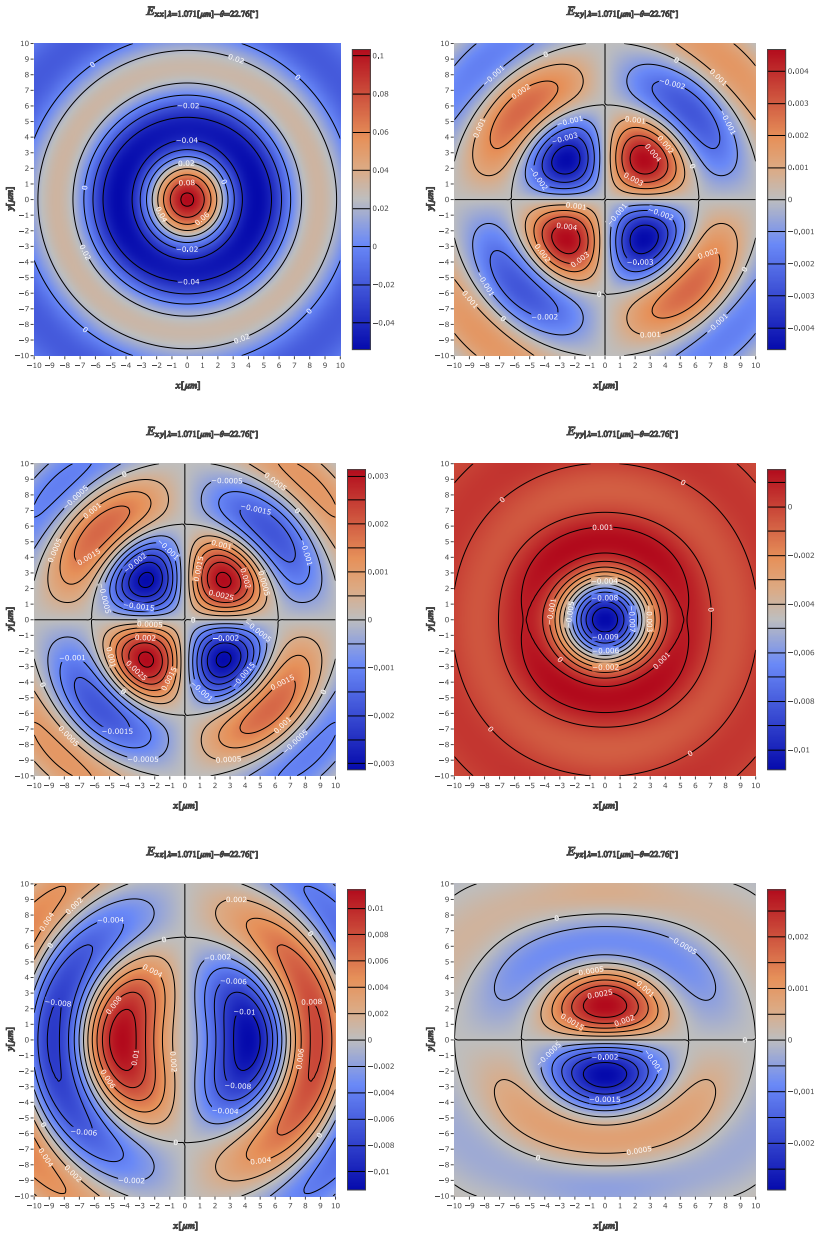

Figure 7.19: Focal fields, from top to bottom, of x, y, z components respectively, upon uniform illumination of x polarized input light (left column) and y polarized light (right column), for a wavelength of $\lambda = 1.071\mu m$ and an $NA = 22.76°$, chosen to be the peak wavelength at the given NA respectively. The scale bars are associated with the value of the normalized scaled field $\mathbf{e}_{f|\Sigma_0}/(kf\sin^2\theta_{max})$. Dimensional units may be found in accordance with scaling factors in Equation 5.3 in relation to the spectral radiance. Only the real field components at phase field $\psi = 0$ are represented for brevity. Zoom in for improved visibility.

7.3.4. PSFs

In Figure 7.20 the PSFs associated with the previous focal fields are also represented, for the various polarization contributions, partly in logarithmic and partly in scalar scales for the same NA and wavelength. The polarizer is affected by the presence of s_2 and s_3 components in the input field. The latter is due to some retardance induced by the multilayer for an arbitrary azimuthal angle due to the complex phase difference between $p - s$ polarizations. Once integrated in the plane, the energy contributions of the s_2, s_3 terms are nill for a uniform input field. Due to the fact, the field E_{yy} in Figure 7.19 is slightly stronger in magnitude than the cross-polarization terms, a spot is retrieved also for y focusing of light, but with stronger azimuthal features and two orders of magnitude below the desired polarization spot. The spot of the x focused input light presents clears ellipticity and not uniform ringing effects. Once

again, to limit those artifacts one shall reduce the focusing half-cone angle to $\theta_{max} = 10°$. The presence of the other polarization contributions affects the extinction ratio of the polarizer. The variation of spot size with wavelength is also observed and conceptually similar to the one depicted in Section 7.2.4.

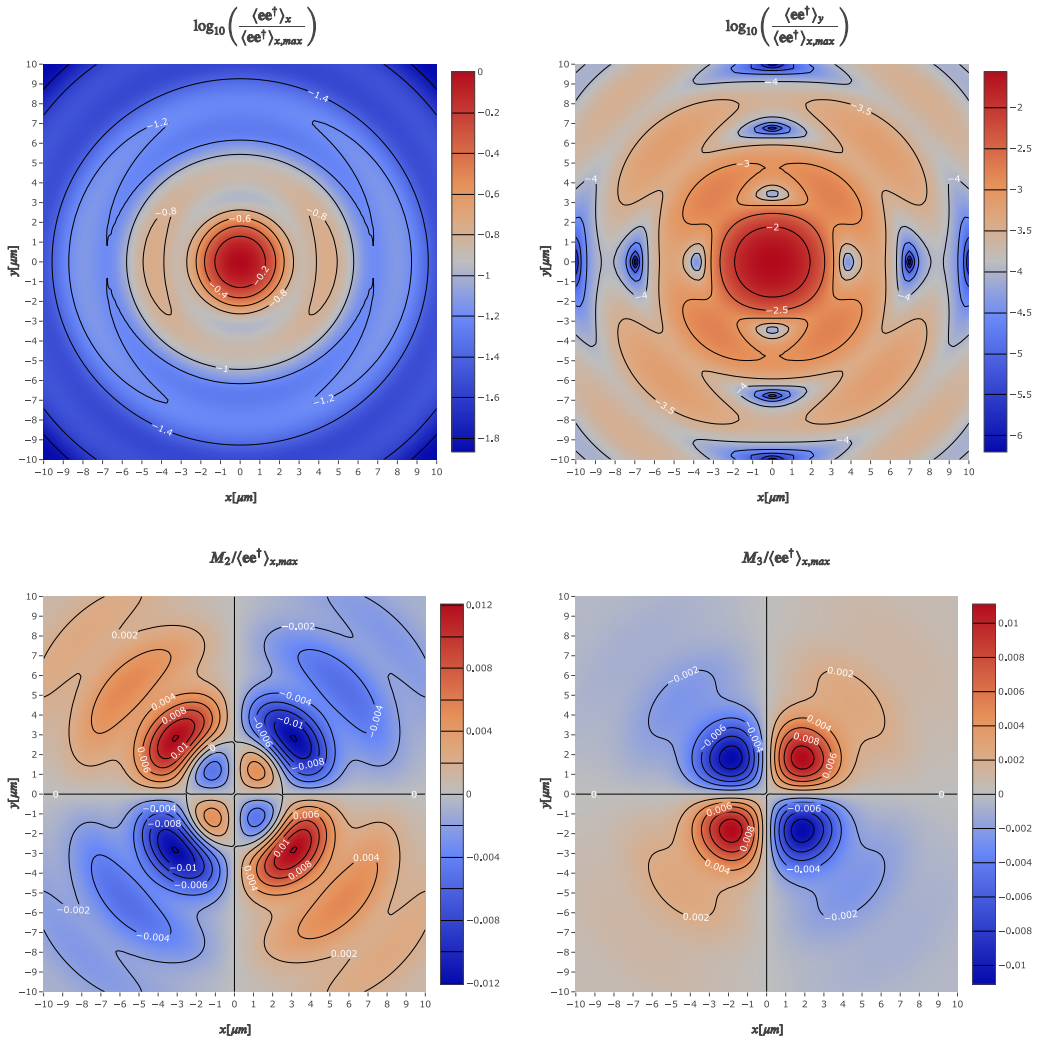

Figure 7.20: On the top row from left to right, focal spots associated with fully polarized x and y light respectively $(s_0 + s1, s_0 - s_1)$, in logarithmic scale, normalized on central value of the x polarized spot. On the bottom row from left to right, contributions due to s_2 and s_3 to those distributions, in linear scale, normalized on the same normalization constant.

7.3.5. OTFs

The MTFs in the radial direction for $\phi = 0$ of this case study are further represented in Figure 7.21. The MTF for x polarized input light is qualitatively similar in behavior to the one presented in Section 7.14, both in variation of focusing angle and of wavelengths. However, aberrations due to angle dependence are less strong due to the higher value of permittivity ϵ_z, minimal up to $\theta_{max} = 15°$. The MTF of the y polarization input, instead, is rather stable with the variation of the focusing angle. The azimuthal variations of the OTFs can be retrieved from the ones of the PSFs in a similar fashion, for example, the contributions of s_2, s_3 are nill in this radial direction.

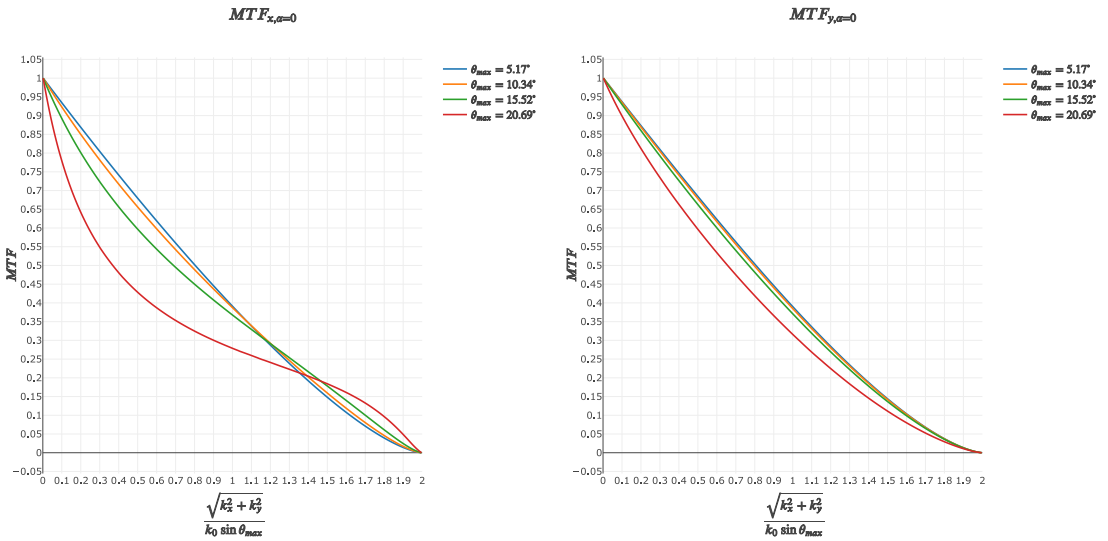

Figure 7.21: OTF module in the radial direction in the k_x versor direction. Left) For fully x polarized light Right) For fully y polarized light.

7.3.6. Finite Transmittances

The finite transmittance are further represented in Figure 7.22 (x and y transmittances are superimposed on each other) and also possess a qualitatively similar behavior to the one depicted in Figure 7.13. A similar diffraction based sizing criteria to the one above discussed is hence verified also for the polarized pixels. The $M_{0,2}, M_{0,3}$ finite transmittance coefficients are nill for this pixel, whereas $\mathcal{T}_x = M_{0,0} + M_{0,1}$, $\mathcal{T}_y = M_{0,0} - M_{0,1}$. The transmission for unpolarized input light is hence retrieved by taking the average of the $\mathcal{T}_x$ and $\mathcal{T}_y$ transmittances. The peak unpolarized transmittance reaches a peak $\mathcal{T}_{unpol} \cong 0.3$ for a pixel pitch of $l_p = 10\mu m$. Since we assume homogeneous statistical angle of polarization on the input light, the band transmittance associated with $\mathcal{T}_{unpol}$ shall be used in the power-budget once a filtering techniques is selected.

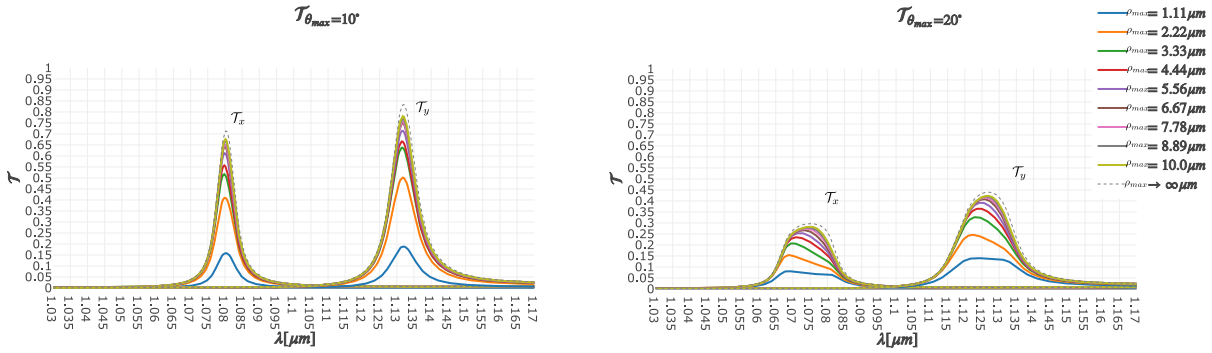

Figure 7.22: Finite transmittances spectrums for a focusing half-cone angle of $\theta_{max} = 10°$ (left) and $\theta_{max} = 20°$ (right). The spectrums for fully x, y polarized light are superimposed in the plots.

7.4. Filtering Techniques

In Section 7.2.2 we have introduced an idealized band-pass filter to depict the dependence of the condition number to its filtering efficiency, but no details were provided on how the band-pass filter may be achieved at a pixel level. In this Section, some design modifications are explored in order to achieve the required filtering. Any additional spectral filter positioned on the structure shall be considered in the modeling as a multilayered structure to correctly account for its coupling with the structure, which we will show to be non-negligible. Various are the possible filtering techniques, in the next paragraphs. Filtering the undesired polarization peak it is strongly preferred since condition number can be limited to the theoretical minimum of $\kappa = \sqrt{2}$. If integration of any of the solutions below depicted is practically too cumbersome or functionally impossible, however, reconstruction may still be performed. We have seen in Figure 7.18 that the energy content of the two polarization transmittances are not necessarily equal, which results in a finite condition number without filtering ($\kappa \cong 7$). Other reconstruction methods with denser matrices are also possible (see [4], which is an experimental demonstration with $\kappa \cong 8$) and require assumptions on the distribution input spectrum and their smoothness, but on the other hand, result in a more compact filter since more wavelengths are simultaneously reconstructed. In applications where the SNR is not the driving criteria, the latter reconstruction methods may also be considered more in-depth.

Double DBR The conceptually easier solution to achieve attenuation of the undesired polarized light is adding on top-bottom of the considered structure another DBR structure with a non-polarization dependent response, exactly tuned at the desired polarization wavelength. With the introduced tools, we have analyzed the transmission behavior of this setup, noticing that it is preferable to use also a cavity with inclusion for the additional DBR in order to avoid un-matched angle-dependence of the transmittance. Even if using a bare-cavity would be preferable in terms of manufacturing ease, doing so would allow covering only one peak without changing the height of the DBR stack in the next pixels and would not match the values of the off-angle permittivity ϵ_z, strongly influencing the angle behavior of the device. As a result, the light would be attenuated much more strongly above $\theta_{max} = 5°$ without the use of a matched inclusion. Fully matching both ϵ_x and ϵ_z seems however not possible with the same geometry of the inclusion (circular-elliptic). Another difficulty arises from the fact that cavities are coupling with each other if the intermediate DBR mirrors are not enough ($n_{mirrors} > 4$), which results in not full attenuation of the undesired polarization peak. Complete attenuation is, in fact, never achieved and quantified to a few percents with the use of a reasonable amount of mirrors. The necessity of using multiple mirrors decreases the overall power transmitted energy (by narrowing the FWHM). Such a filtering solution further requires manufacturing tolerances are well controlled. An example (relative to the optimization of DBR with such filtering techniques) is represented in Figure 7.23. It can be proven that optimal filtering is achieved where the ϵ_x are matched and $\Delta\epsilon_y$ the maximum. The latter quantity is not arbitrary (depends on ϵ_x so on the desired peak location) and is a function of the volume filling factor (in the stationary preliminary model), representative of the fact that only a certain permittivity contrast can be achieved for a given geometry. As a result, the filtering is less efficient for low and high filling factors of the cavity, as can clearly be seen in Figure 7.23. Hence, the DBRs designs is discussed in Section 7.1 requires re-optimization with selection of a different cavity size. We perform this operation in Section 7.5 for all DBRs. The angle behavior of this structure is also rather stable (see Image 7.25a)) and, as can be seen in Figure 7.23 the range of the available bandwidth can be covered with good extinction ratios. Focusing and focal transmission performance are not analyzed for brevity, but the same considerations and methods would apply. The practical implementation of this permittivity values requires the use of gratings or other geometries, for determination of which a better effective model shall be used. In Figure 7.25 the angle-spectrum intensity transmittance is shown for the same structure without the inclusions (and cavity matched properly), which shows the sharp decrease off-angle due to difference in ϵ_z permittivities, better to be avoided. We have observed that is preferable to use a bigger number of mirrors in between the cavities and that, for particular configurations, the desired polarization transmittance may present two peaks even upon matching the optical phase-shifts. That's a likely an (avoidable) effect of the detuning between cavities and mirrors, generally present for an arbitrary inclusion.

Dispersive inclusion In this paragraph, we show how a positive dispersion in ϵ_y can lead to the extinction of the y polarized peak, with the use of a single effective cavity. This consideration is a simple outcome of the inspection of the resonances curves of the DBRs illustrated throughout the report. To practically achieve the required positive dispersion, various solutions may be considered:

- Use of materials with natural positive dispersion law, e.g. $dn/d\lambda > 0$. From inspection of the material database, materials with the required positive dispersion are only highly lossy metals (chromium, gold, magnesium...). The losses associated with such materials are strongly affecting the polarization peak. The introduction of an anisotropic lossy metal may be considered for further studies to achieve a predominant loss only on the undesired polarization direction. In this regard, a study with an artificial k in the effective refractive index n_y has shown to naturally extinguish only one of the peaks. However, the anisotropic inclusion geometry does not necessarily correlate with the anisotropy in the effective parameters until further studies will confirm such.
- Use of scattering elements in Mie resonances: it is well known that particles in the order of magnitude of the wavelength do possess scattering resonance regimes. The effective medium formulation can still be used to separately describe each one of the propagating modes in the structure by considering an artificial permittivity and permeability of the effective cavity, as highly wavelength dependent functions. Prior to the Mie resonance peaks, the effective permittivity possesses strong positive dispersion which may be used for the concept. Mie resonances regime possesses a known analytical solution for a sphere in a uniform medium and elliptical particles of similar dimensions are under study.
- Use of lattice resonances: other phenomena which leads to strong wavelength-dependent effective parameters are lattice resonances, induced by the fact that the scatterers are arranged in a periodic fashion in a lattice of a certain geometry and dimensions $a \cong \lambda$. If the lattice resonances can be excited by the scatterer predominantly in one direction, the required behavior may be achieved also with this solution, since lattice resonances do scatter mainly in the transverse planes. To properly use such resonances, however, a study of the finite structure with multiple resonators orientations is paramount for a sound estimation of those effects.

A more detailed estimation of all those possibilities requires analytical tools not available at the moment and beyond the scope of this report. However, in Figure 7.26, we report the transmissivity spectrum associated with the same structure understudy in the polarized case study, but with a dispersion of $\epsilon_y = \left(\frac{dn_y}{d\lambda}(\lambda - \lambda_0) + n_{y0}\right)^2$, where $\lambda_0 = 0.9\mu m$ and $n_{y0} = 1.87$. Figure 7.26 shows how the introduction of a dispersion shifts the undesired peak further apart and that an optimal value of such dispersion exists, for a given size of the cavity. In Figure 7.26a) a cavity size of $l_{cav} = 325nm$ is used (as in Table 7.1), representative of the first resonance regime of the cavity. In Figure 7.26b) the same plot is shown for a cavity of $l_{cav} = 1.3\mu m$, representative of a resonance regime $m = 4$. By making the cavity longer, the required dispersion may be lowered (in Figure 7.26b) a dispersion of $dn_y/d\lambda \cong 2.5\mu m^{-1}$ would suffice). However, multiple resonances peaks may appear in the spectral response of the desired polarization $\mathcal{T}_x$ (not represented). Also, supporting a resonance mode for higher cavity lengths may be harder. Attenuation, when the dispersion is chosen accordingly, may be as high as the extinction ratio of the mirrors (here, $\cong 5 \cdot 10^{-4}$). This study does not take into account the possible change of cavity permeability. However, the generalized refractive index $n_{eff} = \sqrt{\epsilon_{cav}\mu_{cav}}$ may be used for the purpose to provide a similar analysis, once the latter is better characterized through more advanced models. If the spectral response of the effective parameters may be engineered at desire through scatterers resonances, one may further control more promptly the angle behavior of the filter and all other aspects of its transmissivity.

Anisotropic particles in the yz plane If the effective permittivity tensor of the cavity would be of the type:

$$\overleftrightarrow{\epsilon}_r = \begin{bmatrix} \epsilon_{xx} & 0 & 0 \\ 0 & \epsilon_{yy} & \epsilon_{yz} \\ 0 & \epsilon_{yz}^* & \epsilon_{zz} \end{bmatrix} \tag{7.17}$$

and $\epsilon_{yz} \cong \epsilon_{yy}$, we predict that the y polarized peak would shift towards the lower wavelengths and at the boundaries of the bandgap of the mirrors, as represented in Figure 7.24. Practically, such behavior will

likely be achieved for an inclusion rotated of $\cong \pi/4$ around the x axis or sliced at the same inclination in the plane yz, but the manufacturing implications of such solution are rather dubious. If another less-exotic way of providing a response $\epsilon_{yz} \neq 0$ may be found, this solution may further be considered. It may be also possible to induce attenuation of the s polarization but working, in one of the directions, close to the Brewster angle of the effective cavity.

Tilted Mirrors Various industries have developed DBRs of varying spectral response my using inclined mirrors in the transverse plane. According to our results, such a solution would not provide enough response contrast to significantly change the transmissivity spectrums as desired. Moreover, its integration is very cumbersome considered the multiple DBRs design.

Use of Anisotropic Crystals Special anisotropic properties are typical of birefringent crystals. Coupling a birefringent crystal slab with the filled cavity may provide the required spectral or dispersive response for the attenuation.

7.5. Optimization of the DBRs design

As we previously discussed, various filtering techniques can be used to filter the undesired polarization peak. The double DBR option is down-selected at this stage for the performance characterization, as the more likely to be realizable in practice. The simulation of the DBR transmittance with the introduction of the filtering unit is required to perform a sound SNR budget, which has no value without the latter, being strongly influenced by the filtering efficiency as discussed in Section 7.18. To achieve filtering, we have re-optimized all DBRs by including the filtering unit and changing mainly the cavity size in such a way to work in the region with higher permittivity contrast $\Delta\epsilon_y$. Even if the questionable stationary model is used here to depict the relationship between $\Delta\epsilon_y$ and ϵ_x, this trade-off is representative also of effects inherent with the performance of the real structure, which will present similar dependencies and constraints in relation to the filling factor and the achievable permittivity contrast. The use of such filtering in the modeling also allows us to consider realistic effects of filtering in other concepts which may be used for the purpose: no ideal band-pass filter exists able to fully extinguish the peak, without coupling with the DBR structure with so small contrast in the spectrum.

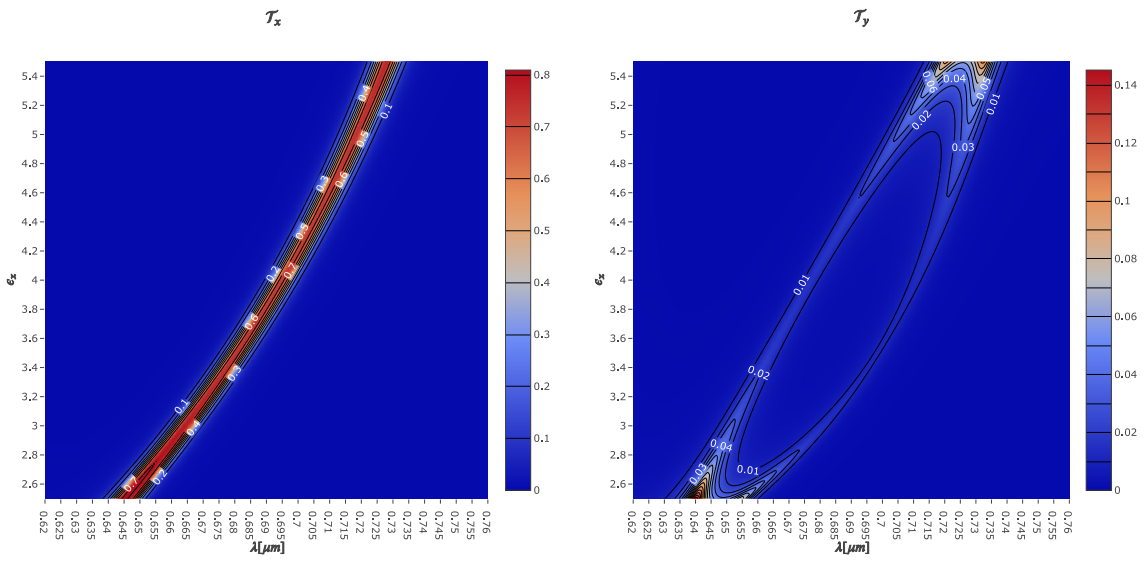

Figure 7.23: Resonance surves for the x (left) and y (right) polarization peaks at normal incidence, for a multi-DBR design (DBR2 of Section 7.5) comprehensive of two cavities with inclusions sized at $AR = 5$ and $AR = 1/5$. The permittivity axis is representative of the match permittivity on the x axis. The simulated material properties, as discussed in Section 7.5, are here dependent on the filling factor for a given ϵ_x which sets the other permittivity values and their contrast. Attenuation of the y peak is achieved, with presence of two spectral peaks, and more efficient for intermediate filling factors.

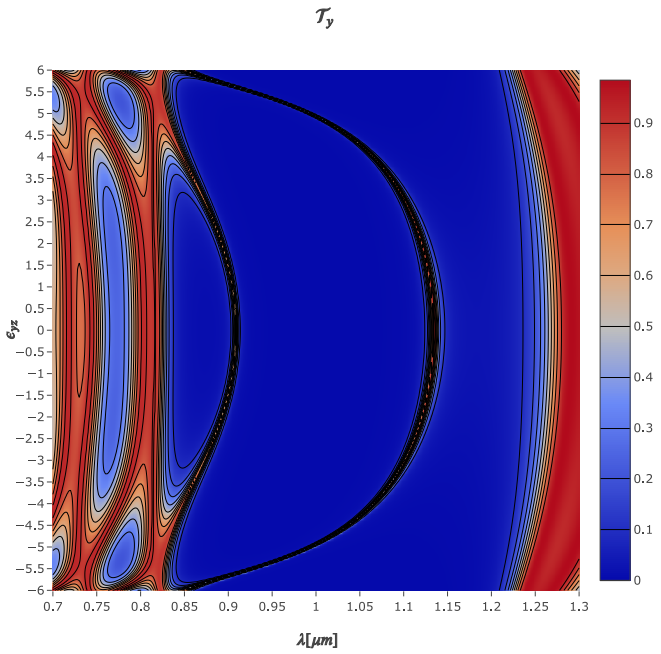

Figure 7.24: Spectrum transmissivity at the variation of ϵ_{yz}, the all others parameters fixed to the one of the polarized pixel case study.

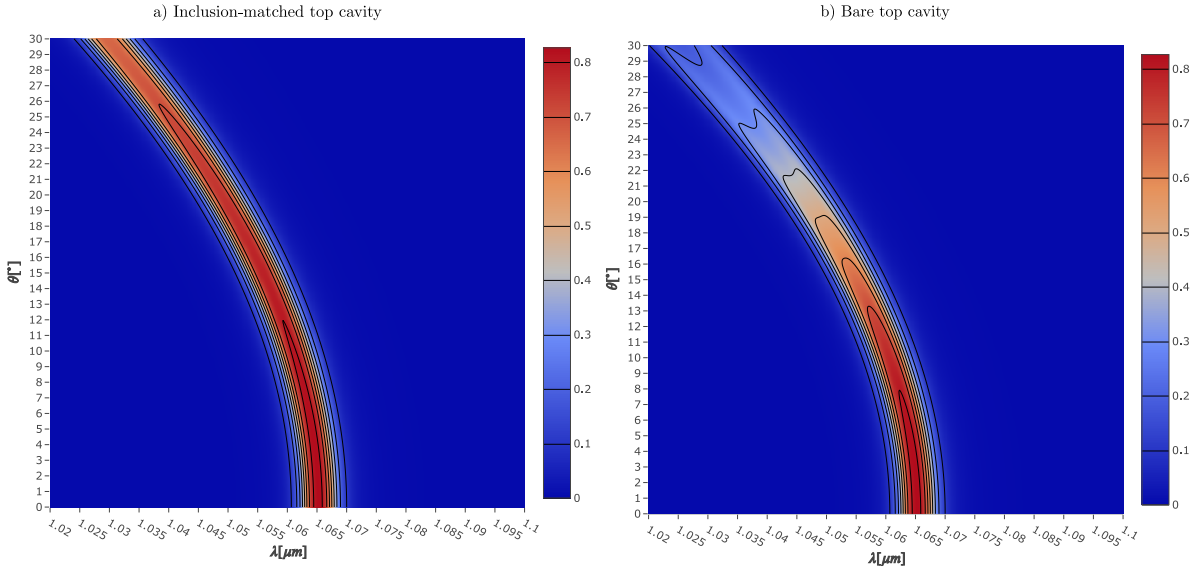

Figure 7.25: a) Angle-spectrum intensity transmittance for two cavities in a multi-DBR with the same off-angle permittivity ϵ_z, representative of two cavities with opportunely sized inclusions b) Angle-spectrum intensity transmittance for two unmatched cavities in the multi-DBR, representative of a bare top cavity. The two spectral peaks are associated with the different angle response of the cavity. Results are reported for succinctness only for the p polarization.

a) $\mathcal{T}_y$ transmittance at $m = 1$ resonance of cavity

b) $\mathcal{T}_y$ transmittance at resonance $m = 4$ of cavity

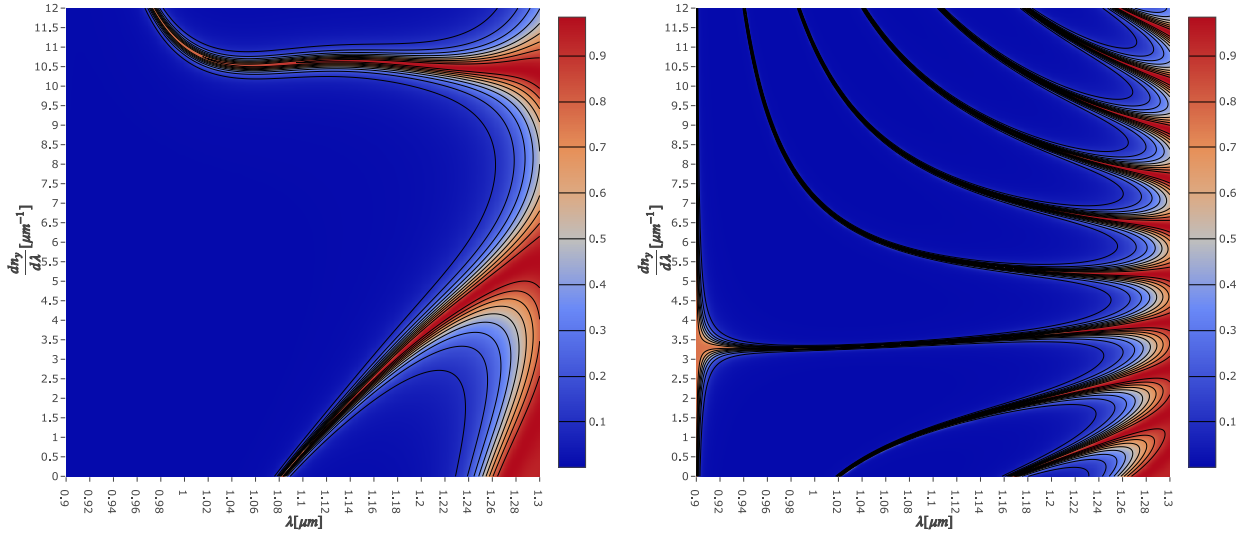

Figure 7.26: a) dispersion-wavelength transmissivity curves for a cavity of $l_{cav} = 325nm$ and same setup of Table 7.3 for DBR4 b) dispersion-wavelength transmissivity curves for a cavity of $l_{cav} = 1.3\mu m$ and same setup of Table 7.3 for DBR4. In both cases, $\lambda_0 = 0.9\mu m$ and $n_{y0} = 1.87$

To sample the DBRs bandgap we use 16 pixels, which enables a resolved sampling for the FWHM under consideration (with exception of a few SWIR pixels). The desired peak location fixes for a cavity length the ϵ_x value. To achieve the higher permittivity contrast allowed by a certain ϵ_x, an aspect ratio of $AR = 5$ is used for the bottom cavity and $AR = 1/5$ for the top cavity, in the polarized channels for all DBRs. The un-polarized channels both possess a cavity with $AR = 1$ and have, otherwise, the same dimensions. We have limited the maximum aspect ratio to $AR = 5$ to consider manufacturing constraints on the achievable aspect ratio and avoid too strong contrast between the $\Delta\epsilon_z$ of the two cavities. The new dimensions of the optimized mirrors and cavity are given in Table 7.2. As clear also from Figure 7.27, sampling of the active DBR regions is achieved with resolved peaks. The required permittivity values are instead represented in Figure 7.28 to achieve such peaks. It can be noted that some off-angle permittivity un-matching $\Delta\epsilon_z$ is present and stronger for the SWIR DBRs, which uses aSi as inclusion material; it seems to have however a minimal effect for a focusing angle of $\theta_{max} = 10°$, hereby used. Consider first only the polarized channels. The FWHM of the various peaks vary in the spectral channels as per Figure 7.29 (plotted against the transmittance peak location). To account for the fact that radiances values are significantly lower in the SWIR, the FWHM in those channels has been slightly degraded to meet power budgets. The FHWM of the VIS channels ranges from $4.5 - 9[nm]$ and the ones of the SWIR channels from $5 - 17nm$. All those results have been derived by considering the focal finite transmittance, including diffraction and spectral adrift of the peaks as predicted by the introduced model. The band transmittances of the DBRs are depicted in Figure 7.29. Even though for brevity, we do not rediscuss the OTF and PSFs of all the designs, we have observed those to be similarly bounded by $\theta_{max} = 10°$ as in the single-DBR design, with slightly a lower diffractive performance due to unmatching of the off-angle behavior of the two cavities. To prove the previous statement, consider the ratio Q_{diff} between the finite pixel band transmittance and the wide one, plotted in Figure 7.29 against the achieved spectral peak location of the finite transmission spectrum for a resonator cell of $10\mu m$ in DBR1 to DBR4 and $20\mu m$ in DBR5-6. As previously discussed, the resonator cell requires to be increased in the last two SWIR channels to avoid diffraction coupling between pixels. Since $Q_{diff} > 74\%$ in all DBRs, diffraction effects are mainly limited within the resonator cell size. It can be observed that the diffraction effect is more pronounced for the initial spectral range of all DBRs in the SWIR. This behavior is easily explained when considering that the ϵ_z off-angle permittivity is lower in that region, resulting in more pronounced angle effects and hence aberrations. If such diffraction performance is limiting the pixel reconstruction due to cross-coupling, we suggest further increasing the pixel size and changing the system architecture accordingly.

The finite transmission focal spectrums of the desired polarization of $\mathcal{T}_x$ are represented in Figure 7.27. It can be seen that coverage of the VIS channels is possible with the use of 16 pixels and all possess a quasi-ideal shape (small uniformities are however present at the starting wavelengths of each DBR range). The transmissions of the SWIR channels are, instead, affected in the lower range due to various reasons: the design of the multiple DBR with the filtering unit requires various considerations and tradeoffs, of which we report the final result. There are optimal values of the number of the mirrors at the margins of the cavity with respect to the ones in between, for which only a finite set of configuration yields spectral peaks of the required shapes. The marginal mirrors number possesses a minimum dictated by the requirements on FWHM and in order to properly attenuate the undesired peak, whereas the number of central mirrors in between the cavities does also require to be above a certain limit to avoid cavity coupling and presence of undesired interference effects. On the other hand, to a higher number of mirrors, the effects of a permittivity contrast off-angle $\Delta\epsilon_z$ and the losses are always more pronounced (included in the model). To counteract the first effect, influencing also the diffraction quality factor as can be seen in Figure 7.29, the aspect ratio may be lowered if the spectral leakings of the undesired polarization are still within the required bounds by doing so. We have also considered that reasonably the sizes of the mirrors and cavity can be well controlled within a nm range, so a small decoupling is always present which affects more and more strongly spectral behavior as the number of mirrors is increased. Even though a complete optimization sweep as not been implemented, we could not determine a configuration with a better spectral performance in the SWIR range which also possesses the required FWHMs, given all the above factors. The small spectral transmittance does however still meet the power budget in Section 9.1. The filtered spectrums $\mathcal{T}_y$, representative of fully y polarized light of the six designs are also represented in Figure 7.27. It can also be noticed that optimal filtering is not possible. We required in fact tradeoff between the number of mirrors used (reducing $\mathcal{T}_y$) and the FWHM, influencing the overall SNR power budget (discussed in Chapter 9.1). The provided configuration allows having enough quality in the spectral peaks and a reasonable filtering efficiency in the other polarization. The latter is worse in the VIS channels (background $< 2\%$), due to the fact that the permittivity contrast between bare medium and inclusion materials is lower, resulting in more leakings, whereas it is minimal to the SWIR channels (background $< 1\%$). The leakings are furthermore pronounced at the margins of the DBRs regions since for small or high filling factors the permittivity contrast is lower. Those considerations directly affect the condition number which is seen to possess a minimum in the center of the DBR bandgap in Figure 7.29 and be quasi-optimal for the SWIR channels. Due to the fact that optimal filtering of the undesired polarization is not achieved, the spectral quality of the filter at FWHM, defined in Section 5.3.4, is also affected. The $M_{0,0}$ peak of our design, being analytically the average between the presented $\mathcal{T}_x$ and $\mathcal{T}_y$ transmittances, possesses two small spectral peaks associated with the permittivities $\epsilon_{y,bottom}$ and $\epsilon_{y,top}$, which do influence the confidence in the statistical mean of the reconstructed radiance. The presence of leakings of the undesired polarization further affects the PDL module of the reconstruction and hence the condition number of the optimal reconstruction matrix, as depicted in Figure 7.29. The achievable spectral resolution depends in detail on the reconstruction method, but we claim that a spectral resolution of $R_\lambda = 4nm$ shall be achievable in the VIS channels since the peaks are resolved, and between $6-10$nm in the SWIR channels. The design may be optimized further in other iterations and, with the use of a more refined permittivity model, the sizes of the required inclusions determined. We finally suggest looking into the possibility of placing some AR coatings to further enhance or attenuate some of the resonance features in the multilayer (e.g. decrease the coupling between cavities), or investigating more in detail other possible concepts of filtering of easier manufacturing.

Regarding the unpolarized channels, the treatment is simplified as only the coefficient $M_{0,0}$ is present in the spectral finite focal transmission. It can be shown that approximately but not exactly, the transmission of the unpolarized channels is double the one of the polarized channels at un-polarized input, as represented in Figure 7.30, which shows the maximum spectral peaks of both polarized and not polarized channels against the location of the wavelength peak for all pixels. The difference between the two polarization is due to intercoupling azimuthal terms τ_{xy}, τ_{yx} and various other effects.

DBR	Usable Bandwidth $[\mu m]$	$l_{cav}[nm]$	$l_{SiO_2}[nm]$	$l_{TiO_2}[nm]$	Configurations of mirrors (on top, between, bottom)
1	0.435 - 0.55	250	85	50	3-5-3
2	0.64 - 0.73	165	122	75	4-7-4
3	0.77 - 0.865	200	146	91	5-8-5
4	0.95 - 1.12	245	171	108	5-9-5
5	1.34 - 1.55	340	240	153	6-10-6
6	1.92 - 2.2	530	332	213	5-9-5

Table 7.2: Proposed DBR arrangements, whose results are being presented. The multilayer are interfacing with air all by means of SiO_2 (at lower refractive index, to minimize reflections at the first and bottom layers). Two cavities of the same height are placed in the multilayered structure which are filled wich inclusions. Cavities are always interfacing with the TiO_2 slabs. Top, between and bottoms numbers are referring to a full stack of double-materials. For example, DBR1 consists in total of 25 slabs, cavities included. The cavity size is kept for simplicity the same for both cavities. Mirrors are sized as the closest thickness within a nm to the quarter wavelength condition at a mean refractive index in the usable bandwidth region of interest. All cavities apart from the one in DBR1 (due to height constraints) work at the $m \cong 1$ resonance mode, downsized to account for the higher permittivity of the cavity due to inclusion filling.

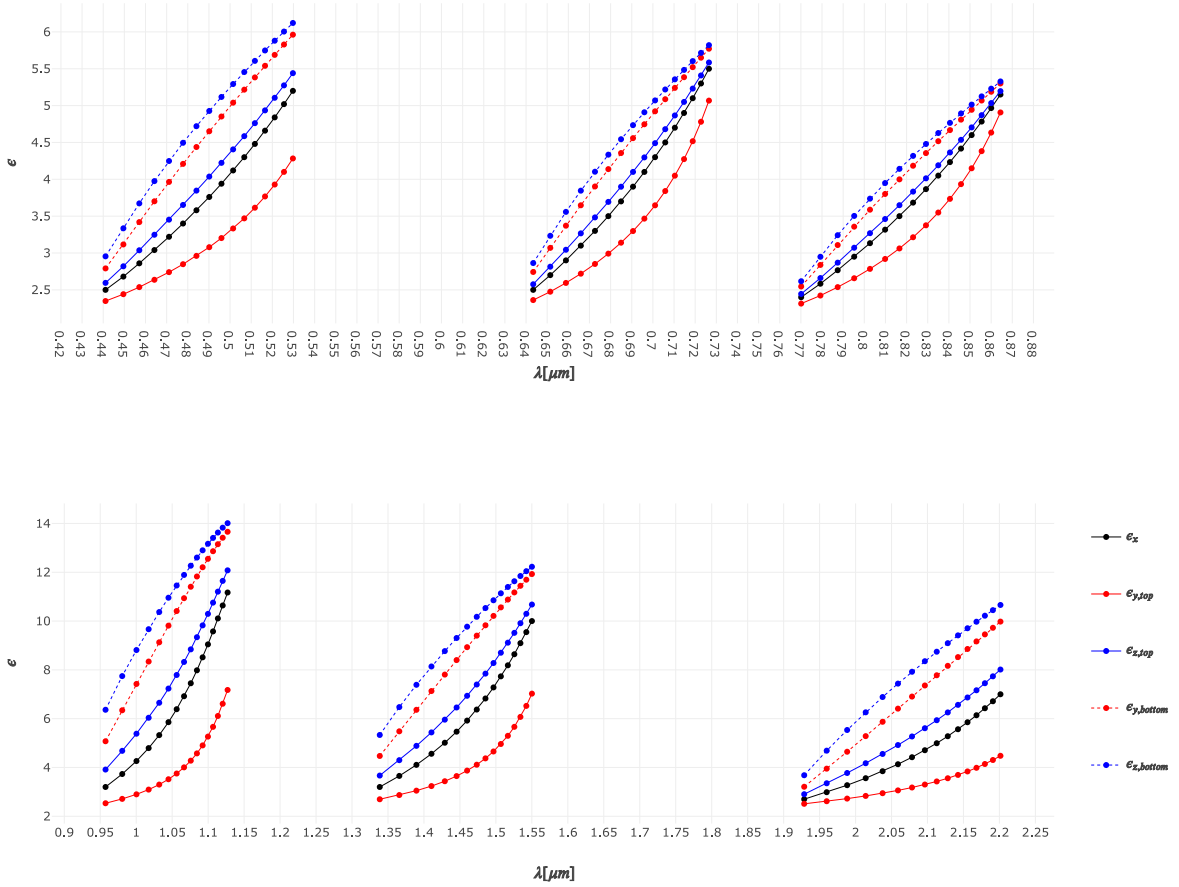

Figure 7.28: Plots of the permittivities of the two cavities in various directions (on top, in the VIS DBRs, at the bottom, in the SWIR DBRs), to achieve the previous transmission spectrums, plotted against the achieved peak of the transmission in the spectrum. The permittivities are representative of the size of the required inclusions, in the first iteration sizable from the stationary model. The permittivity ϵ_x is designed to be the same for both cavities. An aspect ratio of $AR = 5$ is used for the bottom cavity and $AR = 1/5$ in the top cavity. Permittivities ranges on the represented axes are within the range of $SiO_2 - TiO_2$ for the VIS DBRs and $SiO_2 - aSi$ for the SWIR DBRs.

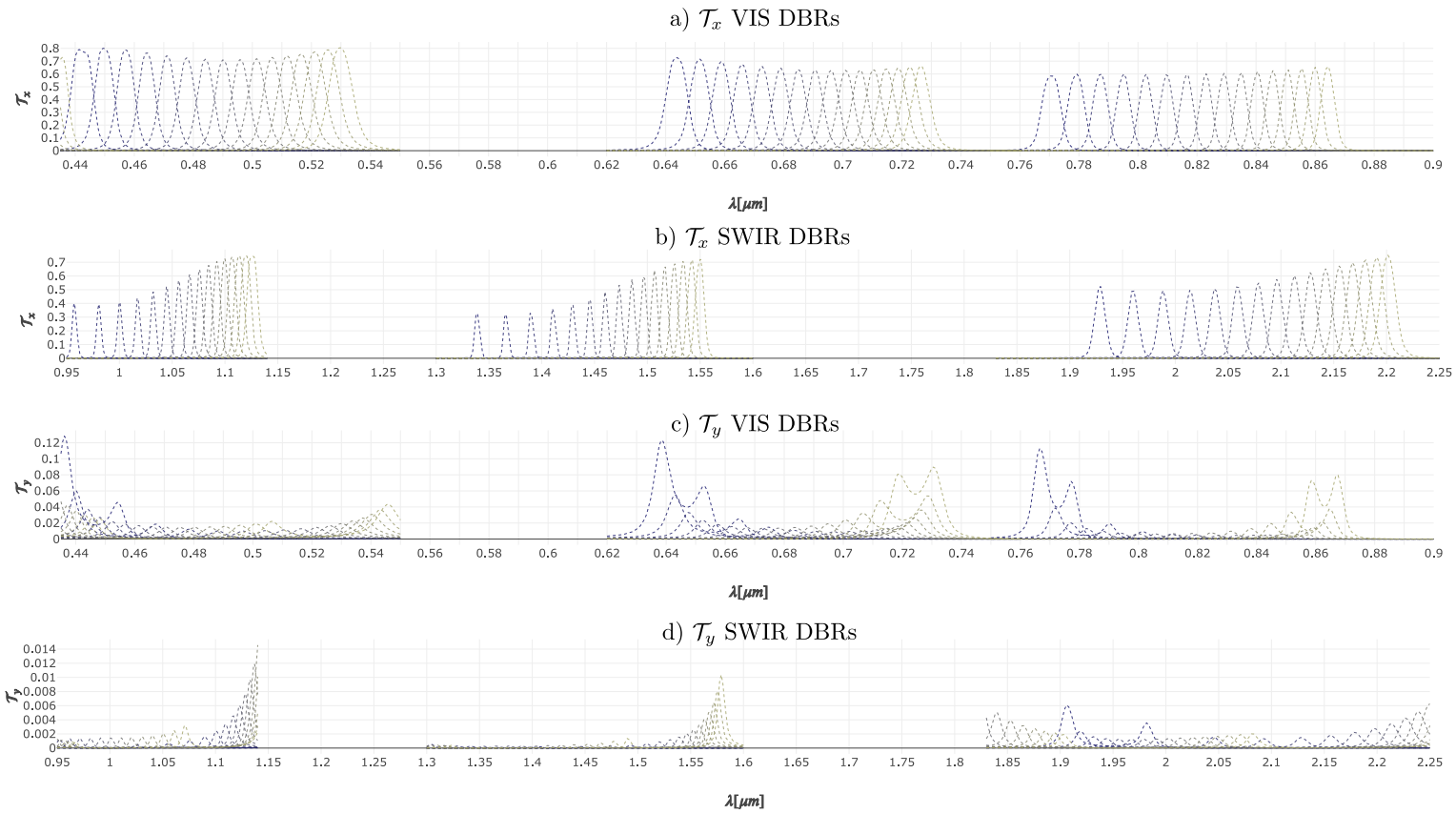

Figure 7.27: Focal finite transmission spectrums in both polarizations, for a fully polarized input in the various spectral channels of the 6 designed multi-DBRs. DBR5 and DBR6 are calulated with a resonator size of $l_r = 20\mu m$, DBR1 to 4 with a resonator size of $l_r = 10\mu m$. An $NA = 10°$ is used for all DBRs.

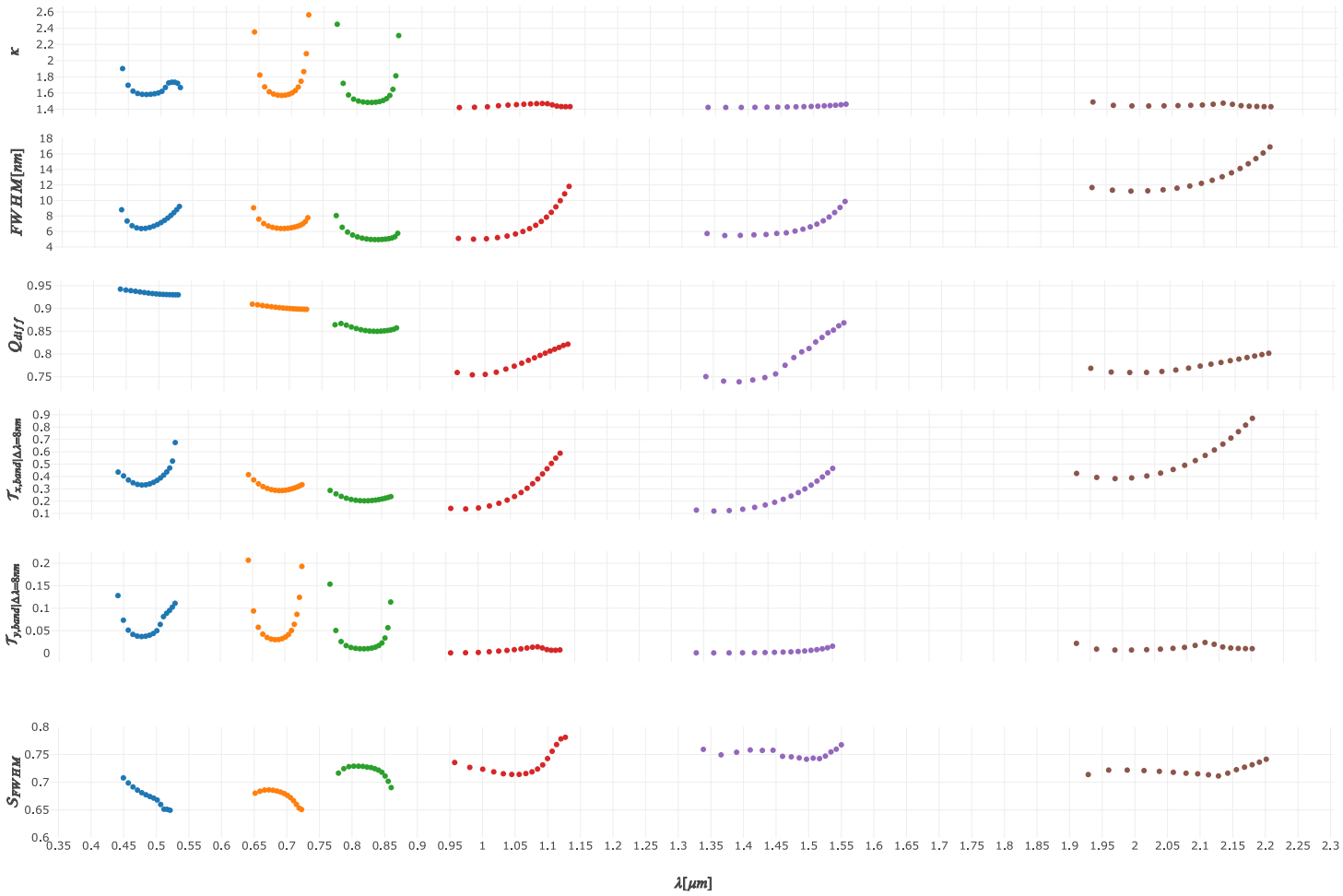

Figure 7.29: Plots of various performance parameters of the DBRs design in the full spectrum. κ representes the condition number of the reconstruction matrix of the finite focal transmissions. FWHM is the full width half maxima of the same transmissions spectrums. Q_{diff} is a diffraction quality factor, ratio between finite and wide band transmittances for each pixel. It represents the ratio of the total power falling on an enclosed region of radius $\rho_{max} = 5\mu m$ (for DBR1 to 4) and $\rho_{max} = 10\mu m$ for DBR5-6. $T_{x,band}$ and $T_y, band$ are, respectively, band transmittances for fully x and fully y polarized light, normalized on a spectral window of $\Delta\lambda = 8nm$, for all DBRs.

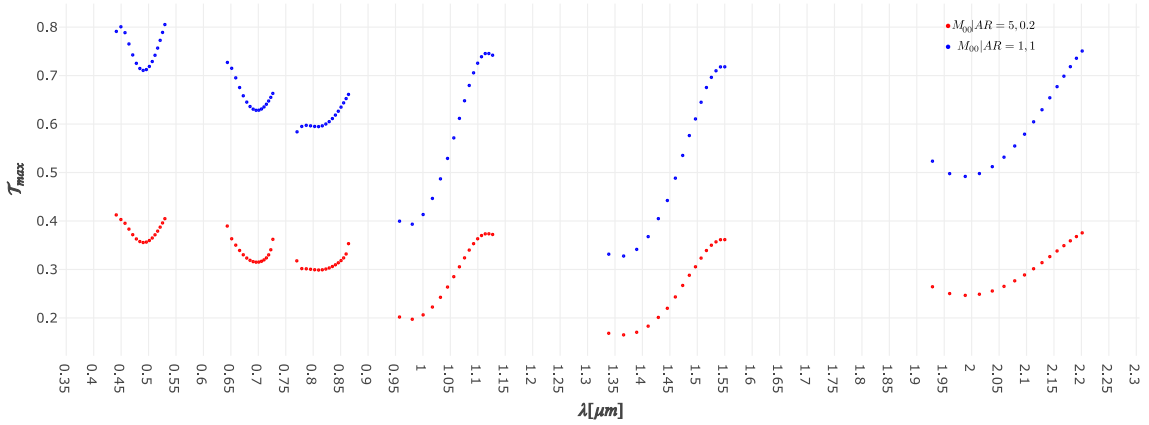

Figure 7.30: Peak (focal, finite) transmittance of the polarized channels (red) and unpolarized ones (blue), for each designed pixel. The actual distributions of the unpolarized channels are not shown for illustration clarity, but similar to the ones previously reported by means of a scaling factor. The polarized transmittance is intended for an un-polarized input.

7.6. Verification of the results

The performance results presented are based on theoretical considerations of multilayered and effective medium models, whereas the diffraction modeling simplifies the treatment proposed in 5.3.1. The plane-wave transmittances codes have been verified extensively through the use of FEM simulations with known anisotropic permittivity tensors for an arbitrary illumination. Various *Python* classes (for an optical slab, for a multilayer, for a double-DBR, etc..) have been developed for the purpose during the whole time-frame of this project and its implementation and numerical performance been tested thoroughly in various configurations. The presence of azimuthal transmittances has been verified through FEM simulations of a polarizer, discussed at the end of Appendix E. The Jones transmission and reflection matrices meet power conservation considerations, as depicted in Appendix A, to numerical precision. Diffraction formulations are, however, hard to verify at the present moment, due to lack of analytical solutions or known accessible experimental results in multilayered focal illumination. However, the treatment is based on diffraction integrals reported in [28] and the expansions meet the proof-check of Equation 5.66, which shall suffice to demonstrate that the expansion is numerically stable and accurate. Expressions of the OTF and enclosed energy are analytical integrals, which are consistent with the Airy distribution formulation for the modes $q = q' = s = s' = 0$ and physically sound for all other modes. Experimental verification of the plane-wave transmittances under arbitrary illumination is also reported in Chapter 8, for a bare cavity.

7.7. Overview of the Results

In this Chapter, we have presented a variety of results for the metasurface characterization in the spectrum and upon focal illumination. It is useful to review the main conclusions of those results:

- 6 DBRs designs, presented in Table 7.1 with their FWHM and transmittance values, can cover the required spectral ranges for aerosol detection. In the visible spectrum, to avoid losses, TiO_2 shall be used as inclusion material for the resonator particles. Due to losses of the SiO_2 in the visible range, transmissivity values are lower and the FWHM shall be traded-off accordingly. The bandwidth which can be covered is smaller than the bandgap of the mirrors, depending on the filtering and reconstruction concept selected. The 6DBRs may be integrated together for each angular band, on a lateral extension of the order of magnitude of millimeters in the along-track direction of the detector.

- Differences of p, s transmittances induce undesired polarization dependence of the non-polarized pixels, only for an aberrated not-uniform input field. This dependence can be limited by controlling the NA of focusing (Figure 7.5)

- The plane-wave transmittance of the polarized pixels shows an infinite number of azimuthal frequencies and cross-coupling terms τ_{xy}, τ_{yx} for a generic illumination angle (Figures 7.15 and 7.16)

- The wide transmittance present a sharp decrease of peak transmittance above $\theta_{max} = 10°$, widening of the FWHM (see Figure 7.17 and 7.6) and spectral shift. The band transmittance associated with such wide transmittance is, however, rather stable in the cone angle (Figure 7.7)
- The focal fields present cross-correlation terms as in [28] (see Images 7.8 and 7.19), of stronger magnitude due to differences of p, s transmittances. They can also be limited by using $\theta_{max} < 10°$. For polarized pixels, azimuthal features are further present and leakings of the undesired polarization field, out of phase.
- The PSFs spots present widening upon stronger NA of illumination and, in particular, strong spectral features, easily depictable by the definition of the finite transmittance (see Figures 7.10 and 7.13)
- The (diffracted) finite transmittances are expected to shift towards smaller wavelengths and change distribution, for small sizes of the pixel pitch, more strongly for bigger focusing angles.
- An oversizing of the pixel pitch of 50% is suggested with respect to what predicted by the Rayleigh diffraction criteria, for a focusing angle of $\theta_{max} = 10°$. Practically a non dimensional variable $\tilde{\rho}_{max} = k\rho_{max} \sin\theta_{max} \cong 6$ shall suffice for all spectral bands to maintain the enclosed energy above 80% throughout the whole spectrum. That results in a doubled resonator cell in the SWIR channels.
- The MTF possess a sharp decrease in frequency above $\theta_{max} = 10°$, is perturbated azimuthally by the polarization terms (of a few percent degrees).
- Aberrations of polarized pixels are expected to be slightly less severe due to higher values of ϵ_z, attenuating the angle dependence. These results shall still be verified functionally through FEM simulations in future work since the geometrical correlation between ϵ_z and geometry particles are not easy to depict.
- Various filtering concepts have been analyzed to filter the undesired polarization peaks in order to improve the available bandwidth without jeopardizing the condition number of the reconstruction. The more promising ones consist in the use of multiple DBRs cavities, to be matched properly, and use of dispersive scatterers (for example, by inducing Mie or Lattice resonances in the structure). Attenuation with the latter method is theoretically possible but shall still be proved functionally through more detailed (FEM) simulations, whereas the first method is more grounded.
- The multi-DBR filtering technique has been down-selected for preliminary estimations and the DBRs design re-optimized to account for cavity coupling and attenuation effects. The performance of 96 pixels has been analyzed in the generality of all their performance parameters, showing that attenuations $< 2\%$ are achievable, with FWHM ranging from $4.5-9[nm]$ in the VIS and $5-17[nm]$ in the SWIR. Diffraction performance is acceptable but to be reviewed for the first pixels of the SWIR DBRs. The condition number is acceptable for VIS and almost ideal for the SWIR channels. Transmission peaks possess good quality. Focal finite transmission of the polarized channels upon non-polarized field ranges from $[0.2 - 0.4]$. Values of the required permittivities are reported and can be used for preliminary sizing of the inclusions, to be iterated over FEM simulations or other techniques.

8

Fabrication & Experimental Results

Disclosure *The structures have been designed by the research group in TNO, in collaboration with TU/e, Friedrich Schiller University of Jena, which also performed the analysis hereby reported, soon to publish in a paper [4]. The manufacturing has been performed by the Fraunhofer Institute for Applied Optics and Precision Engineering & Nonlinear Physics Centre, the Australian National University. Some of those results are included in this report, with kind permission of the involved parties. No rights are reserved for the results in Figures 8.1, 8.6 and 8.8 presented in this Chapter.*
Experimental results are available for preliminary structures including DBR with bare cavity and with inclusions. We discuss the experimental setup and manufacturing process, as well as the measurement setup. We perform an analysis of the polar off-angle measurements of a bare cavity and demonstrate the soundness of the multilayer model for its performance characterization. We analyze the optical results of the patches with inclusions discussed in [4] and discuss the results in terms of the developed theory. Unfortunately, measurement under focused illumination and over azimuthal variations have not been performed, so neither thermal, vacuum or radiation tests. The focus of this first manufacturing phase was showing a demonstration of spectral reconstruction at normal incidence, which has been verified. Subsequent tests shall be planned and the optical and measurement setup properly designed to complete experimental characterization of the structure.

8.1. Manufacturing Techniques: a quick review

Manufacturing techniques of nanostructures of Si fall in the category of lithography manufacturing, with similarity to the integrated circuitry manufacturing. In previous reports, we discussed various imprinting techniques, which can also be revisioned in [62]. In this Section, we quickly brief the reader on vapor deposition processes, used for the manufacturing of the structures under revision. Vapor deposition techniques are used to deposit coatings. Depending on how the thin-film is created, two main categories are distinguishable:

- *CVD*, or *Chemical Vapour Deposition* where chemical reactions between precursors are used to create the thin-film. When used in conjunction with plasma, (*PECVD*) such techniques allow deposition at lower temperatures. The plasma is created between two electrodes by a reactive gas. Hydrogenation and plasma density are important parameters to monitor in the process in order to ensure correct material properties and uniformity [63].
- *PVD* or *Physical Vapor Deposition*, where the thin-film is created by some physical process like sputtering (creation of plasma by a collision of two gases) or electron beam evaporation is used for deposition. Also this in this process plasma can be used (PEPVD) to operate at lower temperatures. In particular, the process can be optimized to manufacture optically resonant monolithic Bragg cavities [64] and mirrors. Optical properties of the mirrors can be tested in-situ during the manufacturing process to monitor tolerancing.

8.2. Manufactured Structures & Geometrical Measurements

Various patches of multilayered structures with mirrors of SiO_2 and TiO_2 have been fabricated by [4] and preliminarily tested for demonstration purposes. Those include:

- Patches of a multilayer with a bare cavity, for measurement of the DBR performance. Those have been tested at normal incidence and off-angle for $\phi = 0$. The analysis of the experimental results of those measurements is discussed in Section 8.4
- Patches of the multilayer with inclusions, for measurement of the two spectral peaks. Those include patches with elliptical inclusions and gratings inclusions. This choice was based on the evaluation of design with a reconstruction of both spectral peaks, but this aspect is unimportant for our analysis.
- A pixelated patch mounted on a commercial CMOS sensor

The structures with inclusions are comprehensive of a total of 29 alternating layers. The top mirrors stack, bottom mirrors stacks and cavity are represented in Figure 8.1 , which shows the manufactured structures and the nanostructures. To deposit the mirrors, a plasma-enhanced *physical vapor deposition*

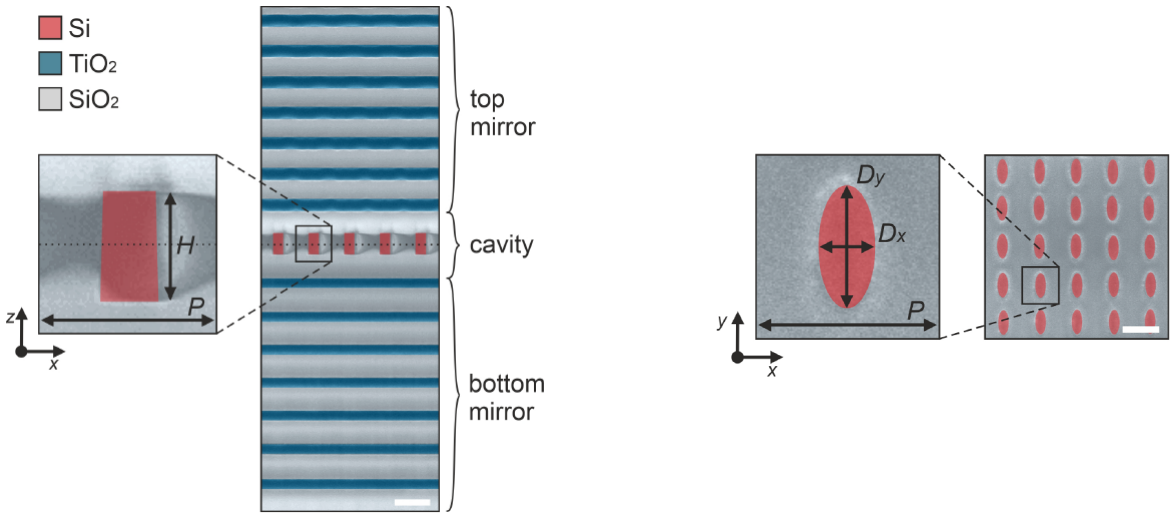

Figure 8.1: left) Manufactured multilayer with false-color for identification of the materials. right) Manufactured inclusions and diameters dimensions. All copyrights to [4]

method (PEPVD) has been used. During the deposition, it is important to avoid polycrystalline growth of the materials to control surface roughness, absorbance and scattering effects [4], which limits the thickness dimensions of the layers. Note that the manufactured top mirror and bottom mirrors are not matched at the same wavelength (e.g. deviate from quarter wavelength condition), which is undesired and has some effects in the spectral transmission calculated. Moreover, the top mirror has been manufactured with a different thickness, for reasons discussed in [4]. On average, the bottom stack thicknesses are centered around $320nm \pm 20, 120nm \pm 20$ for respectively the SiO_2 and the TiO_2, whereas the upper stack thicknesses are centered around $230nm \pm 10, 170nm \pm 10$, except for the upper one of $\cong 100nm \pm 20$. That results in two different bandgaps of the separate stack and, overall, a smaller bandgap of the whole multilayer (see next Section).
The cavity of $l_{cav} \cong 900nm \pm 50$ is embedded with elliptical inclusions of various aspect ratio (with diameters varying from $140nm$ to $360nm$) all with a height of $H = 300nm$ made of amorphous hydrogenated silicon. Details manufacturing are addressed in [4], for which the following steps can be summarized:

- a) Deposition by *plasma-enhanced chemical vapor deposition (PECVD)* of $a-Si:H$ using a gas source
- b) Deposition of a Chromium hard mask ($30nm$)
- c) Spin-coating of an additional resist
- d) Development of the resist with the patterning of the Chromium (by *ion beam etching*)
- e) Etching of the Chromium masking on the Si layer by *inductively coupled plasma reactive ion etching*.
- f) Removal of Chromium by acetone and etchant agents

After production, unfortunately, contamination by Chromium has been observed which is due to the mixing of Chromium with other materials and improper cleaning in step f). Chromium is a lossy material, which resulted in strongly observed losses in the transmission spectra. In general, contamination may be avoided in similar well-developed manufacturing processes, so that the measured transmission intensity won't be representative of a real optimized manufacturing process. The contamination can be visualized also by inspection of the SEM images (small lines are present above the inclusions). The individual resonators present some dimensional variations across the transverse plane but are qualitatively of the desired shape. The maximum tolerancing bounds on their diameters are around $\pm 8nm$. Tolerancing between the transverse placement of the inclusions cannot be unfortunately estimated from those SEM images.
It is also clearly observed that, within the presence of the nanostructures, the top mirrors present roughness. A planarization has been performed after their deposition which limited the roughness variation to $A_w \cong 15nm$. It has been proved in [4] by FEM simulations that with the present configuration and below $A_w \cong 40nm$ the decrease in plane-wave transmission peak is $\Delta\mathcal{T} < 5\%$. However, that result is valid for normal illumination and did not include diffraction and phase effects. To minimize the surface variation in the well-developed manufacturing process, it is suggested to perform detailed studies on etching geometries and dynamics prior the manufacturing. An inclination in height of $\varphi \cong 3°$ is also observed in Figure 8.1, which mainly affects the volumetric filling ratio of the cavity. The diameters D_x, D_y shall in practice be slightly overdesigned (of $\Delta D = \sin\varphi H$) or referenced to the medium section, in order not to observe a spectral shift due to this effect.

8.3. Measurement Setup

The spectral measurement setup used in [4] is represented in Figure 8.2. It consists of:

- a broadband halogen source (*SLS301, Thorlabs, Inc.*)
- a collimation optical unit, to simulate plane-wave illumination
- a linear polarizer mounted on a rotational unit to control the angle of polarization
- a positioning system used to orient the structure.
- an aperture and a lens system to focus the light into the tip of a fiber optic
- a coupled spectrum analyzer with a resolution of $0.02nm$ (*AQ6370B*, Yokogawa)

The aperture is movable and sizeable, in order to analyze various patches of the sample. This choice has resulted useful in the measurement since patches uniformity has been observed to be varying considerably in the transverse direction. Some regions of the patches have shown to present a higher transmission spectrum when the aperture was set to $20\mu m$.
In order to avoid re-orientation of the overall setup, the multilayer is re-oriented by the positioning system, to discern between $p-s$ polarization states (see Section 8.4).

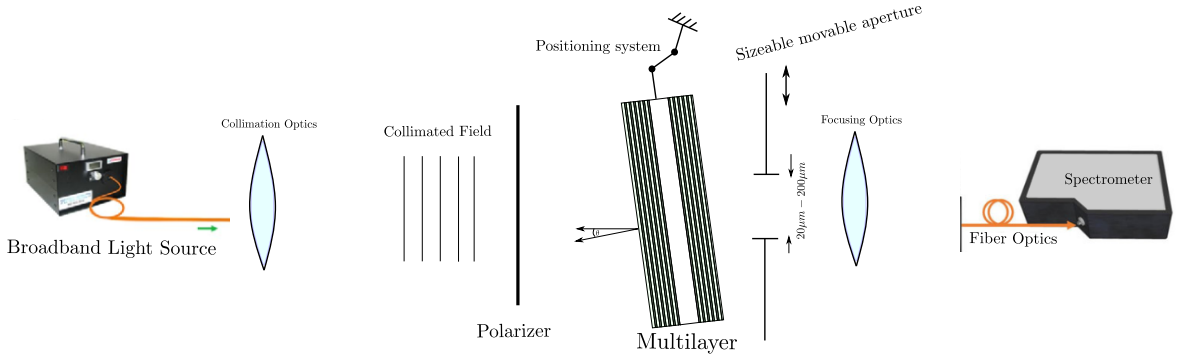

Figure 8.2: Spectral measurement setup used for plane-wave illumination of the manufactured structures

The measurement of the structure has been carried out by means of a focused ion beam and a scanning electron microscope. Their resolution is limited by optical power (not to deteriorate the structures) and measuring time.

8.4. Angle Measurements of the bare cavity

Measurements of the bare cavity without inclusions have been performed also in polar angle variation. Unfortunately, azimuthal angle measurements and measurements of the patches with inclusions have not been performed, since they would have resulted in too many changes in the optical setup and measurement software tools.

In order to avoid modification of the experimental setup, the patches have been rotated on one of the transverse axes during the measurement, whereas the remaining setup (focusing optics, aperture, spectrometer) orientation was left unchanged. By rotating the polarizer, p and s polarization can be discerned. When the polarizer is oriented as the rotation axis used to move the structure, the incoming plane-wave is s polarized. When the polarizer is perpendicular to the rotation axis, the incoming plane-wave is p polarized. Since the detector and fiber-optics are not moved, it is assumed that the complete plane-wave transmittance is measured at the detector without any geometrical apodization due to its polarization. Hence the intensity transmittances measured in this setup, at means of tolerancing in the polarizer angle are given by:

$$\mathcal{T}_{pp} = |\tau_{pp}|^2 \qquad \mathcal{T}_{ss} = |\tau_{ss}|^2 \tag{8.1}$$

The measurements have been carried multiple times to lower the noise and on different points of the patches structures. Moreover, the input spectral intensity is referenced to the same measurement setup by only removing the multilayer from the configuration. It is supposed that reflection coupling between multilayer and all other components can be neglected. Figure 8.4 shows those measurements for three angles and the two polarization states. As observed in the measurements, p and s polarization shift as expected and further depart from each other, s polarization always preceding the p polarization in the spectrum. Such behavior is in accordance with a formal multilayer solution. In the plots, also a fitting solution is represented. Since the geometry of the multilayer is roughly known, we have used a simple optimization tool to fit the measurements with the closest multilayer solution. The mirror lengths of such fitted solutions are in agreement, by variation of $\pm 2nm$ with the manufactured dimensions, which is well within the tolerancing of the measurement. However, that's likely not the global optimum solution since it poorly represented the initial part of the spectrum, which strongly depends on the tolerancing of each individual mirror, not precisely known. The cavity dimension, in particular, settles at $872nm$, even though a first resonance solution is also possible at $388nm$. It has been observed that, for the setup under consideration with not-matched DBR, also the tolerancing on the mirrors heavily influences the position of the spectral peaks and not only the cavity. In the represented fits, the same geometry and configuration are used for all angles and polarizations. The fitted solution well represents the spectral behavior, proving that the multilayer model can be used to estimate the performance of the real structure also off-angle. However, a decrease of the intensity peaks is observed with respect to the (lossless) fitted solution.

A striking observation, at first surprising, is that the s polarization decays off-angles much more than the p polarization. To explain such effect, we have included losses in the above optimal fitted multi-layer

solution, separately for the SiO_2 and TiO_2 materials. We have observed that also theoretically, the s polarization decays in presence of loss much more strongly than the p polarization. Simulated value for ideal case, artificial losses of:

$$k_{SiO2} = 1.2 \cdot 10^{-4} \qquad k_{TiO2} = 1 \cdot 10^{-7} \tag{8.2}$$

and measurement values are represented in the correlation plot in Figure 8.3a) and 8.3b) for respectively spectral shift and transmission peak. The former correlation with the multi-layer fit is rather good, differences being also due to uncertainty on the mirrors dimensions and exact refractive indices. Some higher uncertainties come with the measurement of the peak value, since during the rotation of the structure it may be that misalignment is present. That may result in some differences in the spectral behaviors since the cavity in the patches has been determined to be not uniform. That's likely also the reason for the fastly varying behavior of the measured peak values in Figure 8.3b). Moreover, the peak may be undersampled. We have reasonably assumed a tolerance level of $\Delta\mathcal{T} \cong 0.025$ for both polarization. The correlation of the measurements with the artificial losses is not optimal, implying that the losses may further be angle-dependent or some polarization-dependent apodization in the s polarization was present in the setup. Both graphs, however, imply a faster decay of the s polarization when compared to the variation of the p polarization: the off-angle behavior of the spectrum (especially when un-matched multilayer like the one here under discussion is considered) is a complex analytical function. In general, a variation of the spectrum in the s polarization is always more pronounced (spectral drift, changes of FWHM), which may explain intuitively this effect. A careful observation of the measurements also shows that FWHM widens in the s polarization in the presence of losses more than expected, which shall be further investigated. The values in (8.2) are not necessarily the optimal ones, in fact, the fitting problem presents multiple local optimums of cumbersome determination. The given values are higher than the one expected for the materials (thin-layer). They may, however, be representative of some small contamination in the manufacturing process (but not the chromium contamination issue discussed earlier, which instead affects only the patches with inclusions). Losses have hence an important non-negligible effect in the overall transmission spectrum when considering off-angle behavior.

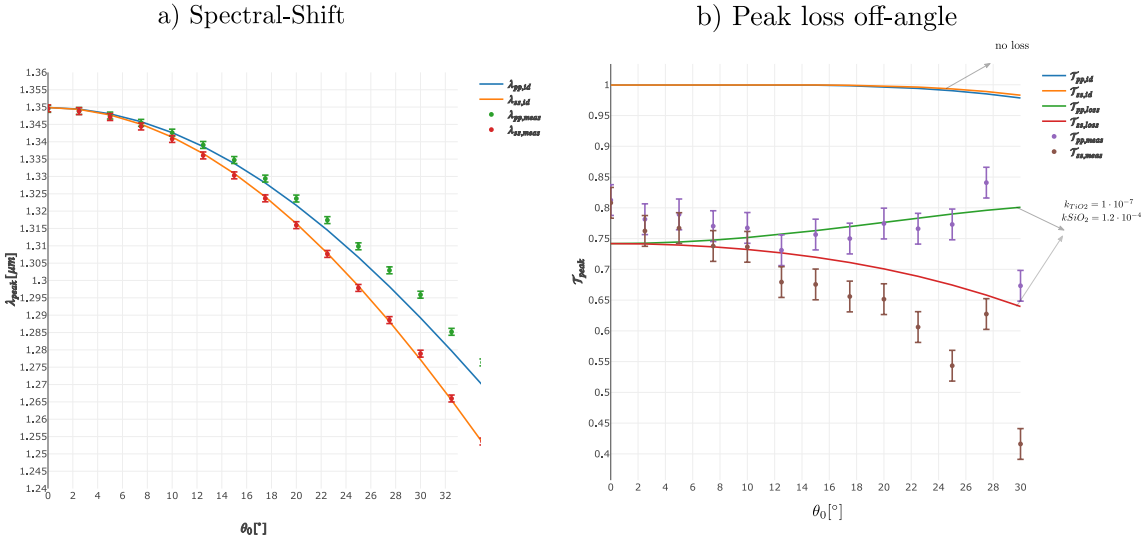

Figure 8.3: a) Spectral-shift off-angle from the measurement and the multilayer-fit (almost independent of loss) b) The peak transmission in intensity is plotted for the various angles and the two polarization states. The estimate such, cubic spline interpolation has been used in the measurements. $\mathcal{T}_{j,id}$ represents the ideal intensity transmittances as estimated from the optimal multilayer fit. $\mathcal{T}_{j,loss}$ represents the transmittances derived from the same model by introducing a small artificial loss in both materials. Finally, $\mathcal{T}_{j,meas}$ represents the measured intensity transmittances, with an assumed uncertainty level of ± 0.025.

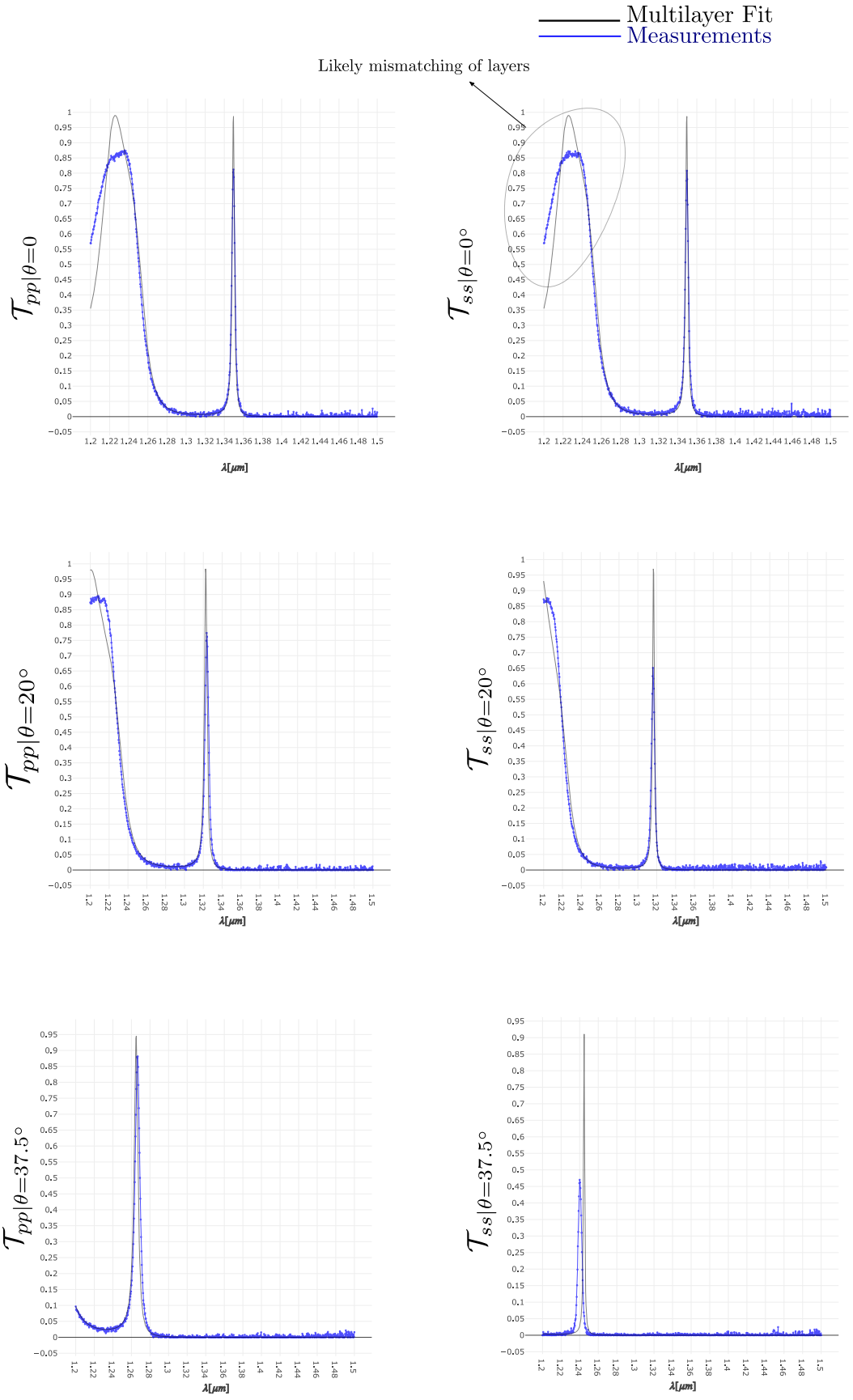

Figure 8.4: Orizontally, from left to right, the p and s polarization intensity plane-wave transmittances. Vertically, the polar angles (only three represented for succinctness). Zoom in for improved visibility.

For completeness and further use, we also report the spectrums of the reflectivity of the two DBRs (top and bottom) and of the total multilayer best fit solution, over a bigger wavelength region in Figure 8.5. As clear from the plots, the two DBRs are not matched, which results in a slightly smaller DBR bandgap than initially expected.

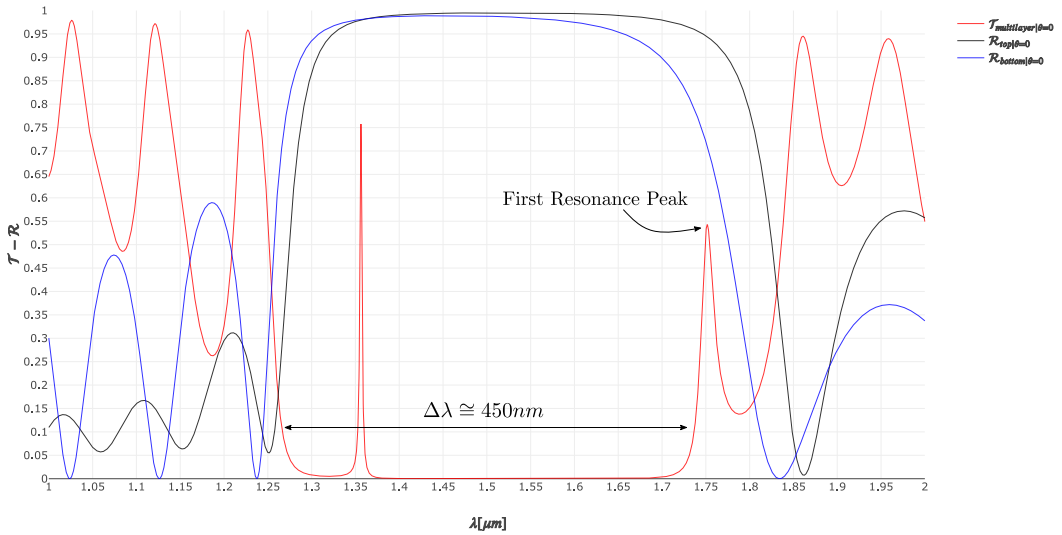

Figure 8.5: In red, the intensity transmission spectrum of the multilayer fitting the experimental results. In blue, the reflectivity of the bottom stack of mirrors ($\cong$ 98.9%). In black, the reflectivity of the upper stack of mirrors, of better performance ($\cong$ 99.5%). The spectrums are inclusive of losses.

8.5. Spectral measurement of nanoresonators patches

As mentioned above, various inclusions design has been manufactured. The manufactured design was meant to demonstrate reconstruction based on two spectral peaks with an arrangement of six pixels, one of them presenting a grating. The dimensions of those inclusions are summarized in Table 8.1, together with their measured spectral peaks. The spectrum measurements of the six pixels are represented in Figure

-	$D_{x[nm]}$	$D_{y[nm]}$	$\lambda_x[\mu m]$	$\lambda_y[\mu m]$
Pixel 1	335 ± 8	145 ± 6	1.463	1.431
Pixel 2	202 ± 5	282 ± 5	1.445	1.462
Pixel 3	162 ± 4	247 ± 4	1.430	1.446
Pixel 4	145 ± 6	335 ± 8	1.431	1.463
Pixel 5	282 ± 5	202 ± 5	1.462	1.445
Pixel 6		134 ± 5		1.432

Table 8.1: Measurement of the elliptical inclusion. Pixel from 1 to 5 are elliptical. Pixel 6 is a grating. The measured location of the spectral peak are also reported.

8.6 in logaritmic scale, as presented in [4]. Spectral peaks associated with the two polarization directions are clearly recognizable in the Figure, on a noisy background. Due to the presence of the Chromium contamination, transmissivity values are $\mathcal{T} \cong 0.2$, but above the noise floor. Moreover, FWHM is also increased with respect to the expected one (see below). To minimize noise, multiple measurements have been performed and the best patches selected. It shall be stressed that in successive manufacturing phases Chromium contamination can be controlled and transmissivity values significantly higher so that the results are qualitatively representative of the spectrum behavior only. To analyze those results from the background introduced in the Thesis, we retrieved the permittivity values of the effective cavity by means of the anisotropic solver developed and further compare those with the ones predicted from the stationary model for the considered structures. In the process, we assume the effective permeability

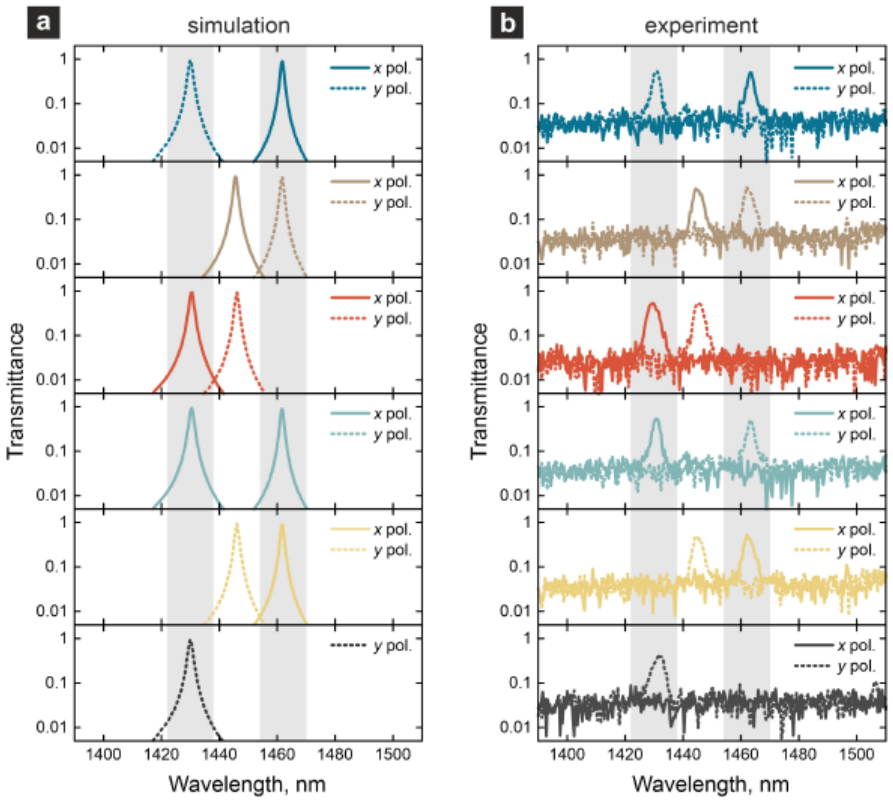

Figure 8.6: a) Illustration of peaks position for the various pixels b) Measured spectral transmission of the six pixels arrangement. All copyrights to [4]

to be unitary since inclusions are supposed to be not in the resonance regime. The mirrors design of the nanostructures samples is the same as the bare cavity, so that we may use the previously fitted multilayer solution for the top and bottom mirrors. The cavity resonances curves of this unmatched DBR, analytically derived, are represented in Figure 8.7. It follows that the spectral peaks in Table 8.6 are achieved with the permittivies in Table 8.2, where those permittivies are compared with the one predicted from the stationary model and, further, with a best fit which frees the effective volume c and the aspect ratio AR as follows:

$$c_{fit} = \frac{c_{real}}{\mathcal{Q}} \qquad AR_{fit} = AR_{real}^{\zeta} \tag{8.3}$$

and converges at $\epsilon_{err} = 10^{-10}$. It is seen that the stationary model, when used with the real geometrical dimensions, always under-estimates the permittivities but overestimates the contrast between permittivities. Roughly, the cavity seems to behave as it would be predicted by using double the real filling factor[1]. It can be shown by FEM (and theoretical considerations) that the value of achieved permittivity depends on the electric field magnitude in the inclusion region with respect to the one of the bare cavity. A higher value of permittivity correlates to a higher field in the inclusion. The value of $\mathcal{Q}$ may be further related to the presence of standing waves in the cavity. We may envision a corrected stationary model which takes into account the distribution of the field in the multilayered structure in an iterative solution method, to account for those effects. It further seems that the permittivity contrast achieved by the real structure is also smaller than what we would predict initially. Such deviations were already expected as discussed in Section 5.3.2, since the stationary model is intrinsically simplified not taking into consideration frequency dependence and coupling between the resonators. Unfortunately, there are not enough data-points to provide further correlations, but the values of best fit $\mathcal{Q}$ and ζ seem rather

[1] we could argue on whether the filling factor shall be calculated with the entire bare cavity volume or the one corrected for the presence of the inclusion. The value of $\mathcal{Q}$ increases of $\cong 3\%$ roughly with such correction. The value of $\mathcal{Q}$ may also be related to the extinction length. The effective cavity height leading to c_{fit} is roughly $440nm$ slightly bigger than the inclusion height

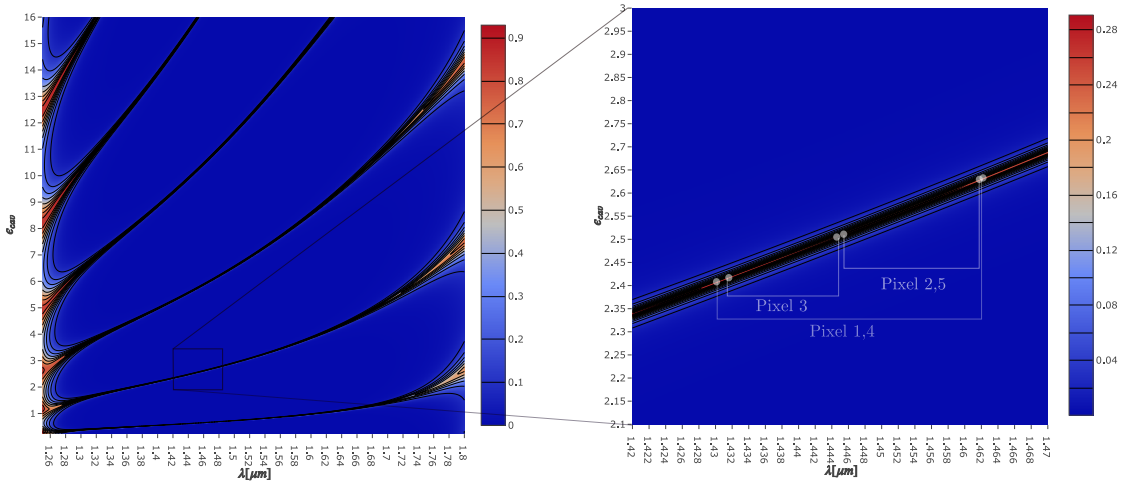

Figure 8.7: Cavity resonance curves of the DBR structure under study, representing effective permittivity of the cavity versus resonance wavelength. On the right, the resonances of the pixels are represented. To match the value of transmissivity module, an artificial loss of $k = 1.2 \cdot 10^{-3}$ has been included in the effective refractive index ($n_{eff} = \sqrt{\epsilon_{cav}}$). The resonance curves depend on the height of the (effective) cavity taken here as $l_{cav} = 0.87 \mu m$.

correlated. It may be interesting in future work to analyze also dependence on the variable $\sqrt{D_x D_y}/P$ and P/λ_{peak}, P being the lattice period.

	$\epsilon_{x,r}^{matching}$	$\epsilon_{y,r}^{matching}$	$\epsilon_{x,r}^{stationary}$	$\epsilon_{y,r}^{stationary}$	$\mathcal{Q}$	ζ
Pixel 1	2.6066	2.408	2.344 ± 0.02	2.234 ± 0.013	0.4775	0.8117
Pixel 2	2.5011	2.6004	2.283 ± 0.014	2.333 ± 0.015	0.4901	0.8876
Pixel 3	2.402	2.5012	2.224 ± 0.01	2.267 ± 0.02	0.4334	0.9092
Pixel 4	2.408	2.6066	2.234 ± 0.013	2.344 ± 0.02	0.4775	0.8117
Pixel 5	2.6004	2.5011	2.333 ± 0.015	2.283 ± 0.014	0.4901	0.8876
Pixel 6	Unknown	2.414		-	-	

Table 8.2: Permittivies retrieved from the resonances curves (matching the measured spectrum, only real permittivity is shown) and permittivies which would be derived from the stationary model in Section 5.3.2. Those are subject to the geometrical tolerancing. Calculation has been performed with $l_{cav} = 0.870 \mu m$ and a lattice size $P = 500 nm$ as in [4]. Material properties are taken as follow: $n_{aSi:H} = 3.7$, $n_{SiO_2} = 1.45$, $n_{TiO_2} = 2.285$ as suggested in [4]

To describe the Chromium loss, we further consider a complex effective refractive index. The retrieved value that matches transmission peaks of $\mathcal{T} \cong 0.28$ are $\Im\{n_{cav,x}\} \cong \Im\{n_{cav,y}\} \cong 1.2 \cdot 10^{-3}$. By using a simple volume averaging of effective properties and assuming that such loss if fully due to Chromium, such loss would be consistent with a volumetric filling factor of $c_{Cr} \cong 0.5\%$ (half-percent), which is rather small but has a not-negligible effect. Our results seem consistent with transmission decay depicted in [4] which performed a similar analysis by means of FEM simulations. In the same reference, an increase of FWHM has also been associated with the presence of Chromium. We verify that inclusion of a loss results in the increase of the FWHM, because loss acts non linearly on the transmissivity spectrum.

8.6. Polar measurements over angles of polarizations

During the experiment, the orientation of the polarizer has been varied to sample the 2π spectrum. From the introduced model and theory, we expect a known results from this operation. One shall in fact consider the plane-wave spectral directional transmittance defined in Section 5.3.3, which leads to the subsequent expression of the transmitted Stokes parameter:

$$s_{(\lambda)}^{out} = \mathbf{M}_{0(\lambda)} \begin{pmatrix} 1 \\ p\cos(2\gamma_0) \\ p\sin(2\gamma_0) \end{pmatrix} \qquad \mathbf{M}_{0(\lambda)}^T = \begin{bmatrix} M_{00} \\ M_{01} \\ M_{02} \end{bmatrix} \tag{8.4}$$

In the above expression we always refer to a small transmittance integrated over the spectral resolution of the spectrometer (not a purely spectral quantity). Using the expression (E.9) in Appendix E for the Jones matrix of the structure, the following relationships applies at normal angle:

$$\mathbb{J} = \begin{bmatrix} I_{0,0} & 0 \\ 0 & I_{1,0} \end{bmatrix} \qquad \begin{bmatrix} M_{00} \\ M_{01} \\ M_{02} \end{bmatrix} = \frac{1}{2} \begin{bmatrix} I_{0,0} I_{0,0}^* + I_{1,0} I_{1,0}^* \\ I_{0,0} I_{0,0}^* - I_{1,0} I_{1,0}^* \\ 0 \end{bmatrix} = \frac{1}{2} \begin{bmatrix} \mathcal{T}_x + \mathcal{T}_y \\ \mathcal{T}_x - \mathcal{T}_y \\ 0 \end{bmatrix} \tag{8.5}$$

where we have considered that for continuity of fields the values of $I_{i,0} = 0, \forall i > 1$ and that the inclusions are oriented as the cartesian frame. The above expression is valid for nill cross-coupling polarization since the Jones matrix is assumed diagonal. Moreover, the spectrums $\mathcal{T}_x$ and $\mathcal{T}_y$ are not overlapping significantly. The transmitted intensity, considering the degree of polarization of the incoming light $p = 1$, is proportional to:

$$s_{(\lambda)}^{out} = \frac{1}{2} \left[(\mathcal{T}_x + \mathcal{T}_y) + (\mathcal{T}_x - \mathcal{T}_y) \cos(2\gamma_0) \right] \cong \begin{cases} \mathcal{T}_x \cos^2 \gamma_0 & \forall \lambda \cong \lambda_x \\ \mathcal{T}_y \sin^2 \gamma_0 & \forall \lambda \cong \lambda_y \end{cases} \tag{8.6}$$

The provided expression can be plotted in a polar angle. In Figure 8.8, this plot is represented, so the experimental results as retrieved in the experiment (only peak wavelength represented). The correlation with the above expression is excellent, which proves that the Jones matrix above can well represent the structure at normal angle and that cross-coupling polarization terms are not present (also valid only for normal angle). Having performed the test also upon not-normal illumination (and significant angles), a more intricate pattern would have been found, varying in module also depending on the azimuthal orientation ϕ which does not play any role at normal incidence. This test and correlation provide an important result, proving that the Jones matrix of the device can be described and retrieved from measurements. It is suggested to consider in the future test also not-normal illumination to retrieve all other parameters of the Jones matrix, which expected expression are depicted in the Appendix E or are in general given by the Zernike transform introduced. The latter measurement may be more cumbersome due to noise requirements when small polar angles are used. A way to retrieve the other parameters is by performing at generic illumination multiple measurements and expanding in a Fourier series the measurements found. The results of those experiments, upon further manipulation, shall be compared with the theoretical expression of Zernike Transforms derived in Chapter 7. The measurement also proves that the structure possesses only two resonant frequencies in the spectrum[2] for all polarization angles and that those are exactly oriented as the nanostructures (assumed in the derivation), which may be argued at first.

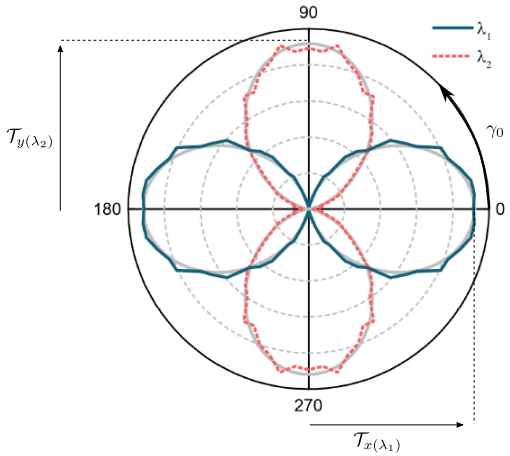

Figure 8.8: Polar plot of various measured transmittances at varying angles of polarization of the polarizer for two wavelengths. The plot is superimposed on the polar plot expected from Equation (8.6). Adapted for notation from reported plot in [4]

[2]assumed that it excites only one cavity resonances in Figure 8.7 for each permittivity

IV

Integration Analysis & Discussion

9
Integration Analysis

In the present Chapter, we apply the detailed performance analysis above introduced for the integration of the filter, as part of the Optical System. The choice of a detector able to cover the spectral ranges of interest and its performance are analyzed, which enables to explicit the final power budget of the pixels designed in Chapters 7. We show how SNR requirements can be met at the same level of specification of 3MI and provide simple engineering performance maps of the filters. Preliminary tolerancing and thermal analysis complement such an integration study. We explicit a final list of integration and definition requirements to be considered when using the spectral filter and elicit some of the obvious benefits of using the concepts in terms of mass and system complexity.

9.1. Power Budget

With the definition of finite transmittance above introduced, we possess enough information on the metasurface transmission response to perform a power budget. For the purpose, a radiance reference spectrum shall be used and the performance of the detector be also characterized.

9.1.1. Reference Spectrum

For the radiance estimation, the internally available dataset of Sentinel 7 MAP (see [7]) has been used, which is reported in image 9.1a). The dataset contains calibrated *Top of Atmosphere* radiances values in various illumination conditions, as maximum and minimum radiances. For power budget estimations, the reference spectrum shall be used, with the understanding that real SNR may be strongly affected by illumination conditions and time of observation. The *cloud* dataset contains also the maximum reference spectrum which shall be tolerated in dynamic range by the detector. We have verified consistency between the reference spectrum used and the freely available GOME Level1B Radiance Products, reported from ESA in *.nc* metadata. In Figure 9.1b) the degree of polarization present in the datasheet has also been represented. The observed decrease for IR wavelengths is consistent with the one reported in [65] and other resources, which also clarifies regarding angles of polarization variations. It naturally follows that the statistical mean of s_1, s_2 is also significantly lower than the one of s_0, which impacts the confidence level of the reconstruction of the former two parameters more than the one of s_0. To maintain the design flexible for our science case, we assume that the angles of polarization realizations have all the same statistical likelihood, but these considerations may be reviewed in future work to optimize the orientation of the structure accordingly. We further suggest in future work to analyze the spatial distribution of radiances for the altitudes discussed in Chapter 6 and subsequent image creation, using the considerations of Section 5.3.9; addition of a BDRF model, atmospheric reflections would be further required for a more detailed study on the input Stokes parameters. It is further assumed that the undesired sunlight and other stray-light sources are further minimized by the use of baffles in the optical system. Finally, it has extensively been reported, and depicted also in our formulation by Equation 5.82, that the radiance fall-off at such high FOV is not negligible (achieving also a factor of 1/10). In 3MI, the design of specially engineered aspheric lenses has been implemented to prevent this fall-off and increase the area of the entrance pupil for the off-angle sub-bundle [2]. We will assume a similar architecture shall be designed also for the present optical system, such to preliminarily neglect the radiometric fall-off in our power budget calculation.
Unfortunately, the provided dataset does not include radiances above $\lambda = 1.1\mu m$. To suffice for the SWIR bands, we extracted from [5] the radiances values there reported, measured from Landsat-8 OLI for vegetation and desert background. We compare those with the reference spectrum of S7 in Figure

9.1c), which shows better agreement with the vegetation spectrum. In the reference spectrum, the absorption peaks are not present. The covered DBR windows are also reported in Figure 9.1c). The critical DBRs for power budget is likely to be DBR5 and DBR6, considered also the decay of radiance with respect to the decay of photon energy for SWIR wavelengths. Unfortunately, expected degrees of polarization spectrums for the SWIR modules have not been retrieved.

a) Radiances from MAP S7 Dataset

b) Degree of polarizations from MAP S7 Dataset

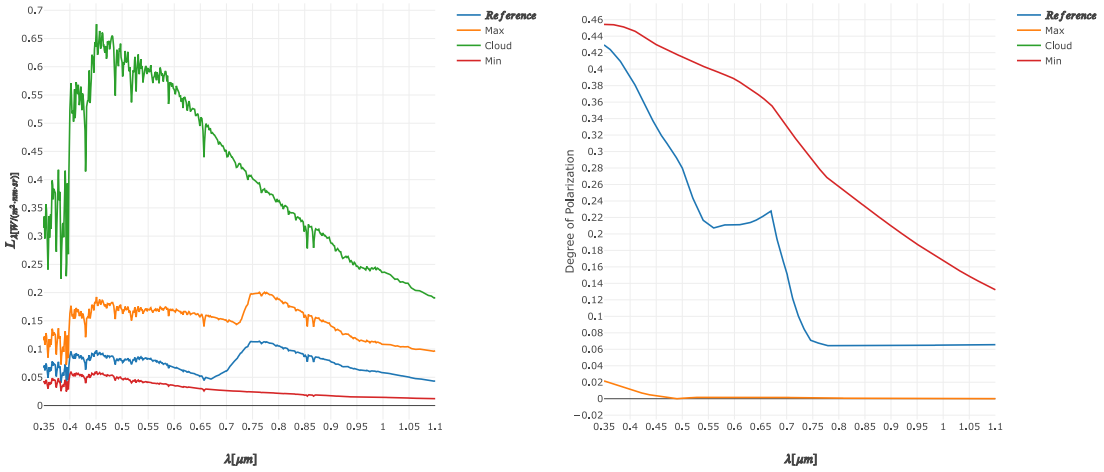

c) Radiance observed from OLI compared to MAP S7 reference

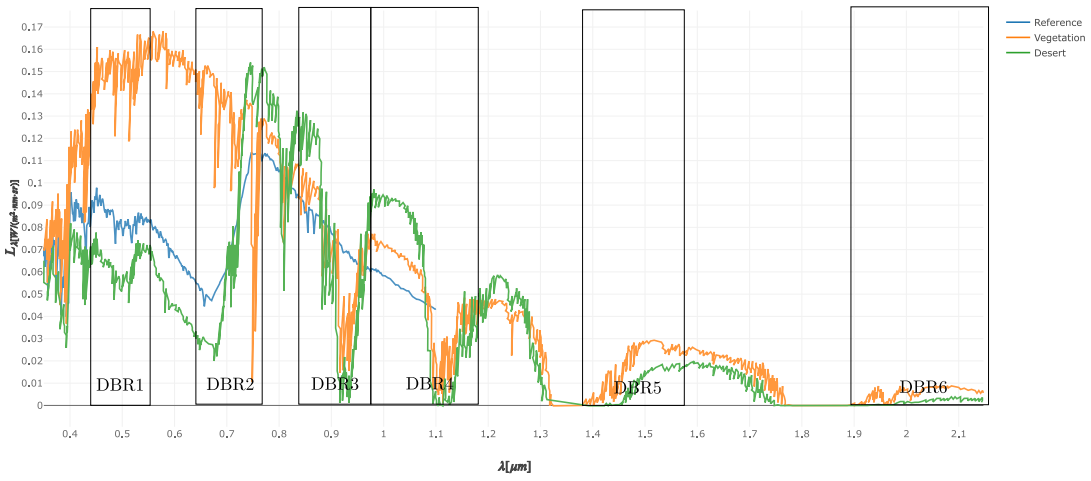

Figure 9.1: a) Spectral radiances values extracted from MAP Sentinel 7 dataset. The reference dataset is used for power budget estimation. b) Degree of polarization spectrum as reported in the same dataset. c) Extracted radiances values from [5] compared with reference MAP S7 Spectrum and covered DBR ranges proposed in Table 7.1.

9.1.2. Detector Choice

The main challenge in selecting a feasible detector for the arrangement proposed in Section 6.7 is, of course, covering all the spectral bands in Table 3.1 with an acceptable quantum efficiency and overall performance of the detector. To maximize the benefits of miniaturization of the filtering concept, we would prefer covering the VIS and SWIR ranges within the same optical system architecture and within one detector. In comparison to SPEX and 3MI similar concepts, such a design solution would provide the bigger advantage in terms of mass and cost reduction of the complete system, at the sake of some compromising in terms of performance (chromatic aberrations, transmittance) still hard to depict for the whole system. However, a solution in which the VIS and SWIR channels are still separated can also be envisioned and still provide some advantages in terms of achieved targets (see Section 9.5 for an overview of target parameters).

Covering bands from $[0.4\mu m, 2.1\mu m]$ within one sensor architecture is an active field of research, with a TRL3 of current development solutions [66], similar to the one of the devices under considerations. Similar *VISIR* detectors are envisioned in many applications involving remote sensing of aerosol and bio-signatures, as in the ATLAST concept [66], Various solutions under investigation:

- a) Electron Multiplying CCDs (EMCCDs): optimized solutions covering also the SWIR exist but are limited by degradation of the phosphorus used in the doping of the n-channels. Radiation exposure shall hence be investigated thoroughly for this solution.
- b) HgCdTe avalanche photodiodes arrays (APD), used also in ESO/VLTI interferometer [67], may provide coverage with $QE > 70\%$ from $[0.4\mu m, 2.5\mu m]$ [66][68]. The main limitations result from the noise induced by the photodiodes in the electronic circuits and their leaking currents, which shall be opportunely optimized. Their figure of merit QE is $\eta_e = 0.7$ up to $1\mu m$ and $\eta = 0.8$ above [66]. Temperature shall be limited to $T \cong 70K$ to avoid leakage currents [66]. They can be integrated on top of CMOS electronic circuits [69].
- c) Conventional HgCdTe with an optimized readout integrated circuit
- d) Various hybrid optimized solutions and cryogenic detectors.

We also report research projects actively integrating VISIR channels for on-ground use, like the following. With the understanding that the characterization shall be improved in the future development of such research, we select case b) for the study.

Integration with the multilayer It is also worth mentioning the concerns related to the integration of the multilayered structure on top of the sensor. It has been demonstrated that successful integration of similar RGB filters can also be accomplished with off-the-shelf sensors (see, for the purpose of this discussion, [70]). Typical architecture involves the use of microlenses to focus the light on the active pixel region, like in Figure 9.2. With the use of such architecture, the multilayered structure shall be placed on top of the microlenses, with opportune sealing and purification of the intermediate medium gaps. The vacuum behavior of such arrangement shall be thoroughly tested and modeled in further work to avoid outgassing and other effects in the space environment, but shall not be within the feasibility of current technology.

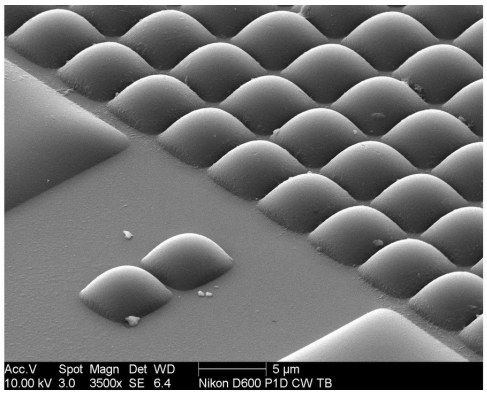

Figure 9.2: Images of the microlenses of a commercial Nikon camera adapted from the web.

Selection of pixel pitch For obvious detection purposes, the size of the resonator cells shall be equal or an integer multiple of the size of the pixel. It is further restricted by diffraction considerations (minimal bound) and spatial resolution required (upper bound) for a given focusing angle. In Section 7.2.5, we performed a sizing of the resonator array size based on diffracted energy at a wavelength of $\lambda \cong 1.1\mu m$, for a focusing angle $\theta_{max} = 10°$, which appeared as the best trade-off between aberrations, off-angle adrift - transmittance decrease and total power. This sizing resulted in a resonator array size of $l_r \cong 10\mu m$. The analysis has been already previously repeated for all spectral bands in Section 7.5. It shows that we can confidently consider that similar plots to the ones of Figure 7.13 would be retrieved for

all wavelengths at the parity of the non-dimensional number $\tilde{\rho}_{max} = k\rho_{max}\sin\theta_{max}$ (even though higher diffraction degradation is associated with smaller values of the permittivity ϵ_z). At parity of focusing angle, a similar pixel sizing for the upper spectral band of DBR6 would hence lead to $l_r \cong 20\mu m$ minimum resonator cell size, which has already been considered in the plots of Section 7.5. In order to use the same pixel pitch across the whole detector, we suggest using a pixel pitch of $l_p = 10\mu m$, but four pixels per one resonator array in DBR5 and DBR6 (to lead a grid $20\mu m \times 20\mu m$ for those bands). The measured charges of all four pixels shall be used during the reconstruction process and further algorithms may be used for the optimization of the spatial resolution-smearings of those spectral channels. Additional required allocation memory shall also be accounted for in the buffering unit of the detector. As a result of more extense diffraction regime, the spatial resolution of the two upper spectral channels is degraded of a factor $\xi <\cong 2$ with respect to what depicted in Table 6.2, but that would be the case for any diffraction-limited system sizing. For those bands, we further assume the SNR is the one predicted by a finite transmittance of enclosing radius $\rho_{max} = 20\mu m$, considered that the measurement is multiple and noise hence reduced subsequently with opportune post-processing.

Characterization of Detector Performance For the noise budget, we consider the noises of a tested HgCdTe avalanche photodiode detector (APD) from [71], which has also been successfully integrated into a Cube-Sat with use of a special detector-cooler assembly discussed in [72]. Specifications of a known developed design are discussed in [73], [74] (Selex ME788 APD), which we will hereby review. APD detectors are used both in astronomy observations and LIDAR applications. We suppose hence that the electronic design for the integration time and fluxes required in remote sensing is possible by opportune optimization. As we already briefly explained, the principle of operation of the detector is based on an APD circuit amplifier. The optical signals first encounter an anti-reflection coating opportunely engineered for the desired wavelengths, and a p-n photodiode formed in the HgCdTe through a via [71]. The via is necessary in order to create an avalanche gain directly at the point of absorption, to avoid limiting noises in the read-out-interface circuit [72], [73]. It further connects directly the n-junction to the read-out integrated circuit [75]. The electronic design used in those circuits further introduced a noise amplification due to the presence of the amplifier, which is strongly dependent on the bias voltage selected (typically, a simil-diode curve). The voltage has a direct correlation with the gain, further affected by temperature. Controlling the gain and temperature are hence important parameters for the operation of the detector, in particular affecting the read-out noise and the cosmetic quality (percentage of bad pixels) of the detector. To further limit read-out noise, [74] suggest the use of special sampling techniques, involving non-destructive readouts and *Fowler preprocessing*, a special multiple non-destructive read-out technique. According to [76] [Chapter 7.4.2], the use of such preprocessing techniques allows limiting to negligible levels $1/f$ noises and kTC noises due to reset of the capacitors in the electronic circuits. However, we claim it would imply faster electronics to perform the multiple non-destructive measurements within the integration time. From the analysis reported in [74], for an optimal design of this detector optimized at $\lambda \cong 2\mu m$ with a cosmetic factor of $c_f = 1\%$, one may either select a bias voltage $\Delta V_g = 12V$ at a cryogenic operating temperature of $T_0 = 30K$, or a voltage $\Delta V_g = 9V$ for $T_0 = 80K$. Much higher operating temperatures are reported in [75] but with more limited bandwidth. The higher temperature is obviously less cumbersome from an integration perspective, with the use of the detector-cooler assembly in [72], but it results in smaller quantum efficiency and worse noise performance. A lower temperature further affects negatively the velocity of the electronics and the read-out access time to each one of the pixels readings. The quantum efficiency dependence with wavelength is not exactly known or reported in those references, but given separately only for the VIS and SWIR bands as a function of temperature and claimed to be rather uniform in the spectrum in [75]. From those resources, $\eta_e \cong 0.7\ \forall\lambda \in [0.4 - 1\mu m]$ and $\eta_e \cong 0.8\ \forall\lambda \in [1\mu m - 2.5\mu m]$. Such dependence seems consistent with the one reported in [66] for the lower temperature value, with coverage between $\lambda \in [0.4 - 1\mu m]$ to be still verified more accurately. The resulting read-out noise does further present an optimum with respect to the number of nondestructive read-outs (at a number of frames $m_f \cong 100$). Given the above, the estimated corrected read-out noise, for , from [74]:

$$\langle n_{ro} \rangle < 40e^{-}[rms] \tag{9.1}$$

which presents a quasi-normal distribution, but may be actually further limited to much smaller values $\cong 1.2e^{-}[rms]$ by additional optimization of the pre-processing algorithms. Regarding dark currents, it

seems from [74] that the introduction of a cut-off wavelength in the quantum-efficiency η_e at $\lambda = 2.5\mu m$ shall suffice to limit the dark currents densities to values of:

$$\langle i_d \rangle \cong 80[e^-/(pixel \cdot s)] \tag{9.2}$$

rather stable in temperature up to $T_0 = 80K$ [73]. Such current corresponds to a noise floor, for a dwell time t_d of approximately:

$$\langle n_d \rangle \cong \sqrt{\langle i_d \rangle t_d} \tag{9.3}$$

In [71] and [74], from experimental results, it is further suggested to include an *APD excess noise factor*, ξ_g into account, due to the fact that the APD operation introduces some randomness in itself. The measurements were both based on laser and on broadband illumination. From the plots there reported we conclude that an APD factor of $\xi_g \cong 1.25$ shall be used, as a first conservative estimation. We further point that the necessity of using high gain in APDs is a result of the LIDAR - very fast integration time, low flux applications. When integrated for our concept in aerosol detection, the necessary gain may likely be smaller, noise performance be mainly shot-limited and the performance be optimized further. Other noises from the electronics readout may be supposed not to be limiting the system (in normal operating conditions) and can be safely neglected at this stage of the analysis.
It is finally interesting to discuss electronic cross-couplings between the pixels, particularly relevant for the present case study and induced by the presence of capacitors in the electronic circuits. In [74] measured cross-correlation between the pixel readings has been measured to be $\langle n_i n_j \rangle < 0.5\%$ with a frame rate time of $t_f = 0.5ms$ (similar to the one we will select). Cross-correlation for smaller frame-rates time are not reported (and likely to be higher). Those cross-correlation between readings will add on the ones present due to diffraction coupling of the resonators and continuity of the wavefront discussed in Section 5.3.1, which are at this point the driving factor for cross-coupling.

9.1.3. Noise Budget

With such knowledge, we may perform a preliminary noise budget of the proposed detector. We summarize, with the help of additional information extracted from the report [67], the following detector performance parameters: we may use the SNR formula reported in [67], adapted for our notation and with addition of the dark current noise:

$$SNR_f \cong \frac{n_f^{abs}}{\sqrt{\xi_g n_f^{abs} + \frac{\langle n_{ro} \rangle^2 + \langle n_d \rangle^2}{G^2}}} \tag{9.4}$$

Where $G = G_{(\Delta V_g)}$ is the gain associated with the bias voltage and n_f^{abs} the number of absorbed charges in a dwell time t_d, from Equation (5.72):

$$n_f^{abs} = \frac{\eta_e L_\lambda A_p \Omega_p \Delta\lambda t_d \overleftrightarrow{\tau} \mathbf{s}_{in}}{e_\gamma} \tag{9.5}$$

where $\overleftrightarrow{\tau}$ is the generalized finite band transmittance defined in Section 7.2.5 and the other parameters summarized in Table G.2. Since the gain acts on amplifying the signal prior read-out, G is at the denominator in (9.4) (see also SNR formulas in [71]). For an operating voltage of $\Delta V_g = 9V$ as suggested at $T_0 = 70K$, the gain can reach values of $G \cong 8$.
The SNR given in (9.4) is representative of a frame, in the dwell time t_d. In particular, the charge itself, n_f^{abs}, is the charge accumulated within a dwell time. We have observed in Chapter 6 that the combination of pixel sizing and required spatial resolutions leads to a high integration time, which would saturate the pixel. Hence we must set that $t_d \cong t_{int}/m_{frames}$, where we neglect the electronics non-destructive read-out time[1]. To avoid saturation and further decrease SNR, we average the input signal in various frames over the whole integration time. That also makes possible to use the sampling Fowler scheme above introduced, using $m_f = 100$. It is well known that, in first-approximation, a SNR frame averaging scales with the square root of the number of frames for a well-developed algorithm and $SNR_f >> 1$, so that:

$$SNR_p \cong \sqrt{m_f} SNR_f \tag{9.6}$$

[1] read-out time comprehensive of reset of the full-frame in [74] is $t_{ro} \cong 500\mu s$, but non-destructive read-out time is hard to estimate without a multiplexer design

Note that since the SNR is mainly shot-limited, calculating the SNR directly with the actual integration time would result in roughly the same result. The implications of frames averaging used in combination with Fowler pre-processing schemes are still partly elusive to us and shall be investigated in future work for more accurate estimations.
The above SNR is further applicable only for non-polarized pixels (where the reconstruction of polarization is not desired). For a polarized arrangement, (9.6) is representative of the SNR at each pixel of the arrangement. The SNRs in the reconstructed Stokes parameters is affected by the condition number reviewed in Section 7.3.2. For an arbitrary polarization angle likelihood, the statistical average transmission is the one of an unpolarized field[2]. Hence:

$$SNR_{pol} = \frac{SNR_p^{(0)}}{\kappa} \tag{9.7}$$

Where $SNR_p^{(0)}$ is this time the SNR to noise associated with the measure of an unpolarized field, e.g. only the term $\tau = M_{0,0}$ (equal for all pixels in the arrangement). Since the maximum $M_{0,0}^{max} = 1/2$ for an ideal bandpass filter and $\kappa_{min} = \sqrt{2}$ at best, the SNR of the reconstructed Stokes parameters is at least halved with respect to the ones of the unpolarized channels. As we already mentioned, the confidence level on s_1, s_2 retrieval may be however negatively biased by the statistical mean of the input field. The value of κ is strongly influenced by the filtering technique used, as we highlighted in Chapter 7.5, which motivated our detailed analysis in terms of attenuation of the undesired polarization.

9.1.4. SNR CURVES

The SNR to noise ratios of various pixels realizations in the optimized double-DBRs of Table 7.2 have been computed from use of equations (9.6) and (9.7), upon calculation of the corresponding finite band transmittances for each case (reported in Section 7.5). Such results are reported for the various radiances dataset in Figure 9.3a) for the unpolarized channels and 9.3b) for the reconstructed Stokes of the polarized channels, whereas Figure 9.3c) shows the number of charges at the pixel in a given time frame, to demonstrate that saturation is not achieved in the higher *cloud* dataset. All the values shall not be intended as spectral quantities, as they are plotted against the achieved spectral peak of the finite transmittance of the given pixel, but they are the result of a spectrum integration. The reference SNR, even though varying for obvious reasons along the various spectral channels, sets above $SNR >\cong 400$ for the unpolarized channels and above $SNR >\cong 190$ for the Stokes parameters retrieval. More uncertainty, due to lack of dataset information, is present in the SWIR channels, which however shows acceptable performance in regions where the radiance is the one predicted by Planck's Law. For calculation purposes, the radiances values reported in Image 9.1 have been smoothened. However, the absorption spectrum and variations figures are still depicted by the interval bars in Figure 9.3. We can notice also that the qualitative behavior of the SNR of the Stokes parameters is not the same as the polarized channels, in the VIS spectrum. This is a result of the fact that the condition number κ, as represented in Figure 7.29 possesses a minimum within the center of each VIS bandgap, due to leakings of the undesired polarization. An important trade-off that has been performed to make such result possible involves the choice of the correct number of mirrors of each DBR, which influences the spectral resolution. It is possible in fact, for future design iterations, to use curves like the one represented in Figure 9.4, where the FWHM at focal illumination and the SNR are represented parametrically for the various half-cone angle of focusing θ_{max} and number of mirrors of the DBR structure. Those curves take into account the main aspects of the analysis performed in Chapter 7: namely, the increase of FWHM with focusing angle and the diffraction. As it can be seen in Figure 9.4, depending on the SNR threshold requested by a given case requirement, it is advantageous to use a smaller number of mirrors above a certain requested FWHM. Also, not all FWHM and SNR requirements are achievable while limiting at the same time diffraction and cone angle normalization effects, for which we shall strive to work in the region of higher slopes in such plots. From those plots, it can be noticed that a design possessing a smaller FWHM is more subject to angle variations and hence also diffraction. It would be interesting in a future study to provide design criteria for the choice of a certain $\tilde{\rho}_{max}$ depending on the required FWHM of the focal transmittance.

[2] for a generically arbitrary distribution of the input Stokes parameters, the statistical average would further depend on the quantity $(M_{0,1} - M_{0,2})p$. One would require to know the expected spectrums of the degree of polarization to provide a more sound estimation

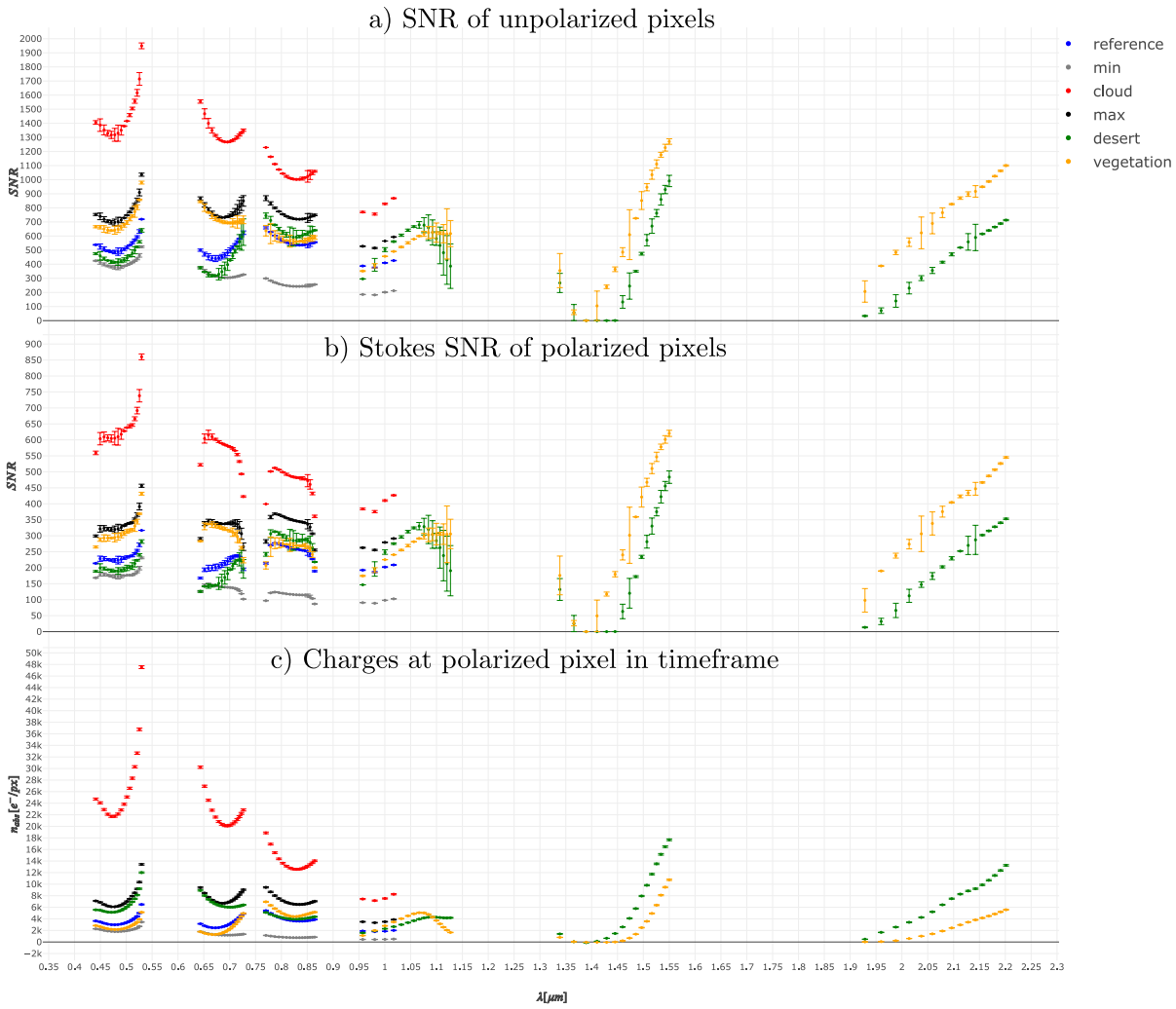

Figure 9.3: In a), b) SNR of the DBR designs in Table 7.2 and the noise budget introduced, against achieved spectral peak of the pixel finite focal transmittance, for various radiances realizations a) for the unpolarized pixels (circular inclusions in both cavities) b) expected for the polarized pixels on the reconstructed Stokes, with $AR = 5, 1/5$ in the two cavities. Interval bars are high frequency features of the radiance spectrums. In c) integrated charges on a pixel in a time frame of $t_f \cong 0.48ms$. Interval bars are, this time, expected noises on the charges values.

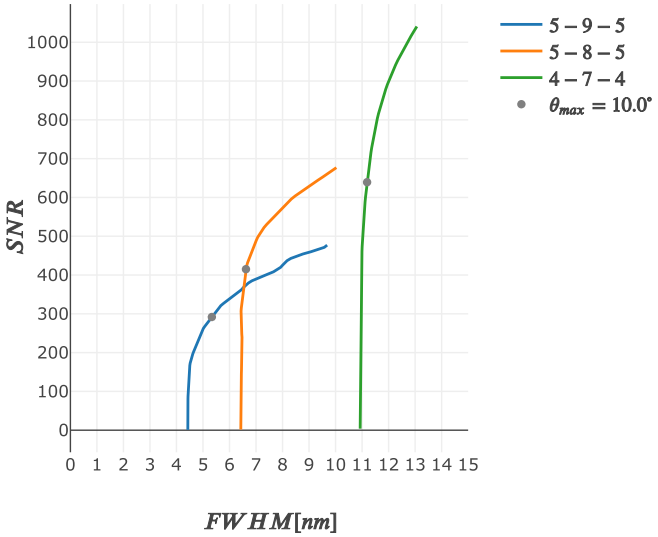

Figure 9.4: Performance maps of DBR4 for various mirrors configurations, as parametric plots in the focusing angle. Reference radiance values are used. Higher signal to noise ratios is associated with configurations with fewer mirrors for the same FWHM. The plots can be used for trade-offs depending on high-level FWHM-SNR requirements. They include diffraction (wobbling) and focusing effects.

9.2. Data Rates

In this Section, we calculate the data-rates required from the electronics front-end to deal with the acquired images. Using an imager arrangement of 2048×2048 pixels, we wish to store the image for every integration time. Even though we have previously mentioned that framing is required not to saturate the pixel and to use the Fowler pre-processing technique, we assume that electronics on each pixel are engineered with a Sample&Hold architecture to store the charges' values (in analogic) for every time-frame. With such an assumption, neglecting conversion and finite times in the electronics (unknown at the moment), the frequency rate of the storing process is given by:

$$f_{int} \cong \frac{1}{t_{int}} = 24Hz \tag{9.8}$$

whereas the frame-rate at the pixel level is given by:

$$f_{fr} \cong \frac{1}{t_{dw}} = 2.4kHz \tag{9.9}$$

By assuming the dept bit of $n_{bits} = 12$ and using $n_{taps} = 3$ channels in the multiplexer registers (for the polarization states of each wavelength and each angular band), we calculated that the processing rate of the $S\&H$ must fulfill:

$$f_{S\&H} = n_{bits} n_{taps} f_{fr} = 10.8kB/s \tag{9.10}$$

Instead, the frame-rate of the imager requires the quick storage of n_{pixels} at best, at a lower frequency rate of f_{int}. The associated storage rate is:

$$f_{st} = f_{int} n_{bits} n_{pixels} = 0.15GB/s \tag{9.11}$$

The expected downlink rate can be calculated by further assuming a certain compression rate and having enough information on the ground station coverage. Even though the latter is unknown yet, the storage rate does seem to be within the capabilities of front-end electronics used in microsatellites. A more detailed study on post-processing techniques and storage requirements in the buffering units of the electronics would certainly be required in future work to further characterize the data gathering for the imager arrangement proposed in Section 6.7.

9.3. Preliminary Thermal Analysis

As we previously discussed, the use of a hybrid APD HgCdTe detector requires cooling at $T_{0,max} = 80K$ to limit dark and leaking currents in the electronics, since we assume possible with a design similar to the one discussed in [72]. The expected thermal variations in various operating regimes are of $\Delta T \cong 20°$ as discussed in Section 3.4.4. A preliminary thermal analysis using a linear model for the expansion of the multilayered structure is simple to implement with the analytical tools discussed in Chapter 4. As we will show, such thermal analysis shows a negligible effect of linear thermal expansion in terms of changes in the spectral transmittance and mechanical interference. Uniform temperature variations, do affect the length of the mirrors' layers in terms of their thickness by means of the thermal expansion coefficient $\alpha_{(T)}$. They further affect the variations of optical properties by means of the thermo-optic coefficient $\partial n/\partial T$, depicting the change of refractive index with temperature. The latter is due to the thermal expansion itself but also to molecular bond changes. Determining those materials properties for TiO_2 and SiO_2 at cryogenic temperatures is not trivial, depending on those also on the manufacturing techniques used to deposit such thin layers. In various references as [77] it is in fact reported that hydrogen incorporation and thickness deposition strongly affect the material properties values. We suggest to investigate in future work through experiments the thermal behavior in vacuum environment. Preliminary materials properties are however reported in [77] and at those websites: link1 and link2 for a temperature of $T_0 \cong 20°$ as per Table 9.1, which we may use in engineering judgment to determine the order of magnitude of the variations of transmissivity.

Material	**Refractive Index**	**Thermal Expansion** $\alpha[1/K]$ (ambient temperature)	**Thermo-Optic Coefficient** $dn/dT[1/K]$ (ambient temperature)
SiO_2	$n = 1.45$	$(5.5 \pm 0.1) \times 10^{-7}$	-0.5×10^{-5}
TiO_2	$n = 2.31$	$(8 \pm 2) \times 10^{-6}$	4.5×10^{-4}

Table 9.1: Material properties retrieved from cited resources, at ambient temperature, for the mirrors and cavity materials

In a very preliminary model, the temperature changes are modeled as follow. The thermal strain $\epsilon_{i(\Delta T)}$ (not to be confused with permittivity) as:

$$\epsilon_{i(\Delta T)} = \alpha_i \Delta T \rightarrow l_i = l_i \alpha_i \Delta T \tag{9.12}$$

where the changes of refractive index are given in this linear regime by:

$$\Delta n_i = \left(\frac{\partial n_i}{\partial T}\right)_{|n=n_{0i}} \Delta T \tag{9.13}$$

The total percentage optical phase change derivative is given by:

$$\frac{\partial \delta_i}{k_0 l_i \partial T} = \left(\frac{\partial n_i}{\partial T}\right)_{|n=n_{0i}} + \alpha_i n_i \tag{9.14}$$

which is negative for the SiO_2 and positive for the TiO_2. For such materials properties, when included in the multilayer model, it has been observed the transmission peak change to be relatively negligible and the spectral peak to be minimal and in the linear regime. For simplicity, only normal angle illumination has been modeled. This spectral peak shift is due to the change of the optical length of the mirrors and the cavity (the latter in particular). The wavelength peak shift derivative $\frac{\partial \lambda_{peak}}{\partial T}$ depends upon the number of mirrors chosen. The results for this sensitivity analysis in DBR4 are reported in Table 9.2, all in linear regime in the interval $\Delta T < 20°$. As those results show, the spectral adrift is rather consistent throughout the various configurations and positive (towards higher wavelength for higher temperatures, due to the negative sign in the value of $\frac{\partial \delta_i}{k_0 l_i \partial T}$). The change of peak transmittance is minimal but increasing towards configurations with more mirrors. Due to the slight detuning of the mirrors, the FWHM (in percentage variation) is slightly smaller than expected. The latter two effects are in either case below one part per thousands for a one degree change.

Configuration	$\partial\lambda_{peak}/\partial T$ $[nm/K^{-1}]$	$\partial\mathcal{T}_{peak}/\partial T$ $[K^{-1}]$	$\frac{\partial\mathcal{B}}{\mathcal{B}\partial T}$ $\mathcal{B}=FWHM$ $[K^{-1}]$
4-6-4	0.092	$-4\cdot10^{-5}$	$-0.96\cdot10^{-3}$
4-7-4	0.093	$-4.4\cdot10^{-5}$	$-1.1\cdot10^{-3}$
5-8-5	0.095	$-1\cdot10^{-4}$	$-1.4\cdot10^{-3}$
5-9-5	0.094	$-2.5\cdot10^{-4}$	$-1.2\cdot10^{-3}$

Table 9.2: Sensitivity analysis results for various multi-DBRs configuration. The initial lengths of the mirrors are taken as per DBR4 in Table 7.2. A value of $\epsilon_x = 5$ is taken, representative of a pixel in the central region of the bandgap. We have verified the values to be rather similar also for other design choices.

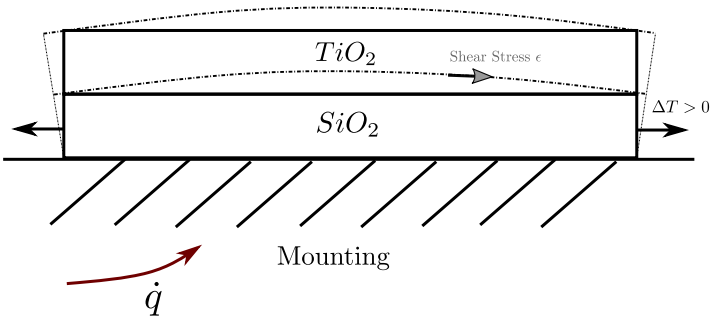

Figure 9.5: Sketch of expected curvature due to the mounting of the structures. The sign of the curvature may, in reality, depend on the relative magnitude of the Young and Poisson properties of the two materials and the mounting concept.

Even if the preliminary 1D analysis shows the negligible effect of the mirrors extension, we cannot conclude that temperature variations do not affect the performance of the multilayered structure. Temperature gradients may in fact unevenly influence the deformations of the filter and induce curvatures in the mirrors, especially once considering a specific mounting of the bottom slabs of the multilayered structure on the detector (as gluing or screwing). As a matter of fact, it is expected the structure to be mainly in a planar-stress regime in the transverse plane (due to limited extension of the thickness with respect to the transverse dimensions and mounting constraints), effects which will naturally induce thermal curvatures $k_{(\Delta T)}$. Such curvatures, as sketched in Figure 9.5, are likely to be the driving effect of any temperature-dependent change in performance that will be measured in the real structure. Their implications are also important in terms of diffraction performance but cannot yet be simulated accurately with the present tools, which would require a coupled thermal-electromagnetic FEM analysis, the down-selection of a mounting concept and a detail thermal-modeling around the detector. Testing of accepted thermal loads upon fracture of the embedded inclusions in the cavity shall also be required in future work; since those strongly depend also on contaminants and manufactured quality of the structures, we strongly suggest thermal testing for the depiction of those. We finally report that in high-power laser applications, also modeling of the heat flow generated by electromagnetic radiation shall be taken into account. For the low power application under consideration, the effect of such heating is surely negligible.

9.4. Preliminary Tolerancing Analysis

When analyzing tolerancing, various aspects are of concern:

- The tolerancing in the dimensions of the mirrors would slightly be detuned. As a result, the bandgap region is mainly affected, as well as the FWHM of the peak. We further show that for a generic permittivity of the cavity (e.g. generic sampling point in the wavelength of the bandgap region) also the spectral peak tends to shift. When coupled with the other tolerancing effect and within the filtering concept downselected in Chapter 7, this mismatch is also expected to cause transmission peak fall-over, since the two cavities would be mismatched.

- The tolerancing in the cavity dimensions further leads to a change in spectral peak position mainly, and once again a transmission peak fall-over when combined with the opportune filtering concept.

- Tolerancing on the particle sizes is expected to change its filling factor, also affecting peak position. In the case of the filtering concept downselected in Chapter 7, additionally to spectral shift, an effect on the transmission peak is also expected if the permittivities ϵ_x of the two cavities are not well matched. Rather than providing figures for the tolerancing of the particle itself, we prefer providing an analysis with respect to the random variable $\Delta\epsilon_x$ between the two cavities, due to the fact the stationary model introduced in Chapter 4 is a coarse approximation of the real structures. The tolerancing on the value $\Delta\epsilon_y$ mainly impacts the attenuation ratio, but not drastically. We point out that in the real structure the value of $\Delta\epsilon_x$ is expected to depend on both D_x, D_y (diameter of the elliptical inclusions), its height and shape properties. To use such a filtering concept, it is hence important to be able to predict beforehand the precise correlation between spectral peak location and sizes of the inclusion.

- Variance between the array structures: if the inclusions are not placed periodically as expected, even an infinitely wide resonator would not be a plane-wave eigenfunction and slightly diffract. In the real structure, such variance may lead to multiple propagating modes of slightly different spectral properties. For such effect, we may expect a broadening of FWHM and higher aberrations. Unfortunately, it is not yet possible to model this latter effect within our formulation. Also FEM simulations would fail in such description, assuming that the errors are systematic between each cell when defining boundary conditions.

- As we observed in Chapter 8, from the manufactured structures wobbling of the mirrors has been observed due to the presence of the scatterers, also after the planarization of the structures. Such wobbling can be observed to be rather consistent in frequency and of an amplitude A_w. A study in [4] upon FEM simulations has demonstrated negligible effect on the transmission of such defects both on FWHM and transmission peak up to $A_w \cong 20nm$, with sharp decreases above this value. The provided value is within the achieved manufactured figure in [4]. The imperfection is however expected to lead to additional diffraction, a study that has not been performed and requires expensive FEM simulations to be tested thoroughly.

With the understanding that many more factors may be considered, we performed some simplified Monte-Carlo simulations to take into account a non-systematic error in the manufactured mirrors (only thickness, not transversal) and in $\Delta\epsilon_x$. In the first case, a random, equally distributed number ζ is included in our model for the model of DBR4 mirrors, in the form:

$$l_i = l_{i0}\left(1 \pm \frac{\langle\zeta\rangle}{2}\right) \tag{9.15}$$

for each slab separately. Once again, various mirrors configurations are analyzed in DBR4. We have retrieved values for the spectral shift, the FWHM and the normal transmission peak at the desired polarization for $n_{points} = 5k$ realizations, as represented in Figure 9.6 (for a configuration of the multi DBR of layers 5-8-5) and 9.7 (for a 4-7-4 configuration). The first important observation to consider is that, for the same percentage variation of $\langle\zeta\rangle$, the effects on performance parameters are more pronounced in the configuration with more mirrors. For the latter, the transmission peak (sampled at 6000 data points in the wavelength) can decrease of a factor 60% for a random variation of 1%. The expected spectral shift settles at around $\Delta\lambda \cong 3nm$ and the FWHM may increase of a factor of 20%. In the configuration with fewer mirrors, the effects on transmission peak are much less pronounced, variations of FWHM roughly halved, whereas variations of the spectral shift are similar. The occurrence of systematic errors has not been analyzed and will be less severe than the one hereby reported. We also clarify that monolithic manufacturing of Bragg reflectors allows controlling the optical reflectivity of the mirrors in-situ while manufacturing. Even though challenging, the provided tolerancing limits may be hence achievable.
A similar analysis has been performed also in the variable $\Delta\epsilon_x$ and is reported in Figure 9.8 for both DBRs configuration in a percentage variation scale with respect to the design value. The variation is this time reported analytically (since in a single variable). For both mirrors, we observe a quasi-quadratic variation of the peak transmittance and the FWHM, whereas the spectral shift is in the linear region (especially for the configuration 4-7-4). The performance of the configuration with more mirrors is

this time significantly affected by the variation of this design variable, possibly its spectrum presenting two peaks above $\Delta\epsilon_x \cong 1.55\%$. We suggest imposing tolerancing of $\Delta\epsilon_x \cong 1\%$, which in terms of real geometrical sizes of the inclusions translate in tolerancing of few nanometers (according to the stationary model, $\pm 4nm$ in the diameters for a fixed height), to better be estimated from FEM simulations. With the proposed filtering technique and tight FWHM requirements, it is hence important to achieve good matching between the design of the inclusions, which requires proper tools to correctly model before-hand their spectral peak location and an extensive testing campaign.

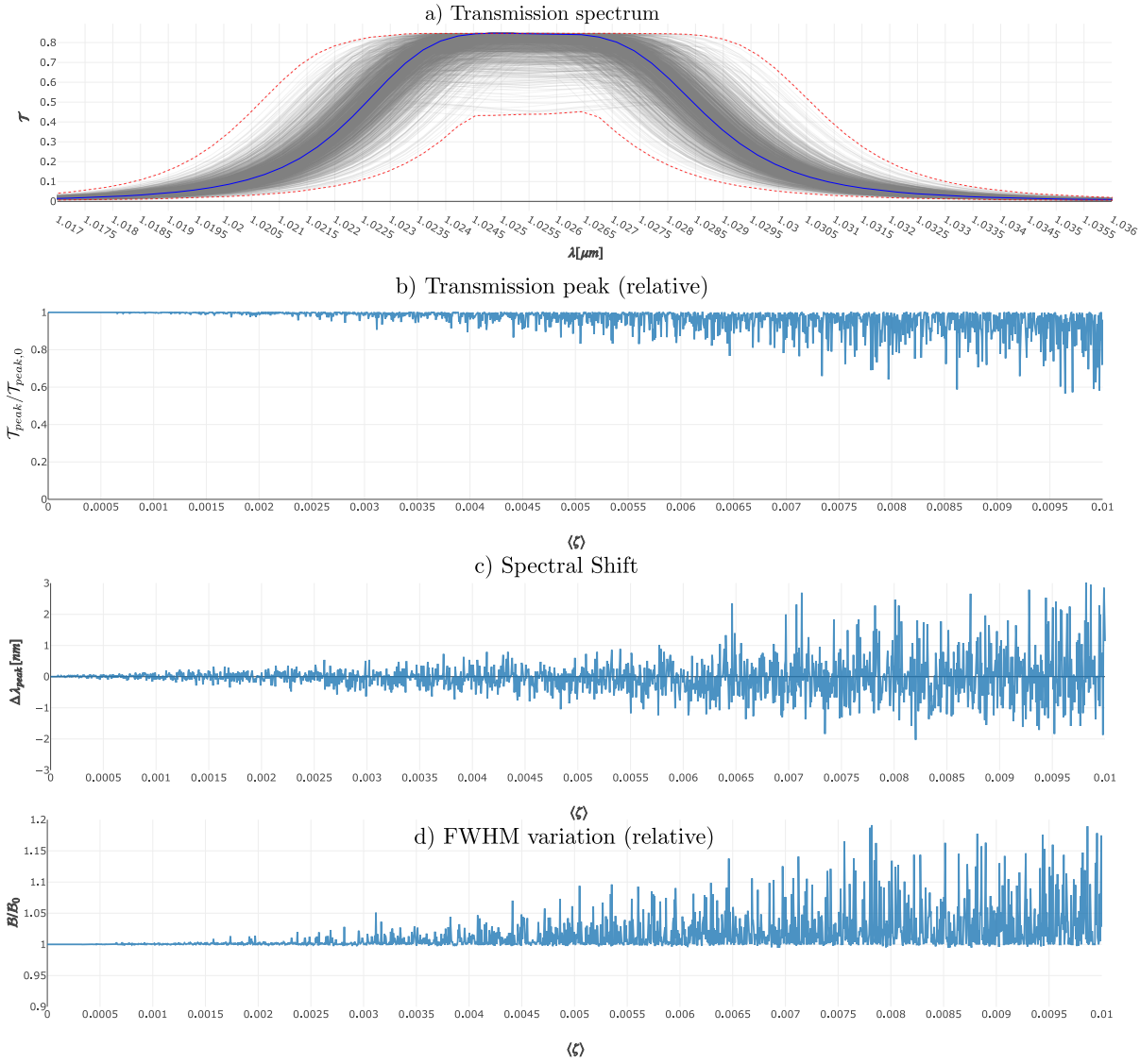

Figure 9.6: Sensitivity study for the mirrors configuration 5-8-5 in DBR4, depicting the variation of the various quantities of interest of the spectrum at normal incidence for various random realizations of $\langle\zeta\rangle$. The design value of inclusion permittivity is taken as $\epsilon_x = 5$.

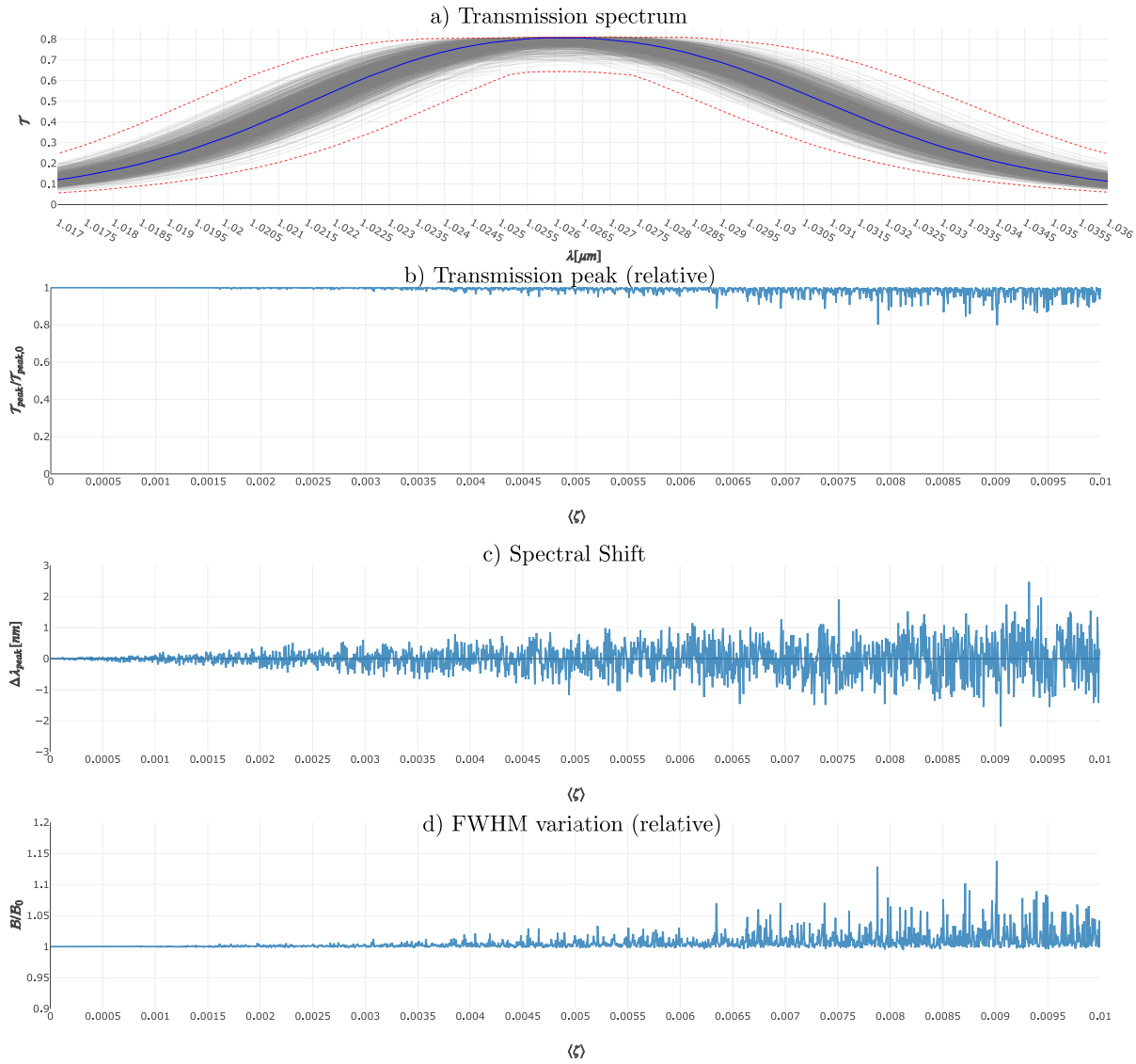

Figure 9.7: Sensitivity study for the mirrors configuration 4-7-4 in DBR4, depicting the variation of the quantities of interest of the spectrum at normal incidence for various random realizations of $\langle\zeta\rangle$. The design value of inclusion permittivity is taken as $\epsilon_x = 5$.

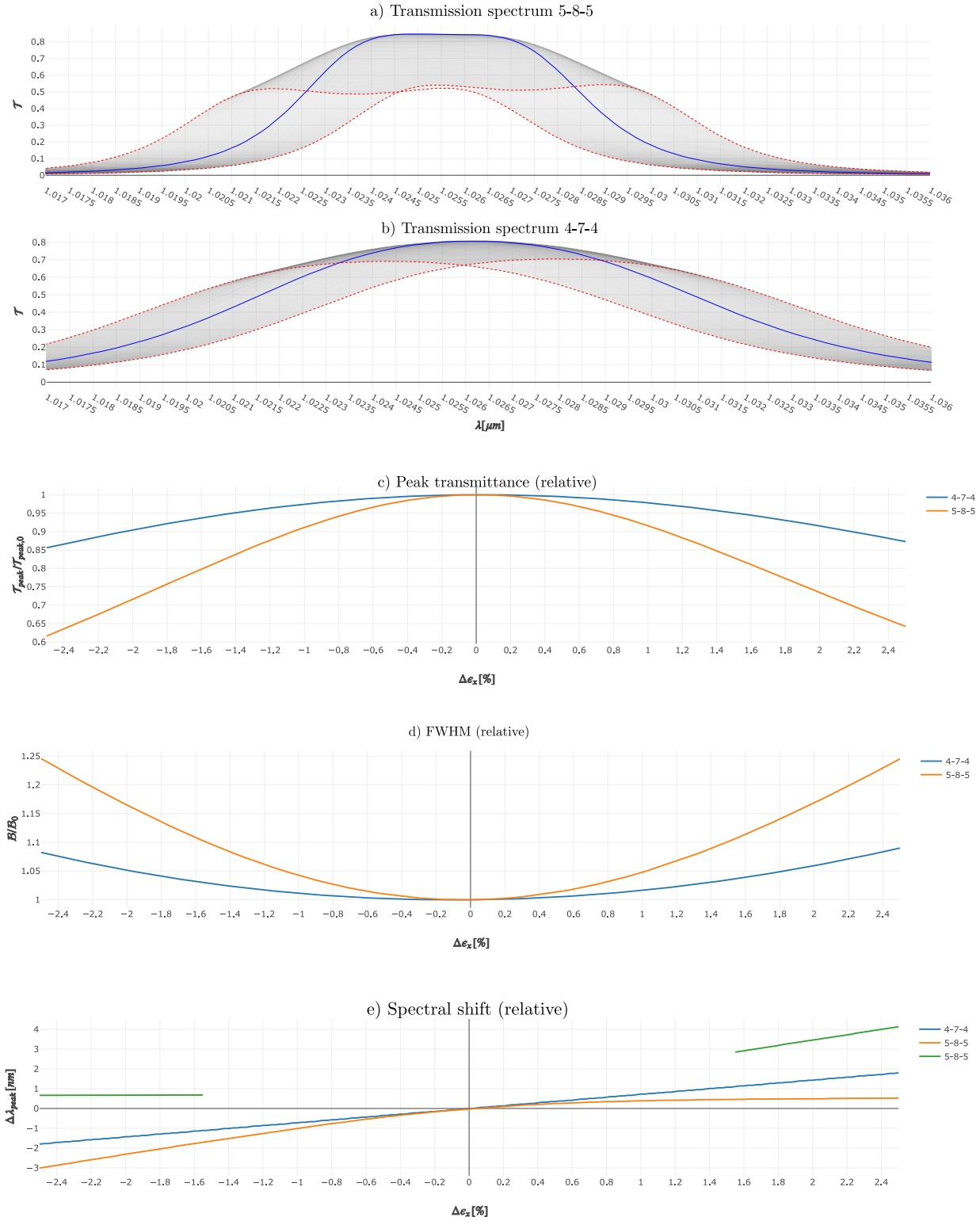

Figure 9.8: Variations of transmission spectrums and performance parameters at a normal angle, for percentage variations of the on-axis permittivity $\Delta\epsilon_x$ with respect to the design values of DBR4. In red the two extreme transmission spectrums are represented (for variations of $\pm 2.5\%$).

9.5. Overview of feasibility study benefits

Within this feasibility study, we have conducted an analysis of the spectral filter by designing various multi-DBR configurations able to cover the VIS-SWIR range with the required spectral resolution and diffraction quality. For a review of the specifications and performance of this design, please review Section 7.5. The power budget, discussed in Section 9.1 is also provisionally met when taking into consideration the mission parameters depicted in Chapter 6. The preliminary tolerancing analysis shows criticality in the values of $\Delta\epsilon_x$ for configurations with narrow FWHM and with a double-cavity filtering concept. The tolerancing values shall, however, be within manufacturing capabilities. In the concept in which VIS-SWIR are integrated together, the development of HgCdTe avalanche detectors of low TRL shall further be advanced. From current developments, they would require cooling at $T \cong 80K$. To cover the required wide range in the VIS and SWIR, at least six different DBRs would be required, to be integrated as explicated in Chapter 7 at detector level.

In comparison with the 3MI concept, the optical system specifications are similar: the system still requires to be telecentric and optics depolarization be well controlled. We point out that the latter can also be actively corrected in the reconstruction process by considering it in the definition of the finite aberrated transmittance. However, a filter wheel would not be anymore required, time resolution be improved and more spectral channels could be integrated at pixel level by sampling in more points the regions of interest, which would lead to an improved spectral resolution upon reconstruction. In the concept in which VIS-SWIR are separated, co-registration is also not required anymore. For example, active calibration may be performed with the use of the un-polarized pixels integrated into the along-track direction and of higher SNR performance, when the optical depolarization is well known. The overall mass and dimensions of the system of our concept are yet unknown for obvious reasons and dictated by the other subsystems. If an integrated VIS-SWIR solution is sought, at the price of some trade-off in chromatic performance and required cooling, the masses and dimensions of the optical units may almost be halved and the design fit in a small satellite to operate in LEO orbits. In an integrated VIS-SWIR solution is too challenging (for example, from the thermal point of view), the integration would still advantage from the removal of the filter wheel (typical mass of the assembly varying between $8 - 20kg$ Moog), which requires extensive thermo-mechanical design for use in space [78] and is a moving part, prone to aligning and failure.

In comparison with SPEX, which achieves coverage between $[0.385, 0.77]\mu m$ in a 6-unit Cubesat with a spectral modulation of the polarization, the introduction of the metasurface filter design would allow eliminating the presence of the polarization pre-optics unit (quarter-wave retarded, multiple order retarder and beam-splitter), which we observe to occupy approximately $2U$ in the DMU Figure 3.2. The use of such components limits the spectral resolution to the achievable modulation period and is subject to deviations in presence of temperature variations [22]. Moreover, the majority of the spectrometer components may also be removed (account for roughly other $2U$), provided that the spectral filtering is achieved at metasurface level. The designs are however not strictly comparable in terms of optical system architecture, operating in a very different modulation technique. For example, we expect depolarization of the optics not to be a driving factor in SPEXone, since the intensity of the Stokes parameters is modulated in the early stages of the optical path. As a result, anti-reflection coatings and aberrations requirements may be likely relaxed in the optical system in SPEXone. The adaptation of such design or a focal plane polarization modulation would likely result in a more compact design of higher spectral resolution, with some more challenging performance trade-offs in the optical system and possible addition of a few lenses. Coverage of the required band may be achieved by the use of two DBRs and would hence be less cumbersome also from a thermal point of view with respect to the wide range $[0.4, 2.5]\mu m$, which we observe also in the very different thermal designs of SPEXone and 3MI.

The benefits of the spectral filter are hence clear in both comparisons. However, much more integration analysis would be required, with the demonstration of a mock-up concept to prove such arguments.

9.6. List of Integration Requirements

One of the driving research objectives of this study is the depiction of integration and definition requirements for the spectral filter, to be extracted from the analysis hereby reported. We have collected a variety of those requirements in Table 9.3, referencing to the analysis results in support.

ID	Category	Requirement	Rationale
R.M.01	Geometry	The size of the resonator cell array shall be $l_r = 10\mu m$ (TBC) in the VIS channels and $l_r = 20\mu m$ (TBC) for the SWIR channels	Derived from Requirement R.04 and R.09. The provided reference, according to the analysis of Chapter 7, shall suffice for a focusing angle $NA = 10°$ to enclose the aberrated energy above $\cong$ 80% (TBC)
R.M.02	Geometry	The size of the resonator cell array shall be matched in integer multiples of the edge pixel size	Required for having imaging
R.M.03	Implementation	The DBRs bandgap designs shall be integrated on the same structure for each angular band for the covered wavelengths supported by the detector choice	Derived from Requirement R.01 and R.13 In case of separate VIS and SWIR channels the requirement is still applicable
R.M.04	Optical	The focusing half-cone angle shall be of $\theta_{max} = 10°$	Direct flowdown from R.03. As the analysis in Chapter 7 shown the provided figure is sufficient to meet SNR and, on the other hand, limit aberrations effects and increase of FWHM off-angle
R.M.05	Geometry	The DBRs bandgap designs, when integrated on the same structure, shall possess at least 5 angular bands	Derived from R.07 and science requirements
R.M.06	Optical	The focusing shall be performed on top of the multilayered structure	Derived from requirements R.09 and R.10 It has been proved that upon resonance the multilayer provides a phase-shift of $\delta \cong \pm\pi/2$ in the higher transmission region, irrespectively of its length. If light is on phase at the top of the structure, the aberrations at the focal plane are hence minimized, as we shown in Chapter 7
R.M.07	Calibration	A non-polarized pixel shall be used for calibration, corrected for the optical depolarization	Substitutes requirements R.08 which shall be modified accordingly
R.M.08	Functional	A filtering unit for the undesired polarization shall be integrated on top of the spectral filter	For reconstruction purposes, since we shown impact on the condition number if such condition is not met
R.M.09	Functional	The filtering unit shall achieve an attenuation of $\mathcal{T}_y < 10\%$ in all covered regions in the spectrum	Derived from requirement R.M.08 to have good spectral quality and condition number
R.M.10	Definition	The filter unit shall be designed accordingly to Table 7.2	Derived from requirement R.M.09 and in order to meet SNR requirement R.06 As shown in Chapter 7
R.M.11	Integration	The multilayer structure shall be placed on top of the detector micro-lens.	Focusing at pixel level is still required through micro-lenses.
R.M.12	Tolerancing	The tolerancing on each slab of the multilayered structure shall be maintained within 1%(TBC) of its thickness	From the analysis performed in Chapter 7 the figure ensures that transmission peak is above 60% spectral shift below $3nm$ and FWHM variation below 20%. Such figures are depending on DBRs mirror designs and shall be iterated with science requirements
R.M.13	Tolerancing	The tolerancing on the matching permittivity $\Delta\epsilon_x$ shall be maintained below 1%(TBC) between the two cavities	From the analysis performed in Chapter 7 it is important to limit the percentual variation of on-axis permittivity to ensure appropriate quality of the spectral peak.
R.M.14	Tolerancing	The inclusion sizes shall be manufactured within $\pm 4nm$ (TBC) in diameters from their design values	Derived from requirement R.M.13, provisionally.
R.M.15	Thermal	The multilayered structure shall be stabilized within $\pm 20°$ at a reference temperature of $T \cong 80K$ when using the HgCdTe avalanche photodiode detector, for concepts requiring both VIS and SWIR coverages	Required to limit read-out noises in the electronics for the wide spectral range.
R.M.16	Reconstruction	Upon reconstruction, the reconstruction matrix shall be corrected for cross-polarization terms from the finite filtering, aberrations and induced polarization from the optics and diffraction effects	In Chapter 5.3.9 we provide a final expression of the image reconstruction process, for which it is required to correct for the above mentioned factor to determine the best reconstruction matrix solving the optimization problem under review.
R.M.17	Functional	The sizes of intermediary mirrors between cavities shall be kept above $n > 4$ when a double cavity filtering concept is used	We have observed in Chapter 7 that such condition ensures minimal coupling between the cavities.
R.M.18	Implementation	The cavity shall interface with TiO_2 mirrors slabs	In order to maximize transmission module and minimize reflection coefficient at the interface. To be reviewed in other stages of the design.
R.M.19	Implementation	The marginal mirrors interfacing with air shall be made of SiO_2	In order to maximize transmission module and minimize reflection coefficient at the interface. To be reviewed in other stages of the design. We assume nill reflection coupling with the microlenses of the detector.
R.M.20	Implementation	The inclusion material shall be TiO_2 in the VIS range and $aSi:H$ in the SWIR	To avoid losses in the VIS range, as we showed in Chapter 7
R.M.21	Guidance	The off-axis permittivity ϵ_z contrast between the two cavities, when using the double cavity filtering concept, shall be traded-off with the extintion ratio in terms of aspect ratio to limit off-angle attenuation.	We observed in Chapter 7 that matching both the ϵ_x and the off-axis permittivity is not possible. However, tweaking the AR is a design choice which enables to control the attenuation ratio in relation to the off-axis transmissivity decrease.

Table 9.3: Main important Integration and Definition requirements derived throughout the report, to be considered when using the spectral filter under study.

10
Conclusion

In the present research study, we have thoroughly analyzed the design, performance and modeling techniques of a spectropolarimetric filter based on metasurfaces, for Space applications.
As discussed in Chapter 3, its integration can lead to significant miniaturization and integration benefits with respect to other conventional optical solutions. Throughout the report, a feasibility study in the context of aerosol determination has been conducted.
The twofold aspects of this research are related to the modeling and to the integration analysis.

Modeling In the analytical methods presented in Part II we have introduced a numerically efficient method to aid the preliminary design of the structure. With respect to expensive FEM simulations, an analytical method aids the efficient evaluation of several designs in a significantly shorter amount of time. We have verified our analytically model in terms of plane-wave response as discussed in Section 7.6. The method consists of an effective material model, coupled with a multilayer formulation and a novel diffraction formulation, to derive a finite spectral transmittance of the filter and an optimal reconstruction matrix. The latter two are the main important performance parameters, including the effects of aberrations of the filter, diffraction and enclosed spectral energy. We have applied such a framework and diffractive solution to aid the selection of various filter configurations through means of *resonances curves* of the multilayer structure, designing a set of filters able to cover the required spectral channels, in Chapter 7. Their electromagnetic performance has been thoroughly analyzed in terms of plane-wave and focal diffraction response for a set of 96 distinct pixels, showing that the spectral filter can provisionally meet the imposed requirements. Important design criteria are retrieved from this performance analysis, directly influencing the integration requirements. The important findings of our EM analysis, relating spot sizes and spectral behavior to focusing NA, are summarized in Section 7.7. With respect to previously existing designs in [1], we have provided a set of possibilities to increase the achievable bandwidth by filtering the undesired polarization, in Section 7.4 and re-optimized the structures and the reconstruction process accordingly. The improved characterization of the structures allows us to further increase, with more confidence, the focusing angles with respect to what proposed in [1], on the other hand imposing a different diffraction sizing of the pixel sizes, as discussed in Section 7.
We applied the modeling techniques to also analyze the performance of manufactured structures in Chapter 8. In that respect, the measured spectral shift of the polarization and loss attenuations of the s polarization do well correlated with theoretically expected dependence for a bare cavity. For structures with inclusions, we retrieve the effective parameters from the test results and provide a possible analytical fit that shows a correlation between the measurements. We further elaborate on how the transmittance response of the structure can be fully retrieved and verified from experimental results in Section 8.6.

Integration A preliminary mission analysis has been performed for a LEO satellite and the main parameters of the optical system been derived in accordance, in order to perform an accurate power budget. We further provided guidance on possible detectors to achieve the required coverage in Section 9.1.2 and analyzed their performance. When integrated with the spectral filters, at means of some performed trade-offs in the FWHM, the power budget is met for both polarized and unpolarized channels. A preliminary 1D thermal analysis shows a negligible effect of the thickness extension of the mirrors. Required tolerancing estimations, as we show in Section 9.4, are driving the performance for a given DBR design and shall be well controlled instead, for which we suggest an experimental characterization

of the structures. We reported a comparison of performance achieved by a system using those spectral filters with respect to 3MI and SPEXone concepts, conjecturing on possible volume and masses benefits in Section 9.5. The possible benefits of the introduction of the metasurface filter concept are striking in both cases, but require a more detailed design of a mock-up demonstrator to be assessed quantitatively. The research objective of the integration is providing integration requirements for an optical designer and the manufacturing, which are reported in Section 9.6.

10.1. Further Recommended Work

Performing a detailed feasibility study of such novel structures is a complex task, involving on one side design and optimization of an optical system and knowledge of system parameters, on the other very detailed formulations for the performance characterization of the structures. Due to a limited amount of time, various aspects of interest are still to be investigated. We summarize those as follows:

- The included transmittance takes into account aberrations induced by the filter, but does preliminarily assume an ideal optics. To perform a more detailed characterization, the performance of the filter shall be analyzed in conjunction with the one of the optical system, which requires the down-selection and optimization of a telecentric and wide-FOV optical system. Once the latter is available, the modeling still holds, by taking into account the opportune transmission response $\mathbb{J}^{(o)}$ of the optical system and the opportune apodization factors. The design of the optical system shall take into account depolarization induced by the optics and, if VIS and SWIR ranges are to be covered simultaneously as proposed, important tradeoffs in terms of chromatic performance.

- The diffractive performance of the structure has been partially characterized, but only the effects of wide resonator aberrations, as depicted in Section 5.3.1, have been analyzed in detail. An important uncertainty relates to the dependence of the PSF with the focal points coordinates. To overcome such uncertainty, we suggest preliminarily oversizing of the resonator cell as depicted in Chapter 7. We discussed possible implementation and advanced models to resolve such dependence in Section 5.3.1 but could not implement or verify those in the present framework. As a result, also the imaging in Section 5.3.9 lacks the required characterization to provide more sensitive figures for the imaging quality of the filters in the spectrum. Figures of the cross-talks between pixels can also only be accurately inferred from such analysis. Important modeling is hence still required to properly characterize the response of the finite structure.

- Modeling of the detector and multilayer interaction shall be further investigated.

- Thermal effects due to the curvature of the structure shall be included in the thermal modeling

- The effective medium model introduced in Section 5.3.2 shall be adapted to better retrieve the effective parameters from the geometrical dimensions of the structure, by means of more elaborated theories and experimental characterization. Such knowledge would allow to further investigate the other filtering concepts proposed in Section 7.4, as for example the resonance dispersion mechanism, which is an elegant filtering solution to control the EM properties of the filter in the spectrum, angle and polarization.

- An extensive experimental campaign shall be conducted to verify the PSF results, as well as cross-couplings, thermal effects, vacuum and radiation behavior of the structures. Material properties at cryogenic temperatures shall further be evaluated experimentally.

- For other applications, another imager arrangement shall also be considered and the response of the structure to spectral coherent illumination be analyzed more in detail.

- A statistical analysis of the best reconstruction methods and algorithms to resolve the optimization problem introduced in 5.3.9 shall be conducted, once the diffractive performance is better characterized.

V

Support Documentation

A

Properties of Scattering and Transfer Matrices

We hereby review some general properties of transfer matrices and derive a close form relationship for an arbitrary dimension linking the scattering and the transfer matrix.
Suppose a transfer matrix $\mathbb{T}_{i\to k}$ links to system state vectors $\boldsymbol{\mathcal{M}}_i$ and $\boldsymbol{\mathcal{M}}_k$ via the relationship[1]:

$$\boldsymbol{\mathcal{M}}_k = \mathbb{T}_{i\to k}\boldsymbol{\mathcal{M}}_i \tag{A.1}$$

We wish to determine the expression of the transformation when referred to the new state vectors, $\boldsymbol{\mathcal{M}}_{in}$, $\boldsymbol{\mathcal{M}}_{out}$ complying with:

$$\begin{aligned}\boldsymbol{\mathcal{M}}_k &= \mathbb{P}_{in,k}\boldsymbol{\mathcal{M}}_{in} + \mathbb{P}_{out,k}\boldsymbol{\mathcal{M}}_{out}\\ \boldsymbol{\mathcal{M}}_i &= \mathbb{P}_{in,i}\boldsymbol{\mathcal{M}}_{in} + \mathbb{P}_{out,i}\boldsymbol{\mathcal{M}}_{out}\end{aligned} \tag{A.2}$$

for certain known permutation matrices $\mathbb{P}_{i,j}$. Rewriting in block matrices notation:

$$\begin{pmatrix}\boldsymbol{\mathcal{M}}_k\\ \boldsymbol{\mathcal{M}}_i\end{pmatrix} = \begin{bmatrix}\mathbb{P}_{in,k} & \mathbb{P}_{out,k}\\ \mathbb{P}_{in,i} & \mathbb{P}_{out,i}\end{bmatrix}\begin{pmatrix}\boldsymbol{\mathcal{M}}_{in}\\ \boldsymbol{\mathcal{M}}_{out}\end{pmatrix} \qquad \begin{bmatrix}\mathbb{I}| & -\mathbb{T}_{i\to k}\end{bmatrix}\begin{pmatrix}\boldsymbol{\mathcal{M}}_k\\ \boldsymbol{\mathcal{M}}_i\end{pmatrix} = 0 \tag{A.3}$$

Is hence immediate to show by substitution and inversion that the scattering matrix fulfilling the relationship:

$$\boldsymbol{\mathcal{M}}_{out} = \mathbb{S}_{k\to i}\boldsymbol{\mathcal{M}}_{in} \tag{A.4}$$

is given by:

$$\mathbb{S}_{k\to i} = \left(\mathbb{T}_{i\to k}\mathbb{P}_{out,i} - \mathbb{P}_{out,k}\right)^{-1}\left(\mathbb{P}_{in,k} - \mathbb{T}_{i\to k}\mathbb{P}_{in,i}\right) \tag{A.5}$$

which is applicable for all dimensionalities of the matrices involved (as far as the transfer matrix is such that the first inversion is possible). Notice that if one starts from $\mathbb{T}_{k\to i}$ instead, an inversion is first required.
An expression can also be determined to compute the transfer matrix from the scattering matrix from the previous. For example, considered the four-dimensional Transfer Matrix which appeared in Chapter 4. We chose the state vectors to be:

$$\boldsymbol{\mathcal{M}}_k = \begin{pmatrix}E^+_{p,k}\\ E^-_{p,k}\\ E^+_{s,k}\\ E^-_{s,k}\end{pmatrix} \qquad \boldsymbol{\mathcal{M}}_i = \begin{pmatrix}E^+_{p,i}\\ E^-_{p,i}\\ E^+_{s,i}\\ E^-_{s,i}\end{pmatrix} \qquad \boldsymbol{\mathcal{M}}_{in} = \begin{pmatrix}E^+_{p,k}\\ E^+_{s,k}\\ E^-_{p,i}\\ E^-_{s,i}\end{pmatrix} \qquad \boldsymbol{\mathcal{M}}_{out} = \begin{pmatrix}E^+_{p,i}\\ E^+_{s,i}\\ E^-_{p,k}\\ E^-_{s,k}\end{pmatrix} \tag{A.6}$$

The permutations matrices are therefore, by construction:

$$\mathbb{P}_{in,k} = \mathbb{P}_{out,i} = \begin{bmatrix}1&0&0&0\\0&0&0&0\\0&1&0&0\\0&0&0&0\end{bmatrix} \qquad \mathbb{P}_{out,k} = \mathbb{P}_{in,i} = \begin{bmatrix}0&0&0&0\\0&0&1&0\\0&0&0&0\\0&0&0&1\end{bmatrix} \tag{A.7}$$

[1] $i\to k$ is used instead of $k\to i$, since final transmission coefficients will be of simpler form which such choice

We hence determine the following pairs:

$$\mathbb{T}_{i\to k} = \begin{bmatrix} t^{pp} & r^{pp}_{-} & t^{sp} & r^{sp}_{-} \\ r^{pp} & t^{pp}_{-} & r^{sp} & t^{sp}_{-} \\ t^{ps} & r^{ps}_{-} & t^{ss} & r^{ss}_{-} \\ r^{ps} & t^{ps}_{-} & r^{ss} & t^{ss}_{-} \end{bmatrix} \qquad \mathbb{S}_{k\to i} = \begin{bmatrix} \tau^{pp} & \tau^{sp} & \rho^{pp}_{-} & \rho^{sp}_{-} \\ \tau^{ps} & \tau^{ss} & \rho^{ps}_{-} & \rho^{ss}_{-} \\ \rho^{pp} & \rho^{sp} & \tau^{pp}_{-} & \tau^{sp}_{-} \\ \rho^{ps} & \rho^{ss} & \tau^{ps}_{-} & \tau^{ss}_{-} \end{bmatrix} \tag{A.8}$$

with:

$$\begin{aligned} \tau_{pp} &= \frac{t^{ss}}{t^{pp}t^{ss} - t^{ps}t^{sp}} & \rho_{pp} &= \frac{r^{pp}t^{ss} - r^{sp}t^{ps}}{t^{pp}t^{ss} - t^{ps}t^{sp}} \\ \tau_{sp} &= -\frac{t^{sp}}{t^{pp}t^{ss} - t^{ps}t^{sp}} & \rho_{sp} &= \frac{-r^{pp}t^{sp} + r^{sp}t^{pp}}{t^{pp}t^{ss} - t^{ps}t^{sp}} \\ \tau_{ps} &= -\frac{t^{ps}}{t^{pp}t^{ss} - t^{ps}t^{sp}} & \rho_{ps} &= \frac{r^{ps}t^{ss} - r^{ss}t^{ps}}{t^{pp}t^{ss} - t^{ps}t^{sp}} \\ \tau_{ss} &= \frac{t^{pp}}{t^{pp}t^{ss} - t^{ps}t^{sp}} & \rho_{ss} &= \frac{-r^{ps}t^{sp} + r^{ss}t^{pp}}{t^{pp}t^{ss} - t^{ps}t^{sp}} \end{aligned} \tag{A.9}$$

The relationships would turn out being more complex if explicited with respect to the inverse matrix $\mathbb{T}_{k\to i}$ (care must be then used for the order in case of non-symmetrical systems). We can verify the consistency of those expressions with the ones reported in Literature in [33]. The approach used has the advantage that, on top of being concise, by changing permutation matrices we can readily use results from other references, which are often not consistent between themselves in terms of signs, nature, or ordering of state-vectors. It could moreover be used for an arbitrary sampling dimension of the state-vector, which would be required for an implementation of the diffraction problem in Section 5.3.1. We further define the Jones matrices of the system as:

$$\mathbb{J}^{+}_{k\to i} = \begin{bmatrix} \tau^{pp} & \tau^{sp} \\ \tau^{ps} & \tau^{ss} \end{bmatrix} \qquad \mathbb{J}^{-}_{k\to i} = \begin{bmatrix} \rho^{pp} & \rho^{sp} \\ \rho^{ps} & \rho^{ss} \end{bmatrix} \tag{A.10}$$

We recognize, hence, $\mathbb{J}^{+}_{k\to i}$ as a transmission matrix and $\mathbb{J}^{-}_{k\to i}$ as a reflection matrix, in the local $p-s$ reference. Conservation of energy obviously imposes some constraints on those coefficients and hence on the transfer matrix. As it is usually stated, when p and s polarization are not coupled as in our case, the conservation of energy reads (in presence of not-absorbing materials):

$$\mathcal{T}_i + \mathcal{R}_i = 1 \tag{A.11}$$

Where $\mathcal{T}_i = \tau_i\tau_i^*$ and $\mathcal{R}_i = \rho_i\rho_i^*$ are respectively the intensity transmissions and reflections of p and s polarization measured along the polarization directions[2]. In the general case, when a scattering matrix is present, it is simple to determine a similar relationship. The fields of the multilayered structure are in fact given in our construction by:

$$\boldsymbol{\mathcal{M}}_{out} = \begin{pmatrix} E^{+}_{p,i} \\ E^{+}_{s,i} \\ E^{-}_{p,k} \\ E^{-}_{s,k} \end{pmatrix} = \begin{bmatrix} \tau^{pp} & \tau^{sp} \\ \tau^{ps} & \tau^{ss} \\ \rho^{pp} & \rho^{sp} \\ \rho^{ps} & \rho^{ss} \end{bmatrix} \begin{pmatrix} E^{+}_{p,k} \\ E^{+}_{s,k} \end{pmatrix} = \mathbb{S}_{lm}\boldsymbol{\mathcal{M}}_{in} \tag{A.12}$$

Where $E^{+}_{p/s,k}$ are excitation fields, $E^{+}_{p/s,i}$ transmitted fields and $E^{-}_{p/s,k}$ are reflected fields, and the matrix $\mathbb{S}_{lm}$ is the left minor of the scattering matrix. Conservation of energy imposes that:

$$\boldsymbol{\mathcal{M}}_{out}\cdot\boldsymbol{\mathcal{M}}^{*}_{out} = \boldsymbol{\mathcal{M}}^{*}_{in}\cdot\mathbb{S}^{\dagger}_{lm}\mathbb{S}_{lm}\boldsymbol{\mathcal{M}}_{in} = \boldsymbol{\mathcal{M}}_{in}\cdot\boldsymbol{\mathcal{M}}^{*}_{in} \tag{A.13}$$

which requires that $\mathbb{S}^{\dagger}_{lm}\mathbb{S}_{lm} = \mathbb{I}$ since it must applies for all entries. Similar formulation would account by using the cartesian frames. We have verified for validation this result to numerical precision for various DBRs multilayers, at $\epsilon_{error} = 10^{-13}$.

[2] expression involving cosine projections are also known in literature but they are instead referred to transverse fields transmissions, which are different for p polarization

B

Evolution of fields in anisotropic dielectric material

In this Section, we derive and validate the formula (4.9) and (4.10) from basic principles. The formula describes the evolution of the tranverse fields in an anisotropic dielectric medium and is reported in [33], [79]. However those papers make use of different reference systems and Gaussian Units and are lengthy to implement, whereas a more concise matricial treatment can be derived in consistency with the notation and references used throughout the report.
To derive formula (4.9) and (4.10) we use the Time Fourier Decomposition of the Maxwell Equations reported in Equation (4.2) and we recast the last two Maxwell equations vectorially using projection techniques. Defining the linear cross-product operator in matricial form:

$$\mathcal{X}_{\{\mathbf{v}\}} = \begin{bmatrix} 0 & -v_z & v_y \\ v_z & 0 & -v_x \\ -v_y & v_x & 0 \end{bmatrix} \qquad \mathcal{X}_{\{\mathbf{v}\}}\mathbf{u} = \mathbf{v} \times \mathbf{u} \tag{B.1}$$

and the cartesian versors $\hat{\epsilon}_x, \hat{\epsilon}_y, \hat{\epsilon}_z$, we can express the rotor operator as a matricial operation. We introduce the Fourier representation of the field explicited in (4.8) and we determine the rotor operator in matricial form:

$$\mathcal{X}_{\{\nabla\}} = \frac{d}{dz}\mathcal{X}_{\{\hat{\epsilon}_z\}} + i\mathcal{X}_{\{k_x\hat{\epsilon}_x + k_y\hat{\epsilon}_y\}} = \frac{d}{dz}\mathcal{X}_{\{\hat{\epsilon}_z\}} + i\mathcal{X}_{\{\mathbf{k}\}} \tag{B.2}$$

Hence the equations (4.9) are of the form (using block matricial notation) :

$$\begin{bmatrix} \mathcal{X}_{\{\hat{\epsilon}_z\}} & 0 \\ 0 & \mathcal{X}_{\{\hat{\epsilon}_z\}} \end{bmatrix} \frac{d}{dz}\begin{pmatrix} \mathbf{E}_{\omega,k} \\ \mathbf{H}_{\omega,k} \end{pmatrix} = \begin{bmatrix} -i\mathcal{X}_{\{\mathbf{k}\}} & i\omega\overleftrightarrow{\mu}\mathbb{I} \\ -i\omega\overleftrightarrow{\epsilon} & -i\mathcal{X}_{\{\mathbf{k}\}} \end{bmatrix} \begin{pmatrix} \mathbf{E}_{\omega,k} \\ \mathbf{H}_{\omega,k} \end{pmatrix} \rightarrow \qquad \mathbb{M}_{\epsilon_z}\left(\frac{d\boldsymbol{\mathcal{F}}^{(\mathbb{R}^3)}_{\omega,k}}{dz}\right) = \mathbb{M}_{\mathbf{k},\omega}\boldsymbol{\mathcal{F}}^{(\mathbb{R}^3)}_{\omega,k} \tag{B.3}$$

where we have introduced the material properties in terms of an arbitrary permittivity tensor $\overleftrightarrow{\epsilon}$ and a permeability tensor $\overleftrightarrow{\mu}$. Materials with girotropic properties or more complex constitutive relationships are disconsidered for the present analysis (but could be included in the same fashion).
When using other expression from literature one shall remember that the final results will be consistent with the convention used in the signs of $i\omega, i\mathbf{k}$ used in the Fourier expansion, which is often not even reported. The system cannot be inverted since the matrix on the left is singular. However, the z component of the field can be computed indepedently to derive a non-singular formulation of this linear problem. For that purpose, we split the linear system in two matricial equations and project those equations on the transverse plane and the z axis separately. Defining the projection matrices:

$$\mathbb{P}_{xy} = \begin{bmatrix} 1 & 0 & 0 & 0 & 0 & 0 \\ 0 & 1 & 0 & 0 & 0 & 0 \\ 0 & 0 & 0 & 1 & 0 & 0 \\ 0 & 0 & 0 & 0 & 1 & 0 \end{bmatrix} \qquad \mathbb{P}_z = \begin{bmatrix} 0 & 0 & 1 & 0 & 0 & 0 \\ 0 & 0 & 0 & 0 & 0 & 1 \end{bmatrix} \tag{B.4}$$

Equation (B.3) is hence split in the two projection as:

$$\begin{cases} \dfrac{d}{dz}\mathbb{P}_{xy}\mathbb{M}_{\epsilon_z}\boldsymbol{\mathcal{F}}^{(\mathbb{R}^3)}_{\omega,k} = \mathbb{P}_{xy}\mathbb{M}_{\mathbf{k},\omega}\boldsymbol{\mathcal{F}}^{(\mathbb{R}^3)}_{\omega,k} \\ \mathbb{P}_z\mathbb{M}_{\mathbf{k},\omega}\boldsymbol{\mathcal{F}}^{(\mathbb{R}^3)}_{\omega,k} = 0 \end{cases} \tag{B.5}$$

where we have made used of the singularity of $\mathcal{X}_{\{\hat{\epsilon}_z\}}$ since $\mathbb{P}_z\mathbb{M}_{\epsilon_z} = 0$. Considering now that the state vectors can be decomposed with the same projection matrices as:

$$\boldsymbol{\mathcal{F}}^{(\mathbb{R}^3)}_{\omega,k} = \mathbb{P}^T_{xy}\begin{pmatrix} E_x \\ E_y \\ H_x \\ H_y \end{pmatrix} + \mathbb{P}^T_z \begin{pmatrix} E_z \\ H_z \end{pmatrix} = \mathbb{P}^T_{xy}\boldsymbol{\mathcal{F}}^{[xy]}_{\omega,k} + \mathbb{P}^T_z\boldsymbol{\mathcal{F}}^{[z]}_{\omega,k} \tag{B.6}$$

We solve the z field from the second of equation of the system (B.5) as :

$$\boldsymbol{\mathcal{F}}^{[z]}_{\omega,k} = \mathbb{M}_{z\to xy}\boldsymbol{\mathcal{F}}^{[xy]}_{\omega,k} \qquad \mathbb{M}_{z\to xy} = -\left(\mathbb{P}_z\mathbb{M}_{\mathbf{k},\omega}\mathbb{P}^T_z\right)^{-1}\left(\mathbb{P}_z\mathbb{M}_{\mathbf{k},\omega}\mathbb{P}^T_{xy}\right) \tag{B.7}$$

Since also the total field can then be represented by only means of the tranverse fields $\boldsymbol{\mathcal{F}}^{[xy]}_{\omega,k}$ by:

$$\boldsymbol{\mathcal{F}}^{(\mathbb{R}^3)}_{\omega,k} = \left(\mathbb{P}^T_{xy} + \mathbb{P}^T_z\mathbb{M}_{z\to xy}\right)\boldsymbol{\mathcal{F}}^{[xy]}_{\omega,k} = \mathbb{M}_{\mathbb{R}^3\to xy}\boldsymbol{\mathcal{F}}^{[xy]}_{\omega,k} \tag{B.8}$$

we finally determine a non singular differential equation by reconsidering the first equation in set (B.5):

$$\frac{d}{dz}\boldsymbol{\mathcal{F}}^{[xy]}_{\omega,k} = \mathbb{P}_i\boldsymbol{\mathcal{F}}^{[xy]}_{\omega,k} \qquad \mathbb{P}_i = \left(\mathbb{P}_{xy}\mathbb{M}_{\epsilon_z}\mathbb{M}_{\mathbb{R}^3\to xy}\right)^{-1}\mathbb{P}_{xy}\mathbb{M}_{\mathbf{k},\omega}\mathbb{M}_{\mathbb{R}^3\to xy} \tag{B.9}$$

The provided formulas is suitable for all forms of permittivity and permeability tensors in a given reference and $k_x, k_y \neq 0$. It moreover explicits the z field components also. We will use in the report the formula (B.9) with a diagonal permittivity tensor and permeability tensors of the form:

$$\overleftrightarrow{\epsilon} = \epsilon_0\begin{bmatrix} \epsilon_{r,x} & 0 & 0 \\ 0 & \epsilon_{r,y} & 0 \\ 0 & 0 & \epsilon_{r,z} \end{bmatrix} \qquad \overleftrightarrow{\mu} = \mu_0\begin{bmatrix} \mu_{r,x} & 0 & 0 \\ 0 & \mu_{r,y} & 0 \\ 0 & 0 & \mu_{r,z} \end{bmatrix} \tag{B.10}$$

for which we explicitly determined:

$$\mathbb{P}_i = \begin{bmatrix} 0 & 0 & \frac{i\eta_0 k_x k_y}{\epsilon_{r,zz}k_0} & \frac{i\eta_0\left(\epsilon_{r,zz}k_0^2\mu_{r,yy} - k_x^2\right)}{\epsilon_{r,zz}k_0} \\ 0 & 0 & \frac{i\eta_0\left(-\epsilon_{r,zz}k_0^2\mu_{r,xx} + k_y^2\right)}{\epsilon_{r,zz}k_0} & -\frac{i\eta_0 k_x k_y}{\epsilon_{r,zz}k_0} \\ -\frac{ik_x k_y}{\eta_0 k_0 \mu_{r,zz}} & \frac{i\left(-\epsilon_{r,yy}k_0^2\mu_{r,zz} + k_x^2\right)}{\eta_0 k_0 \mu_{r,zz}} & 0 & 0 \\ \frac{i\left(\epsilon_{r,xx}k_0^2\mu_{r,zz} - k_y^2\right)}{\eta_0 k_0 \mu_{r,zz}} & \frac{ik_x k_y}{\eta_0 k_0 \mu_{r,zz}} & 0 & 0 \end{bmatrix} \tag{B.11}$$

and

$$\mathbb{M}_{z\to xy} = \begin{bmatrix} -\frac{\epsilon_{r,xz}}{\epsilon_{r,zz}} & -\frac{\epsilon_{r,yz}}{\epsilon_{r,zz}} & \frac{\eta_0 k_y}{\epsilon_{r,zz}k_0} & -\frac{\eta_0 k_x}{\epsilon_{r,zz}k_0} \\ -\frac{k_y}{\eta_0 k_0 \mu_{r,zz}} & \frac{k_x}{\eta_0 k_0 \mu_{r,zz}} & -\frac{\mu_{r,xz}}{\mu_{r,zz}} & -\frac{\mu_{r,yz}}{\mu_{r,zz}} \end{bmatrix} \tag{B.12}$$

where the vacuum impedance definition and the wave-number have been considered:

$$\eta_0 = \sqrt{\frac{\mu_0}{\epsilon_0}} \qquad k_0 = \omega\sqrt{\epsilon_0\mu_0} \tag{B.13}$$

The formulas are equivalent to the one reported in (4.9), once η_0 is recasted in the state vector and k_0 simplified by introducing the wave-vector cosine directors s_x, s_y. We have verified with the expressions reported in [79], [80], [33] that the formulations are equivalent. We first have to transform the matrix $\mathbb{P}_i$ in the incidence plane reference used in [33] and use the parameterization $k_x = \xi\cos\phi, k_y = \xi\sin\phi$ for the purpose. The change of reference system in the incidence plane reads:

$$\mathbb{P}^{(\phi)}_i = \mathbb{R}_{(\phi)}\mathbb{P}_i\mathbb{R}^T_{(\phi)} \qquad \mathbb{R}_{(\phi)} = \begin{bmatrix} \cos\phi & -\sin\phi & 0 & 0 \\ \sin\phi & \cos\phi & 0 & 0 \\ 0 & 0 & \cos\phi & -\sin\phi \\ 0 & 0 & \sin\phi & \cos\phi \end{bmatrix} \tag{B.14}$$

considering that [33], [79] used a Gaussian Units system (as clear by simple dimensional analysis) one can tidely apply the procedure there described by using the local rotated permittivity and permeability tensors on the incidence plane frame:

$$\overleftrightarrow{\epsilon}^{(\phi)} = \left(\mathbb{R}^m_{(\phi)}\right)^T\overleftrightarrow{\epsilon}\mathbb{R}^m_{(\phi)} \qquad \overleftrightarrow{\mu}^{(\phi)} = \left(\mathbb{R}^m_{(\phi)}\right)^T\overleftrightarrow{\mu}\mathbb{R}^m_{(\phi)} \qquad \mathbb{R}^m_{(\phi)} = \begin{bmatrix} \cos\phi & -\sin\phi \\ \sin\phi & \cos\phi \end{bmatrix} \tag{B.15}$$

and determine the same result for $\mathbb{P}^{(\phi)}_i$.

C

Spectral Power and Radiometric Link with Electromagnetic Fields

In this Appendix, we demonstrate the Equations (5.2), (5.3). The treatment is mainly based on the paper [44] and the review [38], which presents a sound dimensional treatment of the Poynting Vector associated with a Fraunhofer far-field propagation of the cross-correlation tensor. We refer the reader to image 6.1 for the symbols used.
In the correlation tensor treatment, two vectors are used both for the object domain and the pupil domain. We start by considering the cross-correlation (electric) tensor of our source, $\mathbb{W}_{(\mathbf{r}_{ob1},\mathbf{r}_{ob2},\omega)}$. Dependance of time due to its quasi-stationarity is omitted for ease of notation. Moreover, we assume a dependance of the type:

$$\mathbb{W}_{(\mathbf{r}_{1ob},\mathbf{r}_{2ob},\omega)} = \tilde{\sigma}_{(\Delta\mathbf{r}_{ob})}\mathbb{W}_{(\mathbf{r}_{ob},\mathbf{r}_{ob},\omega)} \qquad [V^2s/m^2] \tag{C.1}$$

where $\tilde{\sigma}_{(\Delta\mathbf{r}_{ob})}$ is a (weak) correlation functions and $\Delta\mathbf{r}_{ob} = (\mathbf{r}_{2ob} - \mathbf{r}_{1ob})$ and $\mathbf{r}_{ob} = (\mathbf{r}_{2ob} + \mathbf{r}_{1ob})/2$ as represented in Figure 4.2. As described in [23] (see *Coherence Chapter, Quasi-Homogeneous Source*) that's a good model for source which are poorly spectrally correlated as Earth. For example, for a thermal Lambertian source a small degree of coherence with a coherence extent of λ is always present [23] as:

$$\tilde{\sigma}_{(\Delta\mathbf{r}_{ob})} = 2\pi\left(\frac{\sin(k|\Delta\mathbf{r}_{ob}|)}{k|\Delta\mathbf{r}_{ob}|}\right) \tag{C.2}$$

For the limit of small wavelengths this can be approximated by a two-dimensional Delta Dirac as:

$$\tilde{\sigma}_{(\Delta\mathbf{r}_{ob})} = 4\pi^2\delta^2_{(k\Delta\mathbf{r}_{ob})} \tag{C.3}$$

where the scaling factor $4\pi^2$ has been formally determined by operating the limiting procedure $k \to \infty$ in the above Lambertian distribution.
Applying the propagation formula (4.36) for the geometry and notation of Figure 6.1 we determine:

$$\mathbb{W}^{\infty}_{(z_{21},z_{22},\omega)} = \frac{1}{\lambda_0^2}\int_{\mathcal{A}_{sc1}}\int_{\mathcal{A}_{sc2}} \mathbb{W}_{(\mathbf{r}_{ob1},\mathbf{r}_{ob2},\omega)}\left(\frac{e^{ik\Delta z_2}}{z_{21}z_{22}}\right)\cos(\theta_{ob1}+\theta_{in1})\cos(\theta_{ob2}+\theta_{in2})d^2\mathbf{r}_{ob1}d^2\mathbf{r}_{ob2} \tag{C.4}$$

Where integration is carried over the scanning area two times. We consider the local plane tangent to the scanning area, whose normal direction with the vector $\mathbf{z}_2$ forms an angle of $\theta_{ob,j} + \theta_{in,j}$ (angle between $\mathbf{r}_{ob}$ and $\mathbf{z}_2$ in Figure 6.1). That's equivalent to the projection angles used in radiometry. The integration can be simplified considering the source is spatially uncorrelated, which resolves the first integration with the change of variables $(\mathbf{r}_{1ob}, \mathbf{r}_{2ob}) \to (\mathbf{r}_{ob}, \Delta\mathbf{r}_{ob}) \to (\mathbf{r}_{ob}, (\rho_{ob}\cos(\phi_{ob}), \rho_{ob}\sin(\phi_{ob}))$. In fact, for an arbitrary function f:

$$\int_{\mathcal{A}_{sc}} 4\pi^2 f_{(\Delta\mathbf{r}_{ob})}\delta^2_{(k\Delta\mathbf{r}_{ob})}d^2\Delta\mathbf{r}_{ob} = \frac{4\pi^2 f_{(0)}}{k^2} = \lambda_0^2 f_{(0)} \tag{C.5}$$

A highly oscillatory factor in $k|\Delta\mathbf{r}_{ob}|$ would be present by pertaining the real Lambertian distribution. With the above result we determine:

$$\mathbb{W}^{\infty}_{(z_{21},z_{22},\omega)} = \int_{\mathcal{A}_{sc}} \mathbb{W}_{(\mathbf{r}_{ob},\mathbf{r}_{ob},\omega)}\left(\frac{e^{ik\Delta z_2}}{z_2^2}\right)\cos^2(\theta_{ob}+\theta_{in})d^2\mathbf{r}_{ob} \tag{C.6}$$

where we neglected $\Delta\theta_{in,j}$ since $\Delta\theta_{in,j} << \theta_{in,j}$. The expression of Δz_2 is known and given by Equation 6.1. Due to multiplication for $k >> 0$, we cannot simplify Δz_2 in $k\Delta z_2$, but we simplified such small term in the denominator. A Taylor series of this difference reads:

$$\Delta z_2 = -\mathbf{r_{ob}} \cdot (\mathbf{s}_{\perp,2} - \mathbf{s}_{\perp,1}) \tag{C.7}$$

with:

$$\mathbf{s}_{\perp,i} = \frac{\rho_{ei}}{z_2}\begin{pmatrix}\cos\phi_{ei}\\ \sin\phi_{ei}\end{pmatrix} \qquad \mathbf{r}_{e,i} = \rho_{ei}\begin{pmatrix}\cos\phi_{ei}\\ \sin\phi_{ei}\end{pmatrix} \tag{C.8}$$

The format resembles the cosine directions appearing in [44], due to the fact that we are in the far-field. We further note that according to the more useful notation introduced in Chapter 6 the following relationships apply:

$$\frac{d^2\mathbf{r}_{ob}}{z_2^2} = \frac{1}{z_2^2}dq_u dq_v = \frac{h_s^2}{z_2^2}d^2\tilde{\mathbf{q}} = \frac{d\Omega_{gr\to e}}{\cos\theta_n} \qquad \mathbf{r} = \begin{pmatrix}q_u\\ q_v\end{pmatrix} \tag{C.9}$$

Defining

$$\theta_n = \theta_{ob} + \theta_{in} \qquad \cos\theta_g = \frac{h_s}{z_2} \tag{C.10}$$

we further notice that:

$$\Delta z_2 = -\cos\theta_g \tilde{\mathbf{q}} \cdot (\mathbf{r}_{e2} - \mathbf{r}_{e1}) \tag{C.11}$$

We hence rewrite (C.6) as:

$$\mathbb{W}^{\infty}_{(\mathbf{r}_{e1},\mathbf{r}_{e2},\omega)} = \int_{\mathcal{A}_{sc}} \mathbb{W}_{(\mathbf{r}_{ob},\mathbf{r}_{ob},\omega)} e^{-ik\cos\theta_g \tilde{\mathbf{q}}\cdot(\mathbf{r}_{e2}-\mathbf{r}_{e1})} \cos^2\theta_n \cos^2\theta_g d^2\tilde{\mathbf{q}} \tag{C.12}$$

The formula has a particular meaning when considering the radiative intensity in terms of the mean averaged Poynting Vector $\langle \mathbf{S}^{\infty}_{(\hat{\mathbf{s}}_i,t)}\rangle$, also defined in [44] as, (adjusting for notation):

$$\langle \mathbf{S}^{\infty}_{(\hat{\mathbf{s}}_i,t)}\rangle = \hat{\mathbf{s}}_i \int_0^{\infty}\int\int_{\mathcal{A}_{sc}} \frac{1}{2\eta_0}\cos^2\theta_n \cos^2\theta_g \,\mathrm{Tr}\{\mathbb{W}^{[\xi,\eta]}_{(\mathbf{r}_{ob},\mathbf{r}_{ob},\omega)}\} d\omega d^2\tilde{\mathbf{q}} \tag{C.13}$$

where we have further considered the frame transformation $\xi\eta$ locally perpendicular to $\hat{\mathbf{s}}_i$ with the introduced transformation of Chapter 5.1 and the vacuum impedance η_0. From the Poynting Vector expression, with the understanding that it shall be measured in W/m^2 and it represents the carrier of intensity, we can define, by similarity with the expressions in radiometry, the corresponding scalar radiance per unit frequency as:

$$L^{\infty}_{\omega(\hat{\mathbf{s}}_i,\mathbf{r}_{ob})} = \frac{\cos\theta_n}{2\eta_0}\,\mathrm{Tr}\{\mathbb{W}_{(\mathbf{r}_{ob},\mathbf{r}_{ob},\omega)}\}^{[\xi,\eta]} \tag{C.14}$$

where we have used the fact that by definition:

$$\cos^2\theta_g \cos\theta_n d^2\tilde{\mathbf{q}} = d\Omega_{gr\to e} \tag{C.15}$$

The interpretation is now clear: (C.6) describes superposition of monochromatic fields from point-sources, with an arbitrary polarization and a field intensity $\propto$ to the local radiance, which in turns depends on the field generated at the source. The treatment is in very good agreement with the radiometric cosines law, since the geometrical factor $h_s^2/z_2^2 \cong \cos^2\theta_{in}$ as we observe by inspection of Figure 6.4. The cosine angle decrease with the entrance pupil surface projection is, from an electromagnetic treatment perspective, related to the local Fresnel reflection laws at the lenses surface.
Within the derivation, we have assumed ideal free-space propagation of the field, which in reality undergoes scattering and finite transmission in the atmospheric layer. Nevertheless, as also explained in [38], is always possible to define an effective field such to comply with the observed radiance. Moreover, any real optical system realization will not be able to image scattered fields from unknown conjugates, so the rays carrying optical power to the detector are the one following exactly the prescribed geometry. Hence we can considered the radiance in (C.14) as the effective radiance at the entrance pupil, comprehensive of transmission and polarization effects along the ray propagation once $\mathbb{W}_{(\mathbf{r}_{ob},\mathbf{r}_{ob},\omega)}$ has been opportunely corrected to include those. It is also well known that a Lambertian source, by definition, possesses an

isotropic radiance in the different directions, but the implication of such remark on the angular distribution of $\mathrm{Tr}\{\mathbb{W}_{(\mathbf{r}_{ob},\mathbf{r}_{ob},\omega)}\}^{[\xi,\eta]}$ are still elusive to us.
We further point out that radiance is usually defined per unit wavelength rather than per unit frequency. The relation between the two is, due to simple differential analysis:

$$L^{\infty}_{\lambda(\hat{\mathbf{s}}_i,\mathbf{r})} = \left(\frac{\omega}{\lambda_0}\right) L^{\infty}_{\omega(\hat{\mathbf{s}}_i,\mathbf{r})} = \left(\frac{2\pi c_0}{\lambda_0^2}\right) L^{\infty}_{\omega(\hat{\mathbf{s}}_i,\mathbf{r})} \tag{C.16}$$

Combining all together we finally get:

$$\mathbb{W}^{\infty}_{(\mathbf{r}_{e1},\mathbf{r}_{e2},\omega)} = \int_{\mathcal{A}_{sc}} \left(\frac{\lambda_0^2\eta_0}{\pi c_0}\right) \cos^2\theta_g \cos\theta_n L^{\infty}_{\lambda(\hat{\mathbf{s}}_i,\mathbf{r})} \langle \mathbf{e}\mathbf{e}^{\dagger}\rangle e^{-ik\cos\theta_g \tilde{\mathbf{q}}\cdot(\mathbf{r}_{e2}-\mathbf{r}_{e1})} d^2\tilde{\mathbf{q}} \tag{C.17}$$

where the normalized fields are defined by:

$$\langle \mathbf{e}\mathbf{e}^{\dagger}\rangle = \frac{\mathbb{W}_{(\mathbf{r}_{ob},\mathbf{r}_{ob},\omega)}}{\mathrm{Tr}\{\mathbb{W}_{(\mathbf{r}_{ob},\mathbf{r}_{ob},\omega)}\}} \tag{C.18}$$

We have appearance of the quantity $\left(\frac{\lambda_0^2\eta_0}{\pi c_0}\right)$ with other variables appearing in radiation formulations in antenna theories (directivity, gain, etc...). The impedance has also known relationships with the Planck constant and hence electromagnetic photon energy.
We remember the reader the q_u, q_v are not coordinates of points on ground but rather of the moving scanning area with respect to ground, so that the imaging mapping is in reality implicitly dependant on time (but still quasistationary with respect to the frequency of light).
The cross-correlation tensor $\langle \mathbf{e}\mathbf{e}^{\dagger}\rangle$ in the transverse plane $[\xi,\eta]$ is directly related to the Stokes vector, by relationships depicted in 4.4.
In conclusion, we have determined a radiometric link between classic radiometric quantities and electromagnetic ones in the far-field of our observation geometry and clarified on the measured observable and its relationships with the Stokes parameters we wish to measure.

D

Splines Integration Routine

Throughout the report, we have often incurred in functions transforms to be evaluated on extensive grids. In particular implementation of the Zernike Transform appearing in 5.62 is numerically troublesome to implement with standard quadrature and evaluation techniques.
In this Appendix we report the numerical tool implementation for a stable and numerically efficient transform based on splines integration, applicable also for arbitrary scaling of the function. The general shape of the integral of interest is of the form:

$$\mathcal{T}_{[f,g]} = \int_0^{x_{max}} f_{(\alpha x,\mathbf{v})} g_{(x,\mathbf{w})} dx \tag{D.1}$$

where α can be an arbitrary scaling factor $\alpha \in [0,1]$ (also a grid), f is the function which we have to transform in g. For example, in a Zernike Transform g is the radial Zernike polynomial multiplied for x and x_{max} is 1. The function further depend on mute variable grids $\mathbf{v}$ and $\mathbf{w}$. It is assumed that $g_{(x,\mathbf{w})}$ is known analytically and also the indefinite integral:

$$G_{(x,n,\mathbf{w})} = \int x^n g_{(x,\mathbf{w})} dx \tag{D.2}$$

can be analytically resolved. That is the case for all the transforms appearing in the report.
Resolving the integral (D.1) iteratively by means of a simple quadrature requires extensive memory allocation (also in the case of an FFT) and soon becomes time-demanding when thousands of data points are present in the grids. Since the variables $\mathbf{v}$ are mute, the integration can be fully retrieved from the knowledge of the splines coefficient of the function $f_{(x,\mathbf{v})}$ only, when $\alpha \in [0,1]$. Integration is then carried fully analytically in the polynomials of the splines by means of a symbolic toolbox and the splines coefficients are only reinserted in the last step fo the operation. We can in fact write:

$$f_{(\alpha x,\mathbf{v})} \cong \sum_{i=1}^{n_s} \mathbf{f}^T_{c,i(\mathbf{v})} \begin{bmatrix} (\alpha x - x_i)^n \\ (\alpha x - x_i)^{(n-1)} \\ .... \\ (\alpha x - x_i) \\ 1 \end{bmatrix} = \sum_i \mathbf{f}^T_{c,i(\mathbf{v})} \mathbf{p}_{i(x,x_i,\alpha)} \tag{D.3}$$

where $\mathbf{p}_{i(x,x_i,\alpha)}$ is only defined in the interval through $[x_i/\alpha, x_{[i+1]}/\alpha]$ and zero elsewhere and the summation is carried over n_s splines of order n. The splines must be defined with the appropriate boundary conditions (e.g. derivatives at the extreme bounds, known since $f_{(\alpha x,\mathbf{v})}$ is given). The transform is hence given by:

$$\mathcal{T}_{[f,g]} = \left(\sum_{i=1}^{n_s} \mathbf{f}^T_{c,i(\mathbf{v})} \mathbf{G}_{i(\alpha,x_i,\mathbf{w})} \right) (1+\epsilon) \tag{D.4}$$

where ϵ is a truncation error and we have introduced the analytically known integral:

$$\mathbf{G}_{i(\alpha,x_i,\mathbf{w})} = \int_0^{x_{max}} \mathbf{p}_{i(x,x_i,\alpha)} g_{(x,\mathbf{w})} dx \tag{D.5}$$

which, due to the splines definition domain, evaluates to (with $\alpha \in [0,1]$):

$$\mathbf{G}_{i(\alpha,x_i,\mathbf{w})} = \begin{cases} \int_{x_i/\alpha}^{x_{[i+1]}/\alpha} \mathbf{p}_{i(x,x_i,\alpha)} g_{(x,\mathbf{w})} dx & x_{[i]}/x_{max} < x_{[i+1]}/x_{max} \leq \alpha \\ \int_{x_i/\alpha}^{x_{max}} \mathbf{p}_{i(x,x_i,\alpha)} g_{(x,\mathbf{w})} dx & x_{[i]}/x_{max} < \alpha < x_{[i+1]}/x_{max} \\ 0 & \alpha \leq x_{[i]}/x_{max} < x_{[i+1]}/x_{max} \end{cases} \tag{D.6}$$

Hence only some of the splines are active for a given α.
The truncation error can be reduced by maximizing the number of splines. In the calculation implementation, $\mathbf{G}_{i(\alpha,x_i,\mathbf{w})}$ is calculated by means of a symbolic toolbox (*sympy Python toolbox*) and an order of the splines of $n = 3$ is used. In such case, with use of $n_s = 100$ splines, ϵ is in the order of 10^{-9} for most well behaved functions in Zernike or Fourier Transforms. Since $\mathbf{G}_{i(\alpha,x_i,\mathbf{w})}$ does not depend on $\mathbf{v}$, this fast algorithm implementation is not significantly affected by the dimensions of the grids of the input function $\mathbf{f}$, leading to broadcasting of millions of datapoints in seconds on our machine. The function is always a logical function of α depending on the grids spacing discretization. The final transform is hence a linear combination of the splines coefficient of f and it can also be observed that also integrals involving a normalization which is numerically ill-defined, like the one in (5.39), can be computed with arbitrary precision with such method by means of a change of variable through some α.
This approach could also be easily extended to cross-correlation integrals by considering $f_{(\alpha x+\beta,\mathbf{v})}$ for arbitrary α, β.

D.1. Applications to Zernike Transforms

In the case of Radial Zernike Transforms, the radial basis $g_{(x,\mathbf{w})}$ are given by:

$$g_{(x,w=q)} = R^{|q|}_{s(x)} x = \mathbf{p}^T_{(s_{max},x)} \mathbf{c}_{[s,q]} \qquad \mathbf{p}_{(s_{max},x)} = \begin{pmatrix} x \\ x^2 \\ ... \\ x^{s_{max}} \\ x^{s_{max}+1} \end{pmatrix} \tag{D.7}$$

where $R^q_{s(x)}$ is the radial Zernike polynomial on the semisphere. Those radial basis can be described as a subset of a smaller set of polynomial of powers x^n, which allows for further significant improvement in the calculation of the Zernike Transform. Using the previous notation hence, for a Zernike Transform we determine:

$$\mathbf{G}^{[q,s]}_{i(\alpha,x_i)} = \left(\int_{x_{min}}^{x_{max}} \mathbf{p}_{i(x,x_i,\alpha)} \mathbf{p}^T_{(s_{max},x)} dx \right) \mathbf{c}_{[s,q]} \tag{D.8}$$

The matrix integration in parenthesis can be carried in one go when an appropriate symbolic integration routine is used, so that all coefficients are retrieved from successive linear combination. Since the Radial Polynomial $R^{|q|}_{s(x)}$ can be written as:

$$R^{|q|}_{s(x)} = \sum_{j=|q|,step=2}^{s} \frac{(-1)^k (s-k)!}{k!(\overline{\eta}-k)!(\Delta\eta-k!)} \rho^j \qquad k = \left(\frac{s-j}{2}\right) \qquad \overline{\eta} = \left(\frac{s+|q|}{2}\right) \qquad \Delta\eta = \left(\frac{s-|q|}{2}\right) \tag{D.9}$$

It follows that the rational coefficients $\mathbf{c}_{[q,s]}$ are:

$$\mathbf{c}_{[q,s],j} = \begin{cases} \frac{(-1)^k (s-k)!}{k!(\overline{\eta}-k)!(\Delta\eta-k)!} & \forall j \in \mathcal{S} \\ 0 & elsewhere \end{cases} \tag{D.10}$$

where $\mathcal{S}$ is the subset of integer numbers j contained between $|q|$ and s, boundaries included, and of which difference $s - j$ is an even number.
In general, the coefficients are unstable for $s_{max} > 30$ due to memory overflow (on our 64-bit machine) with standard numerical modules techniques. To avoid numerical instability for $s_{max} > 30$, the arbitrary

precision library *mpmath* is used, at the drawback of some slow-down for very high orders ($s_{max} > 200$). Alternatively, the Zernike basis functions could also be defined numerically by means of a stable recursion algorithm, but the broadcasting scheme here proposed could not be used in that case. When the splines spacing and α spacing is chosen opportunely (to be in fractions of integer numbers), the coefficients $\mathbf{G}^{[q,s]}_{i(\alpha,x_i)}$ are also fractions of integer numbers and they can be evaluated at arbitrary precision. Once their evaluation is carried over, the numerical instability is resolved (also close to $x = 1$ where the Zernike Basis if particularly troublesome) and standard numerical techniques can be used for the evaluation of (D.4). In Conclusion, the algorithm is stable for all s and significantly ease the required numerical iterations and accuracy in comparison with a straightforward integration on grids. We have in fact observed that if such arbitrary precision is not used, oscillations in numerical values may strongly affect the transform calculation also for $s_{max} < 30$ for some functions, whereas we are able to achieve transform errors $\epsilon < 10^{-6}$ for an $s_{max} = 80$ for most well behaved functions, limited only by computational time. We further recall that the full Zernike basis $R^{|q|}_{s(x)}$ is a complete set for sufficiently smooth continuous functions in the origin (scaling with x^q in Taylor Expansion). That's assumed to be the case in the transforms on this report due to continuity of the fields at the exit pupil and of the transmission spectrum, which ensures the smoothness. When applied to Diffraction Integral, further, due to multiplication with a Bessel function of order s which is nill in $x = 0$ for $s > 0$, any discrepancy in the transform in the origin does not significantly affect the result. A more accurate study on accuracies would be interesting but is out of the scope for the present Research.

E

Examples of Jones Vectorial Transformations

In Section 5.2 we have introduced a rather lengthy matricial method for determining the Jones transformation of a device. We hereby present some examples for guiding the reader in their use.
For a polarizing lens, the Jones transformation in a $p-s$ frame of the Optics reads (on the tangential plane):

$$\mathbb{J}^{(o)} = \begin{bmatrix} \tau_p & 0 \\ 0 & \tau_s \end{bmatrix} \tag{E.1}$$

The final transformation of the field appearing in (5.15), (assuming no apodization for simplicity) reads:

$$\mathbb{J}_e = \frac{1}{2}\begin{bmatrix} \tau_s + \tau_p\cos(\theta) + (-\tau_s + \tau_p\cos(\theta))\cos(2\phi) & (-\tau_s + \tau_p\cos(\theta))\sin(2\phi) \\ (-\tau_s + \tau_p\cos(\theta))\sin(2\phi) & \tau_s + \tau_p\cos(\theta) + (\tau_s - \tau_p\cos(\theta))\cos(2\phi) \\ -2\tau_p\sin(\theta)\cos(\phi) & -2\tau_p\sin(\phi)\sin(\theta) \end{bmatrix} \tag{E.2}$$

$$\mathbb{J}_h = \frac{1}{2}\begin{bmatrix} (\tau_s\cos(\theta) - \tau_p)\sin(2\phi) & -\tau_s\cos(\theta) - \tau_p + (-\tau_s\cos(\theta) + \tau_p)\cos(2\phi) \\ \tau_s\cos(\theta) + \tau_p + (-\tau_s\cos(\theta) + \tau_p)\cos(2\phi) & (-\tau_s\cos(\theta) + \tau_p)\sin(2\phi) \\ -2\tau_s\sin(\phi)\sin(\theta) & 2\tau_s\sin(\theta)\cos(\phi) \end{bmatrix} \tag{E.3}$$

Which relates fields from a tangential plane of the lens in the ξ, η frame to a cartesian frame of the focal beam. We can verify agreement with the Jones matrices proposed in [28], which describes x polarized light only (left column) with an ideal optics. In the case of ideal optics, the cross-polarization terms scale with $(1-\cos\phi)\sin(2\phi)$, which is known as *maltese* and observed in practical experiments of polarized light as discussed in [28], [24]. As a consequence of intrinsic geometry, the fields have an azimuthal dependance which reflects their polarization direction and will induce an elliptical focal spot. In reality, the coefficients τ_s, τ_p of the optics themselves may be dependant on the two angles. We further observe that the electric field is better transmitted for τ_s polarization rather than τ_p, and vice-versa applies for the magnetic field. When the transmissions of the idealized lens (or any other device so modeled with this matrix) are complex, aberrations may be introduced since p, s transmission does not generally possess the same phase for an arbitrary angle.
We can further observe that the transmitted component of the Poynting Vector along the propagation direction is $\propto 1/2(\tau_p^2 + \tau_s^2)\cos\theta$, as expected, but the electric energy transmitted in the transverse plane (Mueller coefficient M_{00}) is instead $\propto 1/2(\tau_p^2\cos^2\theta + \tau_s^2)$ and is hence negatively biased for the p polarization. Additional projections are in reality present due to radiometric apodization of the rays [28].
One may calculate the Mueller Matrix associated with this plane-wave transformation and determine that the Mueller coefficients are not nill, but vanish after azimuthal integration if the input field is azimuthally uniform. If diffraction is to be accounted for, however, one shall perform the Mueller Transformation after integrating the coherent fields in the cone angle, to correctly account for aberrations and focusing.
The Jones matrix proposed does applies in the absence of a polarizer or any non-axial symmetric device. Suppose a conventional polarizer is engineered such to have a fast and slow axis x, y (cartesian), with no cross-induced polarization. Hence its transformation from and to a cartesian frame would be of the form

$$\mathbb{J}^{(p)}_{|\Sigma_0} = \begin{bmatrix} \tau_x & 0 \\ 0 & \tau_y \end{bmatrix} \tag{E.4}$$

When operating on a collimated beam the principle of operation of this transformation is straightforward, directly influencing the field $\mathbf{e}^{in}_{|\Sigma_0}$ previous refraction. When operating on a focused beam though, the tranformation is significantly more complex, specifically in the case in which also polarization dependent transmissions like the one previously discussed are present. For grasping an understanding, we tentatively seek an extrapolation of the transformation for other angles. Simply generalizing the transformation in the $p-s$ frame as:

$$\mathbb{J}^{(p)} = \Sigma^T \mathbb{J}^{(p)}_{|\Sigma_0} \Sigma \tag{E.5}$$

with Σ the rotation matrix of the focused versors in the $[p, s]$ frame, introduces an undesired scattering effect, leading to the creation of a field in the direction of $\hat{k}$ which is not physical. By geometrical consideration we can conclude that the transformation has to be limited on the transverse $p-s$ plane if no deviation of the wave-vector is present, hence a physical transformation is given by:

$$\mathbb{J}^{(p)} = \Sigma_r^T \mathbb{J}_{|\Sigma_0} \Sigma_r \tag{E.6}$$

Which explicitly reads:

$$\mathbb{J}^{(p)} = \begin{bmatrix} J_{n1}\cos(2\phi) + J_{s1} & J_{k1}\sin(2\phi) \\ J_{k2}\sin(2\phi) & J_{n2}\cos(2\phi) + J_{s2} \end{bmatrix} \tag{E.7}$$

with:

$$J_{n1} = -J_{k2} = -J_{k1} = -J_{n2} = \frac{\tau_x - \tau_y}{2} \qquad J_{s1} = J_{s2} = \frac{\tau_x + \tau_y}{2} \tag{E.8}$$

The coefficients will instead differ in case of coupling with mirrors or presence of other optical devices and further depend also on θ in a realistic system. In particular,cross-couplings ps and sp appear naturally due to the fact that a polarizer breaks the rotational simmetry of the fields.
We have verified that the proposed transformation well represent a polarizer transformation in the $p-s$ frame, by validating a simple Gold grating polarizer simulation from FEM models and fitting with an accuracy of 2% the values of τ_x, τ_y, see Figure E.1. The simulations results have also shown presence of the couplings factors here reported. When represented in the ξ, η frame (closes tranverse fame found by rotation of the $x-y$ frame) the transmission factors are roughly constant. Their variations with θ is in fact better described with the first two terms of Equation (E.5). In the simulated setup, $\tau_x = 0.018, \tau_y = 0.88$. The polarized components of an ideal polarizer ($\tau_x = 1, \tau_y = 0$) scale with $(1 - \cos(2\phi))/2 = \sin^2(\phi)$ in this frame.
We may also determine, as previously, the expression of the complete transformation with inclusion of a lens, and placement of the polarizer in the focused beam. The introduction of the polarizer in that location results in presence of additional azimuthal frequencies. For the electric field:

$$\mathbb{J}_e = \begin{bmatrix} I_{0,0} + 2I_{4,0}\cos(2\phi) + 2I_{9,0}\cos(4\phi) & 2I_{5,0}\sin(2\phi) + 2I_{9,0}\sin(4\phi) \\ 2I_{6,0}\sin(2\phi) + 2I_{9,0}\sin(4\phi) & I_{1,0} + 2I_{7,0}\cos(2\phi) - 2I_{9,0}\cos(4\phi) \\ 2I_{2,0}\cos(\phi) + 2I_{8,0}\cos(3\phi) & 2I_{3,0}\sin(\phi) + 2I_{8,0}\sin(3\phi) \end{bmatrix} \tag{E.9}$$

and for the magnetic field:

$$\mathbb{J}_h = \begin{bmatrix} -2W_{6,0}\sin(2\phi) - 2W_{9,0}\sin(4\phi) & -W_{1,0} - 2W_{7,0}\cos(2\phi) + 2W_{9,0}\cos(4\phi) \\ W_{0,0} + 2W_{4,0}\cos(2\phi) + 2W_{9,0}\cos(4\phi) & 2W_{5,0}\sin(2\phi) + 2W_{9,0}\sin(4\phi) \\ 2W_{2,0}\sin(\phi) + 2W_{8,0}\sin(3\phi) & 2W_{3,0}\cos(\phi) - 2W_{8,0}\cos(3\phi) \end{bmatrix} \tag{E.10}$$

where I_j, W_j are coefficients linearly depending on the matrix $\mathbb{J}^{(p)}$ and on $\sin\theta, \cos\theta$. One may again determine the Mueller Matrix of this transformation, and this time reach the conclusion that the Mueller Coefficients are not nill also upon integration in the azimuthal angle, as expected. The centered cross-correlation components $I_j I_j^*$ only would appear in such integration for the electric energy density and the coefficients $I_j W_j^*$ for the Poynting Vectors components. The latter may be in general complex upon focusing (representing some reactive power). The focal fields upon diffraction integrations further pertain the same azimuthal dependance (see diffraction integral in the variable α of the detector plane), so they are not simply elliptical anymore.
The given transformations are merely simplified examples: in fact, the transformation of the metasurface device presents an infinite order of azimuthal components, we have determined from the coupled transfer matrix method presented in Chapter 4. Nevertheless, it seems that the more relevant numerically are the

ones 'naturally' present from the references frame as here derived. In the metasurface case, moreover, the cross-terms $\tau_{ps,sp}$ are strongly affected by the mirrors couplings, which motivated the use of a more complex treatment, and all the relevant quantities are spectral. In that case we have in fact further considered the exact analytical expression off-angle of the anisotropic layer rather than extrapolating the behavior-off angle.

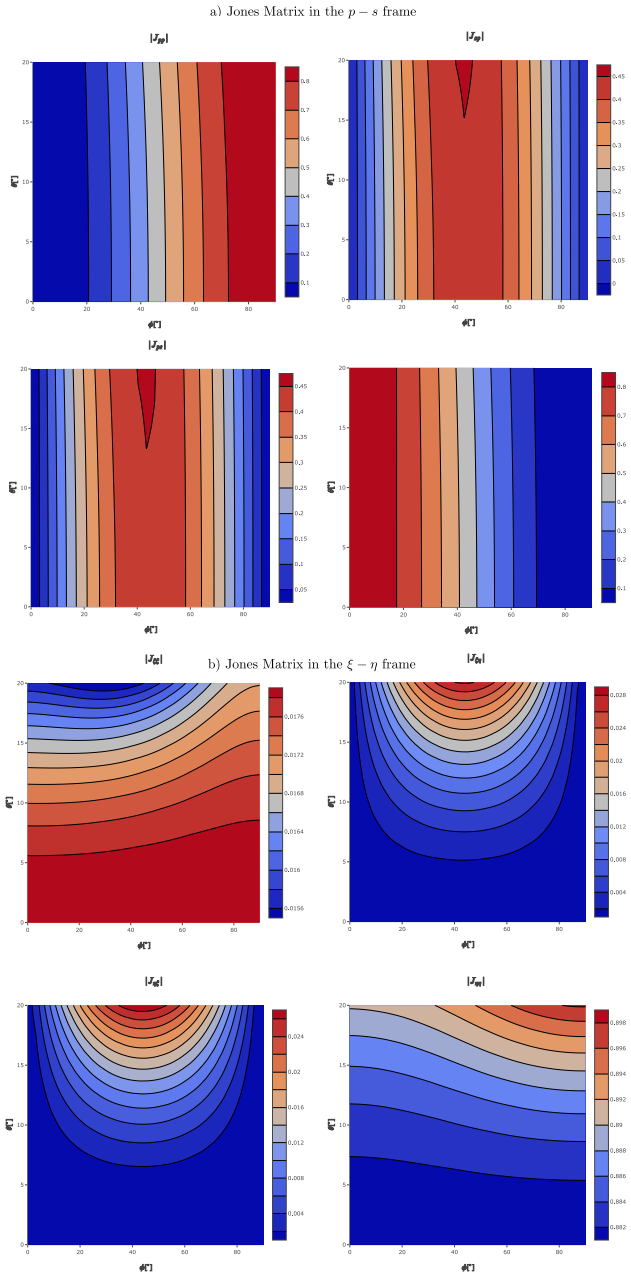

Figure E.1: Simulation results of a Gold grating acting as a polarizer, postprocessed from COMSOL. In a) the fields in the $p-s$ frame are represented. The distribution of this field in the azimuthal angle ϕ well represented the behavior predicted by Equation (E.7). Coupling factors can clearly be seen for $\phi \neq 0$, which are not negligible. b) Same transformation seen in the $\xi-\eta$ frame, the closest tranverse frame found by rotation fo the $x-y$ frame along the s-axis. The the coefficients are roughly constant (see color scale), best fits yields $\tau_x = 0.018, \tau_y = 0.88$ at normal angle. Some intrinsic dependance is present in the polar angle and cross-polarization are induced. This is the *maltese* effect, resulting from the fact that the projection of $x-y$ are not orthonormal in the transverse plane for $\theta \neq 0$. This effect is well described by the matrix formalism.

F

Integral Identities of Zernike Mode Decomposition

In Section 5.3.7 a Zernike Mode has been introduced and several consequent formulas. We perform derivation of the result in that Section in this Appendix.

Demonstration of (5.63) Starting from Equation (5.58) with the change of variables (5.42), considering that:

$$\sin\theta d\theta = \frac{\sin\theta}{\cos\theta} d(\sin\theta) = \frac{\sin^2\theta_{max}}{\cos\theta}\xi' d\xi' \tag{F.1}$$

the integration is recasted as:

$$\mathbf{g}_{f|\Sigma_0} = \mathcal{C}\left\{\int_0^1\int_0^{2\pi} \frac{1}{\cos\theta}\mathbb{J}_{g(\theta,\phi,\lambda)} e^{ik\rho\xi'\sin\theta_{max}\cos(\phi-\alpha)} e^{ikz\cos\theta}\xi' d\xi' d\phi\right\}\bar{\mathbf{e}}_{in}^{[\xi,\eta]} \tag{F.2}$$

where θ now is a function of ξ and:

$$\mathcal{C} = \left(\frac{ikf\sin^2\theta_{max}e^{-ikf}}{2\pi}\right) \tag{F.3}$$

Introducing the effective Jones matrix in Equation (5.60) and the Zernike representation in Equation (5.61) the integral is of the form:

$$\mathbf{g}_{f|\Sigma_0} = \mathcal{C}\left\{\sum_{q=-\infty}^{\infty}\sum_{s=|q|,step=2}^{\infty} \mathbb{J}^{[q,s]}_{g(\theta_{max},kz,\lambda)}\int_0^1\int_0^{2\pi} e^{iq\phi}R^{|q|}_{s(\xi')}e^{ik\rho\xi'\sin\theta_{max}\cos(\phi-\alpha)}\xi' d\xi' d\phi\right\}\bar{\mathbf{e}}_{in}^{[\xi,\eta]} \tag{F.4}$$

The integral in (F.4) is known and reported, along with many other useful identities, in [81], (reference to Eq. (5) of that paper). Adjusting for our notation:

$$\int_0^1\int_0^{2\pi} e^{iq\phi}R^{|q|}_{s(\xi')}e^{ik\rho\xi'\sin\theta_{max}\cos(\phi-\alpha)}\xi' d\xi' d\phi = 2\pi i^s\left(\frac{J_{s+1(\tilde{\rho})}}{\tilde{\rho}}\right)e^{iq\alpha} \tag{F.5}$$

with:

$$\tilde{\rho} = k\rho\sin\theta_{max} \tag{F.6}$$

Final substitution and rearrangement provides the desired expression (5.63)

Demonstration of (5.62) The coefficients reported in (5.62) are expansion coefficients of the effective Jones matrix such that it can be written in form of a Zernike Series (5.61). The azimuthal expansion is merely a Fourier series expansion, reported in many literature resources. The radial expansion follows from orthogonality of the radial Zernike polynomials $R_s^{|q|}$ on the unit circle for a given q. Those are defined in Appendix D. The orthogonality relations of the Zernike complete basis is reported in [81] as:

$$\int_0^1\int_0^{2\pi} R^{|q|}_{s(\xi')}R^{|q'|}_{s'(\xi')}e^{i(q-q')\phi}\xi' d\xi' d\phi = \frac{\pi}{s+1}\delta_{qq'}\delta_{ss'} \tag{F.7}$$

Where $\delta_{jj'} = [1 \forall j = j', 0\ otherwise]$ is the Kronecker Delta. By multiplying (5.61) for an arbitrary Zernike basis and using this identities, relationships (5.62) are found once the 2π scaling factor is used in the Fourier Transform. We have verified with various functions and the splines integration routines that the defined Zernike transform is the series expansion of the initial function.

Demonstration of (5.64) It follows from the expression of the focal fields in Equation (5.63) that (5.64) is verified upon conjugation of the scalar quantities and definition of the Mueller Row vector as:

$$\mathbb{M}^{[q,q',s,s']}_{(\theta_{max},kz,\lambda)} = \left[\mathbb{A}\left(\left(\mathbb{J}^{[2,2]}_{e[q,s]}\right) \otimes \left(\mathbb{J}^{[2,2]}_{e[q',s']}\right)^*\right)\left(\mathbb{A}^{-1}\right)\right]^{[1,3]} \tag{F.8}$$

where $\mathbb{A}$ has been already defined in (4.44). Equation (F.8) is a generalization of the expression (4.43) common in Mueller Formalism. The transformation can arbitrarily be applied to two different matrices since it merely represents an algebric manipulation of matrices such that the trigonometric property:

$$\mathbb{J}^{[2,2]}_{[q,s]}\mathbf{e}^{[\xi,\eta]} \cdot \left(\mathbb{J}^{[2,2]}_{[q',s']}\mathbf{e}^{[\xi,\eta]}\right)^* = \mathbb{M}^{[q,q',s,s']}_{(\theta_{max},kz,\lambda)}\mathbf{s}_{|p=1} \tag{F.9}$$

is generally fulfilled, where the vectorial quantities are defined in Equations (4.38) and (4.39) of this report. In (F.8), the notation $[i,j]$ represent matrix minors and $\otimes$ the Kronecker Product. The first row is extracted by the operation. The Jones matrix are reduced to 2×2 in the $x-y$ frame. It is assumed that the z component of the electric field intensity ($e_z e_z^*$) does not contribute to the detected energy intensity (being associate with fully transverse wave-vectors components, they may end up in stray-light or being reflected at the edges). In Mueller Formalism the Stokes vector are defined conventionally only for two-dimensional fields (more than four Stokes parameters would be required for general three-dimensional fields).

Demonstration of (5.65) Following from expressoin (5.64), integration in a region $\mathcal{A}_p$ of $\left(\frac{s+s'+2}{2\pi}\right) f_{[q,s]} f^{\dagger}_{[q',s']}$ (scaling factors used for normalization convenience) leads to:

$$\mathcal{F}_{[q,s,q',s'](\tilde{\rho}_{max})} = \left(\frac{s+s'+2}{2\pi}\right)\int_{\mathcal{A}_p} i^{s-s'}\left(\frac{J_{s+1(\tilde{\rho})}J_{s'+1(\tilde{\rho})}}{\tilde{\rho}}\right)e^{i(q-q')\alpha}d\tilde{\rho}d\alpha \tag{F.10}$$

For an encircled region $\mathcal{A}_p : \{\tilde{\rho} \leq \tilde{\rho}_{max}\}$ the previous assumes a known analytical solution given by:

$$\mathcal{F}^{(in)}_{[q,s,q',s'](\tilde{\rho}_{max})} = (s+s'+2)\begin{cases} \dfrac{\tilde{\rho}_{max}\left(J_s J_{s'+1} - J_{s'}J_{s+1}\right) + (s'-s)\,J_{s+1}J_{s'+1}}{(s-s')(s+s'+2)} & \forall s \neq s', q = q' \\ \dfrac{\tilde{\rho}_{max}^{2s+2}\ {}_2F_{3(s+1,s+3/2,s+2,s+2,2s+3,-\tilde{\rho}^2_{max})}}{2^{2s+3}(s+1)\Gamma^2_{(s+2)}} & \forall s = s', q = q' \\ 0 & otherwise \end{cases} \tag{F.11}$$

where ${}_2F_3$ is the hyper-geometrical function, all Bessel functions of the first kind are evaluated in $\tilde{\rho}_{max}$ and the set of q, s integers includes only the even combinations $s-|q|, s'-|q'| > 0$. The given solution has been found by manipulation of Wolfram-Alpha resolved integrals. The evaluation of the Bessel and hyper-geometrical functions is performed by means of the *mpmath* Python library. The expression for $\overleftrightarrow{\tau}_{(\hat{s},\lambda)}$ is found by using (5.3.4) and definition of the direction transmittance as in Section (5.3.4).

Demonstration of (5.68) For deriving an explicit expression for $\mathbb{M}^{[q,q',s,s']}_{p(\theta_{max},kz,\lambda)}$, one must consider swapping the indeces of the magnetic field and electric fields according to opportune permutation matrices, in order to determine an expression of the type $\mathbf{e}'_{f|\Sigma_0,x}\mathbf{e}''^*_{f|\Sigma_0,x} + \mathbf{e}'_{f|\Sigma_0,y}\mathbf{e}''^*_{f|\Sigma_0,y}$ for the permutated fields, which is the one used in Mueller Formalism. For example, for p_z (third row of $\mathbb{M}^{[q,q',s,s']}_{p(\theta_{max},kz,\lambda)}$) equation (F.8) could be used with the matrices:

$$\mathbb{J}^{[2,2]}_{e'[q,s]} = \mathbb{J}^{[2,2]}_{e[q,s]} \qquad \mathbb{J}^{[2,2]}_{e''[q,s]} = \mathbb{R}\mathbb{J}^{[2,2]}_{h[q,s]} \qquad \mathbb{R} = \begin{bmatrix} 0 & -1 \\ 1 & 0 \end{bmatrix} \tag{F.12}$$

that's similar to the conventional approach used with the Pauli Matrices in Mueller Formalism.

Demonstration of (5.69) To calculate the OTF, we need to perform the autocorrelation between Zernike Polynomials in the Fourier domain. That's equivalent to the FFT of the product of the Fourier transform of the Zernike Polynomials. Hence we have to calculate the quantity:

$$\mathcal{F}^T\{\langle \mathbf{e}_{f|\Sigma_0}\mathbf{e}^\dagger_{f|\Sigma_0}\rangle\} = \int_{-\infty}^{\infty}\int_{-\infty}^{\infty}\langle \mathbf{e}_{f|\Sigma_0}\mathbf{e}^\dagger_{f|\Sigma_0}\rangle e^{-i(k_x x_f + k_y y_f)}dx_f dy_f \tag{F.13}$$

Re-expressing for convenience in non dimensional variables we determine:

$$\mathcal{F}^T\{\langle \mathbf{e}_{f|\Sigma_0}\mathbf{e}^\dagger_{f|\Sigma_0}\rangle\} = f^2\sin^2\theta_{max}\left\{\sum_{q,q',s,s'}\mathbb{M}^{[q,q',s,s']}_{(\theta_{max},kz,\lambda)}\mathcal{I}^{[q,q',s,s']}_{(\xi_k,\phi_k)}\right\}\mathbf{s}_{in} \tag{F.14}$$

with:

$$\mathcal{I}^{[q,q',s,s']}_{(\xi_k,\phi_k)} = \int_{-\infty}^{\infty}\int_{-\infty}^{\infty}e^{i(q-q')\alpha}i^{s-s'}\left(\frac{J_{s+1(\tilde\rho)}J_{s'+1(\tilde\rho)}}{\tilde\rho^2}\right)e^{-i(\tilde k_x\tilde x+\tilde k_y\tilde y)}d\tilde x d\tilde y \tag{F.15}$$

and the variables defined as:

$$\tilde k_x = \frac{k_x}{k\sin\theta_{max}} = \xi_k\cos\phi_k \qquad \tilde k_y = \frac{k_y}{k\sin\theta_{max}} = \xi_k\sin\phi_k \qquad \tilde\rho = \sqrt{\tilde x^2+\tilde y^2} \tag{F.16}$$

Changing integration variables in polar coordinates:

$$\mathcal{I}^{[q,q',s,s']}_{(\xi_k,\phi_k)} = i^{s-s'}\left\{\int_0^{\infty}\int_0^{2\pi}\left(\frac{J_{s+1(\tilde\rho)}J_{s'+1(\tilde\rho)}}{\tilde\rho}\right)e^{i(\tilde\rho\xi_k\cos(\phi_k-\alpha)+(q'-q)\alpha)}d\tilde\rho d\alpha\right\}^* \tag{F.17}$$

Integrating in α and resolving the conjugation, we determine (using known integrals in [28] and using the scaling factor $(s+s'+2)$ for further convenience):

$$\mathcal{I}^{[q,q',s,s']}_{(\xi_k,\phi_k)} = \left(\frac{2\pi i^{q-q'+s-s'}e^{i(q-q')\phi_k}}{s+s'+2}\right)\mathcal{I}^{[q,q',s,s']}_{(\xi_k)} \qquad \mathcal{I}^{[q,q',s,s']}_{(\xi_k)} = (s+s'+2)\int_0^{\infty}\left(\frac{J_{s+1(\tilde\rho)}J_{s'+1(\tilde\rho)}}{\tilde\rho}\right)J_{q-q'(\tilde\rho\xi_k)}d\tilde\rho \tag{F.18}$$

In [81] an analytical expression for the OTF is also found by integrating the above. This is however overly complicated for the present report. An iterative adaptive quadrature numerical integration to arbitrary precision has been performed for the purpose, which is reasonably efficient in the variables appearing in (F.18). In plots on Figure 5.13 precision has been set to $\epsilon = 10^{-6}$ which is a good compromise for evaluation time.

The OTF is then determining by normalizing the above expression with respect to its value in the origin of the spectrum. We recognize in the origin of the spectrum ($k_x = k_y = 0$) the quantity $\mathcal{F}^T\{\langle \mathbf{e}_{f|\Sigma_0}\mathbf{e}^\dagger_{f|\Sigma_0}\rangle\}_{|\xi_k=0}$ to be, by definition, proportional to the wide pixel transmittance defined in 5.3.4. In fact:

$$\mathcal{F}^T\{\langle \mathbf{e}_{f|\Sigma_0}\mathbf{e}^\dagger_{f|\Sigma_0}\rangle\}_{|\xi_k=0} = \int_0^1\int_0^{2\pi}\tilde{\mathbf{M}}^T_{0(\xi',\phi)}\xi' d\xi' d\phi = \overleftrightarrow{\tau}^{\infty}_{(\lambda,\hat{\mathbf{s}})}\left(\frac{\pi}{\cos^2\theta_{max}}\right)\mathbf{s}_{in} \tag{F.19}$$

To verify the above formulas, the known solution for the correlation of two pupils is known, which correspond to the mode $q = q' = s = s' = 0$ only. That's given by [81]:

$$\overline{OTF}^{(id)} = \frac{2(\arccos(\xi_k) - \xi_k\sqrt{1-\xi_k^2})}{\pi} \tag{F.20}$$

we verified to numerical precision that the first mode computed with (F.18) corresponds to this analytical solution. It is finally important to force in the above functions the conditions of existance of the indeces bases. The above integral is only defined for $|q-q'| \leq |s-s'|$ and when both $q-q', s-s'$ are even or both odd.

Demonstration of (5.82) *The following derivation shall be reviewed in future work.*
To demonstrate (5.82), we recall the convolution property of two functions:

$$\int_{-\infty}^{\infty}\int_{-\infty}^{\infty}g_{(x,y)}h_{(x'-x,y'-x)}dxdy = \frac{1}{4\pi^2}\int_{-\infty}^{\infty}\int_{-\infty}^{\infty}\tilde g_{(k_x,k_y)}\tilde h_{(k_x,k_y)}e^{i(k_x x+k_y y)}dk_x dk_y \tag{F.21}$$

with the Fourier Transform, for $f = g, h$, given by:

$$\tilde{f}_{(k_x,k_y)} = \mathcal{F}^T\{f\} = \int_{-\infty}^{\infty}\int_{-\infty}^{\infty} f_{(x,y)} e^{-i(k_x x + k_y y)} dxdy \tag{F.22}$$

Combining such property with Equation (F.14) and (5.83), and defining the following transform in the focal point (x_{fi}, y_{fi}):

$$\tilde{S}_{0,av} = \mathcal{F}^T\{\mathbb{M}^{[q,q',s,s']}_{(\theta_{max},\lambda,x_{fi},y_{fi})}\mathbf{S}_{av}\} \tag{F.23}$$

The spectral intensity can be retrieved from the OTF spectrum:

$$I_{\lambda(x_f,y_f,\lambda,t)} = \int\int_{\sqrt{k_x^2+k_y^2}<2k\sin\theta_{max}} \frac{\left(\sin^2\theta_{max}\right)}{4\pi^2} \sum_{q,q',s,s'} \tilde{S}_{0,av}\mathcal{I}^{[q,q',s,s']}_{(\xi_k,\phi_k)} e^{i(k_x x + k_y y)} dk_x dk_y \tag{F.24}$$

Integration to provide the energy in the pixel can be carried out directly, considering that it results in a 2D shifted sinc:

$$\int_{A_p} e^{i(k_x x_f + k_y y_f)} dx_f dy_f = \frac{e^{il_p(k_x+k_y)}}{k_x k_y} \tag{F.25}$$

Reordering, expliciting the expression for $\mathcal{I}^{[q,q',s,s']}_{(\xi_k)}$ and re-expressing $S_{0,av}$ in terms of its spectrum, we can also isolate the integration in the OTF spectrum appearing in the charge expression as:

$$\mathcal{G} = \int_0^{2\pi}\int_0^2 i^{q-q'+s-s'}\mathcal{I}^{[q,q',s,s']}_{(\xi_k)} e^{i(q-q')\phi_k} e^{ik\sin\theta_{max}\xi_k((l_p-x_{fi})\cos\phi_k+(l_p-y_{fi})\sin\theta_k)} \frac{d\xi_k d\phi_k}{4\pi^2\xi_k\cos\phi_k\sin\phi_k} \tag{F.26}$$

Where we have explicited the OTF variables in radial coordinates. $\mathcal{G}$ are hence basis function of the Zernike mode expansion depicting the convolution integral appearing in the imaging equations.

G
Symbols

Symbol	Description	Value
ϵ_0	Vacuum permittivity	$8.854 \times 10^{-12} F/m$
μ_0	Vacuum (magnetic) permeability	$1.256 \times 10^{-6} H/m$
η_0	Vacuum (electro-magnetic) wave impedance	376.73Ω
c_0	Velocity of light in vacuum	$299792458 m/s$
π	Pi constant	3.14159...
h	Planck Constant	$6.626 \times 10^{-34} m^2 kg/s$
q_e	Charge of electron	$1.60218 \times 10^{-19} C$
r_{er}	Radius of Earth	$6371 km$
J_2	Coefficient of Earth's second zonal term oblateness perturbation	$1.08263 \times 10^{-3} [-]$
ω_{er}	Angular velocity of Earth	$7.292 \times 10^{-5} rad/s$
g_0	Earth's averaged gravitational field	$9.81 m/s^2$
ω_p	Earth's revolution angular velocity	$1.911 \times 10^{-7} rad/s$

Table G.1: Constants used throughout the report

Symbol	Description	Value
a, P	Lattice size (as measured between parallel edges)	m
$\mathbb{A}$	A matrix appearing in Mueller formulations	-
A_{ep}	Area of Entrance Pupil (or domain of integration)	m^2
$\mathcal{A}_p$	An incident area of propagation	m^2
$\mathcal{A}_s$	Area of the source	m^2
$\mathcal{A}_{sc}$	Scanning area (or domain) on ground (object space)	m^2
AR	Aspect Ratio D_x/D_y of elliptical inclusion diameters	-
c	In effective medium formulation, volume filling factor (as ratio of inclusion volume per bare cavity volume, without correction of the occupied volume of inclusion)	-
c_i	Velocity of light in medium i	m/s
d_i	A distance of propagation	m
D_{ep}	Diameter of circular entrance pupil	m
$\mathbf{E}$	Electric Field	V/m
$\mathbf{E}_\omega$	Electric Field Phasor	$V \cdot s/m$
$\mathbf{E}_{\omega,k}$	Electric Field Phasor in Space Domain	$V \cdot s \cdot m$
$\boldsymbol{\mathcal{E}}^{\pm}_{\omega,k,i,m}$	Polarization directions of electric field for medium i and polarization m, for positive or negative traveling wave	-
$\tilde{\mathbf{E}}$	Electromagnetic deterministic and monochromatic observable with same second-order statistical power	$V\sqrt{s}/m$
$\mathbf{e}$	Normalized electric field	-
$\mathbf{e}^{(top,+)}_{k,f\|\Sigma_0}$	Normalized electric field in the Space Fourier domain, in cartesian frame, at the top of the spectral filter Only forwards traveling component. 3-dimensional	m^2
$\mathbf{e}^{(top,+)}_{k,f\|\Sigma_{[p,s]}(k''_x,k''_y)}$	Same as above, but in the ps transverse frame. 2-dimensional	m^2
e_γ	Energy of a photon	J
f_{eff} or simply f	Focal length of Optical System	m
$f_\#$	F-Number of Optical System, as f_{eff}/D_{ep}	-
$f^{[q,q',s,s']}_{(\phi)}$	Focal fields Zernike basis mode in the detector plane	-
FOV	Field of view (maximum) of the scanner area mapping the detector on ground	rad

Table G.2 continued from previous page

Symbol	Description	Value
$\tilde{\mathcal{F}}_i$	Electromagnetic Field Transverse Vector $(E_x, E_y, \eta_0 H_x, \eta_0 H_y)$ in a medium i	$V \cdot s \cdot m$
$\tilde{\mathcal{F}}_i^{\pm}$	Electromagnetic 4D Field Vector in ps frame $(E_p^+, E_p^-, E_s^+, E_s^-)$	$V \cdot s \cdot m$
$\tilde{\mathcal{F}}_{z,i}$	Electromagnetic z fields vector $(E_z, \eta_0 H_z)$	$V \cdot s \cdot m$
$\boldsymbol{\mathcal{F}}^{\pm(cav,out)}_{(k'_x,k'_y,\omega)}$	4-dimensional field in the ps transmitted and reflected frames, outside of the outer matching plane of the cavity	Various depending on normalization
$\boldsymbol{\mathcal{F}}^{\pm(cav,in)}_{(k_x,k_y,\omega)}$	4-dimensional field in the ps transmitted and reflected frames, outside of the inner matching plane of the cavity	Various depending on normalization
$\boldsymbol{\mathcal{F}}^{\pm(f)}_{(k'_x,k'_y)}$	4-dimensional field in the ps transmitted and reflected frames, at the focal plane	Various depending on normalization
$\boldsymbol{\mathcal{F}}^{\pm(top)}_{(k_x,k_y)}$	4-dimensional field in the ps transmitted and reflected frames, at the top of the filter	Various depending on normalization
$\mathcal{F}_{[q,s,q',s'](\tilde{\rho}_{max})}$	Basis Functions of Zernike Modes solution depicting enclosed energy in a circular region of radius $\tilde{\rho}_{max}$	-
G_{ij}	Etendue subtended between area i and j	m^2
GSD_0	Ground Sampling Distance on ground at nadir, mapping to a sub-pixel (a pixel in the polarized arrangement)	m
GSD_ρ	Effective ground sampling distance mapping the same area of a distorted pixel projection on ground	m
$GSRE$	Ground-Sub-Resolution element on ground (of sub-pixel, pixel of the polarized arrangement)	m
$\mathbb{G}^{(m)}_{(k_x,k_y,k'_x,k'_y,\omega)}$	Transfer matrix of cavity taking into account finite diffraction of the structure	-
$\mathcal{G}_{(klp\,\sin\theta_{max},x_{fi},y_{fi})}$	Basis function in the Zernike mode, depicting enclosed energy in convolution at pixel level	-
h_s	Satellite altitude (referenced at mean radius of Earth r_{er})	m
h_i	Height of inclusion	m
$\mathbf{H}$	Magnetic Field	A/m
$\mathbf{H}_\omega$	Magnetic Field Phasor	$A \cdot s/m$
$\mathbf{H}_{\omega,k}$	Magnetic Field Phasor in Space Domain	$A \cdot s \cdot m$
$\boldsymbol{\mathcal{H}}^{\pm}_{\omega,k,i,m}$	Polarization directions of magnetic field for medium i and polarization m, for positive or negative traveling wave	-
$\mathbf{h}^{(top,+)}_{k,f\|\Sigma_0}$	Normalized magnetic field in the Space Fourier domain, in cartesian frame, at the top of the spectral filter Only forwards traveling component	m^2
h_s	Altitude of spacecraft	km
$\tilde{h}_s$	Altitude normalized on Earth's radius h_s/r_{er}	-
I	Orbital Inclination	rad
$\hat{i}_s, \hat{j}_s, \hat{k}_s$	Local reference solidal with satellite	-
$I_{\lambda(\ldots)}$	Spectral Intensity	$W/(m^2 \cdot \mu m)$
$\mathcal{I}^{[q,q',s,s']}_{(\xi)}$	OTF bases of the Zernike Expansion in the radial direction	-
i	An index or the complex number $\sqrt{-1}$, on context	-
j	Medium or coordinate index, on context	-
$J_{s+1(\tilde{\rho}_{max})}$	Bessel Function of the first kind, of order $s+1$ evaluated at $\tilde{\rho}_{max}$	-
$\mathbb{J}^{\pm}_{k\to i}$	Transmission or Reflection Jones matrices, as minors of the Scattering Matrix $\mathbb{S}_{k\to i}$	
$\mathbb{J}^{(o)}$	(Transmission) Jones matrix of the Optical System	-
$\mathbb{J}^{(m)}_{\|\Sigma}$	(Transmission) Jones matrix of Metasurface (in ps frame)	-
$\mathbb{J}^{+}_{(k_x,k'_x,k_y,k'_y)}$	Transmission Jones matrix of finite diffraction coupled structure	-
$\mathbb{J}^{-}_{(k_x,k'_x,k_y,k'_y)}$	Reflection Jones matrix of finite diffraction coupled structure	-
$\mathbb{J}_e$	Final (Transmission) Jones matrix of transformation from entrance pupil to focal plane for electric field	-
$\mathbb{J}_h$	Same as above, but relating electric field to the (non-dimensional) magnetic field at the focal plane	-
$\mathbb{J}_f$	Jacobian of transformation from non-dimensional coordinates of detector to Earth's surface	-
k	Wave-Number (Module)	$1/m$

Table G.2 continued from previous page

Symbol	Description	Value
$k_0 = \omega/c_0$	Wave-Number in Vacuum for a given frequency ω	$1/m$
$\mathbf{k} = (k_x, k_y, k_z)^T$	Wave-Number (Vector)	$1/m$
$\mathcal{K}_i$	Polarized Arrangement (3 pixels)	-
l_r	Size of resonators cell, as periodic array. Equal or multiple of pixel size	μm
l_p	Lateral extent of a pixel (edge dimension)	μm
L_d	Lateral extent of detector (edge)	cm
$L_{\omega(...)}$	Spectral Radiance (per unit frequency)	$W \cdot s/(m^2 \cdot srad)$
$L_{\lambda(...)}$	Spectral Radiance (per unit wavelength)	$W/(m^2 \cdot \mu m \cdot srad)$
m	Polarization Index	-
m_0	Paraxial magnification factor h_s/f_{eff} from detector to ground	-
$\tilde{\mathbb{M}}_{z\rightarrow xy}$	Projection Matrix of 4-dimension field to z fields in arbitrary layer	-
$\mathbb{M}_i$	Various auxiliary matrices introduced in the report	-
$\boldsymbol{\mathcal{M}}_{k,i}$	A generic state vector of arbitrary dimensions, in Scattering Formulations	Various
$\mathbf{M}_0^{\infty}$	First Mueller Row associated with $\mathbb{J}_e$	-
$\mathbb{M}^{[q,s,q',s']}_{(\theta_{max},kz,\lambda)}$	Mueller Row of the Zernike expansion Jones matrix of the focal fields	-
$\mathbb{M}_{\mathcal{K}_i}$	Optimal reconstruction matrix for arrangement $\mathcal{K}_i$	-
$\hat{n}_{\mathcal{A}_s}$	Normal of Source Area	-
n_i	Refractive index in medium i	-
n_e	Absorbed charges at detector (electrons)	electrons
n_λ	Number of spectral bands in arrangement	-
$\hat{\mathbf{n}}_{ij}$	Normal versor of surface separating mediums i and j	-
P, a	Lattice size (as measured between parallel edges)	m
$\tilde{\mathbb{P}}_i$	Non-dimensional propagation matrix in arbitrary layer i	-
$\mathbb{P}_{in,out}$	A permutation matrix in Scattering Formulations	-
$\mathcal{Q}$	Correction factor in stationary model fit of experimental data, relating filling factors	-
q_u, q_v	(Dimensional) curvilinear coordinates mapping Earth object space	m
$\hat{q}_u, \hat{q}_v$	Local versors describing the tangent space of the mapping surface	-
$\tilde{\mathbf{q}} = (\tilde{q}_u, \tilde{q}_v)$ or $(\tilde{q}_x, \tilde{q}_y)$	(Non-dimensional) coordinates q_u, q_v scaled on satellite altitude h_s	-
$\mathbb{R}_i$	Projection matrix of polarization versors for medium i	-
$\mathbb{R}_{(\mathbf{w},\beta)}$	A matrix representing a rotation of an angle β along the axis $\mathbf{w}$	-
$\mathbb{R}_0$	Projection Matrix $\mathbb{R}_i$ evaluated in vacuum	-
$\mathbf{r}_{ob}$	Distance (vector) from Earth's center of gravity to observation point	m
$r^{ss,pp,ps,sp}$	A coefficient appearing in the minors of the Transfer Matrix	-
$\mathbf{r}_{e,i}$	A vector of point i (from intercept with optical axis) on the pupil	m
$\mathcal{R}$	In general, an intensity reflectance	-
S_w	Swath measured as maximum arc subtended by scanned area on Earth's center of mass	km
$\mathbb{S}_{k\rightarrow i}$	Scattering matrix between state vectors from medium k to medium i	-
$\mathbb{S}_{lm}$	Left-Scattering matrix minor including the transmission and reflection Jones matrices	-
$\mathbf{S}$	Poynting Vector	W/m^2
$\mathbf{S}_\omega$	Poynting Vector in Frequency Domain	$W \cdot s/m^2$
$\mathbf{s} = \mathbf{k}/k_0$	Normalized Wave-Number versor	-
$\mathbf{s}^{(in)}$	Stokes parameters at input of entrance pupil (non-dimensional)	-
SNR^{St}	Signal to Noise ratio of reconstructed Stokes (estimation)	-
$SNR^{(0)}$	Signal to Noise ratio of pixel upon non-polarized input field	-
$\mathcal{S}_{(\Delta\lambda)}$	Spectral Quality of filter, defined as ratio of enclosed spectral energy in $\Delta\lambda$	-
s_x, s_y	Cosine directors of the wave-vector in a transverse plane	-
$s_{\perp,i}$	Cosine directors in the transverse plane projection of arbitrary ray connecting an observation point to a point at the pupil	-

Table G.2 continued from previous page

Symbol	Description	Value
$\hat{\mathbf{s}}_i$	Direction of propagation of incoming ray to pupil from the object source area Alternatively, direction of the incident far-field Poynting Vector	-
Δt	Permanence time of a point on a pixel (or on a detector region)	s
Δt_{ob}	Assumed time-frame in which the observation object has temporally constant emission properties	s
t	Time	s
t_0, t_1, t_2	Some complex-valued scalar functions appearing in Zernike transforms of unpolarized pixels	-
$t_{\lambda,res}$	Spectral time resolution, interval of time over which the temporal nature of the measured field is distinguishable for one wavelength over the full polarization information	s
$t_{(-)}^{pp,ss,ps,sp}$	Various entries of the transfer matrix minors (consistent with state vectors expressions)	-
$\mathbb{T}_i^{[xy,ps]}$	4D Transfer Matrix in xy or in ps frames.	-
$\mathbb{T}_{j(k'_x,k'_y,\omega)}^{\infty}$	4D Transfer matrix of array of resonator, infinitely wide	-
T_{beat}	Beating period	s
$\mathcal{T}$	In general, an intensity transmissivity	-
u	Angle between satellite local direction and ascending node (sum of argument of periapsis and true anomaly)	rad
$\mathbf{v} = (v_x, v_y, v_z)$	A generic vector	Various
$\mathbf{v}_s$	Velocity (vector) of the satellite orbiting Earth with respect to an inertial frame	m/s
v_d	Local observed velocity of a point solid with ground on the detector	m/s
$\mathbf{v}_{gt}$	Ground-velocity, defined as relative velocity of an observed point with respect to satellite	km/s
$\mathcal{V}_{sc}$	Volume domain of scanned region from observation geometry to pupil	m^3
$\mathbb{W}$	Cross-Spectral Density Tensor	V^2s/m^2
$\mathbb{W}^{\infty}$	Cross-Spectral Density Tensor in the far-field	V^2s/m^2
x, y	Some transverse coordinate on a transverse plane	m
x_f, y_f or, on context x, y, ρ	Focal coordinates with respect to Nadir center of detector (cartesian or polar)	m
$\tilde{x}, \tilde{y}, \tilde{\rho}$	Normalized detector coordinates on effective focal length (in Chapter 6). Normalized detector coordinates on $(k \sin\theta_{max})^{-1}$ (in other Chapters)	-
x_{fi}, y_{fi}	Focal coordinates of a generic focal point	m
$\mathcal{X}$	Cross-Product Operator Matrix	-
z_1	Focal distance of the focused image as predicted by the lens equation	m
$\tilde{z}_1$	Non dimensional focal distance over the effective focal length	-
z_2	Distance of (point of) spacecraft from observation point of ground	m
z_{21}, z_{22}	Non paraxial distances from observation point to pupil in geometrical generality, for two points	m
Δz_2	Non paraxial module of the difference between observation vectors connecting ground points to pupil	m
$\mathcal{Z}$	A (radial) Zernike Transform	-

α, α_e	Azimuthal angles of a coherent sub-bundle of rays respectively over focused point on the detector and on entrance pupil	rad
$\alpha_{(\theta_{max})}$	A macroscopic apodization factor due to focusing geometry of the pupil	-
$\overleftrightarrow{\alpha}_{eff}$	Apodization matrix taking into account sub-bundle distribution of input field	-
γ	Linear polarization angle in Poincaré Sphere	rad
Γ	Cross-Correlation tensor	V^2/m^2
δ^n	A delta Diraq function of order n	-
δ	Orientation angle of the axis of the elliptical inclusion	rad
$\hat{\boldsymbol{\varepsilon}}_{\parallel}$	Versor parallel to the transverse plane (perpendicular to incidence plane) Same for both waves directions	-

Table G.2 continued from previous page

Symbol	Description	Value
$\hat{\varepsilon}^{\pm}_{\perp,i}$	Versor parallel to the incidence plane (and perpendicular to wave-vector) for forwards or backward traveling wave.	-
$\overleftrightarrow{\epsilon}_{\omega}$	Permittivity Tensor in Time Frequency Domain	F/m
$\overleftrightarrow{\epsilon}_{eff,\omega}$	Effective Permittivity Tensor in Time Frequency Domain (inclusive of Ohmic Losses)	F/m
$\overleftrightarrow{\epsilon}_{r}$	Effective Relative Permittivity Tensor in Time Frequency Domain	-
$\epsilon_{i(\Delta T)}$	Thermal strain	-
ϵ_i	(Relative) permittivity of inclusion	-
ϵ_m	(Relative) permittivity of bare cavity	-
ζ	Correcting factor in effective model fit of experimental values, as exponential of aspect ratio	-
$\langle\zeta\rangle$	A random number used in Monte Carlo tolerancing analysis	-
ρ	Radius at detector plane, from a defined focal point at (x_{fi}, y_{fi})	m
ρ (on context)	PDL module vector of an optical device, representing polarization power	
$\tilde{\rho}$	Non dimensional variable $k\rho \sin\theta_{max}$, with $\rho = \rho_f$ radius at detector focal plane	-
$\rho^{pp,ss,ps,sp}$	Amplitude (complex) reflection in Scattering Matrix	-
ρ_{ob}	Radial parametrization of obervation point coordinates	m
ρ_{ei}	Radial coordinate at pupil of optical system, in point i, where specified.	m
$\Sigma_i^{[\xi,\eta]}$	Matrix of change of reference frame $[\xi,\eta] \rightarrow [x,y]$	-
$\Sigma_i^{[p,s]}$	Matrix of change of reference frame $[p,s] \rightarrow [x,y]$	-
$\Sigma^{[\phi]}$	Matrix of arbitrary rotation along the third axis of a reference system	-
$\tilde{\sigma}_{(\Delta\mathbf{r}_{ob})}$	A weak spectral correlation function of the Cross-Correlation Tensor $\mathbb{W}$	-
σ_i	Pauli-Matrices used to link Stokes parameters to Cross-Correlation Tensor	-
τ	Difference in measuring time of Cross-Correlation Tensor	s
$\tau^{pp,ss,ps,sp}$	Amplitude (complex) transmittances in Scattering Matrix	-
$\overleftrightarrow{\tau}^{\infty}_{(\lambda,\mathbf{r_{ob}})}$	Spectral Wide Focal Transmittance (directional, in intensity).	-
$\overleftrightarrow{\tau}^{\infty}_{(\mathbf{r}_{ob})}$	Band Wide Focal Transmittance (directional, in intensity).	-
$\overleftrightarrow{\tau}^{\delta,\infty}_{(\mathbf{r}_{ob})}$	Transmittance (row) of a polarized pixel rotated of δ with respect to cartesian frame.	-
$\overleftrightarrow{\tau}^{(f)}_{(\mathbf{r}_{ob},\lambda)}$	Finite Spectral Focal Transmittance (directional, in intensity, including effects of diffraction) in a certain circular enclosed region	-
η	(Electromagnetic) Impedance	Ω
η (on context)	Local variable of streamlines on detector	m
η_b	Finite efficiency of an idealized bandpass filter, used for theoretical analysis of condition number	-
η_e	Quantum efficiency of detector	-
η_r	Relative (Electromagnetic) Impedance	-
χ	Circular polarization angle in Poincare Sphere	rad
χ_s	Auxiliary variable for time-smearing effect description	-
ω	Frequency of monochromatic electromagnetic contribution	s^{-1}
$\tilde{\omega}$	Ratio between angular velocities ω_{er}/ω_s	-
ω_{beat}	Frequency of beating period	s^{-1}
ω_s	Angular velocity of satellite	rad/s
Ω	Longitude of ascending node measured from inertial reference direction	rad
$d\Omega_{gr\rightarrow e}$	Solid angle subtended by an Earth infinitesimal area on (a point) of the pupil	$srad$
Ω_p or simply Ω	Solid angle subtended by pupil on point of pixel Taken as $\pi \sin\theta^2_{max}$	srad
$\Theta_{\lambda(\ldots)}$	Spectral Directional Power	$W/(\mu m \cdot srad)$
$\Theta^{e}_{(\lambda,\mathbf{r}_{ob})}$	Spectral Directional Power at Entrance Pupil of Optical System	$W/(\mu m \cdot srad)$
$\Theta^{\infty(f)}_{(\lambda,\hat{\mathbf{s}})}$	Spectral Directional Power at Focal Plane	$W/(\mu m \cdot srad)$
θ_0	Polar Angle of wave-vector (in vacuum)	rad
θ	Polar angle of focusing of a sub-bundle of rays on optical axis, unless differently specified	rad

Table G.2 continued from previous page

Symbol	Description	Value
θ_{ob}	Polar angle of observation point with Earth's center of gravity	rad
θ_{in}	Angle between chief-rays of a coherent sub-bundle of rays and the optical axis	rad
$\Delta\theta_{in}$	Angular deviation between marginal and chief-ray of a coherent sub-bundle due to non perfect collimation	rad
$\Delta\theta_{scatt}$	Assumed angular range over which the incoming intensity field is angular-independent	rad
$\Delta\theta_{rec}$	Angular resolution extent for consecutive measurements of the same point on ground over Δt_{ob}	rad
θ_r	Half angular (diagonal) resolution of the optical system, mapping chief-ray from center to edge of pixel	rad
θ_n	Radiometric angle between normal of object space tangent area and cosine directors of distance to pupil	rad
θ_g	Geometrical angle defined by $\cos\theta_g = h_s/z_2$	rad
$\Delta\theta_{in}$	Difference between two input rays angles connecting observation point to pupil points	rad
θ_{max}	Maximum focusing half-cone angle	rad
ξ	A transverse plane coordinate for a given plane-wave	m
ξ_k	Radial non-dimensional coordinate in OTF solution, given by $\sqrt{k_x^2 + k_y^2}/(k\sin\theta_{max})$ with k_x, k_y spatial frequencies (in m^{-1}) at focal plane	-
ξ, on context	Local variable of streamlines on detector	m
ξ'	Auxiliary variable $\sin\theta/\sin\theta_{max}$ used in focal integrals	-
$\Delta\xi$	Spatial windowing extent due to velocity smearing on detector	m
κ	Condition number of polarized arrangement reconstruction	-
λ_i	Wavelength in medium i	m
λ_0	Wavelength in vacuum	m
$\Delta\lambda_{co}$	Coherence Spectral Width	m
ψ	Arbitrary phase of the field phasor	rad
ϕ_0	Azimuthal angle of wave-vector (in vacuum)	rad
ϕ	Generally, plane-wave azimuthal angle	rad
ϕ_k (or simply ϕ again)	Azimuthal angle in spectrum OTF solution	rad
$\phi_{ob,i}$	Azimuthal angle parametrization of observation point i on ground	rad
ϕ_{ei}	Azimuthal angle at pupil (from optical axis intercept) of point i	rad
ϕ_e, ϕ_{er}	Azimuthal angles respectively on entrance pupil and on ground for a ray and for an observed point	rad
$\Phi_{\lambda(...)}$	Spectral Power	$W/\mu m$
$\overleftrightarrow{\mu}_\omega$	Effective Permeability Tensor in Time Frequency Domain	H/m
$\overleftrightarrow{\mu}_r$	Effective Relative Permeability Tensor in Time Frequency Domain	$-$

Table G.2: Symbols used throughout the report, ordered alphabetically. Greek Symbols are reported at the end of the list.

References

[1] J. Andrasec, *A Metasurface-Based Miniaturized Spectropolarimeter Design,* (2018).

[2] R. Gabrieli, A. Bartoli, M. Maiorano, U. Bruno, F. Belli, G. Bove, A. Caruso, L. Calamai, I. Manolis, and D. Labate, *3MI OPD optical design: concept and performances,* Optical Systems Design 2015: Optical Design and Engineering VI **9626**, 962628 (2015).

[3] F. Snik, J. H. H. Rietjens, G. van Harten, D. M. Stam, C. U. Keller, J. M. Smit, E. C. Laan, A. L. Verlaan, R. ter Horst, R. Navarro, K. Wielinga, S. G. Moon, and R. Voors, *SPEX: the spectropolarimeter for planetary exploration,* in *Space Telescopes and Instrumentation 2010: Optical, Infrared, and Millimeter Wave* (2010).

[4] L.Pjotr Stoevelaar, J. Berzins, F. Silvestri, S. Fasold, K. Kamali, Z., K. Heiko, F. Eilenberger, F. Setzpfandt, T. Pertsch, S. M. Baumer, and G. Gerini;, *Nanostructure-modulated planar high spectral resolution spectro-polarimeter,* (2020).

[5] J. A. Barsi, K. Lee, G. Kvaran, B. L. Markham, and J. A. Pedelty, *The spectral response of the Landsat-8 operational land imager,* Remote Sensing (2014), 10.3390/rs61010232.

[6] J. S. Tyo, D. L. Goldstein, D. B. Chenault, and J. A. Shaw, *Review of passive imaging polarimetry for remote sensing applications,* Applied Optics **45**, 5453 (2006).

[7] J. Rietjens and A. van Amerongen, *Sentinel 7 MAP Requirements*, Tech. Rep. (2018).

[8] J.-L. Bézy, R. Meynart, M. Porciani, M. Loiselet, G. Mason, U. Bruno, R. De Vidi, I. Manolis, and D. Labate, *The 3MI instrument on the Metop second generation,* **10563**, 122 (2017).

[9] S. J. Wiktorowicz and G. P. Laughlin, *Toward the detection of Exoplanet transits with Polarimetry,* Astrophysical Journal **795** (2014), 10.1088/0004-637X/795/1/12, arXiv:1409.2504 .

[10] L. Rossi and D. M. Stam, *Circular polarization signals of cloudy (exo)planets,* Astronomy and Astrophysics (2018), 10.1051/0004-6361/201832619.

[11] J. Craven-Jones, D. Harrington, J. S. Tyo, M. Escuti, S. Fineschi, D. Mawet, J. Riedi, F. Snik, and A. De Martino, *An overview of polarimetric sensing techniques and technology with applications to different research fields,* Polarization: Measurement, Analysis, and Remote Sensing XI **9099**, 90990B (2014).

[12] L. Rossi and D. M. Stam, *Circular polarization signals of cloudy (exo)planets,* Astronomy and Astrophysics **616** (2018), 10.1051/0004-6361/201832619.

[13] M. I. Mishchenko, G. Videen, V. A. Babenko, N. G. Khlebtsov, and T. Wriedt, *T-matrix theory of electromagnetic scattering by particles and its applications: A comprehensive reference database,* Journal of Quantitative Spectroscopy and Radiative Transfer (2004), 10.1016/j.jqsrt.2004.05.002.

[14] D. Tzarouchis and A. Sihvola, *Light scattering by a dielectric sphere: Perspectives on the Mie resonances,* Applied Sciences (Switzerland) **8** (2018), 10.3390/app8020184.

[15] D. S. Jo, R. J. Park, J. I. Jeong, G. Curci, H.-M. Lee, and S.-W. Kim, *Key factors affecting single scattering albedo calculation: Implications for aerosol climate forcing,* Atmospheric Chemistry and Physics Discussions (2017), 10.5194/acp-2017-1104.

[16] F. Xu, G. van Harten, D. J. Diner, O. V. Kalashnikova, F. C. Seidel, C. J. Bruegge, and O. Dubovik, *Coupled retrieval of aerosol properties and land surface reflection using the Airborne Multiangle SpectroPolarimetric Imager,* Journal of Geophysical Research (2017), 10.1002/2017JD026776.

[17] L. Wu, O. Hasekamp, B. Van Diedenhoven, and B. Cairns, *Aerosol retrieval from multiangle, multispectral photopolarimetric measurements: Importance of spectral range and angular resolution,* Atmospheric Measurement Techniques (2015), 10.5194/amt-8-2625-2015.

[18] O. P. Hasekamp and J. Landgraf, *Retrieval of aerosol properties over land surfaces: Capabilities of multiple-viewing-angle intensity and polarization measurements,* Applied Optics (2007), 10.1364/AO.46.003332.

[19] C. Nazionale, C. Aeronautica, V. Pratica, V. Gobetti, S. Es, V. Einstein, C. Bisenzio, S. Maggiore, U. Generale, and S. Aereo, *METOP-SG 3MI (Multi-viewing Multi-channel Multi-polarization Imaging), a powerful observing mission for future operational applications. Daniele BIRON,* (2013).

[20] S. Grabarnik, J.-L. Bézy, M. Betto, G. Mason, I. Manolis, J. Caron, H. Barré, and R. Meynart, *The MetOp second generation 3MI mission,* , 110 (2017).

[21] X. Chauffleur, G. Marque, A. Weickman, C. Delelis, C. Carvalos, S. Belmana, A. Durieux, and S. Primet, *VNIR and SWIR FPA designs for 3MI instrument: thermal, mechanical and dimensional stability challenges,* (2019).

[22] F. Snik, T. Karalidi, and C. U. Keller, *Spectral modulation for full linear polarimetry,* Applied Optics **48**, 1337 (2009), arXiv:0903.2735 .

[23] M. Bass, *Handbook of Optics (Vol. 1)*.

[24] R. E. Fischer, B. Tadic-Galeb, and P. R. Yoder, *Optical System Design*, p. 809.

[25] K. J. Kasunic, *Optomechanical Systems Engineering* (2015).

[26] W. J. Larson and J. R. Wertz, *Choice Reviews Online* (2013).

[27] Sophocles J. Orfanidis, *Electromagnetic Waves and Antennas* (2008) p. 912.

[28] L. Novotny and B. Hecht, *Chapter 3: Propagation and focusing of optical fields,* Principles of Nano-Optics (2006).

[29] E. M. Born, *Principles of Optics,* Cambridge University Press , 952 (1999).

[30] J. W. Goodman, *Introduction to Fourier Optics McGraw-Hill Series in Electrical and Computer Engineering,* Introduction to Fourier Optics , 491 (1996).

[31] D. M. Grimes and C. A. Grimes, *Classical Electrodynamics,* in *Photon Creation — Annihilation* (2012).

[32] P. Yeh, A. Yariv, C.-s. Hong, and I. Introduction, *Electromagnetic propagation in periodic stratified media.pdf,* **91125**, 423 (1976).

[33] N. C. Passler and A. Paarmann, *Generalized 4 x 4 matrix formalism for light propagation in anisotropic stratified media: study of surface phonon polaritons in polar dielectric heterostructures,* Journal of the Optical Society of America B **34**, 2128 (2017), arXiv:1707.00462 .

[34] N. K. Poulsen, *The Matrix exponential , Dynamic Systems and Control,* , 1 (2008).

[35] R. Starke and G. A. Schober, *Why history matters: Ab initio rederivation of Fresnel equations confirms microscopic theory of refractive index,* Optik **157**, 275 (2018), arXiv:1705.11004 .

[36] H. P. Baltes, *Coherence and the radiation laws,* Applied Physics **12**, 221 (1977).

[37] G. Gbur and T. D. Visser, *Progress in Optics*, Vol. 55 (Elsevier B.V., 2010) pp. 285–341.

[38] Andrey S. Ostrovsky, *Coherent Mode Representations in Optics*, Vol. 66 (2012) pp. 37–39.

[39] T. Kim, R. Zhu, T. H. Nguyen, R. Zhou, C. Edwards, L. L. Goddard, and G. Popescu, *Deterministic signal associated with a random field,* Optics Express **21**, 20806 (2013).

[40] N. G. Parke, *Optical Algebra,* Journal of Mathematics and Physics (1949), 10.1002/sapm1949281131.

[41] K. Sarabandi, *Dyadic Green's Function,* EECS 730 Winter 2009 , 20 (2009).

[42] O. F. Commerce, *A Direct Approach to the Derivation of Electric Dyadic Green ' s Functions,* .

[43] M. Alonso, *Exact description of free electromagnetic wave fields in terms of rays,* Optics Express **11**, 3128 (2010).

[44] J. Tervo and J. Turunen, *Angular spectrum representation of partially coherent electromagnetic fields,* Optics Communications **209**, 7 (2002).

[45] S. Giordano and P. L. Palla, *Dielectric behavior of anisotropic inhomogeneities: Interior and exterior point Eshelby tensors,* Journal of Physics A: Mathematical and Theoretical **41** (2008), 10.1088/1751-8113/41/41/415205.

[46] C. Yeh and F. I. Shimabukuro, *The Essence of Dielectric Waveguides* (2008).

[47] I. Tsukerman and V. A. Markel, *A non-asymptotic homogenization theory for periodic electromagnetic structures,* Proceedings of the Royal Society A: Mathematical, Physical and Engineering Sciences **470** (2014), 10.1098/rspa.2014.0245.

[48] V. Sozio, A. Vallecchi, M. Albani, and F. Capolino, *Closed-form expressions of local effective bianisotropic constitutive parameters for reciprocal metamaterials,* in *8th European Conference on Antennas and Propagation, EuCAP 2014* (2014) pp. 2495–2499.

[49] L. C. Botten, T. P. White, A. A. Asatryan, T. N. Langtry, C. M. de Sterke, and R. C. McPhedran, *Bloch mode scattering matrix methods for modeling extended photonic crystal structures. I. Theory,* Physical Review E - Statistical Physics, Plasmas, Fluids, and Related Interdisciplinary Topics **70**, 13 (2004).

[50] A. Peinado, A. Lizana, J. Vidal, C. Iemmi, and J. Campos, *Optimization and performance criteria of a Stokes polarimeter based on two variable retarders,* Optics Express **18**, 9815 (2010).

[51] J. B. Almeida, *A General Method for the Determination of Matrix Coefficients for High Order Optical System Modelling arXiv : physics / 0410066v1 [physics . optics] 11 Oct 2004,* , 1 (1998), arXiv:0410066v1 [arXiv:physics] .

[52] Opto Engineering, *Telecentric Lenses : basic information and working principles,* Telecentric lens tutorial .

[53] F. J. Bailén, D. Orozco Suárez, and J. C. del Toro Iniesta, *On Fabry–Pérot Etalon-based Instruments. I. The Isotropic Case,* The Astrophysical Journal Supplement Series (2019), 10.3847/1538-4365/aafdb3.

[54] T. Markvart, *The thermodynamics of optical étendue,* Journal of Optics A: Pure and Applied Optics **10** (2008), 10.1088/1464-4258/10/01/015008.

[55] A. Ciccolella, *Mission Analysis aspects for Earth Observations Missions,* (2010).

[56] T. N. A. Press, *Satellite Observations to Benefit Science and Society* (2008).

[57] D. Mortari, M. Wilkins, and C. Bruccoleri, *On Sun-Synchronous Orbits and Associated Constellations,* Paper of the 6-th Dynamics . . . (2004).

[58] A. Romano, *Differentiable manifolds,* in *Modeling and Simulation in Science, Engineering and Technology* (2012).

[59] J. V. Martins, R. Fernandez-borda, and B. Mcbride, *The Harp Hyperangular Imaging Polarimeter and the need for small satellite payloads with high science payoff for science remote sensing,* (2018).

[60] G. G. J. Andrasec , L.P. Stoevelaar , Jonas Berzins, *Assessment study of spectro-polarimeter concepts based on Fabry-Perot cavities and nano-structures,* European Optical Society Biennial Meeting (EOSAM) 2018 (2018).

[61] L. Novotny and B. Hecht, *Principles of Nano-Optics* (2009).

[62] V.-C. Su, C. H. Chu, G. Sun, and D. P. Tsai, *Advances in optical metasurfaces: fabrication and applications [Invited],* Optics Express **26**, 13148 (2018).

[63] D. G. Bhat, *Chemical vapor deposition,* in *Coatings Technology: Fundamentals, Testing, and Processing Techniques* (2006).

[64] H. Knopf, N. Lundt, T. Bucher, S. Höfling, S. Tongay, T. Taniguchi, K. Watanabe, I. Staude, U. Schulz, C. Schneider, and F. Eilenberger, *Integration of atomically thin layers of transition metal dichalcogenides into high-Q, monolithic Bragg-cavities: an experimental platform for the enhancement of the optical interaction in 2D-materials,* Optical Materials Express (2019), 10.1364/ome.9.000598, arXiv:1812.00634 .

[65] J. Takahashi, Y. Itoh, K. Hosoya, P. A. Yanamandra-Fisher, and T. Hattori, *Polarized Transmission Spectrum of Earth as Observed during a Lunar Eclipse,* The Astronomical Journal **154**, 213 (2017), arXiv:1711.01555 .

[66] B. J. Rauscher, M. R. Bolcar, M. Clampin, S. D. Domagal-goldman, M. W. Mcelwain, S. H. Moseley, C. Stahle, C. C. Stark, and H. A. Thronson, *ATLAST detector needs for direct spectroscopic biosignature characterization in the visible and near-IR,* (2015).

[67] P. Feautrier, J. L. Gach, and P. Wizinowich, *State of the art IR cameras for wavefront sensing using e-APD MCT arrays,* Adaptive Optics for Extremely Large Telescopes 4 - Conference Proceedings (2015), 10.20353/K3T4CP1131556.

[68] O. Gravrand and J. Rothman, *HgCdTe quantum detection: From long-wave IR down to UV,* in *Journal of Electronic Materials* (2011).

[69] B. F. Aull, A. H. Loomis, D. J. Young, R. M. Heinrichs, B. J. Felton, P. J. Daniels, and D. J. Landers, *Geiger-Mode Avalanche Photodiodes for Three- Dimensional Imaging,* Lincoln Laboratory Journal (2002).

[70] R. Matthews, M. Sorell, and N. Falkner, *Reverse Engineering the Raspberry Pi Camera V2: A study of Pixel Non-Uniformity using a Scanning Electron Microscope,* (2019), arXiv:1901.03807 .

[71] X. Sun, J. B. Abshire, J. D. Beck, P. Mitra, K. Reiff, and G. Yang, *HgCdTe avalanche photodiode detectors for airborne and spaceborne lidar at infrared wavelengths,* Optics Express **25**, 16589 (2017).

[72] D. Rawlings and G. Averitt, *A linear drive cryocooler for ultra-small infrared sensor systems,* in *Infrared Technology and Applications XL* (2014).

[73] G. Finger, I. Baker, R. Dorn, S. Eschbaumer, D. Ives, L. Mehrgan, M. Meyer, and J. Stegmeier, *Development of high-speed, low-noise NIR HgCdTe avalanche photodiode arrays for adaptive optics and interferometry,* in *High Energy, Optical, and Infrared Detectors for Astronomy IV* (2010).

[74] G. Finger, I. Baker, D. Alvarez, D. Ives, L. Mehrgan, M. Meyer, J. Stegmeier, P. Thorne, and H. J. Weller, *Evaluation and optimization of NIR HgCdTe avalanche photodiode arrays for adaptive optics and interferometry,* High Energy, Optical, and Infrared Detectors for Astronomy V **8453**, 84530T (2012).

[75] A. Singh, V. Srivastav, and R. Pal, *HgCdTe avalanche photodiodes: A review,* (2011).

[76] M. A. Akerman, *Fundamentals of Infrared Detector Operation and Testing,* Fusion Technology (1991), 10.13182/fst91-a29665.

[77] G. A. Lager, J. D. Jorgensen, and F. J. Rotella, *Crystal structure and thermal expansion of α-quartz SiO2 at low temperatures,* Journal of Applied Physics (1982), 10.1063/1.330062.

[78] A. P. Vora, J. B. Rami, A. K. Hait, C. P. Dewan, D. Subrahmanyam, and A. S. Kirankumar, *Mechanical design and qualification of IR filter mounts and filter wheel of INSAT-3D sounder for low temperature,* **10566**, 8 (2017).

[79] D. W. Berreman, *Optics in Stratified and Anisotropic Media: 4x4-Matrix Formulation,* Journal of the Optical Society of America **62**, 502 (1972).

[80] I. Abdulhalim, *Analytic propagation matrix method for anisotropic magneto-optic layered media,* Journal of Optics A: Pure and Applied Optics **2**, 557 (2000).

[81] A. J. E. M. Janssen, *Zernike circle polynomials and infinite integrals involving the product of Bessel functions*, c (2010) pp. 1–45, arXiv:1007.0667 .